

# **Rationalising Pd-Precatalyst Design for Efficient Arylcyanation Reactions**

Joshua Thomas William Bray

*Doctor of Philosophy*

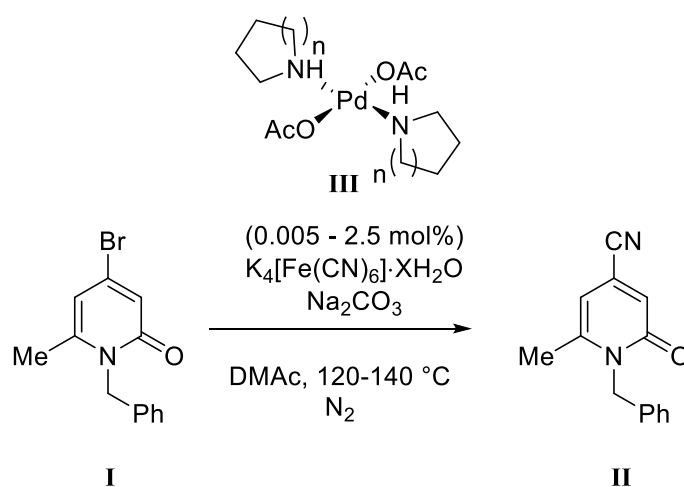
**University of York**

**Chemistry**

September 2016

## Abstract

This thesis describes the use of *in situ* infrared spectroscopy to investigate the kinetics and mechanism of the Pd-catalysed arylcyanation of **I** to give **II**. These studies probe the role of water and Pd concentration to facilitate the formation of small Pd nanoclusters in the Pd-catalysed cyanation of aryl halides. Initially an overview of the role of Pd nanoparticles and Pd nanoparticle precursor complexes in Pd-catalysed reactions is provided, along with a unified mechanism for the formation of catalytically active heterogeneous Pd species under hydrous reaction conditions (Chapter 1).



The application of the established precatalyst **III** ( $n = 2$ ) in extensive kinetic studies of the arylcyanation of **I** have revealed that when using  $\text{K}_4[\text{Fe}(\text{CN})_6] \cdot 3\text{H}_2\text{O}$  as a cyanide source there is clear evidence for heterogeneous catalytic behaviour (Chapter 4). When  $\text{K}_4[\text{Fe}(\text{CN})_6]$  is instead used as a cyanating agent, a significant change in kinetic profile supports a change in precatalyst activation mechanism. Pd concentration and catalyst loading data, along with computational analysis, support a role for small Pd clusters in catalysis (Chapter 5).

A series of novel, amine containing  $\text{Pd}^{\text{II}}$  precatalysts of type **III** have been synthesised (Chapter 2) and their catalytic competency analysed kinetically. They have been found to show considerable promise as highly efficient Pd precatalysts in the arylcyanation reactions and a substrate scope has been established for **III** when  $n = 2$  (Chapter 5).

It has also been found that balancing hexacyanoferrate solubility by ion pairing and addition of specific additives enabled transmetalation, which is key to achieving optimum reaction rates (Chapter 5).

# List of Contents

<b>Abstract</b> .....	<b>1</b>
<b>List of Contents</b> .....	<b>3</b>
<b>List of Figures</b> .....	<b>7</b>
<b>List of Schemes</b> .....	<b>32</b>
<b>List of Tables</b> .....	<b>37</b>
<b>Acknowledgements</b> .....	<b>39</b>
<b>Author's Declaration</b> .....	<b>40</b>
<b>Chapter 1: Introduction</b> .....	<b>41</b>
1.1. <i>The scope and phases of Pd catalysis</i> .....	41
1.1.1. Identifying the nature of the active Pd catalyst.....	50
1.2. <i>Pd catalyst design</i> .....	54
1.2.1. Tuning Pd <sup>0</sup> precatalysts.....	54
1.2.2. The importance of catalyst design for efficient Pd <sup>II</sup> precatalyst activation. ....	57
1.3. <i>Pd-catalysed cyanation</i> .....	68
1.4. <i>Pd(OAc)<sub>2</sub>(HNR<sub>2</sub>) complexes in catalysis</i> .....	75
1.5. <i>Project Aims and Objectives</i> .....	77
1.5.1. Aims.....	77
1.5.2. Objectives.....	77
<b>Chapter 2: Synthesis of Pd<sup>II</sup>(OAc)<sub>2</sub>(HNR<sub>2</sub>)<sub>2</sub> precatalysts</b> .....	<b>78</b>
2.1. <i>Introduction</i> .....	78
2.2. <i>Synthesis of Alicyclic Pd(OAc)<sub>2</sub>(HNR<sub>2</sub>)<sub>2</sub> complexes</i> .....	79
2.2.1. Attempted synthesis of azetidine Pd complex .....	91
2.3. <i>The effect of increasing amine ligand size</i> .....	92
2.4. <i>Mechanism of Pd<sub>3</sub>(OAc)<sub>6</sub> Aminolysis</i> .....	100
2.5. <i>Conclusion</i> .....	109
<b>Chapter 3: Identification and validation of a benchmark reaction for precatalyst screening in Pd-catalysed arylcyanations</b> .....	<b>110</b>
3.1. <i>Introduction</i> .....	110
3.2. <i>Attempted Cyanation of 4-Bromo-6-methyl-2-pyrone</i> .....	111
3.3. <i>Cyanation of N-benzyl-4-bromo-6-methylpyrid-2-one</i> .....	115
3.2.1. Synthesis of N-benzyl-4-bromo-6-methylpyrid-2-one .....	116
3.2.2. Investigating the effect of catalyst solution aging on reaction efficiency .	120

3.2.3. Cyanation of N-benzyl-4-bromo-6-methylpyrid-2-one using preformed Pd(OAc) <sub>2</sub> (HNR <sub>2</sub> ) <sub>2</sub> complexes as catalysts. ....	125
3.4. Conclusion.....	129
<b>Chapter 4: Kinetic studies of the Pd(OAc)<sub>2</sub>(HNC<sub>5</sub>H<sub>10</sub>) catalysed cyanation of N-benzyl-4-bromo-6-methylpyrid-2-one by <i>in situ</i> infra-red spectroscopy under hydrous conditions .....</b>	<b>130</b>
4.1. Introduction.....	130
4.2. Kinetic Investigation using <i>in situ</i> React-IR spectroscopy .....	131
4.2.1. Monitoring the model cyanation reaction by React-IR.....	131
4.2.2. Kinetic studies of the model cyanation reaction under hydrous conditions.....	133
4.3. Tests for the presence of heterogeneous catalysis. ....	140
4.3.1. Finke-Watzky analysis of sigmoidal kinetic plots. ....	140
Mercury poisoning test.....	151
4.4. Studying the absorbance at 2045 cm <sup>-1</sup> .....	152
4.4.1. Characterisation of the species responsible for the absorbance .....	153
4.4.2. Investigating concentration effects of [Fe(CN) <sub>6</sub> ] <sup>4-</sup> on catalysis .....	159
4.5. Conclusions.....	163
<b>Chapter 5: Kinetic studies of the Pd(OAc)<sub>2</sub>(HNR<sub>2</sub>) catalysed cyanation of N-benzyl-4-bromo-6-methylpyrid-2-one by <i>in situ</i> infrared spectroscopy under anhydrous conditions. ....</b>	<b>165</b>
5.1 Screening of <i>trans</i> -Pd(OAc) <sub>2</sub> (HNR <sub>2</sub> ) <sub>2</sub> precatalysts in an anhydrous, model Pd catalysed arylcyanation .....	165
5.2 Concentration effects on catalyst performance.....	170
5.3 Substrate screening.....	175
5.4 DFT studies into the structure of the active catalyst.....	176
5.5 Effect of increased amine ligand size on catalysis .....	179
5.6 Role of Na <sub>2</sub> CO <sub>3</sub> .....	183
5.6.1 Varying Na <sub>2</sub> CO <sub>3</sub> equivalences.....	183
5.6.2 Testing the role of Na <sup>+</sup> in a counterion exchange process .....	188
5.7 Investigating other hexacyanoferrate salts as cyanide sources .....	191
5.8 Conclusions.....	195
<b>Chapter 6: Conclusions and Future Work.....</b>	<b>197</b>
6.1. Conclusions.....	197
6.2. Future work.....	200

6.2.1. Use of $[\text{Pd}(\text{OAc})_2(\text{HNR}_2)]_2$ precatalysts in Pd-catalysed arylcyanation reactions	200
6.2.2. Investigation of “heterogeneity triggers” in Pd-catalysed cross-couplings and C–H functionalisation reactions	201
6.2.3. Use of mixed-metal clusters and use in Pd-catalysed cross-couplings and C–H functionalisation reactions	202
<b>Chapter 7: Experimental Section</b>	<b>206</b>
7.1. <i>General Experimental Techniques</i>	206
Solvents and Reagents	206
Chromatography	206
Nuclear Magnetic Resonance Spectroscopy	207
Infrared Spectroscopy	207
Mass Spectrometry	207
Melting points	208
Elemental Analysis	208
X-Ray Crystallography	208
7.2. <i>Manual treatment of kinetic data</i>	209
7.2.1. Treatment of kinetic data for Finke-Watzky nucleation and autocatalytic growth mechanism by nonlinear sum of least-squares curvefitting	209
7.2.2. Curvefit confidence interval calculations	211
7.3. <i>General procedures</i>	212
7.3.1. General procedure A: React-IR kinetic studies of Pd-catalysed cyanations	212
7.3.2. General procedure B: the synthesis of <i>trans</i> - $\text{Pd}(\text{OAc})_2(\text{HNR}_2)_2$ complexes <sup>110</sup>	215
7.3.3. General procedure C: the synthesis of $[\text{Pd}(\text{OAc})_2(\text{HNR}_2)]_2$ dimer complexes	215
7.3.4. General procedure D: NMR spectroscopy studies of the aminolysis of $\text{Pd}_3(\text{OAc})_6$	216
7.3.5. General procedure E: Non-kinetic Pd-precatalyst screens in the Pd-catalysed arylcyanation of $65^{102b}$	216
7.3.6. General experimental procedure F: Preparative Pd-catalysed cyanation of aryl halides	216
7.4. <i>Synthetic procedures and compound data</i>	217
<b>Appendix 1: Published papers</b>	<b>244</b>
<b>Appendix 2: Tables of extended substrate screen</b>	<b>245</b>

<b>Appendix 3: X-Ray Diffraction Data .....</b>	<b>248</b>
<i>Crystallographic data for compound 48 .....</i>	248
<i>Crystallographic data for compound 49 .....</i>	250
<i>Crystallographic data for compound 50 .....</i>	252
<i>Crystallographic data for compound 52 .....</i>	254
<i>Crystallographic data for compound 53 .....</i>	256
<i>Crystallographic data for compound 58 .....</i>	258
<i>Crystallographic data for compound 69 .....</i>	260
<b>Abbreviations.....</b>	<b>262</b>
<b>References .....</b>	<b>Error! Bookmark not defined.</b>
<b>Appendix 4: <sup>1</sup>H and <sup>13</sup>C NMR data (on CD)</b>	
<b>Appendix 5: CIF Crystallographic data (on CD)</b>	

## List of Figures

Figure 1 Polyvinylpyrrolidone (PVP). .....	42
Figure 2 A 236 atom nanoparticle showing defect sites in yellow. <sup>10</sup> .....	43
Figure 3 Operando XAS and EXAFS fits of 1.8 nm PdNPs during Suzuki cross-coupling reaction. Intensity for “leached” particle obtained by using a control batch of Pd NPs of correct size. Adapted with permission from <i>Angew. Chem.</i> 2010, <i>122</i> , 1864. Copyright of Wiley.....	43
Figure 4 Laskar and Skrabalak’s nanocubes (top) and nanooctahedra (bottom) of comparable edge lengths show remarkable differences in activity and selectivity in the hydrogenation of 2-hexyne. Reprinted (adapted) with permission from (Moitree Laskar and Sara E. Skrabalak <i>ACS Catal.</i> , 2014, <i>4</i> , 1120). Copyright (2014) American Chemical Society. ....	48
Figure 5 Laskar and Skrabalak's nanooctahedra adopt a low energy fcc (111) structure, whereas the nanocubes adopt a higher energy fcc (100) structure. Adapted with permission from <i>Concepts in Nanocatalysis, Nanomaterials in Catalysis</i> , First Edition. Copyright of Wiley.....	49
Figure 6 Computationally it has been found that alkynes coordinate to fcc (100) faces through a stronger binding mode than to fcc (111). Reprinted with permission from ( <i>J. Phys. Chem. B.</i> 2003, <i>107</i> , 217). Copyright (2003) American Chemical Society. ....	49
Figure 7 A typical curvefit for the loss of cyclohexene which provides an excellent curvefit to the F-W 2-step mechanism shown in Scheme 8 and its resultant integrated rate equation, Equation 1. The rate constants $k_1$ and $k_2$ can therefore be experimentally defined, where $k_2$ has to be corrected by a stoichiometry factor of 1400. Reaction conditions: Cyclohexene (4.94 mmol), $[\text{Bu}_4\text{N}]_5\text{Na}_3[(1,5\text{-COD})\text{Ir}\cdot\text{P}_2\text{W}_{15}\text{Nb}_3\text{O}_{62}]$ (0.07 mol%), $\text{H}_2$ (40 psig), 22 °C. Reprinted (adapted) with permission from <i>J. Am. Chem. Soc.</i> 1997, <i>119</i> , 10382-10400. Copyright (2016) American Chemical Society.....	52
Figure 8 Structures of Ru compounds tested by Keppler <i>et al.</i> Counterions (Hind or $\text{Cl}^-$ ) are omitted for clarity. $\text{IC}_{50}$ values are the inhibitory (50%) concentrations in CH1 cells after exposure for 96 hr in the MTT assay. ....	55
Figure 9 Two examples of heterocyclic dba derivatives synthesised by Fairlamb and co-workers.....	56
Figure 10 The three generations of palladacyclic Buchwald precatalysts. ....	58

Figure 11 The single crystal X-Ray diffraction structure of Pd <sub>3</sub> (OAc) <sub>6</sub> with D <sub>3h</sub> symmetry. .....	59
Figure 12 Aminophosphine NP precursor complexes synthesised by Frech <i>et al.</i> ....	63
Figure 13. Frech's aminophosphine precatalysts show sigmoidal kinetic traces, which are characteristic of PdNP catalysis. Adapted with permission from <i>Chem. Eur. J.</i> 2010, 16, 4075-4081. Copyright of Wiley. ....	64
Figure 14. A TEM of highly structured PdNPs stabilised by cucurbit[6]uril. Adapted with permission from <i>Chem. Commun.</i> 2010, 46, 5088. Copyright of the Royal Society of Chemistry. ....	66
Figure 15. A wire frame model of cucurbit[6]uril. Adapted with permission from <i>Chem. Commun.</i> 2010, 46, 5088. Copyright of the Royal Society of Chemistry. ....	66
Figure 16. Two pharmaceutically-active compounds containing the benzonitrile motif. ....	68
Figure 17. The mechanism of the Pd-catalysed cyanation reaction, detailing routes to catalyst poisoning. ....	70
Figure 18 Structure of 48, determined by X-ray diffraction; arbitrary numbering used. Selected hydrogen atoms removed for clarity. Thermal ellipsoids shown with a probability of 50%; numbers in parentheses are standard deviations from the measured value, denoting the error in the measurements. Selected bond lengths (Å): N(1)-Pd(1): 2.043(3), O(1)-Pd(1): 2.015(2), C(1)-N(1): 1.484(4), C(5)-O(1): 1.282(4), C(5)-O(2): 1.243(4). ....	80
Figure 19. Structure of 49, determined by X-ray diffraction; arbitrary numbering used. Selected hydrogen atoms removed for clarity. Thermal ellipsoids shown with a probability of 50%; numbers in parentheses are standard deviations from the measured value, denoting the error in the measurements. Selected bond lengths (Å): N(1)-Pd(1):2.021(2), O(1)-Pd(1): 2.0394(17), O(3)-Pd(1): 2.0300(17), O(5)-Pd(1):1.9969(17), Pd(1)-Pd(2): 3.0377(3), H(1)-O(8):1.98(1). ....	82
Figure 20 Addition of piperidine (2 eq.) to Pd(OAc) <sub>2</sub> yields the piperidine acetate monomer complex, 47. ....	83
Figure 21 Structure of 50, determined by X-ray diffraction; arbitrary numbering used. Selected hydrogen atoms removed for clarity. Thermal ellipsoids shown with a probability of 50%; numbers in parentheses are standard deviations from the measured value, denoting the error in the measurements. Selected bond lengths (Å): N(1)-Pd(1): 2.018(4), O(1)-Pd(1): 2.034(4), O(3)-Pd(1): 1.999(4), O(2)-Pd(1): 2.033(4), Pd(1)-Pd(2): 3.0389(5), H(1)-O(7):2.00(0). ....	84

Figure 22 Crystal structure of bis-trans-[2,2,6,6-tetramethylpiperidinyl- $\kappa$ -NH]palladium(II) diacetate (51) displays hydrogen bonding character. Data obtained from Gaunt <i>et al. Nature</i> , 2014, 510, 129. ....	85
Figure 23. Structure of 52, determined by X-ray diffraction; arbitrary numbering used. Selected hydrogen atoms removed for clarity. Thermal ellipsoids shown with a probability of 50%. Selected bond lengths (Å): N(1)-Pd(1): 2.0638(14), O(1)-Pd(1): 2.0050(12), C(1)-O(1): 1.286(2), C(1)-O(2): 1.236(2). ....	86
Figure 24. Extended lattice structure of 52, determined by X-ray diffraction; arbitrary numbering used. Selected hydrogen atoms removed for clarity. Thermal ellipsoids shown with a probability of 50%. Selected Hydrogen bond lengths and angles and Short-contact bond lengths calculated using Mercury: N(1)-H(1)···O(2): 2.972 Å, 158.93°, C(1)···O(2): 3.000 Å, C(1)-O(2)···C(1) 93.63° .....	87
Figure 25 The potential energy of dipole-dipole interaction can be calculated using their relative orientation and distance. ....	88
Figure 26 Structure of 53, determined by X-ray diffraction; arbitrary numbering used. Selected hydrogen atoms removed for clarity. Thermal ellipsoids shown with a probability of 50%. Selected bond lengths (Å): N(1)-Pd(1): 2.0696(18), O(1)-Pd(1): 2.0191(16), C(1)-O(1): 1.266(3), C(1)-O(2): 1.229(3), C(3)-N(1): 1.481(3). ....	90
Figure 27 Both iminodibenzyl (55) and dibenzazepine (56) were considered interesting potential ligands at Pd(OAc) <sub>2</sub> . ....	92
Figure 28 Structure of 58, determined by X-ray diffraction; arbitrary numbering used. Selected hydrogen atoms and a molecule of pentane (antisolvent) have been removed for clarity. Thermal ellipsoids shown with a probability of 50%; numbers in parentheses are standard deviations from the measured value, denoting the error in the measurements. Selected bond lengths (Å): N(1)-Pd(1) 2.0757(15), Pd(1)-Pd(1) 3.0466(3), O(1)-Pd(1) 2.0147(12), O(2)-Pd(1) 1.9775(12), O(3) Pd(1) 2.0204(13), C(7)-C(8) 1.339(3), C(1)-N(1) 1.454(2). ....	94
Figure 29 Molecular orbital diagram for a Pd <sup>II</sup> -Pd <sup>II</sup> dimer of the type displayed. ....	96
Figure 30 Key interatomic distances in Pd dimers 49, 50, and 58. O···N interatomic distances calculated using Mercury. ....	97
Figure 31 Comparing C-N-C bond angles in the solid state structures of the free ligands 56 and 55 vs complex 58. Images created in Mercury. ....	98

- Figure 32 Structure of 58, determined by X-ray diffraction, rotated to show molecule of pentane in hydrophobic solvent pocket. Hydrogen atoms have been removed for clarity. Thermal ellipsoids shown with a probability of 50%. Image created in Mercury. .... 99
- Figure 33 Hydrolysis of  $\text{Pd}_3(\text{OAc})_6$ . .... 100
- Figure 34 Postulated mechanism of  $\text{Pd}_3(\text{OAc})_6$  aminolysis. .... 100
- Figure 35 Addition of dry piperidine (1 eq.) to  $\text{Pd}_3(\text{OAc})_6$  in  $\text{CD}_2\text{Cl}_2$  converts to 50 *via* 47. Reaction conditions: dry piperidine (1 eq.) added to  $\text{Pd}_3(\text{OAc})_6$  in  $\text{CD}_2\text{Cl}_2$  at room temperature. Black diamond: 47; green club: 50. 1) Immediately after addition of piperidine; 2) 4 days after addition; 3) 5 days after addition; 4) 6 days after addition; 5)  $^1\text{H}$  NMR spectrum of 50; 6)  $^1\text{H}$  NMR spectrum of piperidine; 7)  $^1\text{H}$  NMR spectrum of  $\text{Pd}_3(\text{OAc})_6$ . .... 102
- Figure 36 Zoom of the characteristic acetate section of the spectra in Figure 35 reveals the formation of 47 (black diamond) along with the formation of the desired final product, 50 (green club) from  $\text{Pd}_3(\text{OAc})_6$  (red spade) in the presence of piperidine. Reaction conditions: addition of dry piperidine (1 eq.) to  $\text{Pd}_3(\text{OAc})_6$  in  $\text{CD}_2\text{Cl}_2$  at room temperature. 1) Immediately after addition of piperidine; 2) 4 days after addition; 3) 5 days after addition; 4) 6 days after addition; 5)  $^1\text{H}$  NMR spectrum of 50; 6)  $^1\text{H}$  NMR spectrum of piperidine; 7)  $^1\text{H}$  NMR spectrum of  $\text{Pd}_3(\text{OAc})_6$ . .... 103
- Figure 37 Addition of dry piperidine (1 eq.) to  $\text{Pd}_3(\text{OAc})_6$  in  $\text{CD}_2\text{Cl}_2$  converts to 50 (green clubs) *via* 47 (black diamonds). Reaction conditions: dry piperidine (1 eq.) added to  $\text{Pd}_3(\text{OAc})_6$  in  $\text{CD}_2\text{Cl}_2$  at room temperature. 1) Immediately after addition of piperidine; 2) 19 hours after addition; 3) 1 day after addition; 4) 4 days after addition; 5)  $^1\text{H}$  NMR spectrum of 50; 6)  $^1\text{H}$  NMR spectrum of piperidine; 7)  $^1\text{H}$  NMR spectrum of  $\text{Pd}_3(\text{OAc})_6$ . .... 105
- Figure 38 Zoom of the characteristic acetate section of the spectra in Figure 37 reveals the formation of 47 (black diamond) along with the formation of the desired final product, 50 (green clubs) from  $\text{Pd}_3(\text{OAc})_6$  (red spade) in the presence of piperidine. Reaction conditions: Addition of dry piperidine (2 eq.) to  $\text{Pd}_3(\text{OAc})_6$  in  $\text{CD}_2\text{Cl}_2$  at room temperature. 1) Immediately after addition of piperidine; 2) 19 hours after addition; 3) 1 day after addition; 4) 4 days after addition; 5)  $^1\text{H}$  NMR spectrum of 50; 6)  $^1\text{H}$  NMR spectrum of piperidine; 7)  $^1\text{H}$  NMR spectrum of  $\text{Pd}_3(\text{OAc})_6$ . .... 106
- Figure 39 Addition of dry piperidine (1 eq.) to  $\text{Pd}_3(\text{OAc})_6$  in  $\text{CD}_2\text{Cl}_2$  converts to 50 (green clubs) *via* 47 (black diamonds). Reaction conditions: dry piperidine (1 eq.) added to  $\text{Pd}_3(\text{OAc})_6$  in  $\text{CD}_2\text{Cl}_2$  at room temperature. 1) Immediately after addition of piperidine; 2) 3 minutes after addition; 3) 8 minutes after addition; 4) 14 minutes after addition; 5) 18 minutes

after addition; 6) 7 hours after addition; 7) 19 hours after addition; 8) 43 hours after addition; 9) <sup>1</sup> H NMR spectrum of 50; 10) <sup>1</sup> H NMR spectrum of piperidine; 11) <sup>1</sup> H NMR spectrum of Pd <sub>3</sub> (OAc) <sub>6</sub> . .....	107
Figure 40 Zoom of the characteristic acetate section of the spectra in Figure 37 reveals the presence of Pd <sub>3</sub> (OAc) <sub>6</sub> (red spade) 47 (black diamond) along with the formation of the desired final product, 50 (green clubs). Reaction conditions: Addition of dry piperidine (3 eq.) to Pd <sub>3</sub> (OAc) <sub>6</sub> in CD <sub>2</sub> Cl <sub>2</sub> at room temperature. 1) Immediately after addition of piperidine; 2) 3 minutes after addition; 3) 8 minutes after addition; 4) 14 minutes after addition; 5) 18 minutes after addition; 6) 7 hours after addition; 7) 19 hours after addition; 8) 43 hours after addition; 9) <sup>1</sup> H NMR spectrum of 50; 10) <sup>1</sup> H NMR spectrum of piperidine; 11) <sup>1</sup> H NMR spectrum of Pd <sub>3</sub> (OAc) <sub>6</sub> .....	108
Figure 41 Tautomers and resonance structures of a 2-pyridone. ....	110
Figure 42 Left: <i>Bis-trans</i> -[piperidinyl-κ-NH]Palladium(II) diacetate, Right: <i>trans</i> -bromo( <i>N</i> -succinimidyl)bis(triphenylphosphine)palladium(II). ....	111
Figure 43. Actual products formed in attempted Pd-catalysed cyanation of 4-bromo-6-methyl-2-pyrone (60). ....	113
Figure 44 Nitrile-substituted 2-pyridinones are important chemical motifs within the fine chemical industry. ....	115
Figure 45 <i>N</i> -benzyl-4-bromo-6-methylpyrid-2-one (65). ....	116
Figure 46 The structure of <i>N</i> -benzyl-4-cyano-6-methylpyrid-2-one (69) as determined by X-ray diffraction; arbitrary numbering used. Hydrogen atoms removed for clarity. Thermal ellipsoids shown with a probability of 50%; numbers in parentheses are standard deviations from the measured value, denoting the error in the measurements. Selected bond lengths (Å): C(3)-C(6):1.431(3), C(6)-N(2): 1.150(3), C(1)-O(1): 1.2379(16), C(1)-N(1):1.4052(16), C(5)-N(1): 1.3811(16), C(8)-N(1):1.4717(17).....	120
Figure 47 The effect of aging Pd(OAc) <sub>2</sub> (1 eq.) and piperidine (2 eq.) in DMAc at 80 °C upon the efficiency of the cyanation of 65. <sup>a</sup> Determined by <sup>1</sup> H NMR spectroscopy as a ratio between the signals at 6.80 ppm (65) and 6.85 ppm (69). ....	124
Figure 48 Four Pd precatalysts were screened in the benchmark cyanation reaction, 65 → 69. ....	126
Figure 49 IR spectrum of DMAc. ....	132
Figure 50 IR Spectrum of 69 in DMAc. The red circle highlights the IR absorbance corresponding to the nitrile C≡N stretching frequency of 69. ....	132

Figure 51 *In situ* IR spectra of the cyanation of 65. Reaction conditions: 47 (0.1 mol%),  $K_4[Fe(CN)_6] \cdot 3H_2O$  (0.22 eq.),  $Na_2CO_3$  (1 eq.), DMAc,  $N_2$ , 120 °C. .... 133

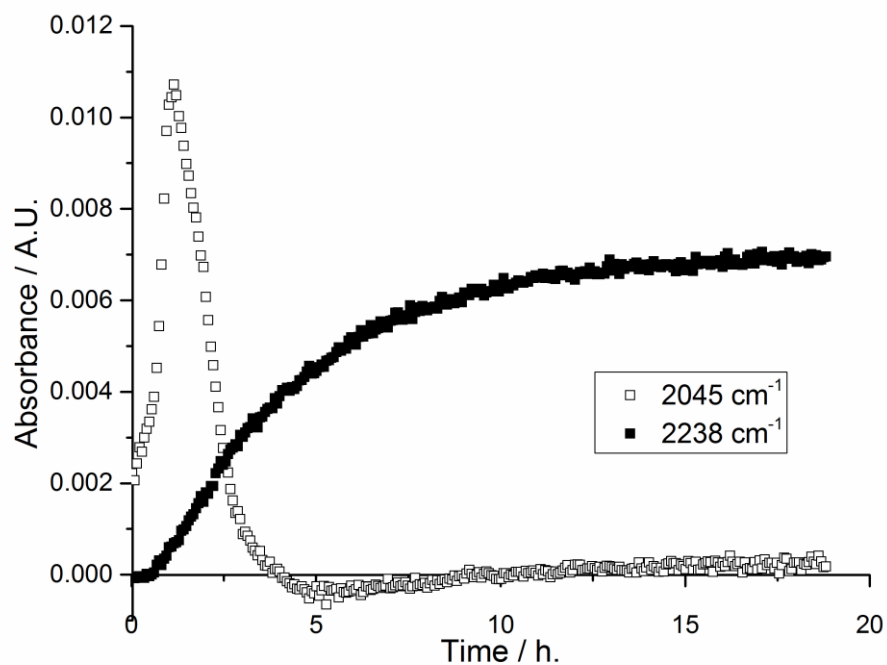


Figure 52 Raw data showing the time resolved formation of product ( $2238\text{ cm}^{-1}$ ) and solubilised  $[Fe(CN)_6]^{4-}$  ( $2045\text{ cm}^{-1}$ ), as characterised later. Reaction conditions: 47 (0.1 mol%),  $K_4[Fe(CN)_6] \cdot 3H_2O$  (0.22 eq.),  $Na_2CO_3$  (1 eq.), DMAc,  $N_2$ , 120 °C. .... 133

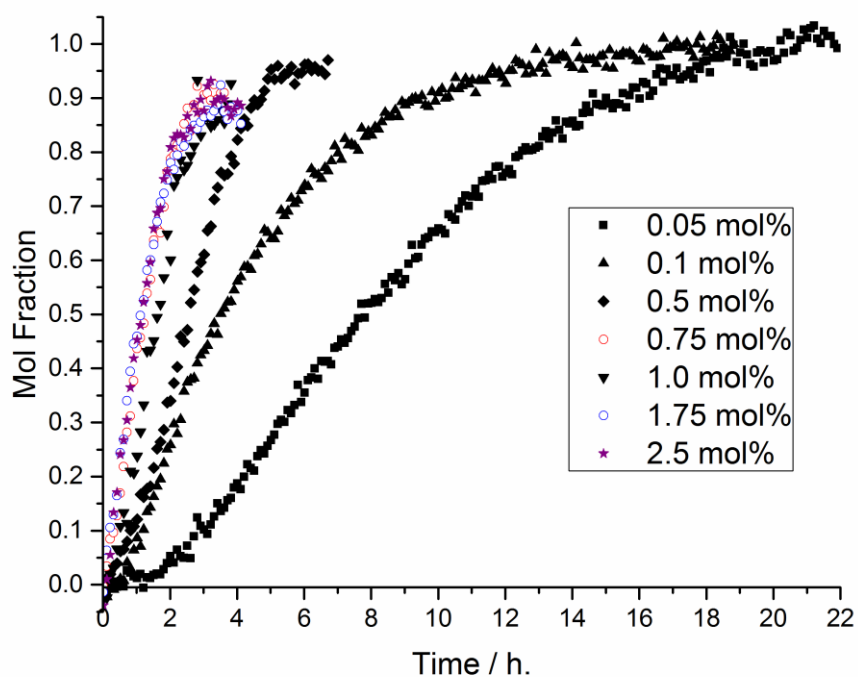


Figure 53 Catalyst loading kinetic investigation of the cyanation of 65 under hydrous conditions. Reaction conditions: 47 (0.05 mol% - 2.5 mol%),  $K_4[Fe(CN)_6] \cdot 3H_2O$  (0.22 eq.),  $Na_2CO_3$  (1 eq.), DMAc,  $N_2$ , 120 °C..... 134

Figure 54 The beginning of the kinetic plots displayed in Figure 53 enlarged to show induction periods. Reaction conditions: 47 (0.05 mol% - 2.5 mol%),  $K_4[Fe(CN)_6] \cdot 3H_2O$  (0.22 eq.),  $Na_2CO_3$  (1 eq.), DMAc,  $N_2$ , 120 °C..... 135

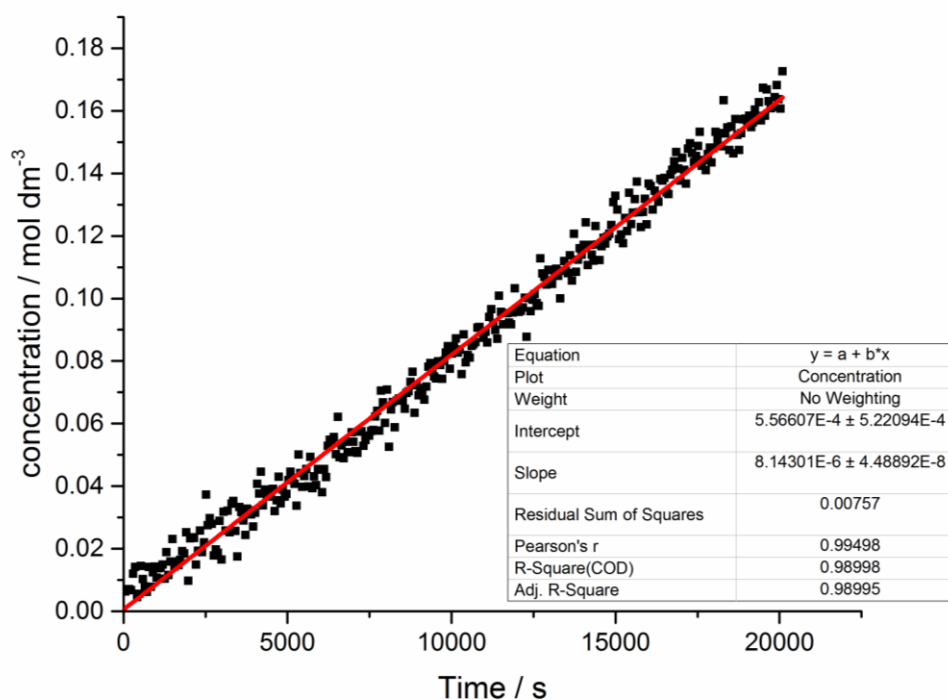


Figure 55 A plot to calculate the observed rate constant,  $k_{\text{obs}}$ , obtained from the peak rate of reaction. Reaction conditions: 47 (0.05 mol%),  $\text{K}_4[\text{Fe}(\text{CN})_6] \cdot 3\text{H}_2\text{O}$  (0.22 eq.),  $\text{Na}_2\text{CO}_3$  (1 eq.), DMAc,  $\text{N}_2$ , 120 °C. .... 136

Figure 56 A graph to show TOF vs Pd catalyst (47) loading. The TOFs of each of the different precatalyst loadings was measured as a gradient of  $\text{TON s}^{-1}$  for the straight line section of the kinetic profiles. Reaction conditions: 47 (0.05 mol% - 2.5 mol%),  $\text{K}_4[\text{Fe}(\text{CN})_6] \cdot 3\text{H}_2\text{O}$  (0.22 eq.),  $\text{Na}_2\text{CO}_3$  (1 eq.), DMAc,  $\text{N}_2$ , 120 °C. .... 137

Figure 57 A plot of  $k_{\text{obs}}$  vs. [Pd] shows there is not a linear relationship between reaction rate and catalyst loading. It also reveals that the  $k_{\text{obs}}$  obtained for 0.0027 mol  $\text{dm}^{-3}$ /0.75 mol% is an anomaly (highlighted in red). Reaction conditions: 47 (0.05 mol% - 2.5 mol%),  $\text{K}_4[\text{Fe}(\text{CN})_6] \cdot 3\text{H}_2\text{O}$  (0.22 eq.),  $\text{Na}_2\text{CO}_3$  (1 eq.), DMAc,  $\text{N}_2$ , 120 °C. .... 138

Figure 58 Calculating the order with respect to Pd *via* the differential method provides a value of 0.435 ( $\pm 0.076$ ). One anomalous point has been highlighted in red, as explained in Figure 57. The point within the bold black circle (0.05 mol%,  $1.80 \times 10^{-4}$  mol  $\text{dm}^{-3}$ ) also appears to be off the expected linear trend. .... 139

Figure 59 Calculating the order with respect to Pd *via* the differential method provides a value of 0.257 ( $\pm 0.02$ ). .... 140

Figure 60 Concentration vs. time curve and data fit to the F-W 2-step mechanism for 0.05 mol% catalyst loading. The resultant rate constant  $k_2$  has been corrected by using a stoichiometry factor of 2000.  $k_1$  confidence intervals: 95% =  $2.4 \times 10^{-2} - 4.1 \times 10^{-2}$   $\text{h}^{-1}$ ; 99%

$= 2.15 \times 10^{-2} - 4.5 \times 10^{-2} \text{ h}^{-1}$ . $k_2$ confidence intervals: 95% = $1.2 \times 10^3 - 1.74 \times 10^3 \text{ M}^{-1} \text{ h}^{-1}$ ; 99% = $1.12 \times 10^3 - 1.84 \times 10^3 \text{ M}^{-1} \text{ h}^{-1}$ .....	144
Figure 61 Visual representations of the 95% (brown line) and 99% (grey line) confidence limits for $k_1$ (left) and $k_2$ (right) for the F-W 2-step curvefit displayed in Figure 60.....	144
Figure 62 Concentration vs. time curve and data fit to the F-W 2-step mechanism for 0.1 mol% catalyst loading. The resultant rate constant $k_2$ has been corrected by using a stoichiometry factor of 1000. $k_1$ confidence intervals: 95% = $1.06 \times 10^{-1} - 1.78 \times 10^{-1} \text{ h}^{-1}$ ; 99% = $9.6 \times 10^{-2} - 1.92 \times 10^{-1} \text{ h}^{-1}$ . $k_2$ confidence intervals: 95% = $2.5 \times 10^2 - 8.50 \times 10^2 \text{ M}^{-1} \text{ h}^{-1}$ ; 99% = $1.56 \times 10^2 - 9.6 \times 10^2 \text{ M}^{-1} \text{ h}^{-1}$ .....	145
Figure 63 Visual representations of the 95% (brown line) and 99% (grey line) confidence limits for the limits for $k_1$ (left) and $k_2$ (right) for the F-W 2-step curvefit displayed in Figure 62. ....	145
Figure 64 Concentration vs. time curve and data fit to the F-W 2-step mechanism for 0.5 mol% catalyst loading. The resultant rate constant $k_2$ has been corrected by using a stoichiometry factor of 200. $k_1$ confidence intervals: 95% = $0.05 - 0.13 \text{ h}^{-1}$ ; 99% = $0.04 - 0.15 \text{ h}^{-1}$ . $k_2$ confidence intervals: 95% = $360 - 670 \text{ M}^{-1} \text{ h}^{-1}$ ; 99% = $320 - 720 \times 10^2 \text{ M}^{-1} \text{ h}^{-1}$ . ....	146
Figure 65 Visual representations of the 95% (brown line) and 99% (grey line) confidence limits for the limits for $k_1$ (left) and $k_2$ (right) for the F-W 2-step curvefit displayed in Figure 64. ....	146
Figure 66 Concentration vs. time curve and attempted data fit to the F-W 2-step mechanism for 1.0 mol% catalyst loading. The resultant rate constant $k_2$ has been corrected by using a stoichiometry factor of 100. $k_1$ confidence intervals: 95% = $6.0 \times 10^{-2} - 6.2 \times 10^{-1} \text{ hr}^{-1}$ ; 99% = $2.0 \times 10^{-2} - 7.3 \times 10^{-1} \text{ hr}^{-1}$ . $k_2$ confidence intervals: 95% = N/A; 99%: N/A.....	148
Figure 67 Visual representations of the 95% (brown line) and 99% (grey line) confidence limits for the limits for $k_1$ (left) and $k_2$ (right) for the attempted F-W 2-step curvefit displayed in Figure 66.....	148
Figure 68 Concentration vs. time curve and attempted data fit to the F-W 2-step mechanism for 2.5 mol% catalyst loading. The resultant rate constant $k_2$ has been corrected by using a stoichiometry factor of 40. $k_1$ confidence intervals: 95% = $2.8 \times 10^{-1} - 8.8 \times 10^{-1} \text{ hr}^{-1}$ ; 99% = $1.5 \times 10^{-1} - 9.5 \times 10^{-1} \text{ hr}^{-1}$ . $k_2$ confidence intervals: 95% = N/A; 99%: N/A.....	149

Figure 69 Visual representations of the 95% (brown line) and 99% (grey line) confidence limits for the limits for $k_1$ (left) and $k_2$ (right) for the attempted F-W 2-step curvefit displayed in Figure 68.....	150
Figure 70 Mercury drop test experiment. Reaction conditions: 47 (0.5 mol%), $K_4[Fe(CN)_6] \cdot 3H_2O$ (0.22 eq.), $Na_2CO_3$ (1 eq.), $N_2$ , 120 °C, DMAc. Hg (200 eq. with respect to Pd) added with vigorous stirring after 93 mins.....	151
Figure 71 Dissolution profile of “[Fe(CN) <sub>6</sub> ]” (followed by monitoring IR absorbance at 2045 $cm^{-1}$ ) under normal conditions and during Hg poisoning experiment. Reaction conditions: 47 (0.5 mol%), $K_4[Fe(CN)_6] \cdot 3H_2O$ (0.22 eq.), $Na_2CO_3$ (1 eq.), $N_2$ , 120 °C, DMAc. Hg (200 eq. with respect to Pd) added with vigorous stirring after 93 mins. ....	152
Figure 72 3D <i>in situ</i> IR spectra of KCN in DMAc at 120 °C. ....	153
Figure 73 Time resolved dissolution of KCN in DMAc at 120 °C, monitored at 2045 $cm^{-1}$ . ....	154
Figure 74 <i>In situ</i> IR spectrum of $K_4[Fe(CN)_6] \cdot 3H_2O$ , $Na_2CO_3$ and 65 in DMAc at 120 °C. ....	155

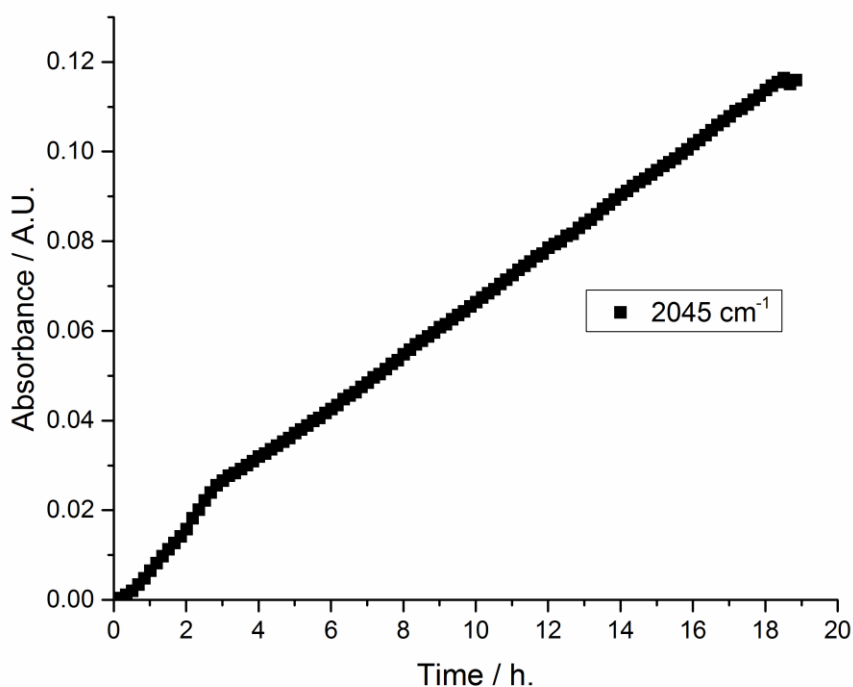


Figure 75 Time resolved study of the absorbance at 2045  $cm^{-1}$ . Reaction conditions: 65 (1 eq.),  $K_4[Fe(CN)_6] \cdot 3H_2O$  (0.22 eq.),  $Na_2CO_3$  (1 eq.),  $N_2$ , 120 °C, DMAc. .... 155

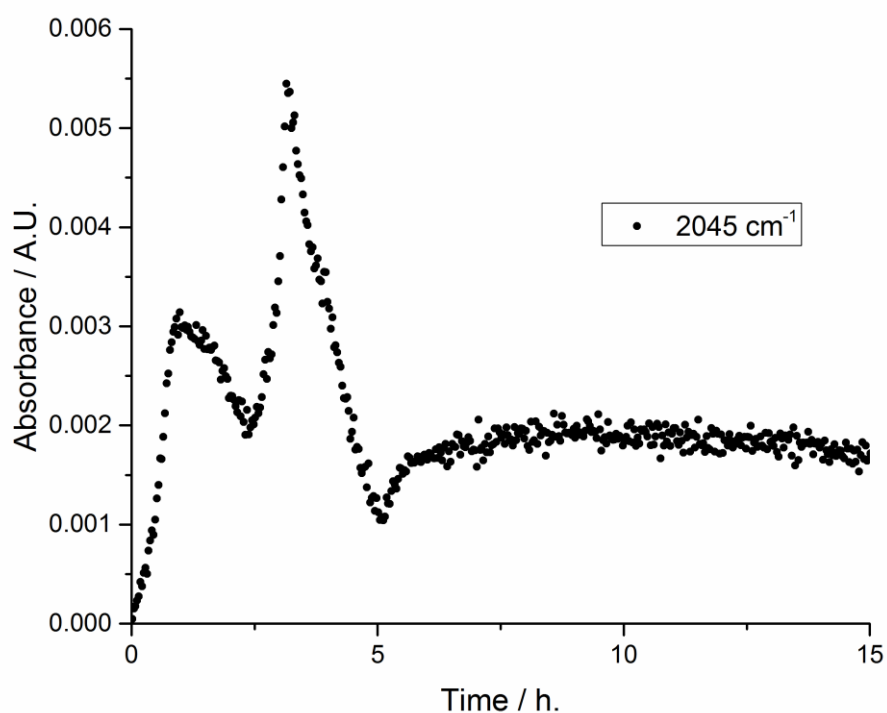


Figure 76 Time resolved study of the absorbance at  $2045\text{ cm}^{-1}$ . Reaction conditions: 47 (0.5 mol%),  $\text{K}_4[\text{Fe}(\text{CN})_6]\cdot 3\text{H}_2\text{O}$  (0.22 eq.),  $\text{Na}_2\text{CO}_3$  (1 eq.),  $\text{N}_2$ ,  $120\text{ }^\circ\text{C}$ , DMAc. .... 156

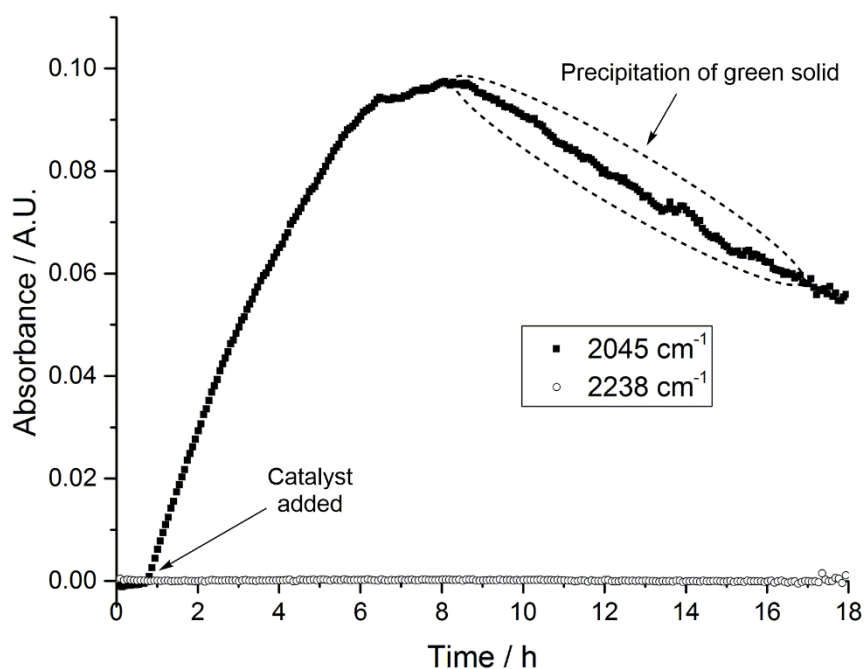


Figure 77 Raw absorbance data showing the metal cyanide and product (69) absorbances at  $2045\text{ cm}^{-1}$  and  $2238\text{ cm}^{-1}$  respectively under anhydrous reaction conditions in the absence of

Na <sub>2</sub> CO <sub>3</sub> . Reaction conditions: 47 (0.05 mol%), 65 (1 eq.), K <sub>4</sub> [Fe(CN) <sub>6</sub> ] (0.22 eq.), N <sub>2</sub> , 120 °C, DMAc. ....	157
Figure 78 ATR-IR spectrum of green precipitate formed after 8 hours under reaction conditions but in the absence of Na <sub>2</sub> CO <sub>3</sub> . Reaction conditions: 47 (0.05 mol%), 65 (1 eq.), K <sub>4</sub> [Fe(CN) <sub>6</sub> ] (0.22 eq.), DMAc, N <sub>2</sub> , 120 °C.....	158
Figure 79 Expanded section of IR-region between 1800-2400 cm <sup>-1</sup> of the ATR-IR spectrum shown in Figure 78.....	158
Figure 80 ATR-IR spectrum of K <sub>4</sub> [Fe(CN) <sub>6</sub> ].....	159
Figure 81 Expanded section of IR-region between 1800-2400 cm <sup>-1</sup> of the ATR-IR spectrum shown in Figure 80.....	159
Figure 82 Hartwig <i>et al.</i> showed that formation of ArCN from complexes such as 71 was remarkably fast (first order rate constant = 11×10 <sup>-4</sup> s <sup>-1</sup> ) at room temperature. <sup>109</sup> .....	160

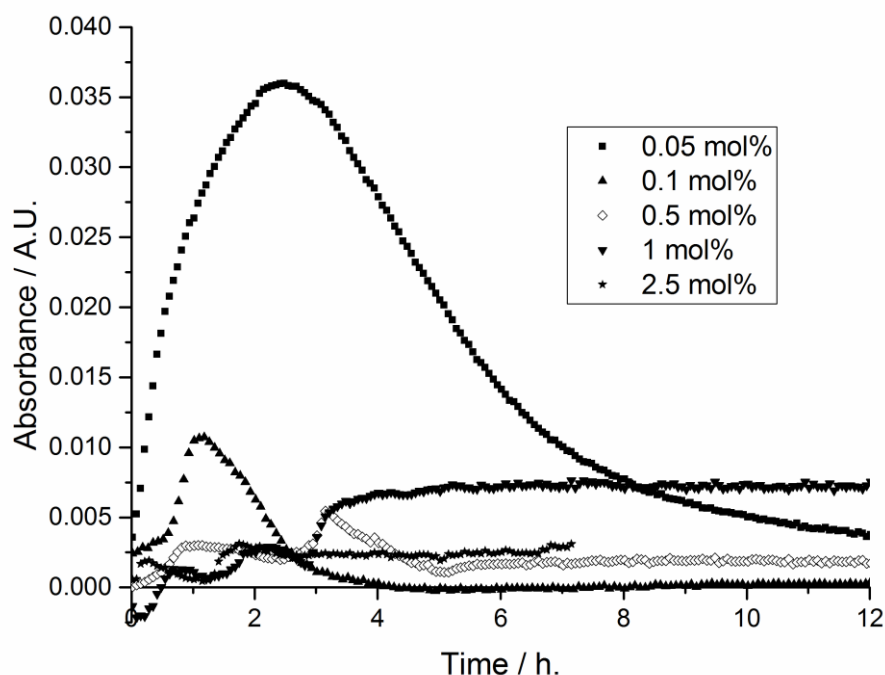


Figure 83 Monitoring the change in absorbance at 2045 cm<sup>-1</sup> allows a qualitative insight into the amount of [Fe(CN)<sub>6</sub>]<sup>4-</sup> in solution throughout the course of the reaction when carried out with differing 47 catalyst loadings. Reaction conditions: 47 (0.05 – 2.5 mol%), K<sub>4</sub>[Fe(CN)<sub>6</sub>]·3H<sub>2</sub>O (0.22 eq.), Na<sub>2</sub>CO<sub>3</sub> (1 eq.), N<sub>2</sub>, 120 °C, DMAc. ....

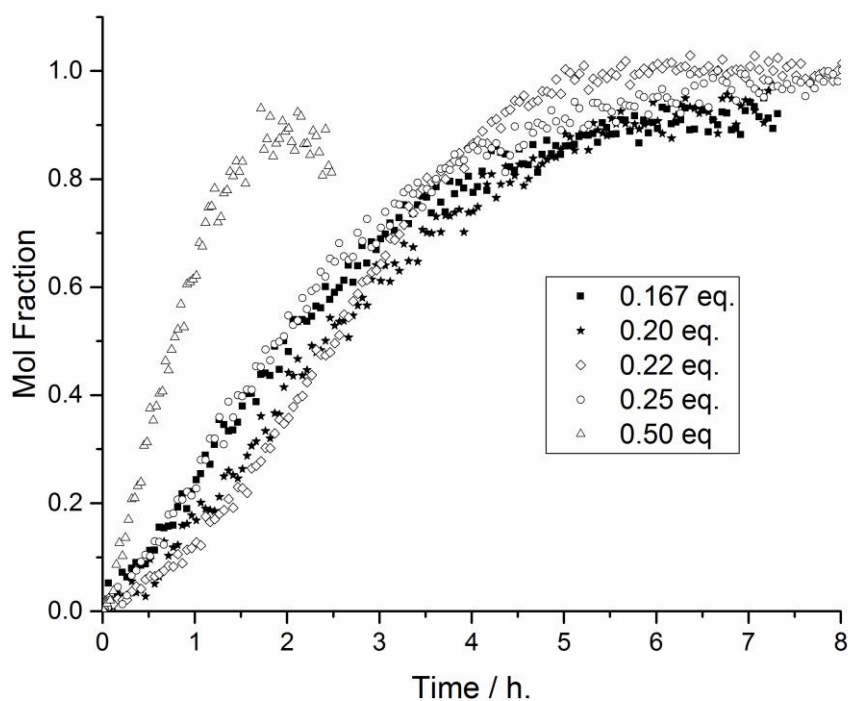


Figure 84 Varying equivalence of  $K_4[Fe(CN)_6] \cdot 3H_2O$  has little effect on reaction rate, until a vast excess of “CN” is added. Reaction conditions: 47 (0.5 mol%),  $K_4[Fe(CN)_6] \cdot 3H_2O$  (0.167 – 0.5 eq.),  $Na_2CO_3$  (1 eq.),  $N_2$ , 120 °C, DMAc..... 162

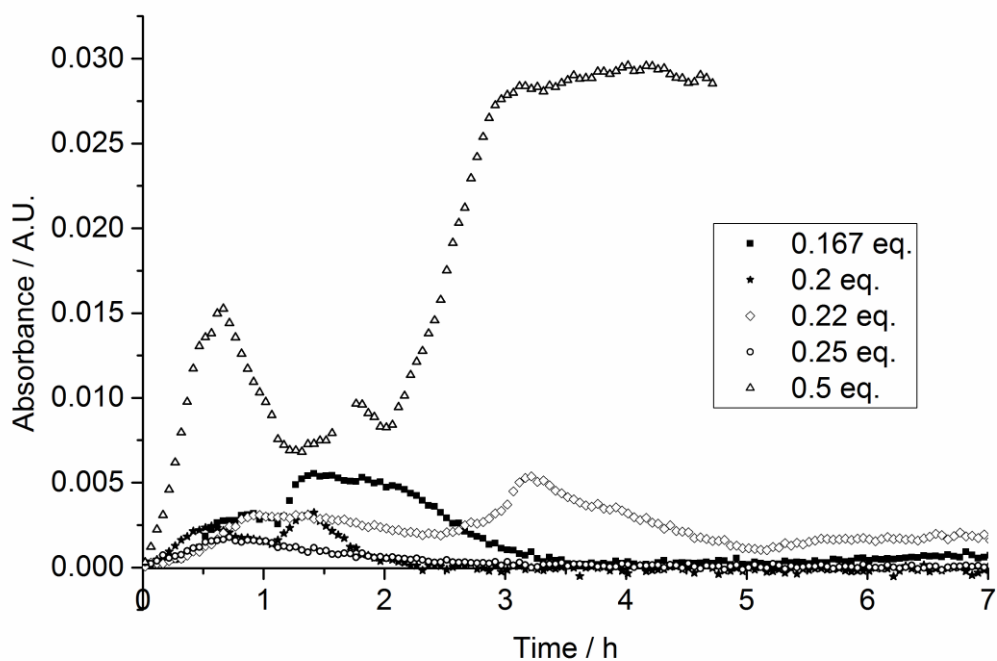


Figure 85 Real time analysis of  $[Fe(CN)_6]^{4-}$  (at  $2045\text{ cm}^{-1}$ ) upon variation of

$K_4[Fe(CN)_6] \cdot 3H_2O$  equivalences. Reaction conditions: 47 (0.5 mol%),  $K_4[Fe(CN)_6] \cdot 3H_2O$  (0.167 – 0.5 eq.),  $Na_2CO_3$  (1 eq.),  $N_2$ , 120 °C, DMAc..... 163

Figure 86 A series of *trans*-Pd(OAc)<sub>2</sub>(HNR<sub>2</sub>)<sub>2</sub> precatalysts. .... 165

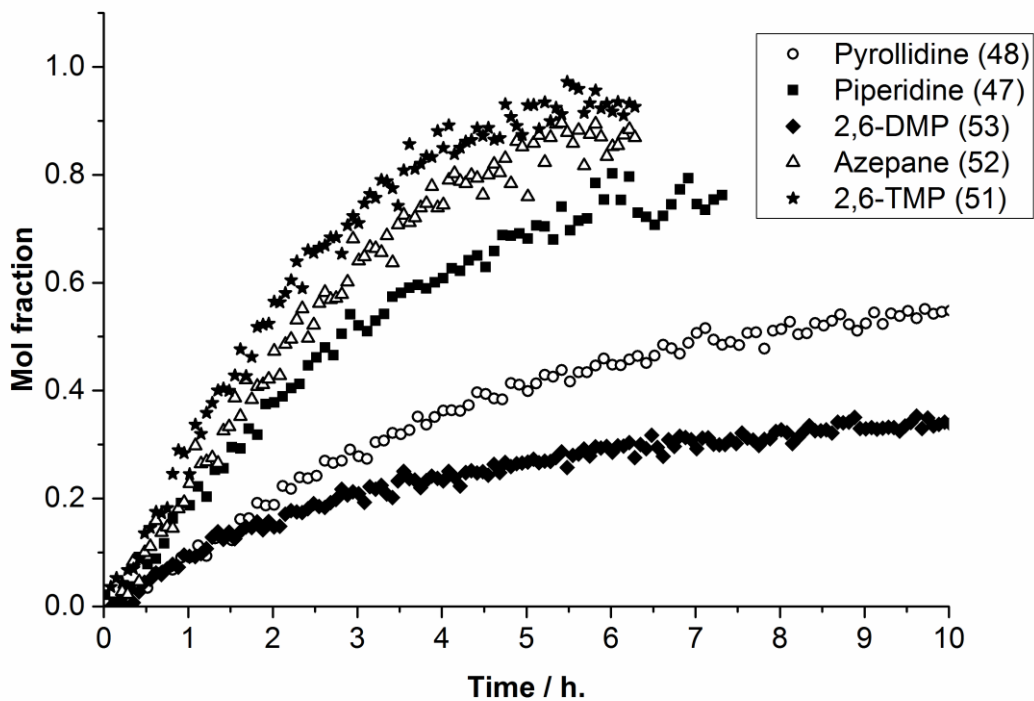


Figure 87 Comparison of precatalyst activity in the cyanation of *N*-benzyl-4-bromo-6-methyl-2-pyridinone (65). Reaction conditions: Precatalyst (0.01 mol%, 72  $\mu$ M),  $K_4[Fe(CN)_6]$  (0.22 eq.),  $Na_2CO_3$  (1 eq.), DMAc,  $N_2$ , 140 °C. .... 167

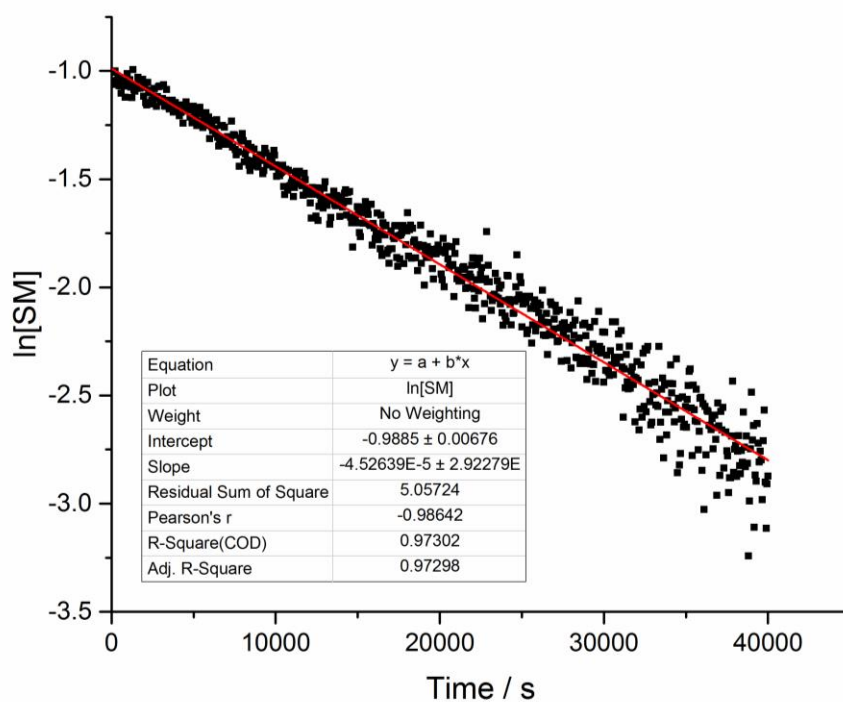


Figure 88 Plotting  $\ln[65]$  vs time (initial 40000 s) for the arylocyanation of 65 catalysed by precatalyst 47 provides a straight line with a good quality linear fit. .... 168

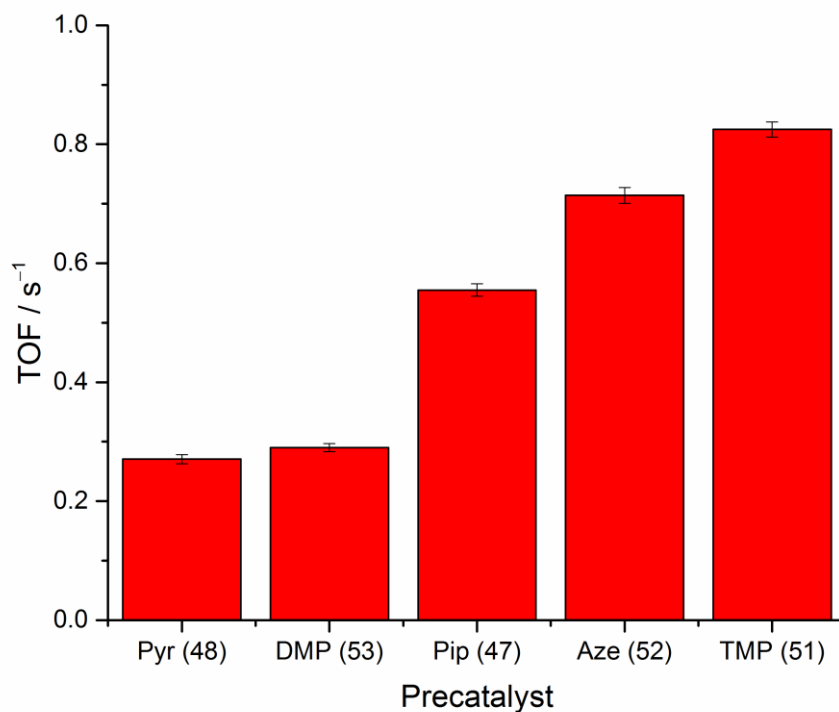


Figure 89 The TOFs of each of the different precatalyst was measured as a gradient of TON

$\text{s}^{-1}$  for an initial period of 5400 seconds (1.5 h).<sup>147</sup> Reaction conditions: Precatalyst (0.01 mol%, 72  $\mu\text{M}$ ),  $\text{K}_4[\text{Fe}(\text{CN})_6]$  (0.22 eq.),  $\text{Na}_2\text{CO}_3$  (1 eq.), DMAc,  $\text{N}_2$ , 140 °C. .... 169

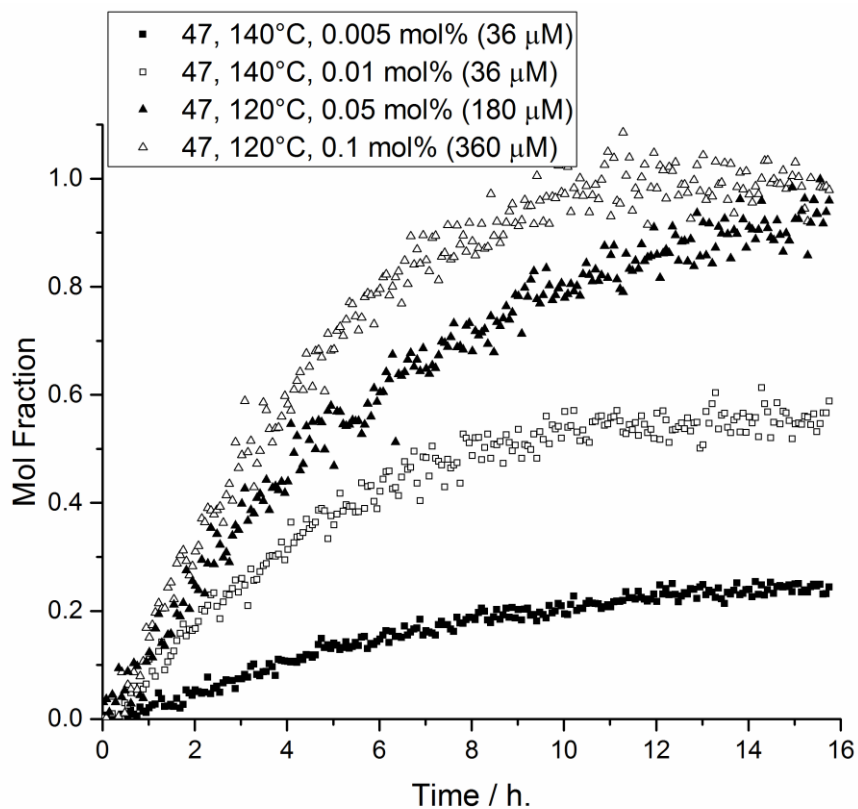


Figure 90 Reaction profiles for the reaction  $65 \rightarrow 69$  at different precatalyst 47 loadings and temperatures under anhydrous conditions. Reaction conditions: Precatalyst 47 (0.005 – 0.1 mol%, 36 – 360  $\mu\text{M}$  Pd),  $\text{K}_4[\text{Fe}(\text{CN})_6]$  (0.22 eq.),  $\text{Na}_2\text{CO}_3$  (1 eq.), DMAc,  $\text{N}_2$ , 120–140 °C.

..... 171

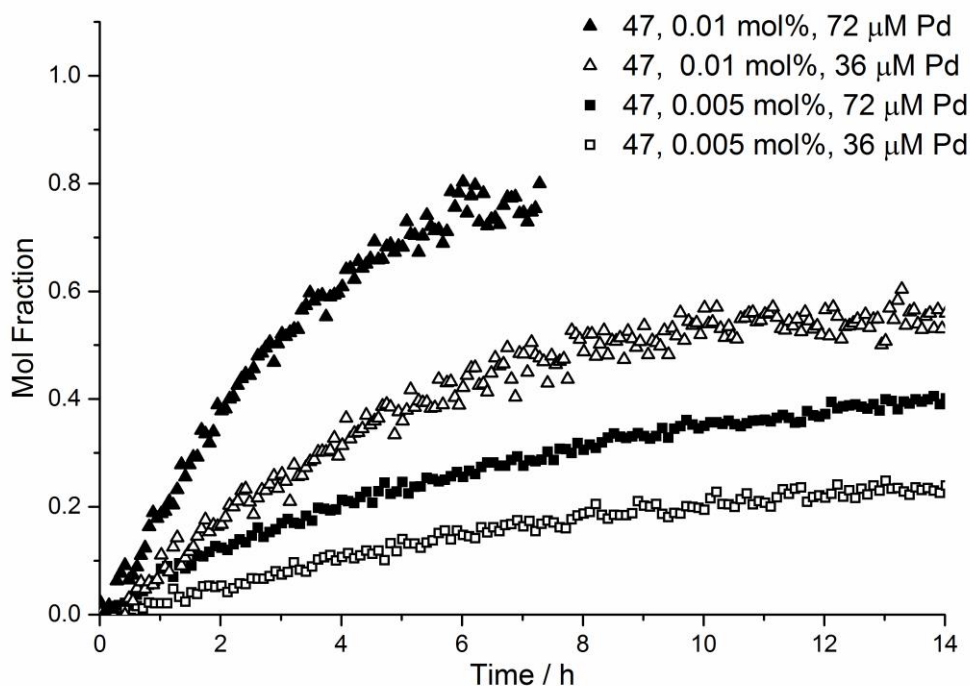


Figure 91 Reaction profile for reaction  $65 \rightarrow 69$  with increased  $[\text{Pd}]$  and reaction concentrations while maintaining constant catalyst loadings under anhydrous conditions. Reaction conditions: Precatalyst 47 (0.005 or 0.01 mol%, 36 or 72  $\mu\text{M}$  Pd),  $\text{K}_4[\text{Fe}(\text{CN})_6]$  (0.22 eq.),  $\text{Na}_2\text{CO}_3$  (1 eq.), DMAc,  $\text{N}_2$ , 140 °C. .... 172

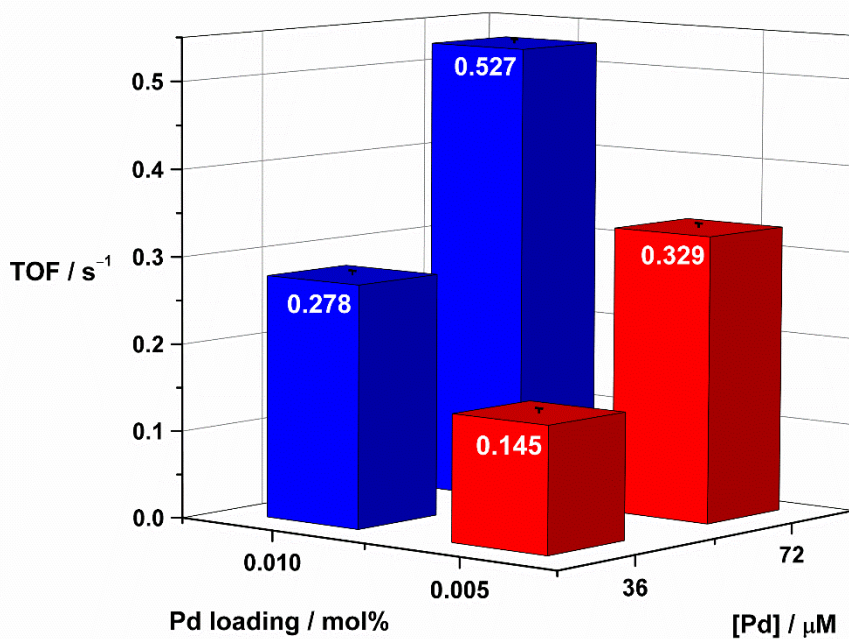


Figure 92 Effect of  $[\text{Pd}]$  on catalyst TOFs in the cyanation of 65 under anhydrous conditions. The TOF was measured as a gradient of  $\text{TON s}^{-1}$  for an initial period of  $1.2 \times 10^4$  seconds (3.3

h.). Precatalyst used: 47, other reaction conditions: $K_4[Fe(CN)_6]$ (0.22 eq.), $Na_2CO_3$ (1 eq.), DMAc, $N_2$ , 140 °C.....	174
Figure 93 Reaction conditions: ArBr (1 eq., 1.4 mmol), 47 (0.01-0.1 mol%), $K_4[Fe(CN)_6]$ (0.22 eq.), $Na_2CO_3$ (1 eq.), DMAc (2 ml), $N_2$ , 140 °C, 16 h. <sup>a</sup> Using $K_4[Fe(CN)_6]$ (0.44 eq. with respect to 1,4-dibromobenzene). Inset graph shows the catalyst loading-Pd concentration ( $\mu M$ ) relationship under substrate screen conditions.....	175
Figure 94 Frontier molecular orbitals for 83 and 84. Calculations performed by Prof. Ian Fairlamb.....	178
Figure 95 Structural analogy of 83, $Pd^0-[Pd_nL_oX_p]$ , with a $Pd-[L]$ .....	179
Figure 96 The dimeric complex 58 was tested as a precatalyst in the aryacyanation of 65. ....	180

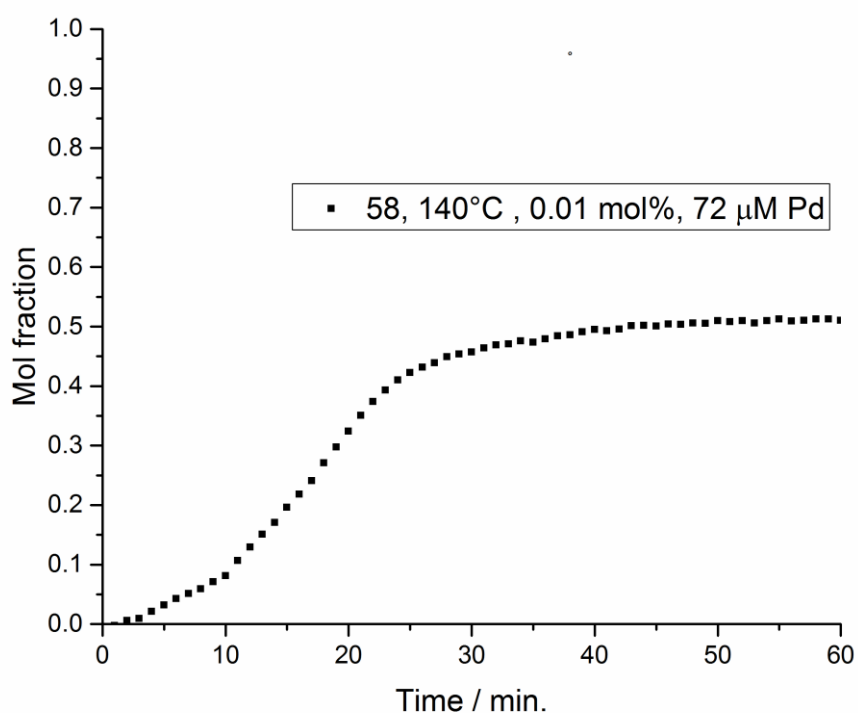


Figure 97 Reaction profile for  $65 \rightarrow 69$  using 58 as a precatalyst. Reaction conditions: Precatalyst 58 (0.005 mol%, Pd concentration = 72  $\mu M$ ),  $K_4[Fe(CN)_6]$  (0.22 eq.),  $Na_2CO_3$  (1 eq.), DMAc,  $N_2$ , 140 °C..... 180

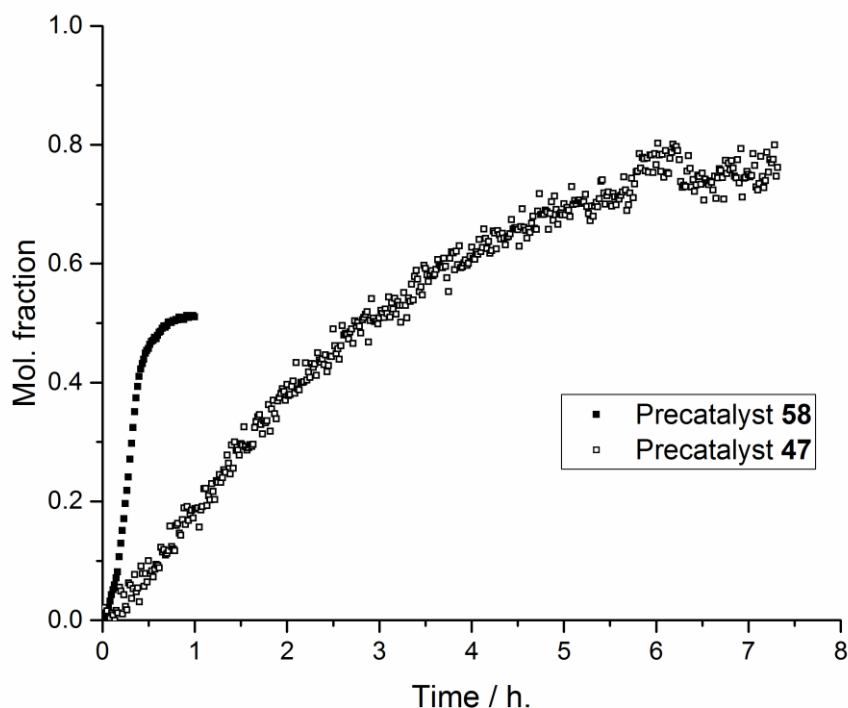


Figure 98 Direct comparison for the reaction profiles of the cyanation of 65 with piperidine (47) or dibenzazepine (58) as ligands at Pd shows their relative rates. Catalyst loadings: with precatalyst 47 (0.01 mol%, Pd conc = 72  $\mu\text{M}$ ); with precatalyst 58 (0.005 mol%, Pd conc = 72  $\mu\text{M}$ ). Other conditions:  $\text{K}_4[\text{Fe}(\text{CN})_6]$  (0.22 eq.),  $\text{Na}_2\text{CO}_3$  (1 eq.), DMAc,  $\text{N}_2$ , 140  $^\circ\text{C}$ . 181

Figure 99 The TOFs of each of the different precatalysts was measured as a gradient of TON  $\text{s}^{-1}$  for an initial period of 5400 seconds (1.5 h.), except from 58 which was for the most active period from 1200-2400 (20-40 minutes). Catalyst loadings: with precatalyst 58 (0.005 mol%, Pd conc = 72  $\mu\text{M}$ ); with all other precatalysts: (0.01 mol%, Pd conc = 72  $\mu\text{M}$ ) Other conditions:  $\text{K}_4[\text{Fe}(\text{CN})_6]$  (0.22 eq.),  $\text{Na}_2\text{CO}_3$  (1 eq.), DMAc,  $\text{N}_2$ , 140  $^\circ\text{C}$ ..... 182

Figure 100 Hypothetical structures for the active catalyst species formed under cyanation conditions from 58..... 182

Figure 101 One unit of the molecular cage substructure used to support PdNPs capable of catalysing arylcyanations in the absence of additives.<sup>106</sup> ..... 184

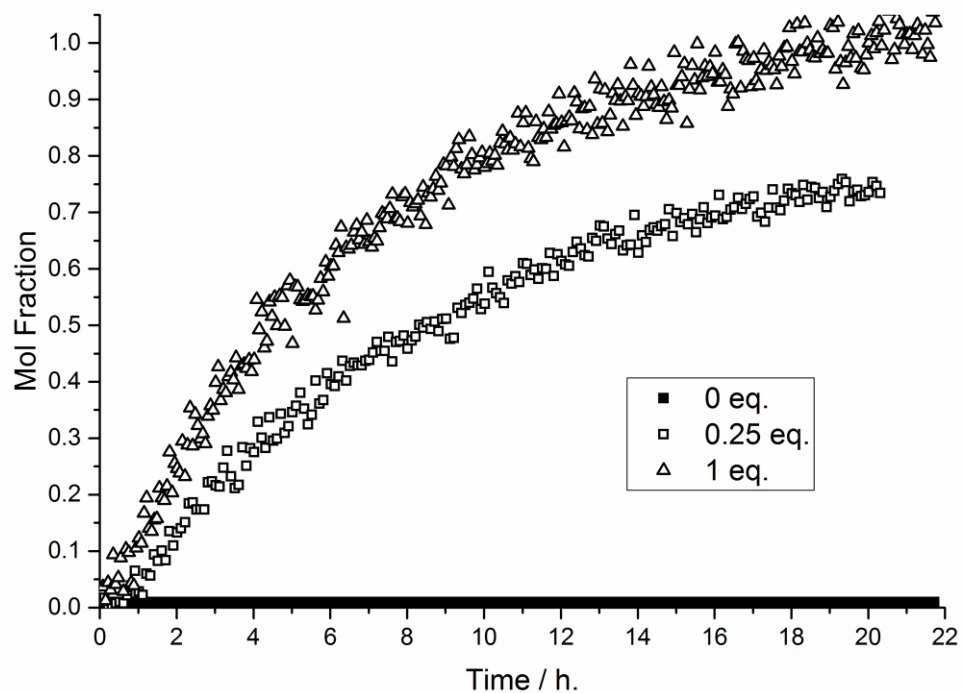


Figure 102 Reaction profiles for reaction  $65 \rightarrow 69$  with varied  $\text{Na}_2\text{CO}_3$  equivalences. Reaction conditions: Precatalyst 47 (0.05 mol%, 180  $\mu\text{M}$ ),  $\text{K}_4[\text{Fe}(\text{CN})_6]$  (0.22 eq.),  $\text{Na}_2\text{CO}_3$  (0 – 1 eq.), DMAc,  $\text{N}_2$ , 120  $^\circ\text{C}$ ..... 185

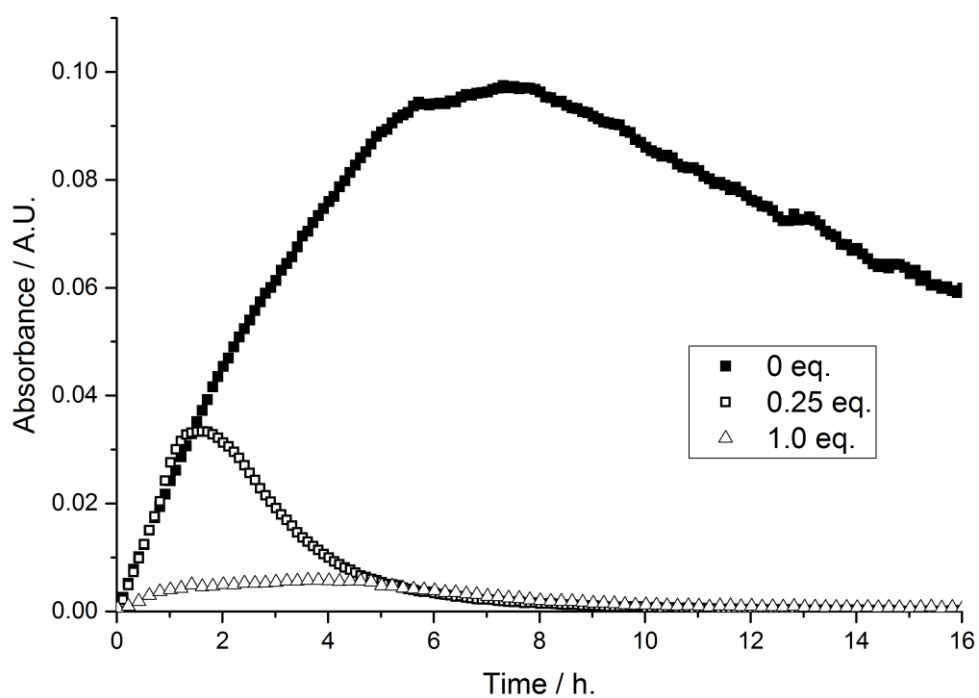


Figure 103  $[\text{Fe}(\text{CN})_6]$  ( $2045 \text{ cm}^{-1}$ ) traces with varied  $\text{Na}_2\text{CO}_3$  equivalences. Reaction

conditions: Precatalyst 47 (0.05 mol%, 180  $\mu$ M),  $K_4[Fe(CN)_6]$  (0.22 eq.),  $Na_2CO_3$  (0 – 1 eq.),  
 DMAc,  $N_2$ , 120  $^\circ$ C..... 186

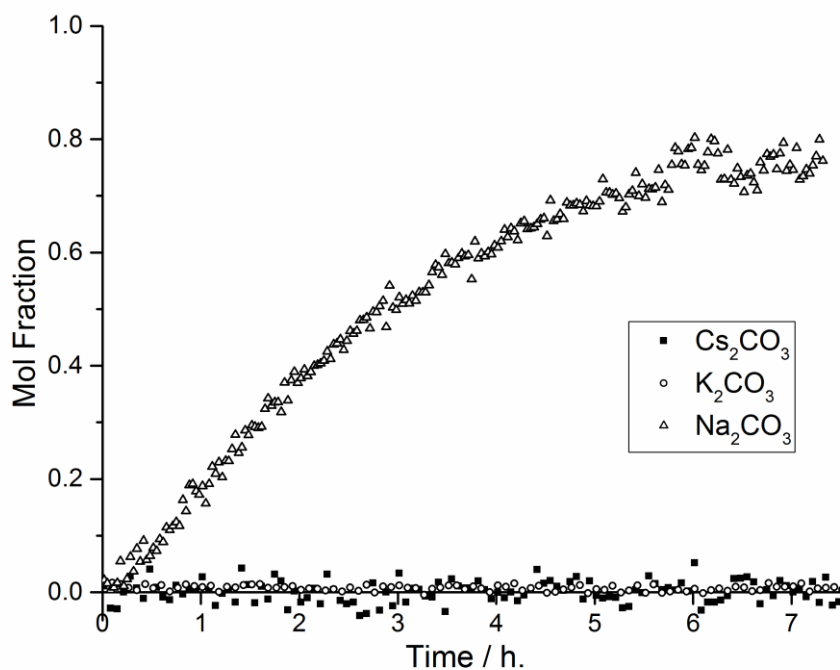


Figure 104 Reaction profiles for formation of cyanopyridone with different carbonate additives. Reaction conditions: Precatalyst 47 (0.01 mol%, 72  $\mu$ M),  $K_4[Fe(CN)_6]$  (0.22 eq.),  
 $X_2CO_3$  (1 eq.), DMAc,  $N_2$ , 140  $^\circ$ C..... 187

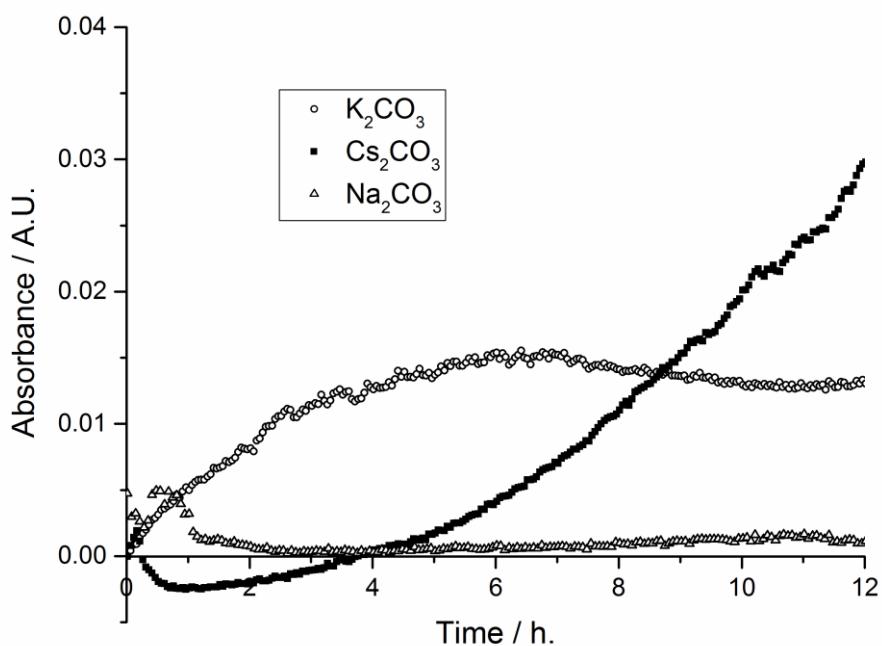
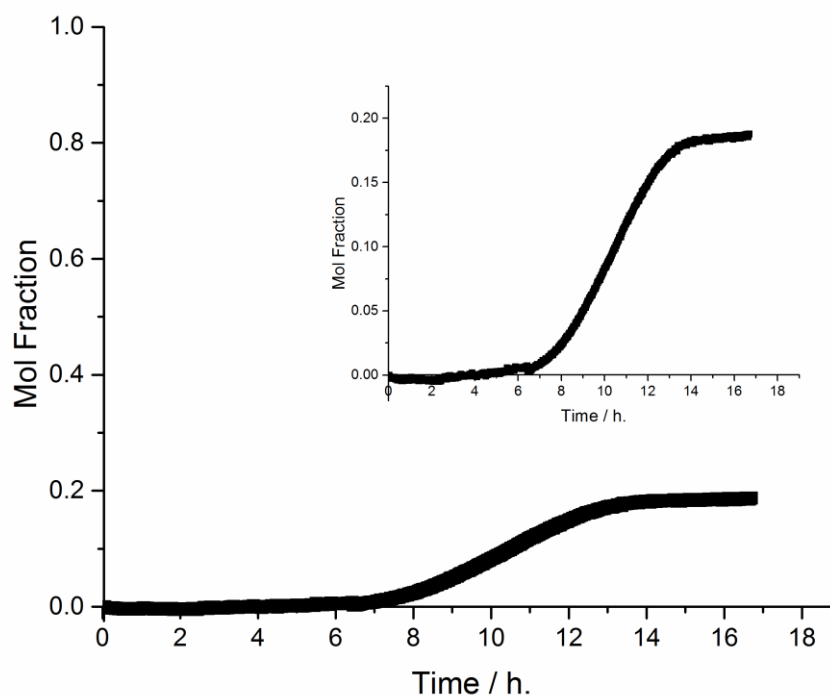


Figure 105  $[Fe(CN)_6]^{4-}$  traces in the attempted cyanation of 65 with different carbonate

- additives, shown in Figure 104. Reaction conditions: Precatalyst 47 (0.01 mol%, 72  $\mu$ M),  $K_4[Fe(CN)_6]$  (0.22 eq.),  $X_2CO_3$  (1 eq.), DMAc,  $N_2$ , 140  $^{\circ}C$ . ..... 188
- Figure 106 Replacing  $Na_2CO_3$  with sodium halide salts still resulted in partial conversion of starting material. Reaction conditions: 47 (0.05 mol%, 180  $\mu$ M),  $K_4[Fe(CN)_6]$  (0.22 eq.), NaX (1 eq.), DMAc,  $N_2$ , 120  $^{\circ}C$ , 17 h. .... 189
- Figure 107 The three reactions reached different conversions at reaction completion and gave different coloured solutions. This was presumably due to the formation of varying  $K_xNa_y[Fe(CN)_z]$  species through counterion swapping and consumption of starting material. .... 190
- Figure 108 The appearances of these four hexacyanoferrate complexes are distinct due to their differing electronic and molecular structures. .... 191



- Figure 109 Reaction profile when  $Na_4[Fe(CN)_6]$  was used as a cyanide source and 47 as a precatalyst in the cyanation of 65. Reaction conditions:  $Na_4[Fe(CN)_6]$  (0.22 eq.),  $Na_2CO_3$  (1 eq.), precatalyst 47 (0.01 mol%, 72  $\mu$ M), DMAc,  $N_2$ , 120  $^{\circ}C$ . Inset graph shows enlargement of reaction profile up to 20 % conversion. .... 193

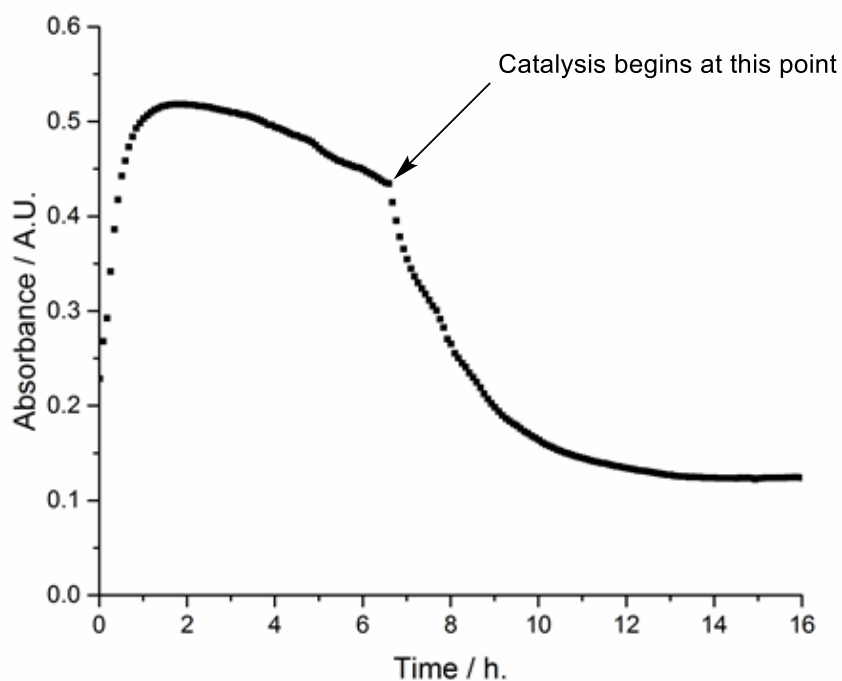


Figure 110 The trend of the hexacyanoferrate absorbance (at  $2061\text{ cm}^{-1}$ ) when using  $\text{Na}_4[\text{Fe}(\text{CN})_6]$  as a cyanide source. Reaction conditions:  $\text{Na}_4[\text{Fe}(\text{CN})_6]$  (0.22 eq.),  $\text{Na}_2\text{CO}_3$  (1 eq.), precatalyst 47 (0.01 mol%,  $72\text{ }\mu\text{M}$ ), DMAc,  $\text{N}_2$ ,  $120\text{ }^\circ\text{C}$ . ..... 194

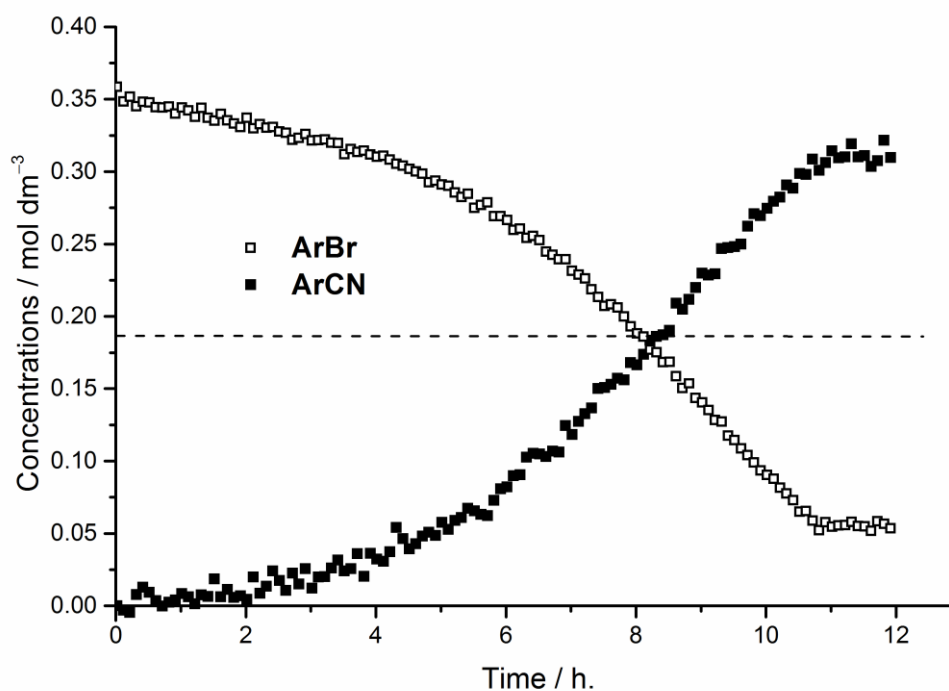


Figure 111 Reaction profile for reaction  $65 \rightarrow 69$  using Prussian red ( $\text{K}_3[\text{Fe}(\text{CN})_6]$ ) as a cyanating agent. Dotted line indicates the point at which the concentration of starting material

and product are equal. Reaction conditions: Precatalyst 47 (0.5 mol%, 1.8 mM),  $K_3[Fe(CN)_6]$  (0.22 eq.),  $Na_2CO_3$  (1 eq.), DMAc,  $N_2$ , 120 °C..... 195

Figure 112 Six  $Pd^{II}$  amine complexes investigated as precatalysts in the arylycyanation of 65 during this study..... 197

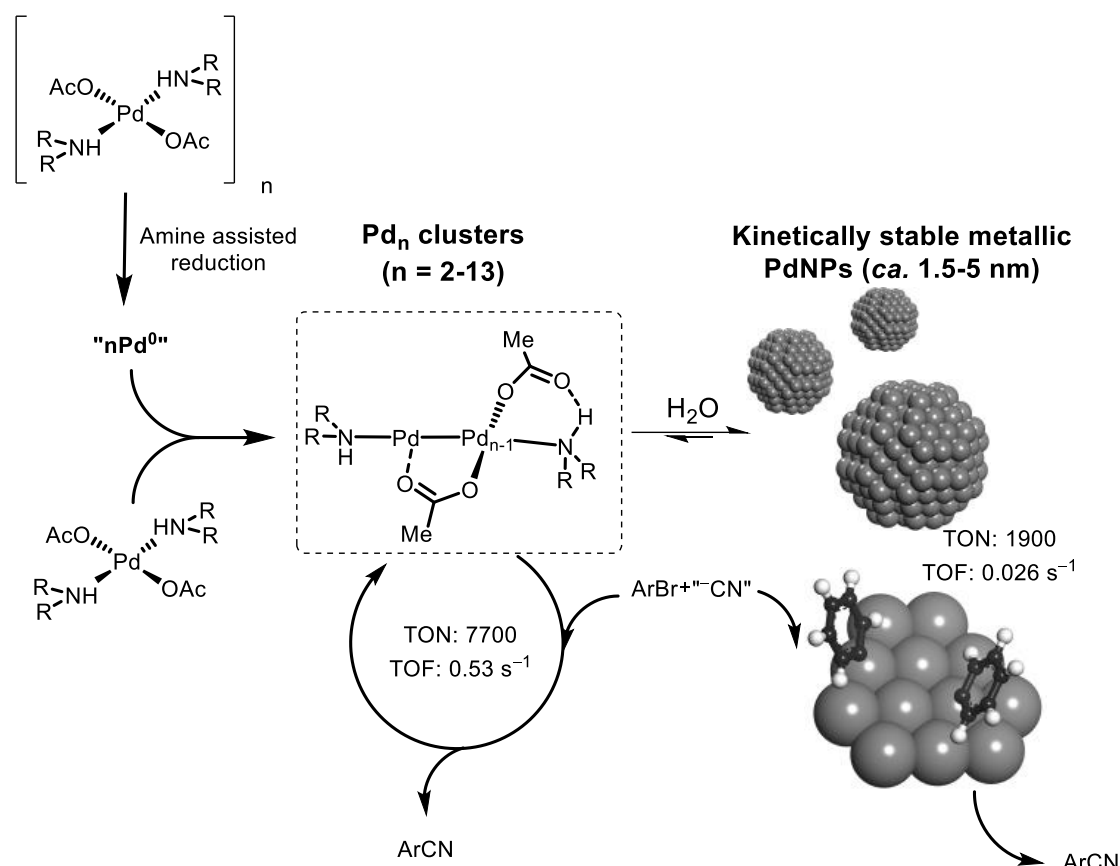


Figure 113 The nature of the active catalyst formed from precatalysts such as 47 in  $Pd$ -catalysed arylycyanation reactions is dependent upon  $Pd$  concentration, catalyst:substrate ratio and the presence of water..... 198

Figure 114 Potential substituted dibenzazepine ligands. .... 200

Figure 115 By incorporating Equation 1 into a nonlinear least-squares data fit, a suitable F-W 2-step mechanism curvefit can be achieved using Excel Solver for the consumption of starting material using 0.05 mol% 47 and  $K_4[Fe(CN)_6] \cdot 3H_2O$  ..... 210

Figure 116 Visual representation of the 95% (brown line) and 99% (grey line) confidence limits for the limits for  $k_1$  for the F-W 2-step curvefit for a precatalyst (47) loading of 0.1 mol%..... 211

Figure 117 Visual representations of the 95% (brown line) and 99% (grey line) confidence limits for the limits for  $k_1$  for the attempted F-W 2-step curvefit. .... 212

Figure 118 Picture of experimental set up for kinetic experiments using the React IR..... 214

Figure 119 Structure of 48, determined by X-ray diffraction; arbitrary numbering used. Selected hydrogen atoms removed for clarity. Thermal ellipsoids shown with a probability of 50%; numbers in parentheses are standard deviations from the measured value, denoting the error in the measurements. A molecule of water has been removed from the unit shell for clarity. Selected bond lengths (Å): N(1)-Pd(1): 2.043(3), O(1)-Pd(1): 2.015(2), C(1)-N(1): 1.484(4), C(5)-O(1): 1.282(4), C(5)-O(2): 1.243(4). ..... 248

Figure 120 Structure of 49, determined by X-ray diffraction; arbitrary numbering used. Selected hydrogen atoms removed for clarity. Thermal ellipsoids shown with a probability of 50%; numbers in parentheses are standard deviations from the measured value, denoting the error in the measurements. Selected bond lengths (Å): N(1)-Pd(1):2.021(2), O(1)-Pd(1): 2.0394(17), O(3)-Pd(1): 2.0300(17), O(5)-Pd(1):1.9969(17), Pd(1)-Pd(2): 3.0377(3), H(1)-O(8):1.98(1). ..... 250

Figure 121 Structure of 50, determined by X-ray diffraction; arbitrary numbering used. Selected hydrogen atoms removed for clarity. Thermal ellipsoids shown with a probability of 50%; numbers in parentheses are standard deviations from the measured value, denoting the error in the measurements. Selected bond lengths (Å): N(1)-Pd(1): 2.018(4), O(1)-Pd(1): 2.034(4), O(3)-Pd(1): 1.999(4), O(2)-Pd(1): 2.033(4), Pd(1)-Pd(2): 3.0389(5), H(1)-O(7):2.00(0). ..... 252

Figure 122 Structure of 52, determined by X-ray diffraction; arbitrary numbering used. Selected hydrogen atoms removed for clarity. Thermal ellipsoids shown with a probability of 50%. Selected bond lengths (Å): N(1)-Pd(1): 2.0638(14), O(1)-Pd(1): 2.0050(12), C(1)-O(1): 1.286(2), C(1)-O(2): 1.236(2). ..... 254

Figure 123 Structure of 53, determined by X-ray diffraction; arbitrary numbering used. Selected hydrogen atoms removed for clarity. Thermal ellipsoids shown with a probability of 50%. Selected bond lengths (Å): N(1)-Pd(1): 2.0696(18), O(1)-Pd(1): 2.0191(16), C(1)-O(1): 1.266(3), C(1)-O(2): 1.229(3), C(3)-N(1): 1.481(3). ..... 256

Figure 124 Structure of 58, determined by X-ray diffraction; arbitrary numbering used. Selected hydrogen atoms and a molecule of pentane (antisolvent) have been removed for clarity. Thermal ellipsoids shown with a probability of 50%; numbers in parentheses are standard deviations from the measured value, denoting the error in the measurements. Selected bond lengths (Å): N(1)-Pd(1) 2.0757(15), Pd(1)-Pd(1) 3.0466(3), O(1)-Pd(1) 2.0147(12), O(2)-Pd(1) 1.9775(12), O(3) Pd(1) 2.0204(13), C(7)-C(8) 1.339(3), C(1)-N(1) 1.454(2). ..... 258

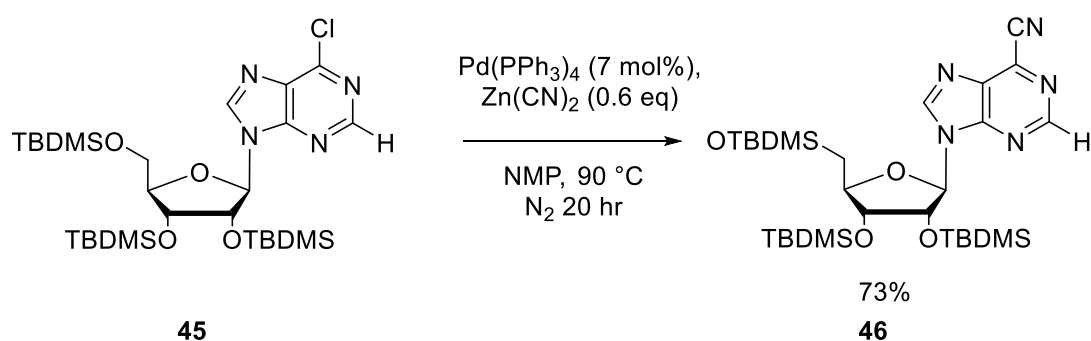
Figure 125 The structure of N-benzyl-4-cyano-6-methylpyrid-2-one (69) as determined by X-ray diffraction; arbitrary numbering used. Hydrogen atoms removed for clarity. Thermal

ellipsoids shown with a probability of 50%; numbers in parentheses are standard deviations from the measured value, denoting the error in the measurements. Selected bond lengths (Å): C(3)-C(6):1.431(3), C(6)-N(2): 1.150(3), C(1)-O(1): 1.2379(16), C(1)-N(1):1.4052(16), C(5)-N(1): 1.3811(16), C(8)-N(1):1.4717(17)..... 260

## List of Schemes

Scheme 1 The key Stille macrocyclisation reaction in the final step of the total synthesis of phacelocarpus-2-pyrone A.....	41
Scheme 2 Suzuki-Miyaura reaction catalysed by polymer supported PdNPs. ....	42
Scheme 3 Regioselective C–H functionalisation of benzothiophene using Pd/C reported by Glorius <i>et al.</i> ....	44
Scheme 4 Using a traditionally homogeneous catalyst system, in the presence of MgO gives selective arylation at the C2 position of indole.....	45
Scheme 5 Selective C–H functionalisation of indole at the C3 position using [Pd(NH <sub>3</sub> ) <sub>4</sub> ]Na/Y reported by Djakovitch <i>et al.</i> ....	45
Scheme 6 These conditions allow for soluble PdNPs to be formed <i>in situ</i> .....	46
Scheme 7 Typical PdNP catalytic behaviour was observed in this benchmark Sonogashira coupling. ....	46
Scheme 8 The kinetic analysis of the hydrogenation of cyclohexene by the precatalyst [Bu <sub>4</sub> N] <sub>5</sub> Na <sub>3</sub> [(1,5-COD)Ir·P <sub>2</sub> W <sub>15</sub> Nb <sub>3</sub> O <sub>62</sub> ] allowed for the extrapolation of the rate constants k <sub>1</sub> , k <sub>2</sub> and k <sub>3</sub> from a reporter reaction (4) proceeding <i>via</i> a sigmoidal kinetic profile at k <sub>obs</sub> . ....	51
Scheme 9 Changing substituent, “R” considerably effects the rate of Pd-catalysed cross-coupling reactions. ....	57
Scheme 10 Fundamental work by Bedford <i>et al.</i> has changed the way Pd <sub>3</sub> (OAc) <sub>6</sub> speciation should be perceived under working reaction conditions. <sup>68</sup> .....	60
Scheme 11 Unified mechanism for the speciation and activation of Pd <sub>3</sub> (OAc) <sub>6</sub> in Suzuki-Miyaura reactions when in the presence of water. Inset: TEM image adapted with permission from <i>Catalysis Science &amp; Technology</i> 2012, 2, 316-323. Copyright of the Royal Society of Chemistry.....	61
Scheme 12 Frech <i>et al.</i> performed kinetic experiments on this benchmark Heck-reaction, including water dosing experiments and Hg <sup>0</sup> drop tests. ....	65

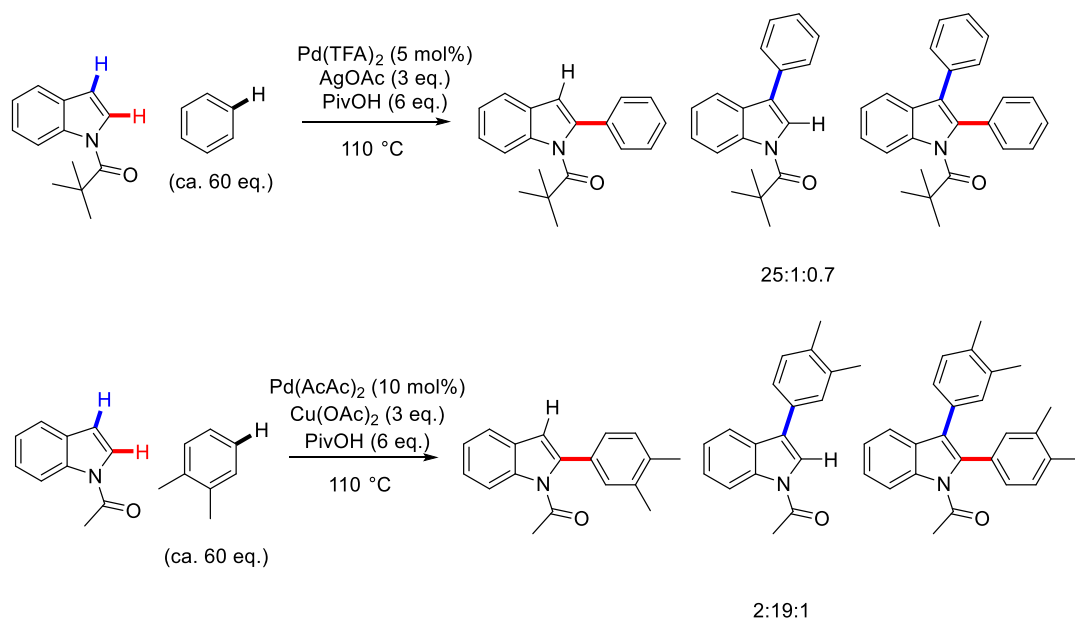
Scheme 13 Bedford <i>et al.</i> report exceptional catalyst TON's across a range of simple substrates and electron deficient aryl chlorides in Suzuki reactions.....	67
Scheme 14 Semenov and Smushkevich's synthesis of 5-phenyl-1-(tributylstannyl)tetrazole. .....	68
Scheme 15 Sakakibara's initial conditions for the cyanation of aryl halides.....	69
Scheme 16 The domino Heck-cyanation step towards the total synthesis of (S)- enantioenriched esermethole, 42.....	69
Scheme 17 Sells' synthesis of 2-cyanoadenosine (no equivalences given).....	71



Scheme 18 Gunderson's cyanation of protected 4-chloroadenosine. ....	72
Scheme 19 Beller's ligand free aryl-cyanation procedure. ....	72
Scheme 20 The benchmark Suzuki-Miyaura coupling used by Boykin <i>et al.</i> ....	75
Scheme 21 The complex $\text{Pd}(\text{OAc})_2(\text{piperidine})_2$ was found to be a PdNP precursor, and competent catalyst in Pd-catalysed C–H functionalisations .....	76
Scheme 22 A general scheme for the synthesis of a range of $\text{Pd}(\text{OAc})_2(\text{HNR}_2)_2$ compounds. .....	78
Scheme 23 The proposed route towards $\text{Pd}(\text{OAc})_2[(\text{CH}_2)_4\text{NH}]_2$ . ....	79
Scheme 24 Impure pyrrolidine resulted in less than 2 equivalents of amine being added, and the acetate dimer 49 forming along with the desired product, 48. ....	79
Scheme 25 Adding freshly distilled pyrrolidine (2 eq.) to $\text{Pd}(\text{OAc})_2$ afforded solely the pyrrolidine acetate monomer complex 48. ....	80
Scheme 26 Synthesis of the pyrrolidine acetate dimer complex, 49. ....	81
Scheme 27 Addition of piperidine (1 eq.) to $\text{Pd}(\text{OAc})_2$ affords the piperidine acetate dimer complex, 50. ....	83
Scheme 28. Synthesis of $\text{Pd}(\text{OAc})_2[(\text{CH}_2)_6\text{NH}]_2$ . ....	86

Scheme 29 The synthesis of 53.....	89
Scheme 30 Attempted synthesis of 54.....	91
Scheme 31 Attempting to neutralise azetidine hydrochloride with <i>n</i> -BuLi unfortunately resulted in the formation of Pd black.....	91
Scheme 32 Attempted synthesis of 57.....	92
Scheme 33 Addition of 56 (2 eq.) to Pd(OAc) <sub>2</sub> resulted in the exclusive formation of the equivalent Pd dimer complex, 58.....	93
Scheme 34 Optimised synthesis of 58.....	99
Scheme 35 Addition of differing equivalences of dry piperidine to Pd <sub>3</sub> (OAc) <sub>6</sub> will result in the formation of 50, potentially <i>via</i> an observable aminolysis intermediate.....	101
Scheme 36 Mechanism of aminolysis of Pd <sub>3</sub> (OAc) <sub>6</sub> with piperidine to 50. Where $k_1 \approx k_2 > k_3 > k_{-1} \approx k_{-2} > k_{-3}$ .....	104
Scheme 37 Beller's conditions, used in the attempted Pd-catalysed cyanation of 4-Bromo-6-methyl-2-pyrone (60).....	111
Scheme 38 Synthesis of dipyronylether, 62.....	114
Scheme 39 Bromination of 4-hydroxy-6-methyl-2-pyrone. <sup>131</sup> .....	114
Scheme 40 Synthesis of 4-cyano-6-methyl-2-pyrone (61) <i>via</i> Rosenmund-von Braun reaction.....	115
Scheme 41 Synthesis of N-benzyl-4-hydroxy-6-methylpyrid-2-one, 66.....	116
Scheme 42 The improved synthesis of N-benzyl-4-bromo-6-methylpyrid-2-one, 65.....	117
Scheme 43 Treatment of 66 with PBr <sub>3</sub> in DMF afforded the 3-formylated derivative 67.....	117
Scheme 44 Treatment of 66 with POBr <sub>3</sub> .....	118
Scheme 45 Hypothesised mechanism for P <sub>4</sub> O <sub>10</sub> deactivation in the presence of water.....	119
Scheme 46 Synthesis of N-benzyl-4-cyano-6-methylpyrid-2-one using Rosenmund-von Braund conditions.....	119
Scheme 47 The benchmark reaction chosen for the initial screening of Pd precatalysts.....	121
Scheme 48 Aliquots of the catalyst solution were taken at set intervals and used in the benchmark reaction.....	124
Scheme 49 A series of kinetic experiments on the catalyst, 47, were carried out using <i>in-situ</i> IR spectroscopy.....	131

Scheme 50 The Finke-Watzky nucleation and autocatalytic growth mechanism. Provided $k_3 \gg k_2 > k_1$ it is possible to calculate the values of $k_1$ and $k_2$ using the kinetics for the summative pseudoelementary step (4).....	142
Scheme 51 Suggested mechanism for the formation of catalytic precursor, "A". S = DMAc .....	143
Scheme 52 The benchmark reaction developed for kinetic analysis of catalytic efficiency using <i>in situ</i> infrared spectroscopy.....	166
Scheme 53 Autocatalytic growth of higher order Pd <sub>n</sub> clusters, exemplified here for n = 2: Computational calculations (DFT methods in Gaussian09: wb97xd/dgdzvp-def2tzv) show that 83 and 84 are energetically feasible species, with 84 being <i>ca.</i> 15.4 kcal mol <sup>-1</sup> lower in energy – an accessible barrier for the aryl cyanation reaction conditions). Calculations performed by Prof. Ian Fairlamb. ....	176
Scheme 54 Reaction conditions to study effects of alternative Na <sub>2</sub> CO <sub>3</sub> equivalences in the cyanation of 65.....	184
Scheme 55 Reaction conditions under which the effects of three NaX salts as additives were tested in the cyanation of 65 using precatalyst 47. ....	188
Scheme 56 Reaction conditions used to test alternative hexacyanoferrates as cyanide sources in the cyanation of 65.....	191
Scheme 57 Using the optimised conditions used in the synthesis of 58 a range of dimeric [Pd(OAc) <sub>2</sub> (HNR <sub>2</sub> ) <sub>2</sub> ] precatalysts could be synthesised.....	200
Scheme 58 Glorius <i>et al.</i> report the highly regioselective C–H arylation of polyaromatics by Pd/C. <sup>152</sup> .....	201



- Scheme 59 Switch in the regioselectivity of the direct arylation of N-protected indole in the presence of differing terminal oxidants.<sup>156</sup> ..... 203
- Scheme 60 Synthesis of heterodimetallic Pd-Cu/Ag acetate clusters.<sup>161</sup> ..... 204
- Scheme 61 The reduction of Pd(II)-Zn(II) acetate clusters under H<sub>2</sub> provides well defined PdZn alloy nps.<sup>157f</sup> Adapted with permission from *Catal. Lett.* 2006, 112, 155-161. Copyright of Springer. .... 205
- Scheme 62 The synthesis of Pd(OAc)<sub>2</sub>(HNR<sub>2</sub>)Cu(OAc)<sub>2</sub>(HNR<sub>2</sub>) complexes, and use as precursors for catalysts of type 88. .... 205

## List of Tables

Table 1. Attempted optimisation of Pd-catalysed cyanation of 4-Bromo-6-methyl-2-pyrone (60).....	112
Table 2 Attempted optimisation of Pd-catalysed cyanation of 4-Bromo-6-methyl-2-pyrone (60).....	113
Table 3 Optimisation of the synthesis of 65. ....	118
Table 4 The four different catalyst solutions screened in the benchmark reaction. ....	121
Table 5 Product conversions from the benchmark reaction using the four catalyst solutions outlined in Table 4. ....	123
Table 6 Conversions of the benchmark reaction 65 →69 using the three monomeric, preformed Pd(OAc) <sub>2</sub> (HNR <sub>2</sub> ) <sub>2</sub> precatalysts after four hours reaction time, compared with <i>in situ</i> catalyst, 70, and Pd(OAc) <sub>2</sub> . ....	127
Table 7 Maintaining the optimal Pd concentration of 33.5 ppm while using 52 as a catalyst in the arylcyanation of 65 allowed for improved catalytic activity. ....	128
Table 8 The effect of Pd catalyst loading on observed rate of reaction, <i>k</i> <sub>obs</sub> , TON and TOF. ....	136
Table 9 Values calculated from the kinetic traces displayed in Figure 91. Catalyst TOFs were measured as a gradient of TON s <sup>-1</sup> for an initial period of 11,880 seconds (3.3 h.) Reaction conditions: Precatalyst 47 (0.005 or 0.01 mol%, 36 or 72 μM), K <sub>4</sub> [Fe(CN) <sub>6</sub> ] (0.22 eq.), Na <sub>2</sub> CO <sub>3</sub> (1 eq.), DMAc, N <sub>2</sub> , 140 °C. ....	173
Table 10 Variation of the cyanide source. ....	192
Table 11 Attempted optimisation for arylcyanation of 89.....	245
Table 12 Attempted optimisation for the arylcyanation of 89 in the presence of XPhos ..	245
Table 13 Attempted optimisation for the arylcyanation of 89 in the presence of additives. ....	247
Table 14 Crystal data and structure refinement for ijsf1464 (Compound 48) .....	249
Table 15 Crystal data and structure refinement for ijsf1331 (Compound 49) .....	251
Table 16 Crystal data and structure refinement for ijsf1515 (Compound 50) .....	253
Table 17 Crystal data and structure refinement for ijsf1402 (Compound 52) .....	255
Table 18 Crystal data and structure refinement for ijsf1470 (Compound 53) .....	257

Table 19 Crystal data and structure refinement for ijsf1514 (Compound 58) .....	259
Table 20 Crystal data and structure refinement for ijsf1330 (Compound 69) .....	261

## **Acknowledgements**

First and foremost I must extend my enormous thanks to Ian Fairlamb for giving me the opportunity to work with him over the past five years. I am massively thankful for all of the help and support he has provided me, while allowing me to work independently and let my own research ideas blossom through my own experimentation. Beyond this, Ian has always been keen to have a pint or two over a curry after the long Friday afternoon group meetings; I hope we'll have the chance to do this again over the coming years. I'd also like to express my thanks to my industrial supervisor Mark Ford who has kept the project on the straight and narrow and provided crucial insight into the complicated results and kinetic data, all in the name of lower catalyst loadings!

I have had the pleasure during my time working in York to supervise five outstanding undergraduate students, Amy, Pash, Magdalene, Julien and Khai, whose diverse projects, jokes and hard work have enriched my Ph.D. massively.

The entire Fairlamb group (now over 50 people have crossed my path!) have been an invaluable source of support and laughs. In particular I would like to express my gratitude to Sara and Tom (for convincing me to do this), Charlotte (for keeping E114 running), Tom (for the pub, gin and juice and San Fran), Jess (for Sunday afternoon pints in the Derry and being my personal inorganic chemistry support group), Jonny (for the ceaseless banter), Lyndsay (for being there for a good old moan), Philippa (for a mental first year), Alan (for keeping coffee interesting), George Platt (for being a ReactIR buddy), Anders (for your dry humour) and Ben (for your hard work and laughs, I still owe you a pint!).

Additionally thanks go to Heather Fish and Pedro Aguilar (NMR), Charlotte Elkington (ReactIR), Karl Heaton (MS), Adrian Whitwood (XRD) and Graeme McAllister (CHN) for the technical support I have received.

My family have always provided me with their sincere and undivided support throughout the entire of my education. It is safe to say that without the encouragement from my parents and brother to get back up when I was down over these past few years then getting this far would have been impossible.

Finally my most heartfelt thanks go to Blanca who has tolerated and supported me in every conceivable way throughout the course of my PhD, especially in the hard times towards the end. I hope that she knows that I could not have done this without her.

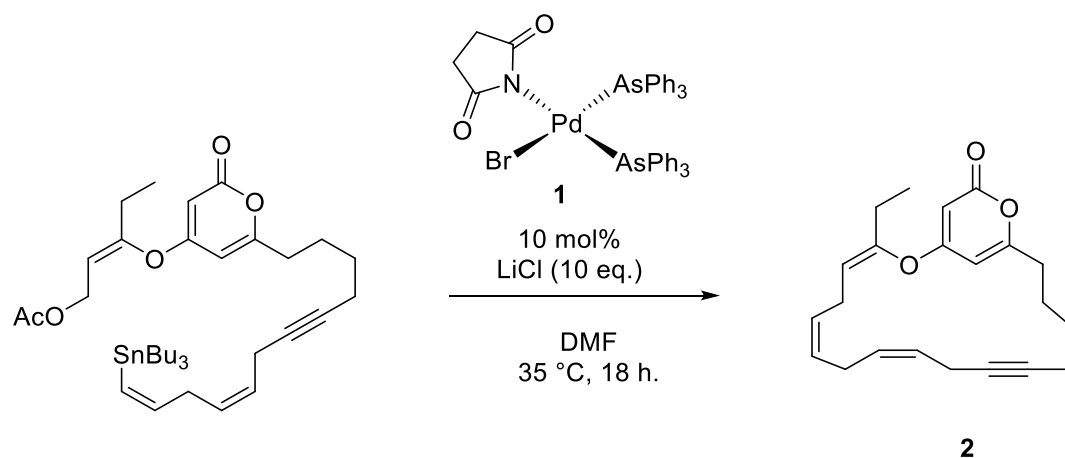
## **Author's Declaration**

The work presented in this thesis is my own except where referenced or clearly indicated in the body of the text. The work was carried out at the University of York between October 2012 and September 2016, and has not previously been presented for an award at this or any other university.

## Chapter 1: Introduction

### 1.1. The scope and phases of Pd catalysis

A better understanding of the true catalytic species in palladium-catalysed cross-coupling reactions is the key to engineering more efficient catalysts in the future. Since their discovery and application by key scientists in the field (notably awarded the Nobel Prize in 2010) its use, and the investigation into the mechanisms by which it facilitates such a diverse array of chemical transformations, has been paramount to the progression of modern synthetic chemistry.<sup>1</sup> Pd plays an integral part in the synthesis of many natural products and important structural motifs.<sup>2</sup> The recent total synthesis of the 2-pyrone containing natural product phacelocarpus-2-pyrone A (**2**) utilises a Stille macrocyclisation reaction catalysed by the imidate containing precatalyst **1**.<sup>3</sup> Precatalyst **1** has also been found to be very efficient in the room temperature Stille cross-couplings of benzyl chlorides.<sup>4</sup> Ongoing studies into the mechanism of catalyst activation in these reactions present a mechanistic dichotomy for the role of oxygen in the formation of catalytically active Pd nanoparticles.<sup>5</sup>



**Scheme 1** The key Stille macrocyclisation reaction in the final step of the total synthesis of phacelocarpus-2-pyrone A.

Due to it being a fast dwindling, expensive resource, academia and industry are constantly striving to design more efficient Pd catalysts which can achieve higher turn-over numbers (TON) in order to allow for lower catalyst loadings. The design of molecular Pd catalysts and their ligands has advanced hugely, leading to TONs of up to a million in some Suzuki-Miyaura reactions on activated aryl chlorides.<sup>6</sup> However in many Pd-catalysed reactions, these expensive and highly specialised catalysts may not be required, as it has been proven that the active catalytic species for many Pd<sup>0/II</sup> catalytic cycles transpires from palladium

nanoparticles (PdNPs).<sup>7</sup> It has become accepted over the past couple of decades that PdNPs are formed as part of the active catalyst system in many palladium catalysed cross-coupling reactions, such as the Suzuki-Miyaura and Mizoroki-Heck.<sup>8</sup> There is evidence for the fact that in some reactions these PdNPs may act as Pd reservoirs; they release molecular/small clusters of Pd by leaching. In other systems PdNPs have been shown to behave as true heterogeneous catalysts: where the reaction takes place solely on the surface of the nanoparticles. Key work supporting the role of surface catalysed Pd cross-coupling was provided by Davis *et al.* by carrying out a spatially resolved Suzuki-Miyaura reaction utilising an AFM cantilever coated in PdNPs on a monolayer of aryl bromides tethered to a gold surface.<sup>9</sup> Fairlamb and co-workers also reported evidence for surface catalysed Suzuki-Miyaura reactions by *operando* XAS (X-ray absorption spectroscopy) and EXAFS (extended X-ray absorption fine structure). Their catalyst of interest was polyvinylpyrrolidone (PVP) (3) supported PdNPs (Scheme 2).<sup>10</sup>

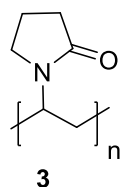
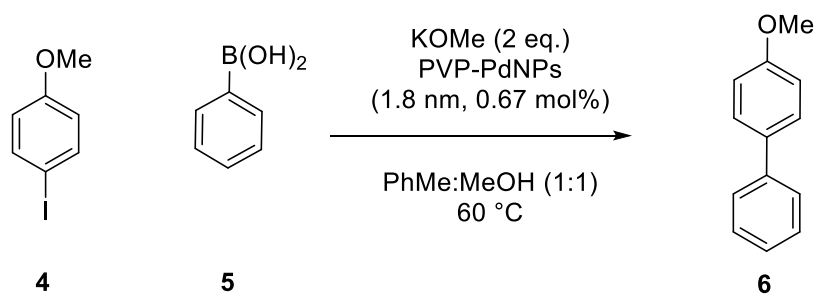


**Figure 1 Polyvinylpyrrolidone (PVP).**



**Scheme 2 Suzuki-Miyaura reaction catalysed by polymer supported PdNPs.**

These extensive experiments showed that the relative turn-over frequency (TOF) of the catalyst was directly related to NP size, and therefore the number of surface atoms. However when the coupling rate was normalised to the surface atoms that only occupy edge and vertex positions on the NP, defect sites shown in yellow in Figure 2, catalyst TOF was found to be independent.

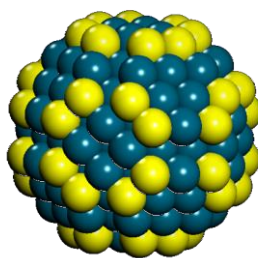


**Figure 2 A 236 atom nanoparticle showing defect sites in yellow.<sup>10</sup>**

The operando XAS and EXAFS studies on the benchmark cross-coupling (Scheme 2) show conclusively that over the course of the reaction no leaching of Pd atoms from the 236 atom NPs occurs. These data are modelled against the XAS measurements of a 188 atom NP and it is clear to see that the characteristic drop in intensity for the smaller NP does not happen at any point during the reaction. The EXAFS measurements also show a constant first shell coordination number indicating that the initial NP structure is preserved throughout the course of the coupling reaction.

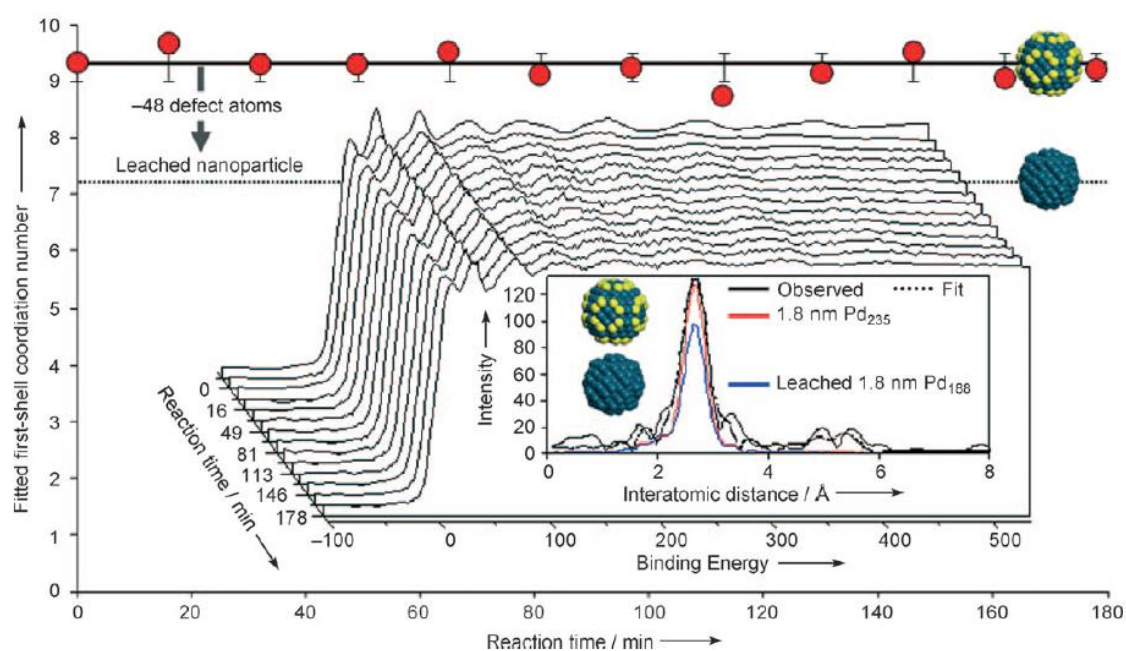
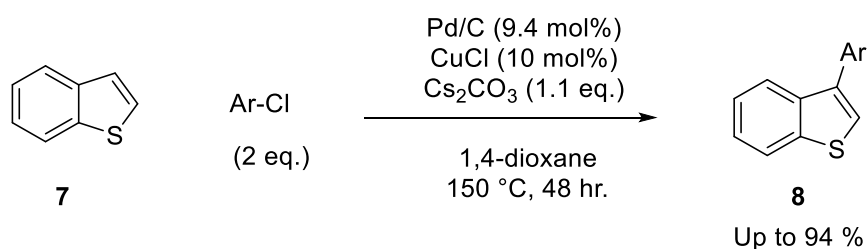


**Figure 3 Operando XAS and EXAFS fits of 1.8 nm PdNPs during Suzuki cross-coupling reaction. Intensity for “leached” particle obtained by using a control batch of Pd NPs of correct size. Adapted with permission from *Angew. Chem.* 2010, 122, 1864. Copyright of Wiley.**

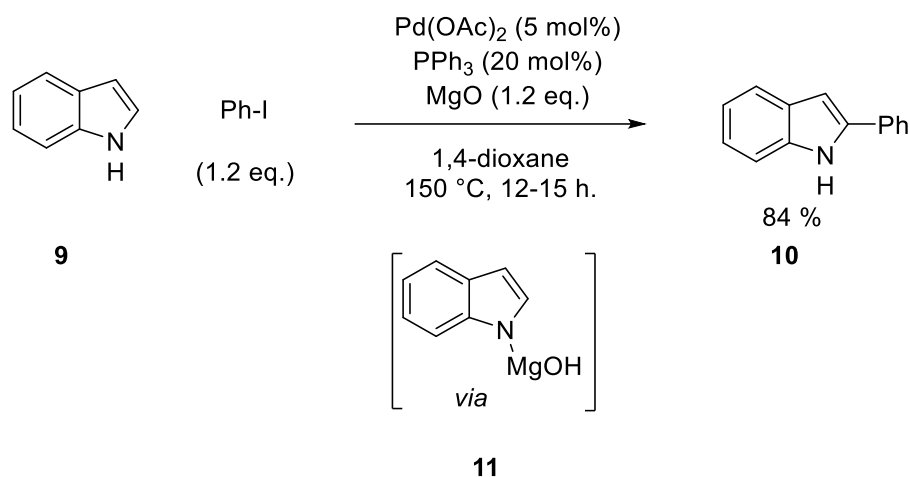
A study by Blackmond *et al.* showed similar results when probing the surface of PdNPs in a Heck reaction. It was found that the initial reaction rate dramatically dropped when plotted against NP size, but when normalised against defect sites, the relative rate stayed constant.<sup>11</sup> Another key discovery was that Pd<sub>2</sub>(dba)<sub>3</sub>-dba supported on PVP, and size controlled PdNPs

on PVP (1.7 nm) actually outcompeted the rate of a traditional “homogeneous” Pd catalyst  $\text{Pd}_2(\text{dba})_3\cdot\text{dba}$ , proving that in some cases heterogeneous Pd catalysts should be used preferentially over customary Pd catalysts.<sup>11</sup> Along with increased efficiency it has been reported that the use of heterogeneous Pd catalysts can promote selectivity for reactions to occur at previously difficult sites. Both Glorius *et al.* and Djakovitch *et al.* have individually presented the first completely regioselective direct C–H functionalisations of benzothiophene and indoles respectively at the C3 positions by using heterogeneous Pd catalysts (Scheme 3, Scheme 5).<sup>12</sup>



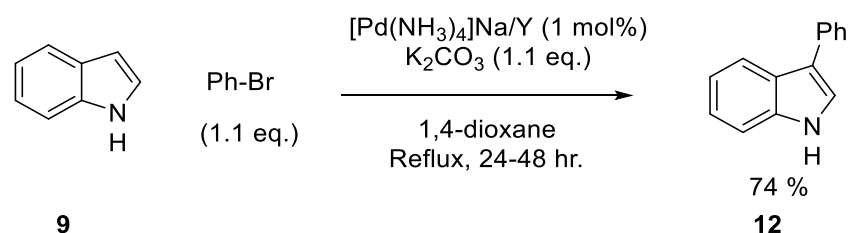
**Scheme 3 Regioselective C–H functionalisation of benzothiophene using Pd/C reported by Glorius *et al.***

These two examples show evidence for the different mechanisms of heterogeneous *vs* homogeneous catalysis allowing for exclusive C3 arylation, whereas previously it has been reported that unsupported Pd catalysts have shown regioselectivity towards the C2 positions in both benzothiophenes and indoles.<sup>13</sup> Sames *et al.* provided a mechanistic study into the factors that may govern the selectivity of C2 or C3 arylation on indole.<sup>14</sup> Potential mechanisms towards explaining the different factors that may govern the regioselectivity between C2 *vs* C3 arylation are discussed, and it was found that selectivity is governed by a number of complicated effects including steric bulk of the Pd ligands and complexation of Mg to the free NH, as in **11**, Scheme 4.



**Scheme 4** Using a traditionally homogeneous catalyst system, in the presence of MgO gives selective arylation at the C2 position of indole.

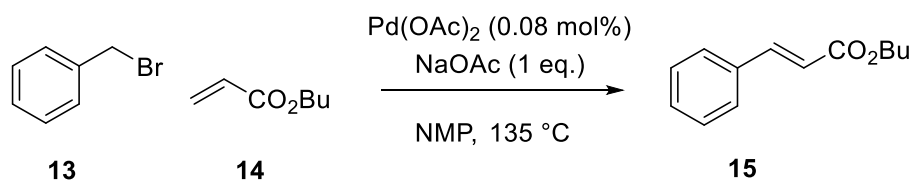
The data supports a hypothesis that C2 arylation occurs by initial electrophilic substitution at the C3 position, followed by migration of Pd to C2 and subsequent reductive elimination. Increased steric bulk around the Pd and the nitrogen inhibits this migration, favouring C3 arylation; this may explain why C3 arylation of indole occurs almost exclusively when heterogeneous Pd catalysts are utilised (Scheme 5).



**Scheme 5** Selective C–H functionalisation of indole at the C3 position using  $[\text{Pd(NH}_3)_4]\text{Na/Y}$  reported by Djakovitch *et al.*

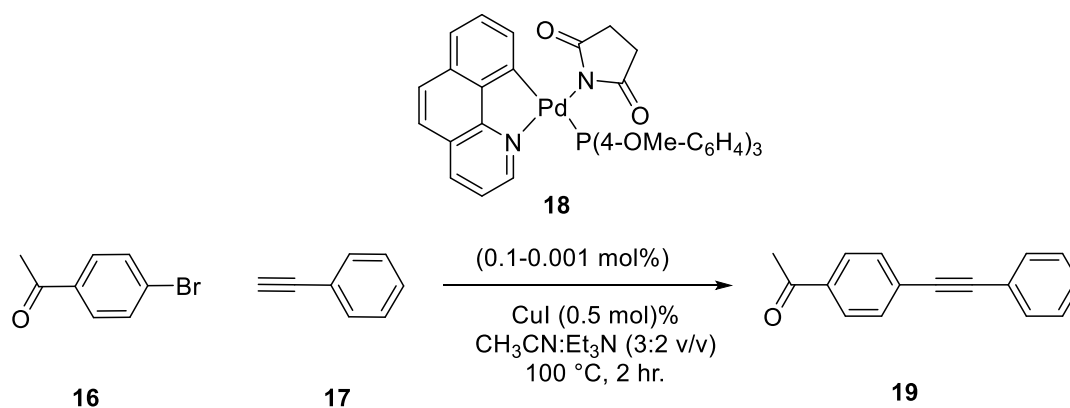
In many Pd-catalysed reactions, particularly those which occur in unligated or phosphine free systems, PdNPs form *in situ*. These PdNPs can be stabilised in solution by the addition of certain reagents and by controlling the coordination sphere around Pd. This is particularly important when anions (such as halides and acetate) in solution can serve to affect the rates of key steps in the catalytic cycle.<sup>15</sup> The knowledge surrounding the dependence of catalyst activity on additives, solvents and by-products in systems such as those found by Jutand and co-workers,<sup>15</sup> and phosphine-free systems reported by Jeffery<sup>16</sup> have been further developed following the investigation of *N*-alkyl ammonium halide salts,<sup>17</sup> halide anions<sup>18</sup> and solvent stabilisation effects<sup>19</sup> on small Pd clusters. However, even in the presence of such stabilisation effects, the formation of Pd nanoclusters of adequate catalytic activity is still

dependant on achieving correct catalyst and reaction concentration,<sup>20</sup> catalyst to substrate ratio<sup>7, 21</sup> and reaction rate (catalyst TOF, and therefore reaction temperature).<sup>8</sup> The use of suitable stabilising solvents, such as N-methyl-2-pyrrolidinone (NMP), dimethyl formamide (DMF) or dimethylacetamide (DMAc) and an appropriate base, such as sodium acetate, has been shown by de Vries and co-workers to form soluble Pd clusters from Pd(OAc)<sub>2</sub>.<sup>7</sup> In a high temperature Heck reaction on **13** (Scheme 6) the Pd clusters formed exhibit TOFs higher than a benchmark palladacycle at comparable catalyst loadings.



**Scheme 6** These conditions allow for soluble PdNPs to be formed *in situ*.

High catalyst loadings in this reaction were also found to decrease final conversion dramatically; *i.e.* 1.28 mol% Pd gives a substantially lower yield. This is because at higher catalyst loadings greater Pd aggregation occurs, leading to insoluble Pd black. By reducing the catalyst loading to 0.08 mol% Pd, a medium was found whereby the rate of Pd aggregation matched the rate of oxidative addition, allowing for efficient catalyst turn-over. A similar inverse correlation of catalyst activity with catalyst concentration was observed by Fairlamb and co-workers, who observed a dramatic decrease in TOF upon increasing the catalyst loading of **18** from 0.001 mol% to 0.01 and 0.1 mol% in a benchmark Sonogashira coupling (Scheme 7).<sup>21</sup> This behaviour is typical of a reaction catalysed by PdNPs, the inhibition of catalysis upon higher catalyst loadings suggests that agglomeration of Pd is occurring at higher concentrations, removing it from the active catalyst phase.



**Scheme 7** Typical PdNP catalytic behaviour was observed in this benchmark Sonogashira coupling.

In the past, heterogeneous catalysts have often suffered from the stigma that they suffer from a lack of selectivity towards individual reactions, especially in organic synthesis. This, coupled with the often increased activity of heterogeneous catalysts, unfortunately can lead to unwanted side reactions when a poorly defined catalyst is utilised with an inadequate understanding of the reaction system. A typical example of this is the common misunderstanding that the addition of phosphine ligands (typically  $\text{PPh}_3$  when complexed to precatalysts in the form of  $\text{Pd}(\text{PPh}_3)_4$  or  $\text{PdCl}_2(\text{PPh}_3)_2$ ) provides a unified homogeneous mechanism in Pd-catalysed cross-coupling reactions. In fact it is known that  $\text{PPh}_3$  itself can not only act as a ligand for small Pd clusters<sup>22</sup> but also as template for their formation.<sup>23</sup> Phosphines are also well reported for their ability to stabilise larger, Pd nanoparticles.<sup>24</sup>

A common problem encountered by synthetic chemists as a result of a fairly widespread misunderstanding of the mechanism of heterogeneous catalysis and its inherent catalyst structure-activity relationship is the overhydrogenation of alkynes to alkanes while using a poorly structurally-defined heterogeneous Pd catalyst.<sup>25</sup> However, since the end of the 1990's the vast development of nanosciences has led to nanocatalysis emerging as a domain of its own, bridging the two fields of heterogeneous and homogeneous catalysis. The aim of nanocatalysis is to develop techniques to create well defined catalysts which display the positive aspects of both homogeneous (selectivity, ease of synthesis) and heterogeneous catalysts (efficacy, stability, recovery).<sup>26</sup> As with any emerging area of science, this allowed for previously inaccessible solutions to be found for existing problems.<sup>27</sup>

An elegant example of the precise and reproducible synthesis of nanocatalysts to gain understanding of a process and common synthetic problem (the overhydrogenation of alkynes mentioned *vide supra*) is provided by Laskar and Skrabalak.<sup>28</sup> They reported an extensive investigation on the effect of different Pd nanocluster geometries on partial alkyne hydrogenation. This shed considerable light on why poorly defined heterogeneous Pd catalysts can cause so many problems with overhydrogenation and *cis-trans* isomerisation.

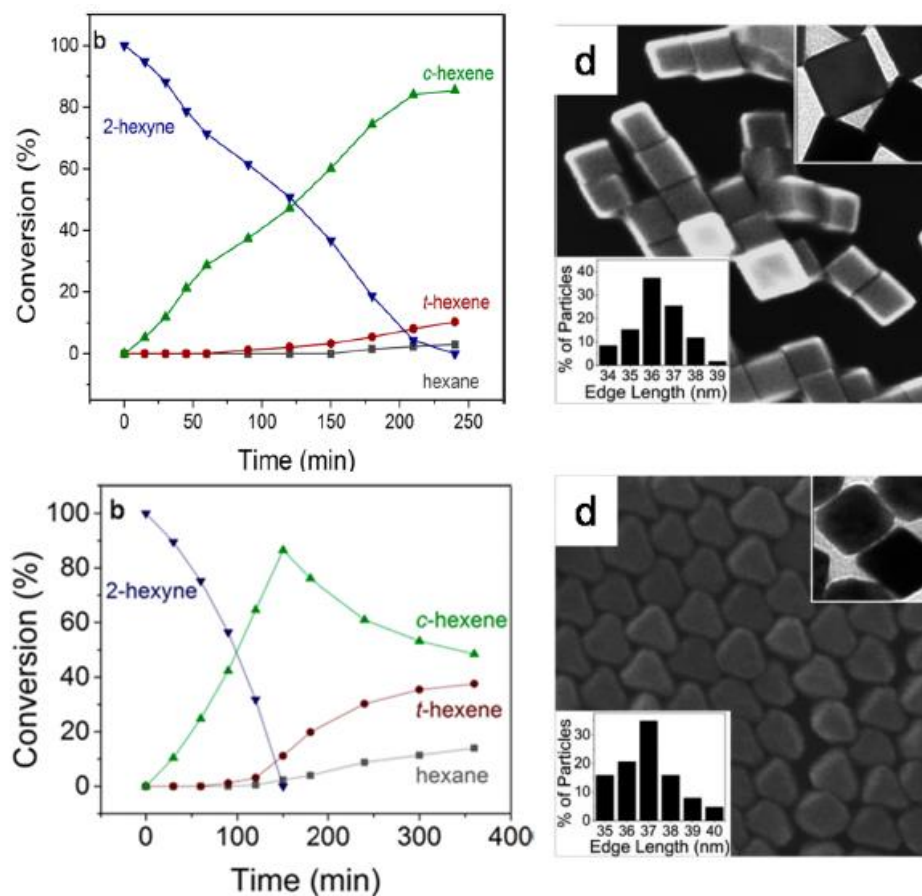


**Figure 4** Laskar and Skrabalak's nanocubes (top) and nanoctahedra (bottom) of comparable edge lengths show remarkable differences in activity and selectivity in the hydrogenation of 2-hexyne. Reprinted (adapted) with permission from (Moitree Laskar and Sara E. Skrabalak *ACS Catal.*, 2014, 4, 1120). Copyright (2014) American Chemical Society.

Laskar and Skrabalak synthesised a wide range of sizes of Pd nanocubes and nanoctahedra, before studying all of their activities in the hydrogenation of 2-hexyne. The difference in activity between the two shapes at comparable edge lengths is worth highlighting here. Inspection reveals that despite both catalysts having the same 37 nm edge length, the nanoctahedra (Figure 4, bottom) show a much higher activity.

These kinetic traces also show that for both catalysts, isomerisation from *cis*-2-hexene to *trans*-2-hexene and over hydrogenation only occur after all 2-hexyne has been consumed, this is easily rationalised by the higher binding affinity of alkynes to a well ordered metal surface than alkenes, causing preferential alkyne binding. Therefore in order for isomerisation or hydrogenation of the alkene to occur, the majority of the alkyne must have been consumed.

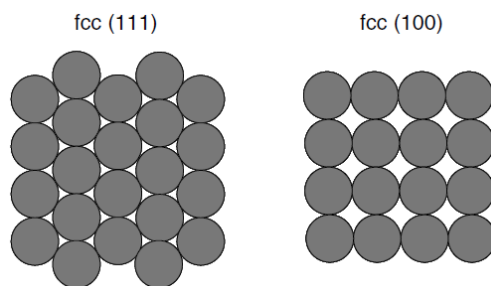


**Figure 5** Laskar and Skrabalak's nanoctahedra adopt a low energy fcc (111) structure, whereas the nanocubes adopt a higher energy fcc (100) structure. Adapted with permission from *Concepts in Nanocatalysis, Nanomaterials in Catalysis, First Edition*. Copyright of Wiley.

The higher efficiency of the nanoctahedra catalyst can be easily passed-off as a result of simple increased surface area, but after closer inspection it is evident that another effect is at play. The increase in activity was normalised with respect to the total number of surface atoms over all sizes of both catalysts. When the nanocube catalyst's percentage atoms in face sites increased by 0.5% the activity was found to have doubled. However, when the percentage atoms in face sites of the nanoctahedra increased by a 1.5%, the activity increased twelve-fold. This means that the higher TOF for the nanoctahedra is not only due to the increased surface area, but can be explained again by binding affinities of the alkyne to the catalyst surface. Due to the stronger binding (4-atom- $\mu$ -bridging) of alkynes to the nanocubes' high energy fcc (100) surface, hydrogenation of the alkyne followed by alkene adsorption is slow. The higher TOF and activity of the nanoctahedra is therefore due to the alkynes weaker binding (2-atom-di- $\sigma$ -bridging) to the lower energy fcc (111) surface, resulting in a lower adsorption/desorption energy barrier and faster catalysis (Figure 6).<sup>29</sup>

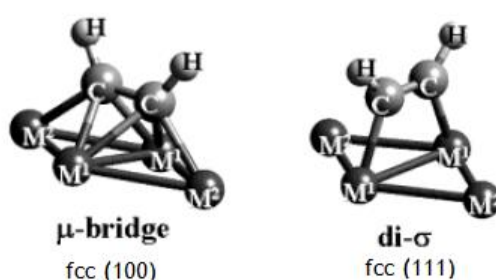


**Figure 6** Computationally it has been found that alkynes coordinate to fcc (100) faces through a stronger binding mode than to fcc (111). Reprinted with permission from (*J. Phys. Chem. B.* 2003, 107, 217). Copyright (2003) American Chemical Society.

Parallels can therefore be drawn between the intricacies in nanocatalyst surface design and the optimisation of a molecular catalyst-ligand system. The understanding behind how to design highly efficient nanocatalysts, and molecular precursors to nanocatalysts is therefore a pressing issue and highly prevalent in current literature.

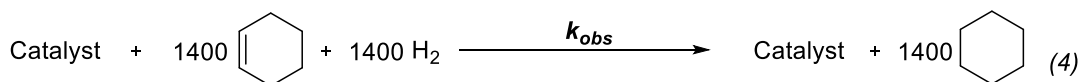
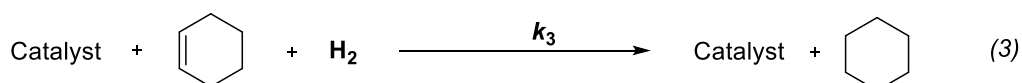
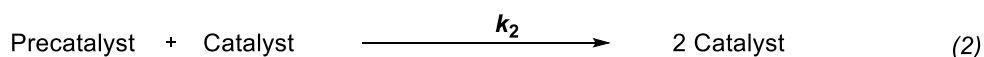
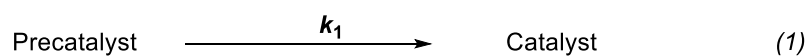
### 1.1.1. Identifying the nature of the active Pd catalyst

The use of transition metal complexes as precatalysts in reductive catalysis is commonplace, although the species added to a reaction is often not the true catalyst species. In order for catalysis to occur an activation step must instead occur *in situ*. While molecular precatalysts can proceed to a different, discrete homogeneous species, under reducing reaction conditions the formation of the active catalyst in the form of metal nanoclusters is also possible. Indeed the use of nanocatalysts has evolved into an independent field of study owing to their unique ability to fulfil a niche which is unobtainable by traditional homogeneous catalysts;<sup>26</sup> see also Section 1.1. Nanocatalysts do offer advantages and can result in a higher catalytic efficiency. However, sometimes the formation of bulk metal can be deleterious. This comes down to them simply being catalytically inactive or because it results in unwelcome side reactions.<sup>30</sup> In order to optimise catalytic and reaction efficacy, understanding the true nature of the active catalyst is necessary.

A plethora of experiments and tests have been developed by the scientific community to elucidate the phase by which catalysis is occurring. Finke and Widegren<sup>31</sup> and Crabtree<sup>32</sup> have published two key reviews of this area, both reporting the diverse array of tools available to chemists to answer this question; a select few of the most relevant tests are listed herein but for further information and an even wider range of experiments testing for catalyst hetero/homogeneity these two reviews are excellent. Such a wide range of tests have become necessary due to both the requirements of individual reaction conditions and the requirement for multiple pieces of evidence; *i.e.* one experiment which provides a positive outcome for the presence of heterogeneous catalysis, or *vice versa*, is not enough to paint an accurate picture of the active catalyst species.

The most compelling piece of evidence for the proliferation of a heterogeneous catalyst species from a molecular precatalyst is the presence of a significant induction period and therefore a sigmoidal reaction profile upon kinetic analysis. The presence of an induction period must be considered as significant evidence for the “catalyst” added to the reaction mixture must in fact be a precatalyst and catalytically incompetent in its original form. When a reaction is performed under reducing conditions sigmoidal kinetic profiles should provide suspicion of the formation of a heterogeneous catalyst species *in situ*. The formation of metal nanoparticles has been shown to transpire *via* a mechanism comprising of at least two steps: the slow diffusive growth (induction period) and the autocatalytic surface growth (rapidly accelerating, self-proliferative formation of the active catalyst). Work by Finke *et al.* has

resulted in this mechanism being dubbed the ‘Finke-Watzky 2-step mechanism’ (herein called the ‘F-W 2-step mechanism’) Scheme 8.



**Scheme 8** The kinetic analysis of the hydrogenation of cyclohexene by the precatalyst  $[\text{Bu}_4\text{N}]_5\text{Na}_3[(1,5\text{-COD})\text{Ir}\cdot\text{P}_2\text{W}_{15}\text{Nb}_3\text{O}_{62}]$  allowed for the extrapolation of the rate constants  $k_1$ ,  $k_2$  and  $k_3$  from a reporter reaction (4) proceeding *via* a sigmoidal kinetic profile at  $k_{\text{obs}}$ .

Upon hydrogenation of cyclohexene with precatalyst  $[\text{Bu}_4\text{N}]_5\text{Na}_3[(1,5\text{-COD})\text{Ir}\cdot\text{P}_2\text{W}_{15}\text{Nb}_3\text{O}_{62}]$ , Finke and Watzky found the kinetic profile to be of the type shown in Figure 7, and provided an excellent curvefit to the integrated rate equation resultant from Scheme 8, Equation 1.<sup>33</sup>

$$[A]_t = \frac{\frac{k_1}{k_2} + [A]_0}{1 + \frac{k_1}{k_2[A]_0} \times e^{(k_1+k_2[A]_0)t}}$$

**Equation 1.** The integrated rate equation for the 2-step, Finke-Watzky nucleation and autocatalytic growth mechanism.

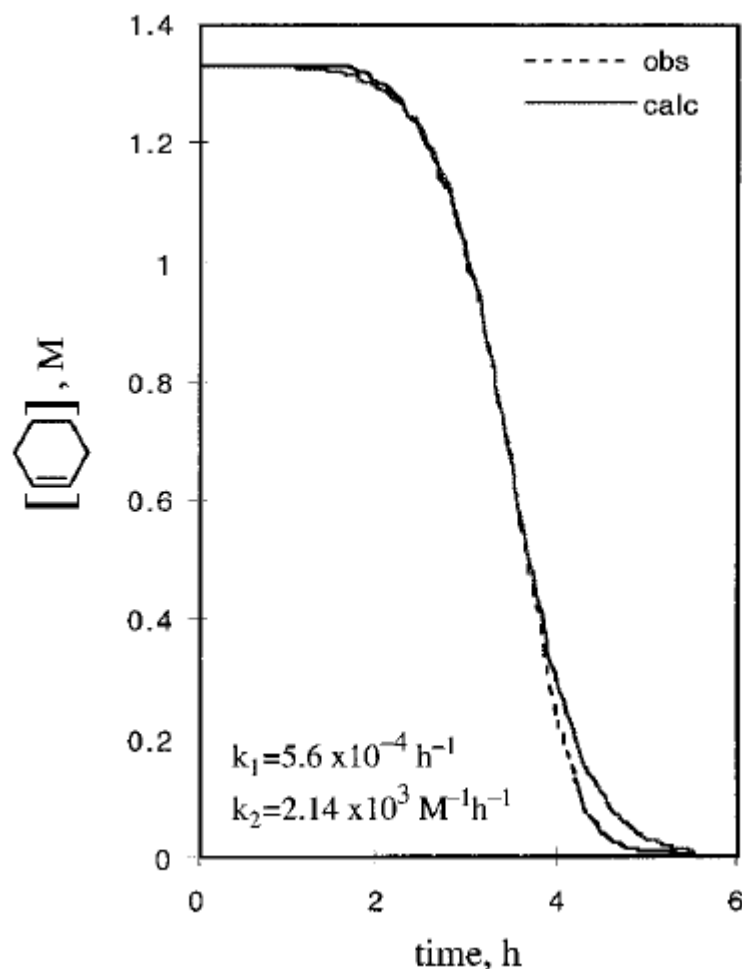


**Figure 7** A typical curvefit for the loss of cyclohexene which provides an excellent curvefit to the F-W 2-step mechanism shown in Scheme 8 and its resultant integrated rate equation, Equation 1. The rate constants  $k_1$  and  $k_2$  can therefore be experimentally defined, where  $k_2$  has to be corrected by a stoichiometry factor of 1400. Reaction conditions: Cyclohexene (4.94 mmol),  $[\text{Bu}_4\text{N}]_5\text{Na}_3[(1,5\text{-COD})\text{Ir}\cdot\text{P}_2\text{W}_{15}\text{Nb}_3\text{O}_{62}]$  (0.07 mol%),  $\text{H}_2$  (40 psig), 22 °C. Reprinted (adapted) with permission from *J. Am. Chem. Soc.* 1997, 119, 10382-10400. Copyright (2016) American Chemical Society.

While the evidence provided by Finke and Watzky has been reported for an Ir catalysed hydrogenation of cyclohexene, such sigmoidal reaction profiles have also been found to be ubiquitous in reactions found to be catalysed by a heterogeneous transition metal species formed *in situ*, including Pd.<sup>34</sup> It is also important to be aware that sigmoidal reaction profiles have been reported for both non-metal catalysed reactions,<sup>35</sup> and reactions which proceed by transition metal catalysis that have been proven to be homogeneous.<sup>36</sup> Indeed factors as simple as product-assisted catalyst solubility can give rise to sigmoidal kinetic traces.<sup>37</sup> Thus the observation of a sigmoidal kinetic curve as shown in Figure 7 is good evidence to start the investigation of heterogeneous catalyst species, but additional evidence for their presence is required.

Further kinetic evidence for the formation of catalytically-competent heterogeneous species from homogeneous precatalysts can be a non-linear relationship between reaction rate and catalyst loading. If the reaction rate does not increase in proportion to the increase in catalyst loading then this may indicate that for every molecule of precatalyst added to the reaction mixture, not every metal atom may be taking part in catalysis. Upon calculation of the order of reaction with respect to catalyst, if a partial order (*i.e.* below 0.5)<sup>38</sup> is obtained then this may be representative of a multinuclear catalyst species, involved in a complex multistep process. Similarly, as described in Section 1.1, upon calculating catalyst turnover frequencies (TOF) if upon decreasing catalyst loading an increased TOF is obtained, this may be representative of heterogeneous catalysis taking place.<sup>7-8, 20-21</sup>

One of the simplest and most common ways of supporting a claim for heterogeneous catalysis is by proving the existence of metal nanoparticles by either dynamic light scattering (DLS)<sup>39</sup> or by transmission electron microscopy (TEM).<sup>20, 40</sup> TEM is a highly sensitive technique, whereby very small metal particles (down to *ca.* 1 nm) can be observed from an aliquot of a reaction mixture. Despite its apparent ease and ubiquitous use in the field, the simple presence of NPs in a transmission electron micrograph is not enough evidence to claim the catalytic competency of said particles. The presence, size and morphology of NPs do not portray their ability to perform catalysis in the absence of kinetic evidence. On the other hand, due to the lower end resolution of TEM being *ca.* 1 nm, the absence of apparent NPs by TEM does not eliminate the possibility that clusters below 1 nm in size exist, and are catalytically active. To corroborate this, the ability for the microscope to detect of nanoparticles of metal with low densities (such as 1<sup>st</sup> row transition elements) at the low end of its resolution is decreased further. Like TEM, DLS allows the detection of high density particulates in the reaction mixture, but allows for the *operando* acquisition of data. This has similar downfalls to TEM imaging along with a lower resolution (limit of detection > 5 nm) but has the added bonus that it can be time resolved, allowing the corroboration of kinetic evidence to coincide induction periods/catalyst decay with the formation of large metal aggregates.

The catalytic role of heterogeneous species in metal-catalysed reactions can be further probed by the use of both molecular and heterogeneous catalyst poisoning experiments by addition of species such as strong ligands CS<sub>2</sub><sup>41</sup> and PPh<sub>3</sub><sup>42</sup> or metallic Hg.<sup>43</sup> Each poisoning experiment should be conducted quantitatively, in the presence of kinetic evidence for the cessation of a catalytic process. The addition of <<1 eq. with respect to catalyst of a strong ligand to a heterogeneous catalytic processes is thought to prevent their continuation by preferentially binding to the catalytically active defect sites of metal nanoparticles. However, if ≥1 eq. of poisoning ligand is required, the reaction is assumed to be homogeneous in nature.

However, such strong ligand experiments are only trustworthy for reactions at  $<50\text{ }^{\circ}\text{C}$ , higher temperature assist the dissociation of such ligands from the catalyst, negating its effect. <Widegren, 2003 #176; Widegren, 2003 #78> In contrast, the addition of metallic mercury is an effective test for the presence of heterogeneous metal catalyst species at high temperatures and has been widely used through the literature.<sup>30, 39a, 43</sup>  $\text{Hg}^0$  is proposed to poison heterogeneous metal catalysts *via* the formation of an amalgam with the metal nanoparticle, or by coating its surface – thus inhibiting further catalysis. However, the Hg drop test must be used in conjunction with other evidence, as false positive results may be encountered – such as the side reaction of Hg with organic starting materials and some single-metal complexes.<sup>44</sup>

## 1.2. Pd catalyst design

Traditionally, the focus when designing a transition metal (pre)catalyst for a process the key parameters to control are the oxidation state of the metal centre along with the electronic and steric effects of the ligands at the metal. Understanding the role of the ligands in enabling catalytic turn-over is key to optimising a reaction.

Tertiary phosphine ligands are ubiquitous ligands in homogeneous catalysis due to the ease with which they can be both sterically and electronically tuned. Tertiary phosphines are capable of donating electron density through a  $\sigma$ -donor interaction and but are also capable of accepting electron density from a metal centre into the P–R  $\sigma^*$  orbital.<sup>45</sup> By carefully changing the substituents on the phosphine R-groups it is possible to tune the electronic properties of the metal centre and the strength of the M–L  $\sigma$ -bonding interaction to assist oxidative and reductive processes at the metal centre, *i.e.* stronger  $\pi$ -accepting ligands facilitate reductive elimination. Likewise, by changing the steric bulk of the phosphine ligand (and therefore its Tolmans cone angle)<sup>46</sup> it is possible to control a metal complex's coordination number. Doing so means that the equilibria defining association/dissociation in catalytic cycles can also be governed *i.e.* more sterically demanding phosphine ligands facilitate oxidative addition to C–X bonds at monodentate  $\text{Pd}^0\text{L}$  species.<sup>46</sup>

The exploitation of such parameters as  $\sigma$ -donation *vs*  $\pi$ -acceptor strength, steric bulk and the bite angles of bidentate ligands<sup>47</sup> is commonplace in the literature. Interestingly, fairly little attention has been given to the redox potentials of Pd precatalysts and their ligands.

### 1.2.1. Tuning $\text{Pd}^0$ precatalysts

One of the most important factors involved in designing an effective Pd precatalyst is the redox potential of the complex. Its redox potential defines a number of key attributes which determine whether a Pd complex is capable of catalysis; such as catalyst activation under reaction conditions, oxidative addition and reductive elimination. An analogous system outside the bracket of catalysis where achieving this is also important has been shown by Keppler *et al.* It was reported that the redox potential of antineoplastic ruthenium<sup>III</sup> prodrugs (the ease with which they are reduced to the active Ru<sup>II</sup> complex) can directly affect their *in vitro* potency.<sup>48</sup> They ran a study on a range of Ru<sup>III</sup> indazole complexes, where a direct correlation between anti-tumour activity and increasing ease of reduction was discovered (Figure 8).

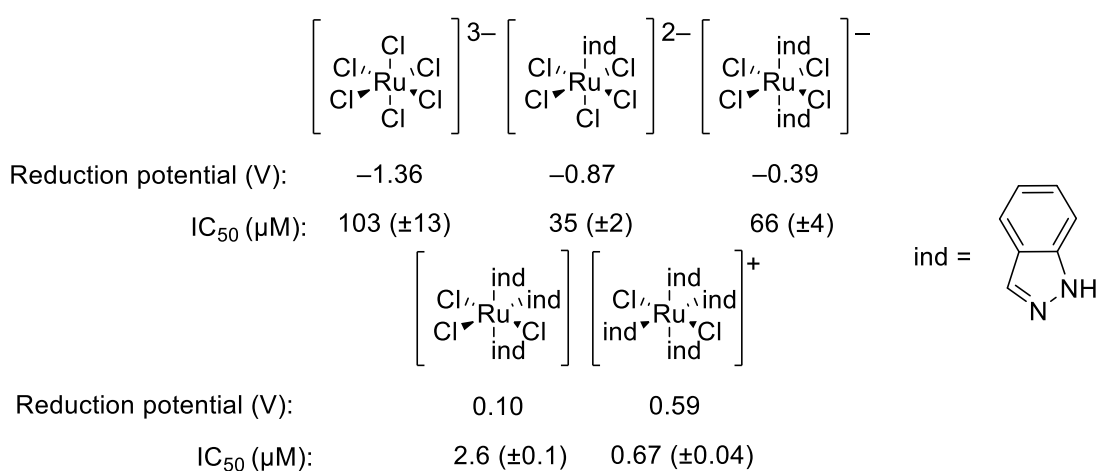


**Figure 8 Structures of Ru compounds tested by Keppler *et al.* Counterions (Hind or Cl<sup>-</sup>) are omitted for clarity. IC<sub>50</sub> values are the inhibitory (50%) concentrations in CH1 cells after exposure for 96 hr in the MTT assay.**

This discovery has allowed a way of purposefully designing Ru complexes so that they are more easily reduced when exposed to the environment around a cancer cell, and although a different area, one may also use the same principle in design for tuning catalysts. Given that Pd catalysis is reliant on the ability of the Pd species to oxidatively add, transmetallate and subsequently reductively eliminate there is a conceivable relationship between Pd complex reduction potentials (which can be measured by cyclic voltammetry) and their ability to perform effective catalysis. Studies on the electrochemistry of Pd complexes and their catalytic efficacies in cross-coupling reactions aids correlation between a complex's reduction potential and its catalytic competency.<sup>49</sup> It is possible to directly control the reduction potential of Pd complexes by simple ligand design. A direct example of this is the effect of different oxidation potentials of the complexes Pd( $\eta^2$ -dba-H)(dppe) and Pd( $\eta^2$ -th<sub>2</sub>-dba)(dppe) on their rates of oxidative addition into iodobenzene (Figure 9). It was found that

the lower the oxidation potentials of each complex, the slower their rate of oxidative addition into the Ar–I bond.<sup>50</sup> Thus providing a potential way of controlling the rate of oxidative addition and therefore the concentration of Pd<sup>II</sup> intermediates and problematic side reactions.

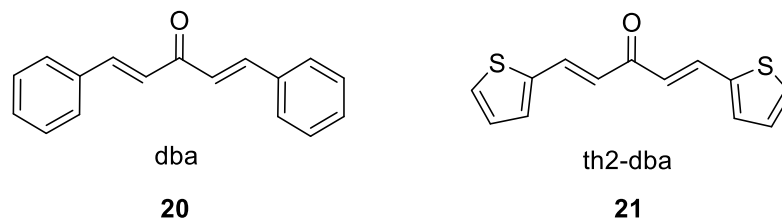
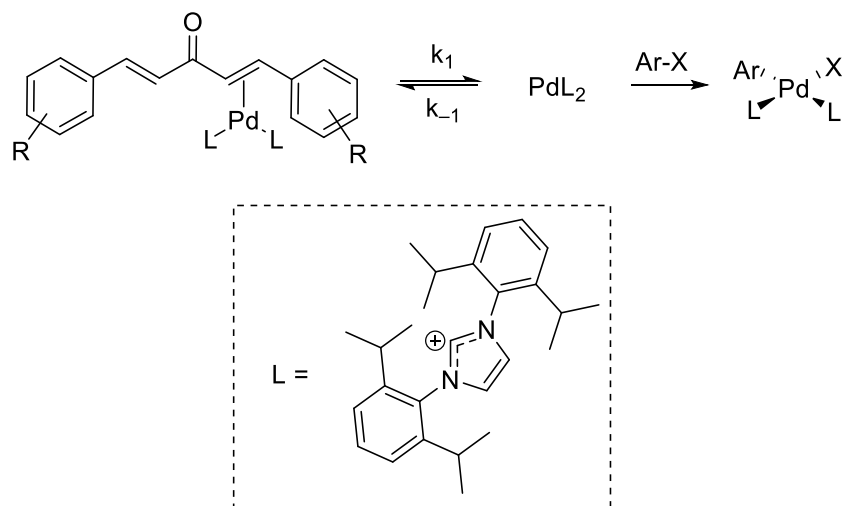


**Figure 9** Two examples of heterocyclic dba derivatives synthesised by Fairlamb and co-workers.

Given the non-innocent nature of dba ligands towards the rate of oxidative addition at Pd<sup>0</sup> to aryl halides,<sup>49</sup> utilising a range of Pd complexes furnished with substituted dba ligands in a Suzuki-Miyaura reaction (in the presence of *N*-heterocyclic carbene ligands) revealed that the reaction rates were considerably affected by the electron density in the coordinative alkene ligand.<sup>51</sup> Increasing electron density at the dba ligand reduces its capability as a  $\pi$ -acceptor at Pd<sup>0</sup>, therefore facilitating ligand dissociation; moreover, electron withdrawing substituents increase the  $\pi$ -acidity of the coordinated alkene, impeding its dissociation. Experimental work revealed that electron rich dba analogues (such as *p*-OMe) increase the rate of reaction, whereas electron withdrawing substituents (such as *m*-NO<sub>2</sub>) slow the rate. Subsequent computational work supported this hypothesis,<sup>52</sup> confirming that the rate determining step under the reaction conditions tested (Suzuki-Miyaura,  $\alpha$ -arylation<sup>53</sup> and Heck arylation<sup>54</sup>) was the rate of dissociation of the dba ligand prior to oxidative addition to the C–X bond ( $k_1$ , Scheme 9).



**Scheme 9** Changing substituent, “R” considerably effects the rate of Pd-catalysed cross-coupling reactions.

Thus, simple ligand tuning in precatalyst design can have a marked effect on the efficacy of catalysis and taking steps to understand the mechanisms by which these differences occur can facilitate the development of cheaper, more efficient catalytic processes.

### 1.2.2. The importance of catalyst design for efficient Pd<sup>II</sup> precatalyst activation.

Buchwald and co-workers have exemplified how an understanding of precatalyst activation mechanisms and structure-activity relationships (SARs) can result in the development of several generations of precatalyst and phosphine ligand design. Similar progressions have also been made through the literature regarding the SARs of NHC containing PEPPSI (Pyridine, Enhanced, Precatalyst, Preparation, Stabilisation and Initiation) Pd<sup>II</sup> precatalysts.<sup>55</sup> Initial investigations by Buchwald *et al.* into the use of bulky, bidentate phosphines such as **22** began by using the readily available Pd precatalyst Pd(OAc)<sub>2</sub>.<sup>56</sup> Despite this system allowing for user friendly access to aryl chloride activation in Suzuki-Miyaura couplings there was still a possibility for multiple reaction pathways with Pd(OAc)<sub>2</sub>. These included the incomplete reduction of all Pd<sup>II</sup> to Pd<sup>0</sup> or lack of total complexation of Pd to the activating ligand and were considered significant, but surmountable, drawbacks. Subsequently, this system was markedly improved by its replacement with the air and moisture stable palladacyclic complex, **23**. The phosphine ligand is interchangeable and the amine bound NH group could be easily deprotonated *in situ* by a base, facilitating reductive elimination of the desired catalyst (L)Pd<sup>0</sup> and indoline.<sup>57</sup> Unfortunately, due to the low acidity of the NH proton catalyst activation was only possible at elevated temperature in the presence of a weak base, limiting the scope of the precatalyst. Following the work carried out by Albert *et al.* on 2-

aminobiphenyl palladacycles,<sup>58</sup> and investigations into the synthesis of carbazoles through intramolecular Buchwald-Hartwig aminations<sup>59</sup> this scaffold was then used to make a range of precatalysts of structure type **24**.<sup>60</sup> Owing to the increased acidity of the anilinyll NH, deprotonation could occur in the presence of phosphate or carbonate bases at room temperature, resulting in the subsequent reductive elimination of (L)Pd<sup>0</sup> and the formation of a discrete, innocent side product (carbazole). Unfortunately, due to the steric implications of an incorporated chloride, more bulky, bidentate phosphine ligands (such as **22**) could not be used. In order to circumvent this a further adaptation to the precatalyst structure was employed to allow the utilisation of ligands such as **22**. Instead of chloride, the less coordinative mesylate counterion was introduced, allowing for the synthesis of the state-of-the-art Generation 3 Buchwald precatalysts (**25**).<sup>61</sup>

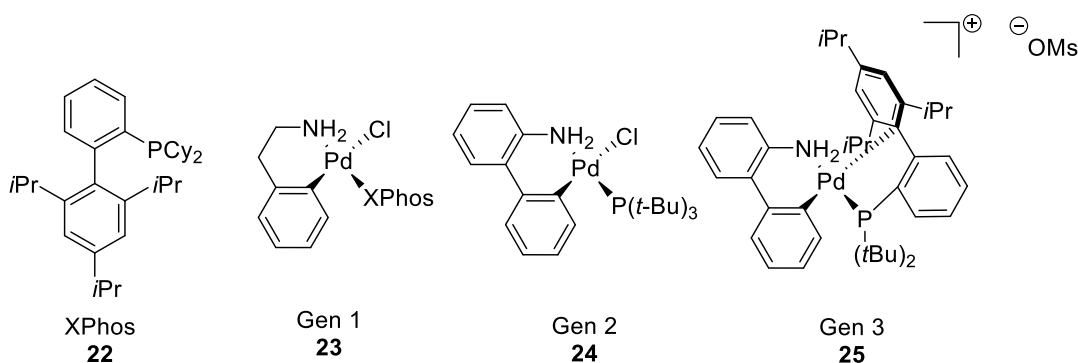


**Figure 10** The three generations of palladacyclic Buchwald precatalysts.

It is commonplace in Pd-catalysed cross-coupling reactions for Pd<sup>II</sup> precatalysts to be used in place of Pd<sup>0</sup> precatalysts. This is partly due to the availability and price of Pd<sup>II</sup> salts (such as PdCl<sub>2</sub> and Pd(OAc)<sub>2</sub>), and thanks to their ease of handling. However, one of the drawbacks of using a Pd<sup>II</sup> precatalyst can be the requirement for catalyst activation (*i.e.* reduction from Pd<sup>II</sup> to Pd<sup>0</sup>) prior to catalyst turnover.<sup>62</sup> Perhaps the most commonly utilised Pd precatalyst is Pd(OAc)<sub>2</sub>; throughout the literature it is referred to as “Pd(OAc)<sub>2</sub>”, despite the fact that polymeric variants can be common contaminants and that in its ultrapure form it actually resides as a trimer of the type displayed in Figure 11.<sup>63</sup> In 2012 upon discovery of a NO<sub>2</sub><sup>-</sup> contaminated batch, work within the Fairlamb research group highlighted the importance of determining Pd<sub>3</sub>(OAc)<sub>6</sub> purity prior to use.<sup>64</sup> Although little distinction was found between the low purity material and ultrapure Pd<sub>3</sub>(OAc)<sub>6</sub> in the catalytic processes tested (C–H functionalisations), the nitrite anion did interfere with the stoichiometric synthesis of a range of Pd<sup>II</sup> precatalysts. However, given the prevalence of redox active NO<sub>x</sub> species in Pd catalysed processes<sup>65</sup> it is not difficult to conceive how a low purity catalyst batch containing

these ligands may impede reaction efficiency. Indeed it has been reported that recrystallisation of  $\text{Pd}_3(\text{OAc})_6$  from benzene improved reaction efficiency.<sup>66</sup>

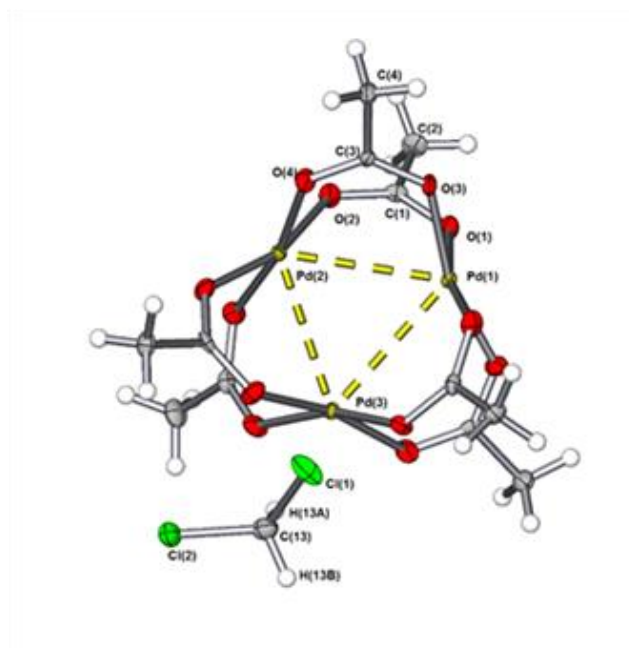
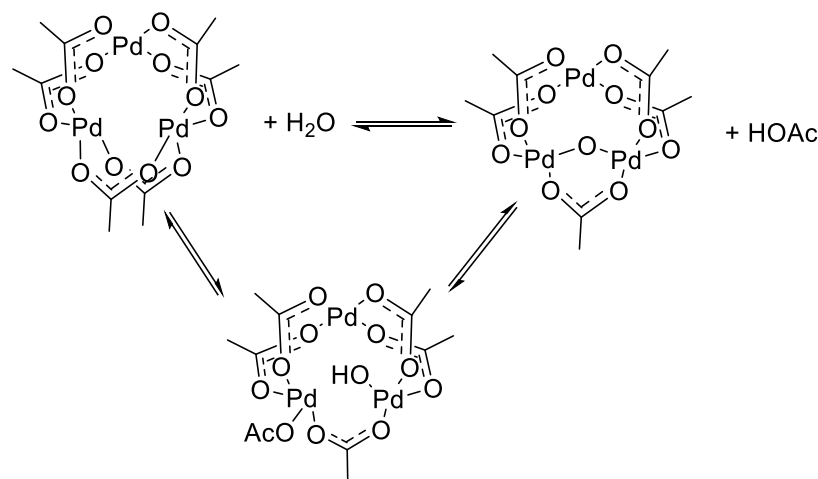


**Figure 11** The single crystal X-Ray diffraction structure of  $\text{Pd}_3(\text{OAc})_6$  with  $D_{3h}$  symmetry.

Further to these findings, Colacot *et al.* have also reported the presence and deleterious effect of the polymeric contaminant  $[\text{Pd}(\text{OAc})_2]_n$ .<sup>63, 67</sup> Despite there being only a small effect in high temperature Buchwald-Hartwig aminations, increased reaction times were required to achieve comparable yields in model  $\alpha$ -carbonyl arylation and Mizoroki-Heck reactions. It was also reported that when the synthesis of palladacycle (**25**) was attempted from  $[\text{Pd}(\text{OAc})_2]_n$ , no conversion of starting material was observed; when this was repeated using  $\text{Pd}_3(\text{OAc})_6$ , 98% yield was achieved.

Further to this work on the potentially detrimental contamination of  $\text{Pd}_3(\text{OAc})_6$ , a recent publication by Bedford *et al.* has successfully characterised the hydrolysis and alcoholysis products of the  $\text{Pd}_3(\text{OAc})_6$  trimer under aqueous and alcoholic conditions (Scheme 10).<sup>68</sup> Given that alcohols<sup>69</sup> and water<sup>60, 70</sup> are common solvents (and even co-solvents in Suzuki-Miyaura cross-coupling processes)<sup>71</sup> the importance of understanding the mechanisms of the speciation processes of  $\text{Pd}_3(\text{OAc})_6$  is paramount for optimising catalytic efficiencies.

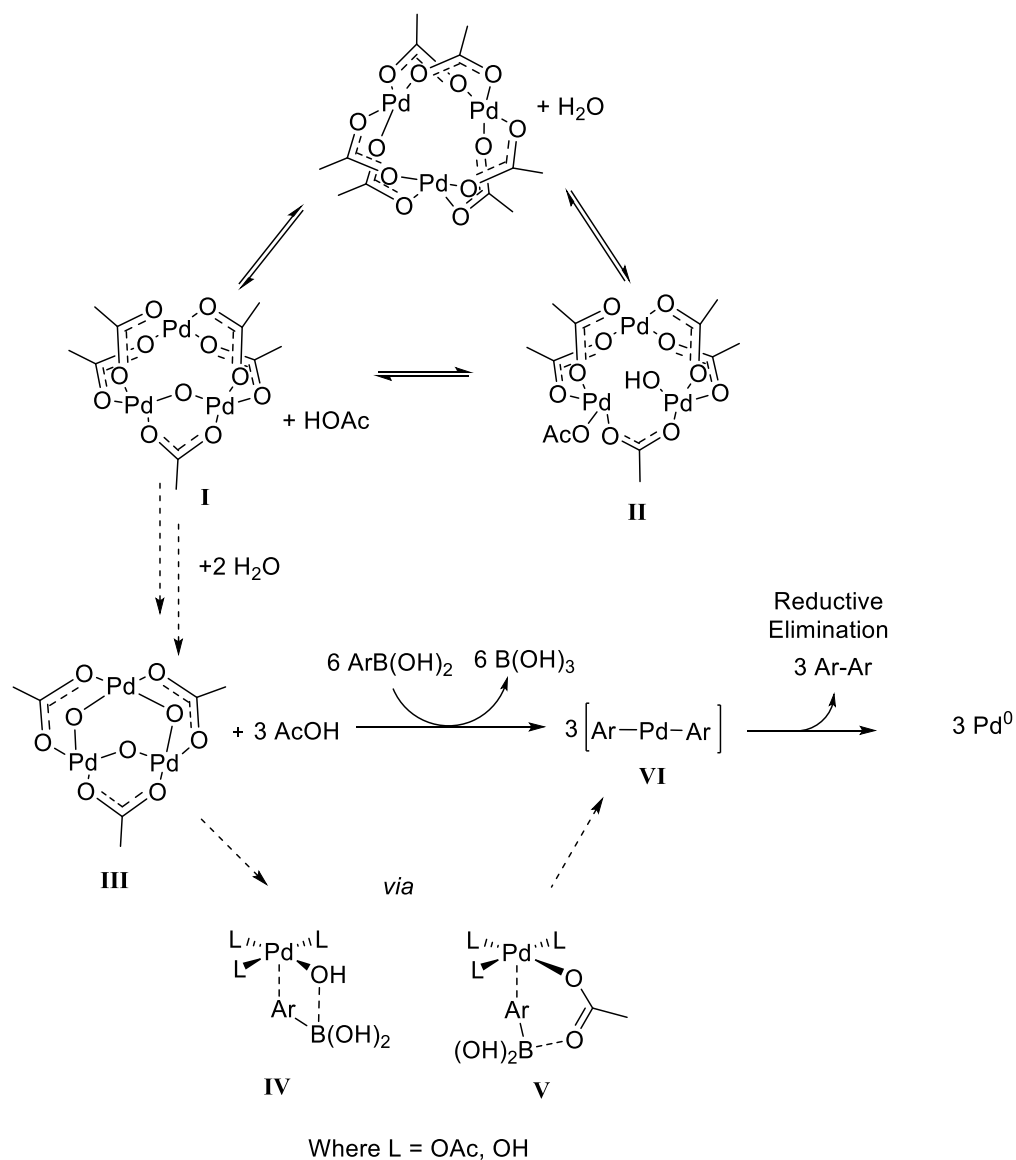


**Scheme 10 Fundamental work by Bedford *et al.* has changed the way  $\text{Pd}_3(\text{OAc})_6$  speciation should be perceived under working reaction conditions.<sup>68</sup>**

It could be argued that if under the reaction conditions the catalyst used responds in the desired manner, these speciation events are not of huge importance; however, upon application of a chemist's catalytic methodology to a large scale process the lack of understanding about any reaction by which catalytic efficiency could be impeded (such as the formation of off cycle " $\text{L}_n\text{Pd-ZnBu}$ " species detected by ESI mass spectrometry in Pd-catalysed Negishi reactions)<sup>72</sup> may result in an entire process failing to be economically viable.<sup>73</sup>

Previous work published by Hii *et al.* on the speciation of  $\text{Pd}_3(\text{OAc})_6$  revealed that in the presence of water and aryl boronic acids,  $\text{Pd}(\text{OAc})_2$  was rapidly reduced to  $\text{Pd}^0$  and facilitated the formation of catalytically competent nanoparticles under Suzuki-Miyaura reaction conditions. Fairlamb *et al.* also reported the formation of mixed bridging oxo-acetate Pd dimer species upon transmetallation with boronic acids.<sup>74</sup> A similar mixed oxo-acetate dimer species was also reported by Wie *et al.* upon reaction of  $\text{Pd}(\text{OAc})_2(\text{PCy}_3)_2$  with stoichiometric water in the presence of excess  $\text{NaOAc}$ .<sup>75</sup> Hii *et al.* reported that oxygen was found to impede catalyst activation, but also prevented the formation of large aggregates of  $\text{Pd}^0$ , presumably due to the formation of  $\text{PdO}$  species *in situ*. A unifying mechanism for the activation of  $\text{Pd}_3(\text{OAc})_6$  in Suzuki-Miyaura reactions based upon the evidence given by Fairlamb, Bedford and Hii is given in Scheme 11. The step wise hydrolysis of  $\text{Pd}_3(\text{OAc})_6$  proceeds *via* the formation of acetic acid and **I**. Continued addition of water would result in the formation of the oxo-acetate bridged trimer **III** and rapid transmetallation with  $\text{ArB}(\text{OH})_2$  *via* species **IV** or **V**. Although transmetallation may occur at a trimeric cluster such as **III**, dimeric and monomeric species are both thermodynamically accessible and feasible intermediates under reaction conditions.<sup>76</sup> A short lived species of type **VI** was postulated by Hii *et al.* to then

undergo reductive elimination to form  $\text{Pd}^0$  and a biphenyl organic product. The  $\text{Pd}^0$  then proceeds to aggregate and form catalytically active Pd clusters (as shown in Scheme 11). At dilute Pd concentrations (*i.e.* low catalyst loadings) the formation of these PdNPs is likely to proceed by slow nucleation, autocatalytic surface growth, this is characterised by a sigmoidal reaction profile.<sup>34a, 77</sup> Hii *et al.* also postulated that water played a role in the leaching of small clusters/mononuclear Pd from nanoparticulate surfaces.<sup>70a</sup>



**Scheme 11** Unified mechanism for the speciation and activation of  $\text{Pd}_3(\text{OAc})_6$  in Suzuki-Miyaura reactions when in the presence of water. Inset: TEM image adapted with permission from *Catalysis Science & Technology* 2012, 2, 316-323. Copyright of the Royal Society of Chemistry.

The hypothesis that water also played a crucial role in the leaching of highly active Pd species from the surfaces has been further supported by insightful work performed by Jutand *et al.*<sup>40</sup> Water,  $\text{K}_2\text{CO}_3$  and phenyl boronic acid were all shown to individually assist the leaching of

either monoatomic or small clusters of Pd from Au-Pd core-shell nanoparticles in Suzuki-Miyaura reactions. Not only was this leaching necessary for catalytic activity, it is also of note that the leached species were *remarkably* efficient at performing catalysis. Given the low concentrations of Pd detected in solution after leaching (sub 1 ppm Pd) 95% yields were achieved after only 4 hours at room temperature. Indeed, synthesising Au-Pd core-shell nanoparticles with different surface morphologies (and therefore different defect site: size ratios, at differing surface energies) had significant effect upon their catalytic efficiencies in Suzuki-Miyaura reactions, suggesting (coupled with the evidence provided by Jutand *et al.*) that leaching of catalytically competent Pd species is more facile at higher energy defect sites.<sup>78</sup>

It is therefore critical to consider: i) the role of efficient catalyst activation; ii) the competency of discretely synthesised nanoparticulate Pd catalysts in both surface catalysis and processes progressing *via* leached Pd species; iii) the effect of key additives (such as water) as these all have significant effects upon catalyst efficiencies in cross-coupling processes. The design and synthesis of a range of precatalysts capable of activating to form small, highly catalytically active Pd nanocatalysts is highly desirable. A Pd nanoparticle precursor complex is designed to be such a thing; they are specifically designed in order to undergo controlled degradation to form catalytically active Pd nanoparticles. When designing PdNP precursor complexes a difficult balance of catalyst stability must be struck. If the complex is too stable then no degradation will occur and no nanoparticles will form, and if the complex is too unstable then degradation will occur too fast and form large, unreactive Pd aggregates (Pd black).

Frech *et al.* reported the synthesis of a series of dichloro-bis(aminophosphine) complexes which showed a range of catalytic activities in Suzuki-Miyaura cross-couplings (Figure 12).<sup>79</sup>

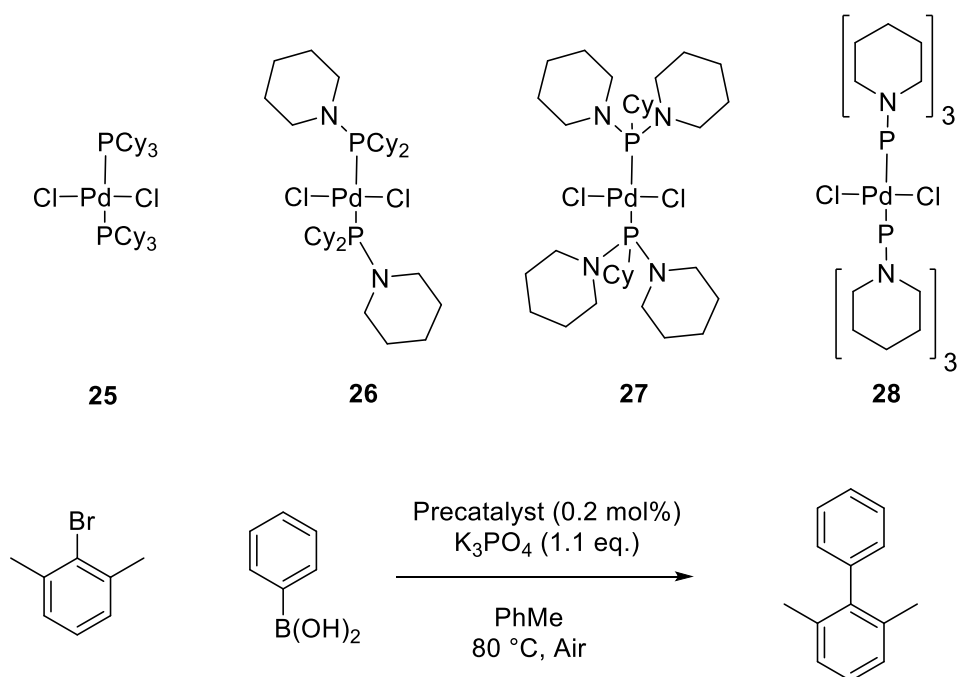


**Figure 12 Aminophosphine NP precursor complexes synthesised by Frech *et al.***

All aminophosphine Pd complexes displayed high activity in Suzuki-Miyaura cross-coupling reactions and displayed sigmoidal reaction profiles (Figure 13). Sigmoidal kinetic traces are representative of the need for pre-catalyst activation and often in metal catalysed reactions they signify the role of surface catalysis at NPs.<sup>31, 33, 77, 80</sup> Precatalysts **26** and **27** were comparable in rate and efficacy. However, when the most stable aminophosphine complex, **26**, was used the reaction reached completion after 10 minutes, whereas **27** only achieved *ca.* 90%. **28** still proved to be more efficient than **25**, despite its inferior activity with respect to **26** and **27**.

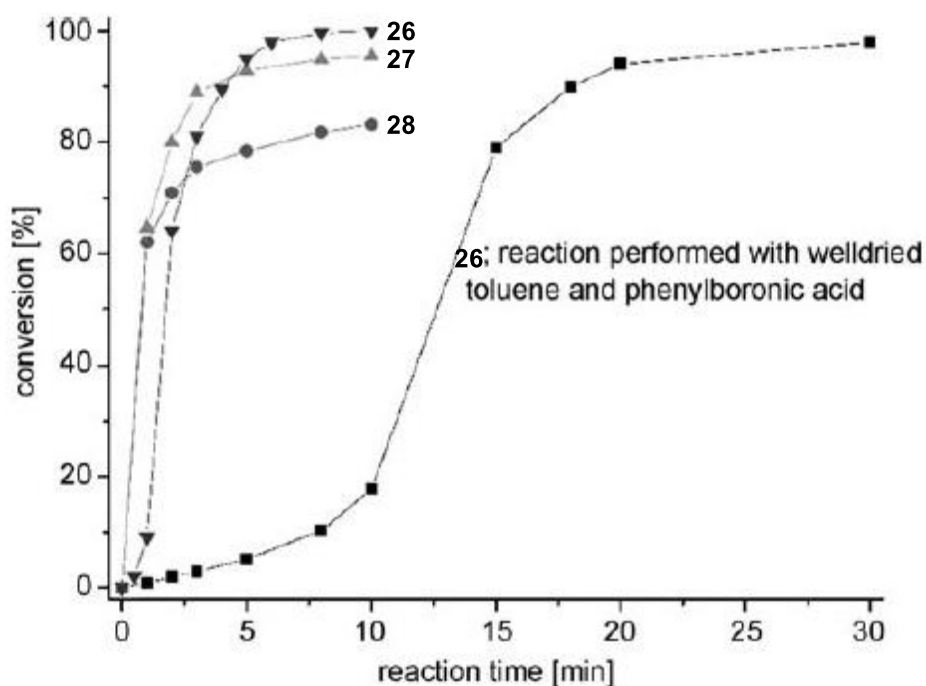
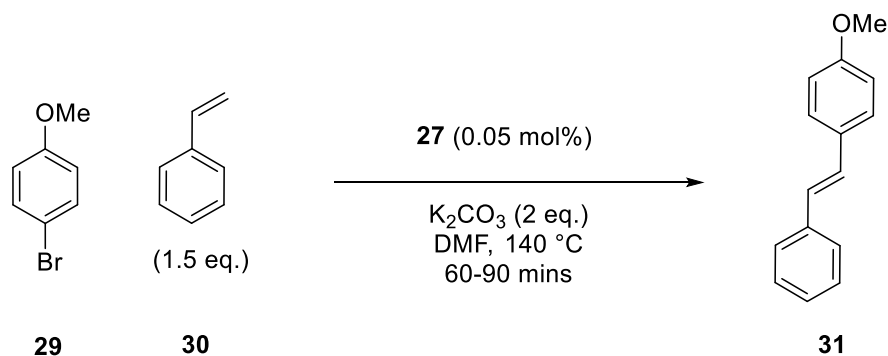


**Figure 13.** Frech's aminophosphine precatalysts show sigmoidal kinetic traces, which are characteristic of PdNP catalysis. Adapted with permission from *Chem. Eur. J.* 2010, 16, 4075-4081. Copyright of Wiley.

Repeating the reaction with **26** as a precatalyst in rigorously dried toluene resulted in a much longer induction period (*ca.* 10 minutes). Addition of regulated amounts of water to dry solvent resulted in a significantly reduced induction period, indicating that water plays a key role in the decomposition and activation mechanism of these catalysts. Direct addition of water to the aminophosphine complexes in THF followed by heating resulted in their direct decomposition and formation of dicyclopophosphate, cyclohexylphosphonate and phosphate. They observed that the more P–N bonds present in the complexes, the faster this decomposition occurred and when compared with their catalytic activity, the rate of this activation step appears to be crucial: either too stable (**25**) or fragile (**28**) resulted in poor catalyst activity.

In a later study, Frech *et al.* characterised a binuclear Pd species  $[L_2Pd^{II}_2X]^+$  which appeared not only to be catalytically active in Suzuki cross-coupling reactions but to be stable in solution ( $L = (C_5H_{10}N)_2(C_6H_{12})P$ , as in complex **26**).<sup>81</sup> This species formed throughout the reaction and was characterised after completion by ESI mass spectrometry in positive ion mode. In addition, when the reaction mixture was dosed with further starting material the reaction reinitiated and the only Pd species visible by ESI mass spectrometry was  $[L_2Pd^{II}_2X]^+$ .

Importantly, Frech *et al.* have also demonstrated that these aminophosphine Pd complexes exhibit high catalytic activity in a range of cross-coupling reactions including Negishi, Heck, and cyanations.<sup>43, 82</sup> The diversity of the precatalysts appears to be based on their ability to perform as effective catalyst *via* both the molecular and nanoparticulate catalytic phases, and the tuning of catalytic activity by controlled addition of water.



**Scheme 12** Frech *et al.* performed kinetic experiments on this benchmark Heck-reaction, including water dosing experiments and  $Hg^0$  drop tests.

When complex **27** was used in the Mizoroki-Heck reaction, catalyst loadings as low as 0.0001 mol% could be used on a 0.5 mol scale in the coupling of bromobenzene with styrene. However it was found that for more sterically demanding substrates a catalyst loading between 0.01-0.05 mol% was required. When the reaction between **29** and **30** (Scheme 12) was deliberately dosed with water (15  $\mu$ l) the induction period was found to significantly reduce from 20 to 5 minutes, but caused the overall conversion to drop to 90%. When 30  $\mu$ l of water was added, the induction period was again reduced to only 2.5 minutes, but the rate of reaction and overall conversion to drop dramatically to *ca.* 63% after 90 minutes. For comparison, the reference reaction (2.5  $\mu$ l of water added) proceeded to complete conversion within 60 minutes, with an induction period of 20 minutes. Frech *et al.* stated that as with the Suzuki reaction, controlling these induction periods is therefore crucial to the catalytic activity of PdNP precursor catalysts. However, as discussed in Section 1.1 their explanation that activity is dictated simply by size may not be entirely justified.

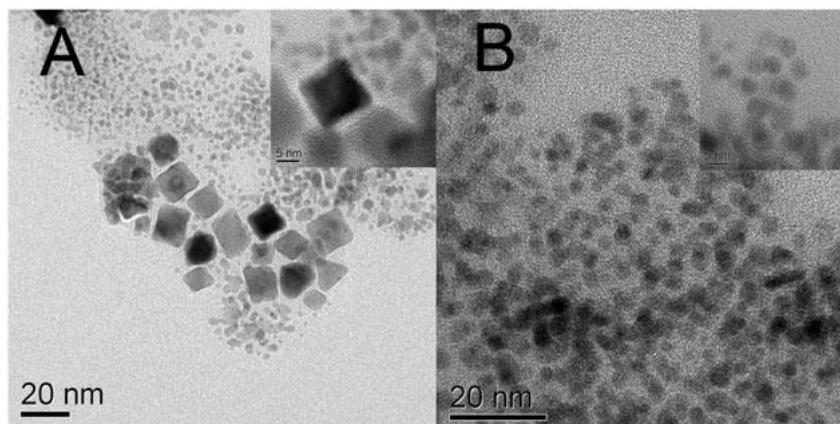


**Figure 14.** A TEM of highly structured PdNPs stabilised by cucurbit[6]uril. Adapted with permission from *Chem. Commun.* 2010, 46, 5088. Copyright of the Royal Society of Chemistry.

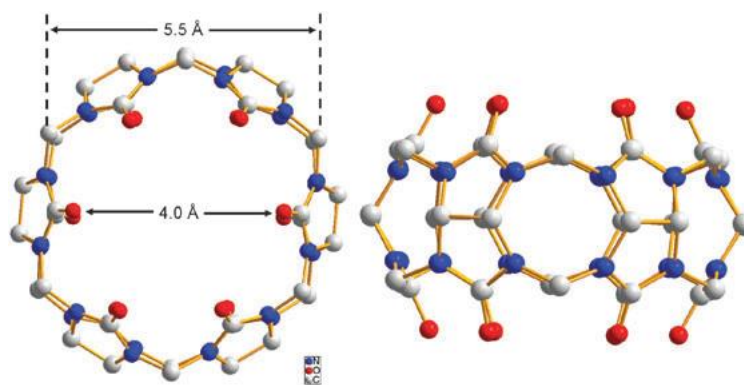
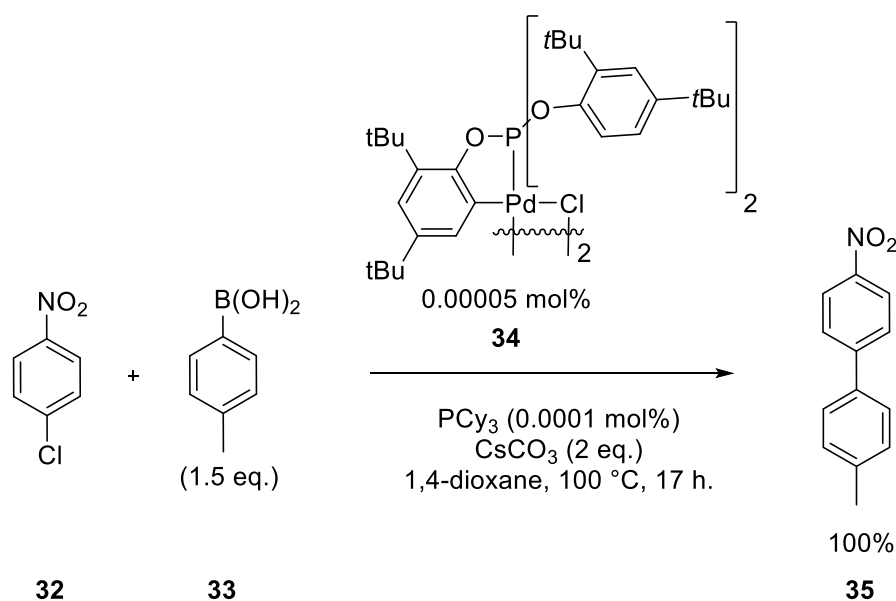


**Figure 15.** A wire frame model of cucurbit[6]uril. Adapted with permission from *Chem. Commun.* 2010, 46, 5088. Copyright of the Royal Society of Chemistry.

Cao *et al.* reported the synthesis of highly structured PdNPs stabilised by cucurbit[6]uril (Figure 14, Figure 15).<sup>83</sup> Studies by FT-IR were conducted to further characterise the PdNPs. These confirmed that there was no change in the IR spectrum of the cucurbit upon stabilisation of the PdNPs, indicating that no covalent interactions between the stabilising cucurbit and the PdNPs were present. Although these PdNPs were not shown to be able to operate on a very low catalyst loading in Suzuki-Miyaura couplings (only reported as 0.5 mol%) they demonstrate exceptional activity towards aryl chlorides, a feat not accomplished by many PdNP catalysts. This performance has been attributed to the uniform size and shape of the NPs, along with the capability of the cucurbit ligands to encapsulate aromatic molecules in their cavity, increasing the chance of contact between the substrates and the Pd catalyst. They also reported that the catalyst retained high activity in both the Heck and Suzuki reactions, even after the fifth recycle.<sup>84</sup>

Many solid-supported PdNP catalyst systems have been developed. The most common supports are polymers, silica and different allotropes of carbon.<sup>85</sup> Certain specialist supported

PdNP catalysts can provide high catalytic activity, such as by Siamaki *et al.* with Pd on graphene. This catalyst permits Suzuki-Miyaura cross-coupling on simple bromoarenes with a catalyst loadings as low as 0.007 mol%, and proceeded to completion after only 5 minutes in a microwave at 80 °C.<sup>85d</sup> Despite the odd exceptional example, many supported PdNPs provide only adequate catalytic activity in cross-coupling reactions. On the whole they have so far struggled to reach the outstanding TONs of one million achieved in Suzuki-Miyaura reactions on activated aryl chlorides by single ligand, molecular catalyst systems such as that published by Bedford and co-workers (Scheme 13).<sup>6</sup>



**Scheme 13 Bedford *et al.* report exceptional catalyst TON's across a range of simple substrates and electron deficient aryl chlorides in Suzuki reactions.**

A more likely route towards highly active PdNPs is their stabilisation by more labile surfactants, such as loosely coordinating solvents. Obora *et al.* provide an excellent example of this in their preparation of DMF stabilised Pd nanoclusters.<sup>19a</sup> These pre-synthesised NPs display exceptional catalytic activity in Suzuki reactions with TONs comparable with those achieved by **34**, as well as biaryl Stille couplings using catalyst loadings as low as  $10^{-4}$  mol%.<sup>19b</sup> Given this, the use of precatalysts in coordinative solvents (such as DMF, NMP and DMAc) as precursors to PdNPs may provide access to similar activities.

### 1.3. Pd-catalysed cyanation

Since its discovery in 1973 and its substantial optimisation thereafter, Pd-catalysed cyanation of aryl halides has become one of the most common routes to benzonitriles. Although benzonitriles can be made in many different ways, the most popular routes towards them have previously been the Rosenmund-von Braun and the Sandmeyer reaction.<sup>86</sup> However, each have significant drawbacks including very high temperatures (up to 250 °C) along with the use of stoichiometric toxic copper reagents (CuCN) and therefore equivalent heavy metal waste. While being present as a substructure in many biologically-active compounds, *i.e.* agrochemicals, pharmaceuticals (Figure 16) and natural products, it also plays a key role for the introduction of further important functional groups such as amides, triazoles,<sup>87</sup> tetrazoles and primary amines.<sup>88</sup>

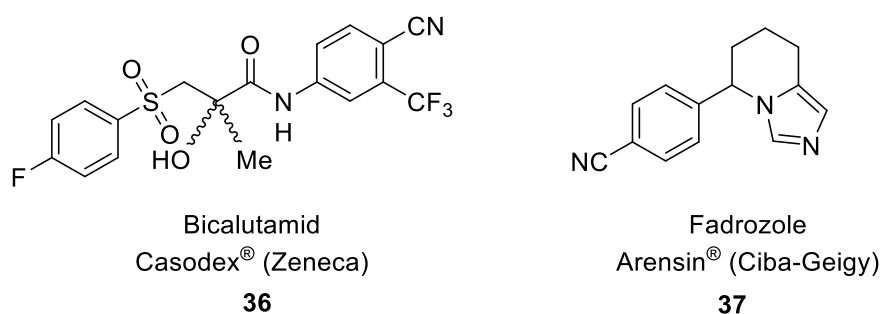
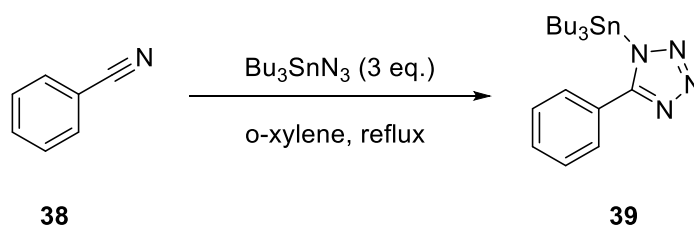


**Figure 16. Two pharmaceutically-active compounds containing the benzonitrile motif.**

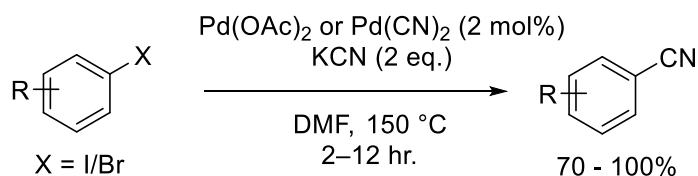
Not only is the tetrazole moiety commonplace in pharmaceuticals (it is often used as a replacement for carboxylic acid groups),<sup>89</sup> their formation can allow the synthesis of interesting structural motifs and synthetic handles. A good example of this is the formation of the *N*-tributylstannyltetrazole, **39**, from cyanobenzene and Bu<sub>3</sub>SnN<sub>3</sub> (made *in situ* from Bu<sub>3</sub>SnCl and NaN<sub>3</sub>) reported by Semenov and Smushkevich (Scheme 14).<sup>90</sup>



**Scheme 14 Semenov and Smushkevich's synthesis of 5-phenyl-1-(tributylstannyl)tetrazole.**

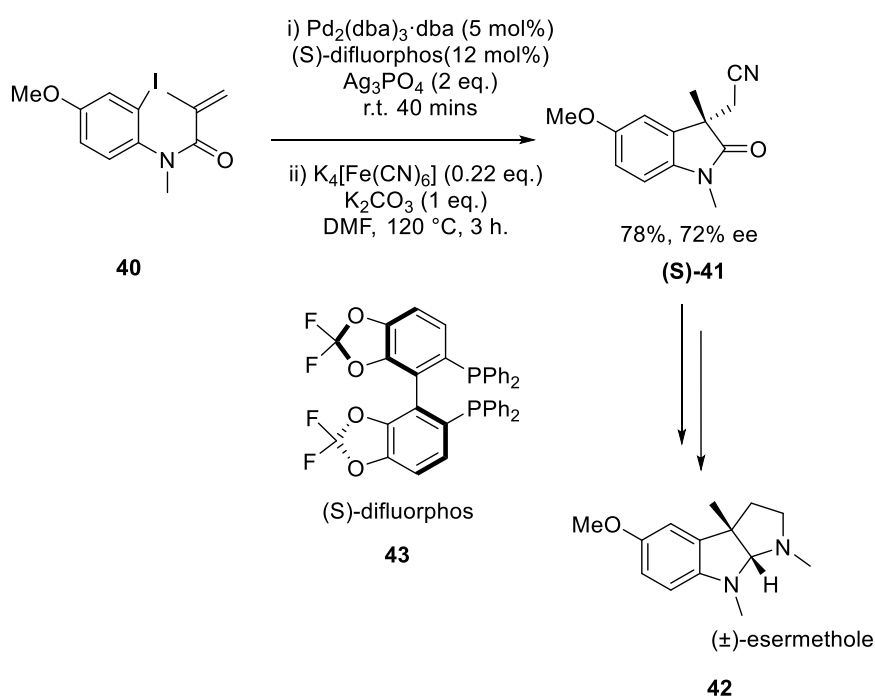
Despite the obvious importance of developing and optimising routes to emplace a cyano group, little optimisation of the Pd-catalysed cyanation reaction occurred until within the past

couple of decades. A key progression over the years has been the gradual move towards less toxic sources of cyanide, which have subsequently allowed for lower Pd catalyst loadings and less need for additives. Initially, Sakakibara *et al.* reported the reaction to proceed using a Pd<sup>II</sup> salt such as Pd(CN)<sub>2</sub> or Pd(OAc)<sub>2</sub> and the highly toxic cyanide salt, KCN, in DMF (Scheme 15).<sup>91</sup>



**Scheme 15 Sakakibara's initial conditions for the cyanation of aryl halides.**

Not only can Pd-catalysed cyanation be used for the introduction of a simple functional group, but in a few instances it has been used to enantioselectively create a new stereocentre. A domino intramolecular Heck-cyanation by Zhu *et al.* allowed the total synthesis of (±)-esermethole (79% ee) (**42**, Scheme 16). This methodology has also been applied to the total synthesis of (±)-physostigmine and horsfiline (racemic).<sup>92</sup>

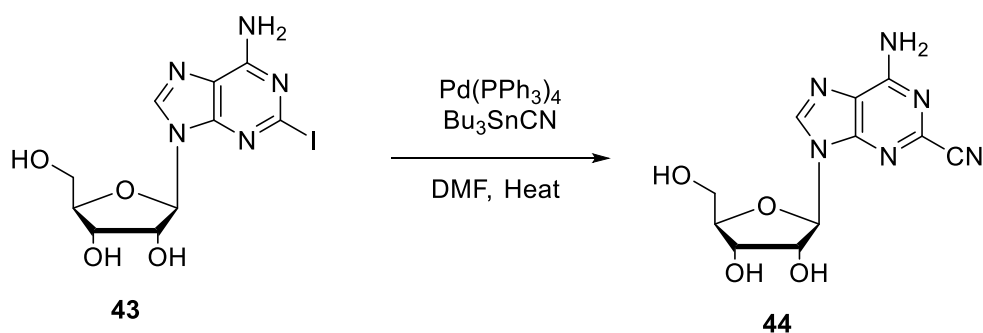


**Scheme 16 The domino Heck-cyanation step towards the total synthesis of (S)-enantioenriched esermethole, 42.**



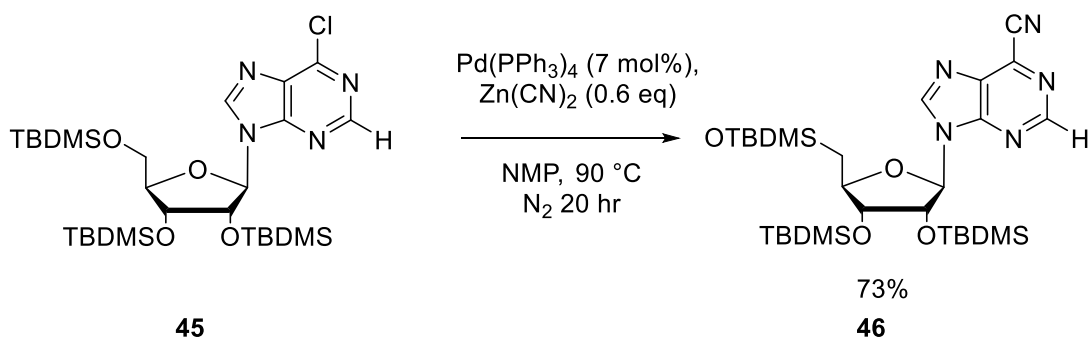
It was also found that the rate of reductive elimination to form Ar–CN competes directly with  $\text{PR}_3/\text{CN}$  ligand exchange if the cyanide ion concentration is too high. This causes the formation of a catalytic graveyard of completely inactive  $[\text{Pd}(\text{CN})_4]^{2-}$  species, reducing the catalytic efficiency. Feasibly, reductive elimination of Ar–CN can occur (and has been observed) from the tricoordinate complex  $[\text{Pd}(\text{CN})_2\text{Ar}]^{2-}$ , however with excess  $\text{CN}^-$  present in solution the formation of this complex by the dissociation of  $\text{CN}^-$  from  $[\text{Pd}(\text{CN})_3\text{Ar}]^{2-}$  is unlikely.<sup>93</sup> This catalyst poisoning problem is most prevalent for more labile  $\text{CN}^-$  sources, *e.g.* KCN, NaCN and  $\text{ZnCN}_2$ , and has been broadly combatted in the literature by addition of reducing agents, the most common of which being catalytic Zn metal and stoichiometric  $\text{Zn}^{\text{II}}$  salts.<sup>95</sup> It has also been found that the addition of diamine co-catalysts such as tetramethylethylenediamine (TMEDA) or 2,2'-bipyridine are able to prevent the deactivation of catalysts such as  $\text{Pd}(\text{PPh}_3)_4$  while enabling the cyanation of aryl chlorides.<sup>96</sup> Williams and Yang reported that catalytic  $\text{Bu}_3\text{SnCl}$  can act as an effective co-catalyst as a phase transfer agent. It was capable of shuttling  $\text{CN}^-$  into solution in the form of  $\text{Bu}_3\text{SnCN}$ , thus increasing the rate of transmetalation while keeping the concentration of free  $\text{CN}^-$  in solution low. Inevitably this allowed for a reduced catalyst loading of 0.5 mol%  $\text{Pd}_2(\text{dba})_3 \cdot \text{CHCl}_3$ , while still maintaining good yields in the cyanation of simple aryl halides.<sup>97</sup>

Tributyltin cyanide has also been used as a cyanide source in the cyanation of the much more complicated and sensitive 2-iodoadenosine, **43**. Unfortunately, no reagent equivalence, temperature, time or characterisation are given (Scheme 17).<sup>98</sup>



**Scheme 17** Sells' synthesis of 2-cyanoadenosine (no equivalences given).

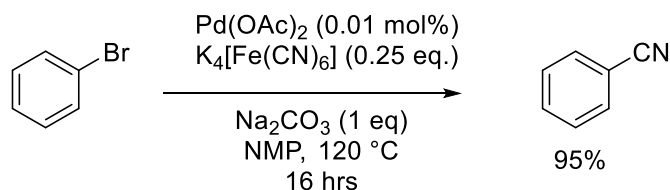
The more covalent nature of the zinc cyanide bond in  $\text{Zn}(\text{CN})_2$ , and its reasonably low solubility in organic solvents has allowed for cyanations to be carried out on difficult (including protic) substrates. Of note are the syntheses of purine carbonitriles by Gunderson, one key example is shown below (Scheme 18).<sup>99</sup>



**Scheme 18 Gundersen's cyanation of protected 4-chloroadenosine.**

The reduced solubility of  $\text{Zn(CN)}_2$  coupled with the addition of both catalytic Zn dust and  $\text{Zn(OAc)}_2$  allowed Chidambaram *et al.* to report a decreased catalyst loading (0.1 mol%  $\text{Pd}_2(\text{dba})_3/0.25$  mol% DPPF).<sup>100</sup> Unfortunately this was only tested on a series of simple aryl bromides. However, further progress on the cyanation against a range of substituted aryl and allyl chlorides was made by the addition of a bulky phosphine (**22**), catalytic Zn dust and sulphuric acid, while using  $\text{Pd(OAc)}_2$  as a catalyst.<sup>101</sup>

Arguably, the biggest advancement in the past decade in the field of Pd-catalysed cyanation reactions was the discovery of  $\text{K}_4[\text{Fe(CN)}_6]$  and its trihydrate,  $\text{K}_4[\text{Fe(CN)}_6]\cdot\text{H}_2\text{O}$  as a mild, non-toxic and highly covalent cyanide source made by Beller *et al.* and Weissman and co-workers respectively (Scheme 19).<sup>102</sup> Importantly, the more covalent nature of potassium hexacyanoferrate not only renders it completely non-toxic but also allows for the concentration of  $\text{CN}^-$  in solution to remain very low at high reaction temperatures without the need for expensive additives. Implicitly this means that the formation of catalytically inactive  $[\text{Pd(CN)}_3\text{R}]^{2-}$  complexes are significantly reduced, allowing for drastically lower catalyst loadings.



**Scheme 19 Beller's ligand free aryl-cyanation procedure.**

Key papers published by Frech *et al.* and Grushin *et al.* provide detail regarding the mechanisms of catalyst deactivation in the Pd-catalysed cyanation of haloarenes, specifically with the cyanide sources  $\text{K}_4[\text{Fe(CN)}_6]$  and  $\text{Zn(CN)}_2$ .<sup>43, 93</sup> In both papers, multiple poisoning experiments were carried out on a series of Pd sources including  $\text{Pd(PPh}_3)_4$ ,  $\text{Pd(I)(Ph)(PPh}_3)_2$ , Pd/C (5%) and Frech's NP precursor complex,  $\text{Pd(Cl)}_2[\text{P(NC}_5\text{H}_{10})(\text{C}_6\text{H}_{11})_2]_2$  (**26**). They were

all exposed to large excesses (up to 20 equivalents with respect to Pd) of the labile  $\text{CN}^-$  source tetrabutylammonium cyanide in NMP and in all cases, 100% conversion to the catalytically incompetent complex  $[\text{Pd}(\text{CN})_4]^{2-}$  was observed at 25 °C. The same was observed when  $\text{Zn}(\text{CN})_2$  and KCN were used in place of tetrabutylammonium cyanide. However when Frech's aminophosphine Pd complex **26** was subjected to 20 eq. of  $\text{K}_4[\text{Fe}^{13}\text{CN}_6]$  at 25 °C in NMP, no conversion was observed. Only when this reaction was heated to 140 °C for 48 hours was stepwise conversion of **26** to  $[\text{Pd}^{13}\text{CN}_4]^{2-}$  and  $[\text{Pd}^{13}(\text{CN})_2]$  detected. In stark contrast, when suspensions of Pd/C (5%) in NMP were subjected to the same conditions (20 eq.  $\text{K}_4[\text{Fe}^{13}\text{CN}_6]$  at 140 °C for 24 hours) absolutely no Pd cyanide complexes were observed. This result suggests that the effect of catalyst poisoning from  $\text{K}_4[\text{Fe}(\text{CN})_6]$  on heterogeneous Pd sources (specifically NPs) may be unobservable. This provides good evidence for the conclusion that PdNP catalysts may be a solution to the cyanide poisoning problem.

To support this discovery, Frech *et al.* reported the cyanation of many substituted aryl bromides using  $\text{K}_4[\text{Fe}(\text{CN})_6]$  as a cyanide source and **26** as a precatalyst with loadings as low as 0.05 mol%. They also conducted a series of tests to investigate the true nature of the catalysis, including separately dosing the reaction mixture with mercury, polyvinylpyridine and triphenylphosphine. All caused a significant drop in conversion in the reaction, as did increasing the catalyst loading to greater than 0.2 mol%; this was attributed to the formation of Pd black.<sup>7,21</sup>

With these results in mind, it is interesting to see that Zhu and Cai utilised 1 mol% Pd/C (5 wt.% Pd) in the cyanation of a series of simple aryl iodides and bromides in NMP with excellent yields.  $\text{Bu}_3\text{N}$  was used as an additive and even allowed the cyanation of an activated aryl chloride (*p*- $\text{CF}_3\text{C}_6\text{H}_4\text{Cl}$ ), albeit in low yield – 4%.<sup>103</sup> Pd/C displayed good catalytic activity up to the fourth recycle and was later reported to give quantitative cyanation of 4-bromoanisole in a 2:1 mixture of PEG4000/water and 1 equivalent of sodium fluoride as a base when the reaction was conducted in a microwave. When more difficult aryl chloride substrates were tested, a stoichiometric amount of KI was added to aid cyanation of the activated substrate 4-chloroacetophenone, and even then only a 48 % yield was recorded.<sup>104</sup>

PdNPs supported on CuO were also found to catalyse cyanation and Suzuki reactions on *p*-iodotoluene. The reactions were catalysed by 1 mol% Pd with no additive present, in DMF at 120 °C for 15 hours. Unfortunately, only aryl iodides were converted and the catalyst was not found to be reusable.<sup>105</sup> Similarly, recent work showed a dendrimer supported PdNP catalyst being used in Pd catalysed arylcyanations. High catalyst loadings were required

throughout in order to facilitate the transformation (2-4 mol% Pd), but quite remarkably there was no requirement for any additive.<sup>106</sup> Throughout the development of the field after the introduction of  $K_4[Fe(CN)_6]$  as a cyanating agent, additives such as  $Na_2CO_3$  have always appeared to have been variable and system dependant, but still a requirement. These additives have yet to be assigned a concrete role in the reaction mechanism, but presumably assists the transmetallation step. However, despite this significant progression no suggestions as to why this was the case, or mechanistic work in an attempt to explain this was included in either publication. This is discussed further in Chapter 5.

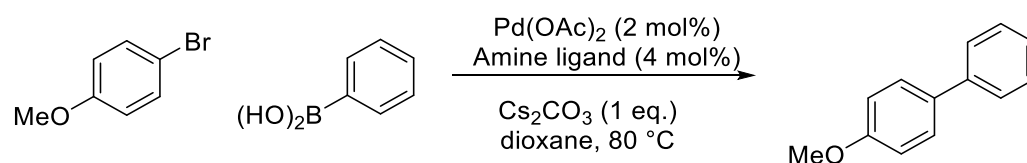
More recent work by Buchwald *et al.* shows the utility of their third generation precatalyst **25** (as outlined in section 1.2.2) to cyanate a wide range of aryl- and heteroaryl chlorides.<sup>107</sup> Using  $K_4[Fe(CN)_6] \cdot 3H_2O$ , it was possible to cyanate a wide range of coupling partners at only 100 °C under aqueous conditions. However, it was necessary to use upwards of 0.2 mol% catalyst loadings and a large excess of  $^-CN$  (as 0.5 eq. of  $K_4[Fe(CN)_6] \cdot 3H_2O$ ). Interestingly, only 0.125 eq. of KOAc was required as an additive to facilitate the reaction, showing that a suitable additive is capable of facilitating efficient transmetallation catalytically. Good reaction rates were achieved as many substrates afforded good yields of product within 2 hours. They have further extended this work to showcase its use in positron emission topography (PET). The virtually instantaneous cyanation of pharmacologically relevant aryl bromides in the presence of stoichiometric cyclooctadienyl-PdXPhos and  $H^{11}CN$  was used to synthesise a range of [ $^{11}C$ ]-labelled pharmaceuticals compatible for use in PET.<sup>108</sup>

A stoichiometric study on the productive process of Pd-catalysed cyanation carried out by Hartwig *et al.* has also recently revealed that reductive elimination of  $Ar-CN$  from  $Pd(CN)(Ar)L$  complexes (where L is a bidentate phosphine) is similar in nature to the migratory insertion event in Pd-catalysed carbonylations. Importantly, this work has highlighted that despite electron-deficient aryl coupling partners undergoing more facile oxidative addition they have a detrimental effect on the rate of reductive elimination. The experimental evidence displayed a significant decrease in rate of reductive elimination at  $Pd^{II}$  with more electron deficient aryl groups. However, computational data shows little difference in transition state energies for reductive elimination, instead significant thermodynamic factors were found for the increased ease of reductive elimination for electron-rich species. Electron-withdrawing substituents were found to stabilize the arylpalladium species but destabilize the aryl nitrile product.<sup>109</sup>

Despite the push towards lower catalyst loadings and the use of supported PdNPs in cyanation reactions, relatively little work has been reported on the direct role and mechanism of PdNPs formed *in situ* from stable palladium precatalysts.

#### 1.4. $Pd(OAc)_2(HNR_2)_2$ complexes in catalysis

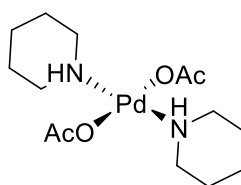
Initial studies regarding the use of primary and secondary amines with bulky R-groups (*e.g.*  $Cy_2NH$  and 1-adamantanamine) as effective ligands at Pd were carried out by Boykin *et al.* in the synthesis of biaryls under Suzuki-Miyaura conditions. Those with less bulky R-groups (*e.g.* diisopropylamine and aniline) along with tertiary amines (such as  $NEt_3$  and diisopropylethylamine) furnished lower yields in the benchmark Suzuki-Miyaura cross-coupling reaction.<sup>69</sup>



**Scheme 20** The benchmark Suzuki-Miyaura coupling used by Boykin *et al.*

Upon attempting the synthesis of the  $Pd(OAc)_2(HNR_2)_2$  complexes of secondary and tertiary amines, they remark upon their stability, stating that tertiary amines do not form stable complexes with Pd, but instead decomposed at room temperature to Pd black. On the other hand, secondary amines formed stable  $Pd(OAc)_2(HNR_2)_2$  complexes, and proved to be efficient catalysts in the model Suzuki-Miyaura reaction, even at room temperature. This shows an initial hint that the relationship between these complex's stabilities and their catalytic activity in cross-coupling reactions is a key one; tuning that stability/activity ratio may be the key to designing a PdNP precursor complex which can provide a highly active catalytic system.

Work within the Fairlamb group has shown that piperidine provides a semi-stable complex with Pd, **47**, which degrades upon heating in DMF to form PdNPs (discussed further in Chapter 2).<sup>110</sup> This, coupled with the evidence provided by Frech *et al.* that PdNPs may be the answer to Pd-catalysed cyanation's inherent problem with catalyst poisoning provides a suitable starting point for designing a highly active Pd precatalyst.<sup>43</sup>



47

**Scheme 21 The complex Pd(OAc)<sub>2</sub>(piperidine)<sub>2</sub> was found to be a PdNP precursor, and competent catalyst in Pd-catalysed C–H functionalisations**

Kinetic investigations into the effects of Pd(OAc)<sub>2</sub>(HNR<sub>2</sub>)<sub>2</sub> precatalyst structure, water, additives and K<sub>4</sub>[Fe(CN)<sub>6</sub>] on PdNP precursor catalytic activities should provide a wealth of information regarding the reaction mechanism and the optimisation of both reaction conditions and precatalyst design.

## 1.5. Project Aims and Objectives

### 1.5.1. Aims

- I. To design a series of Pd precatalysts capable of performing Pd-catalysed arylcyanations at very low catalyst loadings.
- II. Investigate the mechanism of Pd-catalysed arylcyanation and to utilise novel findings to increase reaction efficiency, specifically relating to Pd catalyst loadings,

### 1.5.2. Objectives

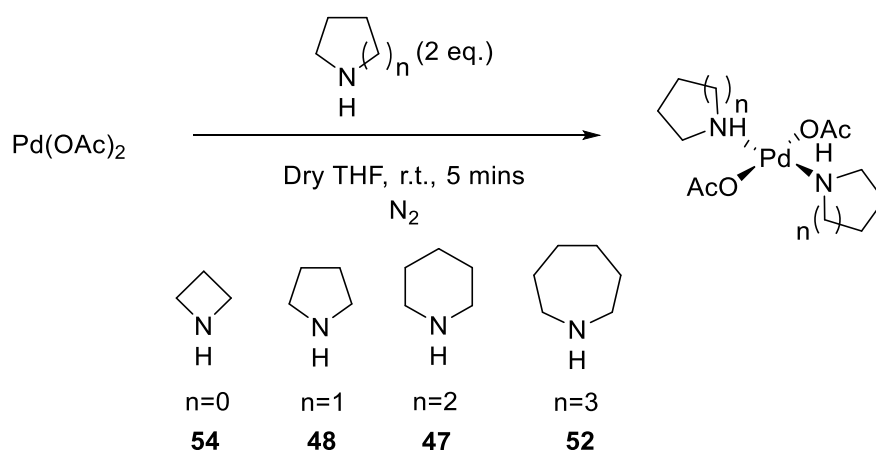
- I. To develop a series of Pd precatalysts of type  $\text{Pd}^{\text{II}}(\text{OAc})_2(\text{HNR}_2)_2$  for use in Pd catalysed arylcyanation reactions. (Chapter 2)
- II. To establish a suitable benchmark arylcyanation reaction with which to compare the relative activities of the Pd precatalysts synthesised in Chapter 2. (Chapter 3)
- III. Utilise *in situ* infrared spectroscopy in kinetic studies to investigate the mechanism by which the Pd-catalysed cyanation of **65** transpires when using  $\text{K}_4[\text{Fe}(\text{CN})_6] \cdot 3\text{H}_2\text{O}$  as a cyanide source. (Chapter 4)
- IV. Investigate the effect of  $\text{K}_4[\text{Fe}(\text{CN})_6]$  concentration on catalyst efficiency in the Pd-catalysed cyanation of **65**. (Chapter 4)
- V. Using kinetic studies quantitatively analyse and compare the catalytic efficiencies of the precatalysts **48**, **47**, **52**, **53**, **51** and **58** in the Pd-catalysed arylcyanation of **65** when using  $\text{K}_4[\text{Fe}(\text{CN})_6]$  as a cyanide source. (Chapter 5)
- VI. Exploit mechanistic investigations into the roles of concentration, additives and counterions to improve catalyst efficiencies in Pd-catalysed arylcyanations. (Chapter 5)

## Chapter 2: Synthesis of Pd<sup>II</sup>(OAc)<sub>2</sub>(HNR<sub>2</sub>)<sub>2</sub> precatalysts

### 2.1. Introduction

Pd(OAc)<sub>2</sub>(HNR<sub>2</sub>)<sub>2</sub> complexes are competent catalysts in room temperature Suzuki-Miyaura cross-coupling (SMCC) reactions and in direct C–H functionalisation reactions of complex nucleoside derivatives.<sup>69, 110</sup> The first Pd(OAc)<sub>2</sub>(HNR<sub>2</sub>)<sub>2</sub> complexes synthesised by Boykin and Tao showed good activity in SMCC reactions under mild conditions, however their synthesis was limited to simple secondary and primary amines due to stability issues. They reported that while secondary and primary amine complexes were simple to make and completely air stable, the attempted complexation of tertiary amines (such as triethylamine and Cy<sub>2</sub>NMe) with Pd(OAc)<sub>2</sub> resulted in direct decomposition and formation of Pd black. In order to design an effective PdNP precursor, a balance needs to be struck between the complex being too unstable (rapid formation of Pd black) and being so stable that no degradation occurs at all to form desired nanoparticles (as discussed in Chapter 1).

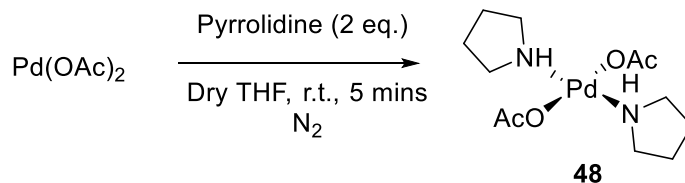
Complex **47** has been shown previously to mediate the C–H arylation of 2'-deoxyadenosine with stoichiometric CuI,<sup>110</sup> and the metal nanoparticles formed from it under these reaction conditions have been characterized as small (ca. 1.5 nm by TEM) DMF-stabilized spherical truncated icosahedra containing a (111) surface.<sup>20</sup> With this in mind, it provides a good basis for the design of a range of Pd(OAc)<sub>2</sub>(HNR<sub>2</sub>)<sub>2</sub> complexes as PdNP precursors for use as precatalysts.



**Scheme 22 A** a general scheme for the synthesis of a range of Pd(OAc)<sub>2</sub>(HNR<sub>2</sub>)<sub>2</sub> compounds.

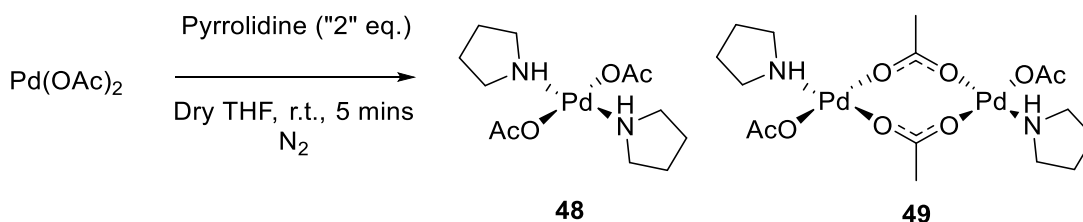
## 2.2. Synthesis of Alicyclic $\text{Pd}(\text{OAc})_2(\text{HNR}_2)_2$ complexes

The first to be attempted was the synthesis of pyrrolidine complex **48**, which was carried out with “2 equivalents” of non-distilled amine directly from the bottle.



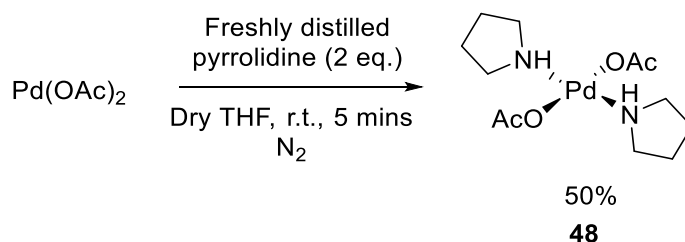
**Scheme 23** The proposed route towards  $\text{Pd}(\text{OAc})_2[(\text{CH}_2)_4\text{NH}]_2$ .

Upon recrystallisation of the crude product, two compounds crystallised. One with yellow crystals, the other red. Upon characterisation by  $^1\text{H}$  NMR and LIFDI MS it was apparent that both the desired product ( $\text{Pd}(\text{OAc})_2[(\text{CH}_2)_4\text{NH}]_2$ ) and its acetate dimer, **49**, had formed in the reaction. This was due to the pyrrolidine taken straight from the reagent bottle being impure, and below the calculated amount of pyrrolidine.



**Scheme 24** Impure pyrrolidine resulted in less than 2 equivalents of amine being added, and the acetate dimer **49** forming along with the desired product, **48**.

This hurdle was surmounted by distillation of the pyrrolidine immediately prior to use, allowing the addition of exactly 2 equivalents of the amine, affording the desired compound in an adequate 50% yield. It was also observed that both Pd complexes were unstable in solution (even in dry solvent), with Pd black forming within minutes of dissolution. Over extended periods at room temperature these compounds also decompose in the solid-state.



**Scheme 25** Adding freshly distilled pyrrolidine (2 eq.) to  $Pd(OAc)_2$  afforded solely the pyrrolidine acetate monomer complex **48**.

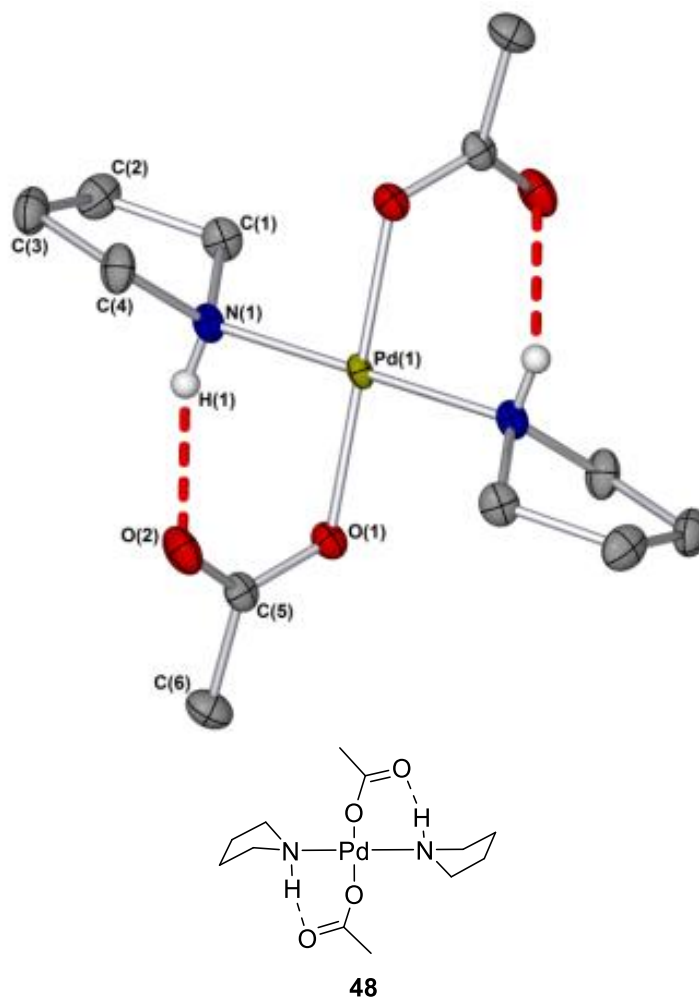
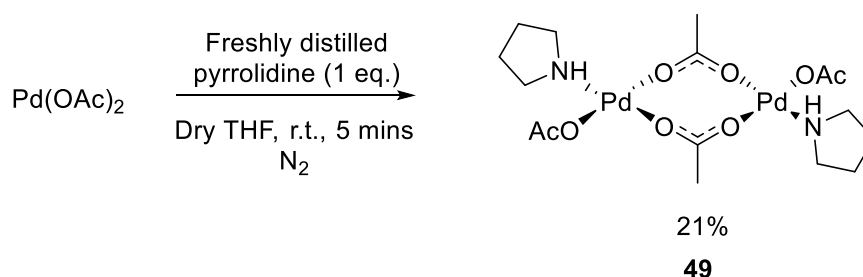


**Figure 18** Structure of **48**, determined by X-ray diffraction; arbitrary numbering used. Selected hydrogen atoms removed for clarity. Thermal ellipsoids shown with a probability of 50%; numbers in parentheses are standard deviations from the measured value, denoting the error in the measurements. Selected bond lengths (Å): N(1)-Pd(1): 2.043(3), O(1)-Pd(1): 2.015(2), C(1)-N(1): 1.484(4), C(5)-O(1): 1.282(4), C(5)-O(2): 1.243(4).

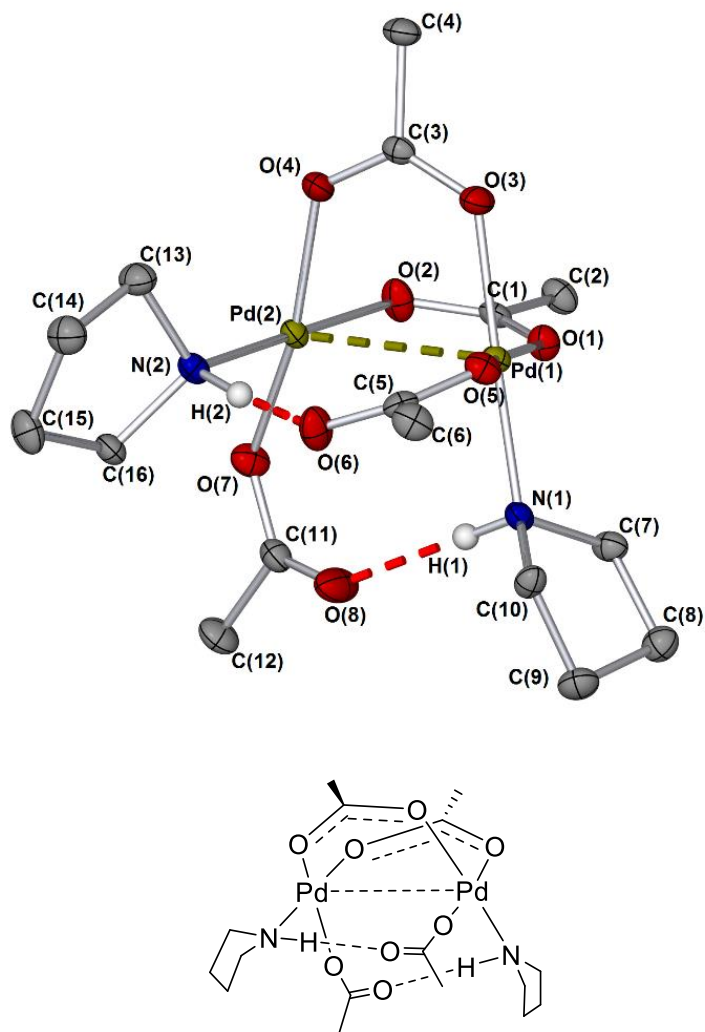
Importantly this allowed the observation of an unexpected compound, opening-up another possible range of compounds, the acetate Pd dimers of each of the suggested amine complexes. Theoretically these could be synthesised by addition of only 1 equivalent of amine *per* Pd. Thus, adding 1 equivalent of freshly distilled pyrrolidine to  $Pd(OAc)_2$

provided the acetate dimer, **49**. Despite complete conversion of Pd(OAc)<sub>2</sub>, multiple recrystallisations under inert atmosphere were required to afford pure **49**, this resulted in the final isolated yield being poor, at 21%. This poor yield was later found to be due to the mechanism of Pd<sub>3</sub>(OAc)<sub>6</sub> aminolysis, as is discussed in Section 2.4.



**Scheme 26** Synthesis of the pyrrolidine acetate dimer complex, **49**.

It was also possible to crystallise the pyrrolidine acetate dimer complex (**49**, Figure 19) and the monomer complex (**48**, Figure 18). Both crystal structures show important structural intricacies and support the <sup>1</sup>H NMR data. In the <sup>1</sup>H NMR spectrum of the monomer (**48**) the signal corresponding to the N–H proton appears at 6.00 ppm, showing it is significantly deshielded. Presumably (as displayed in the solid-state structure obtained by X-ray diffraction, Figure 18) this is due to intramolecular hydrogen bonding between it and the adjacent acetate group as was originally proposed by Boykin *et al.*<sup>69</sup> However, in the <sup>1</sup>H NMR spectrum of the acetate Pd dimer, **49**, the N–H signal is even further downfield, at 7.03 ppm, suggesting even stronger hydrogen bonding character. This evidence is supported upon studying the crystal structure of **49** (Figure 19), where it is clear that hydrogen bonds between H(2)–O(6) and H(1)–O(8), cause both pyrrolidines and acetates to be pinned back.



49

**Figure 19.** Structure of 49, determined by X-ray diffraction; arbitrary numbering used. Selected hydrogen atoms removed for clarity. Thermal ellipsoids shown with a probability of 50%; numbers in parentheses are standard deviations from the measured value, denoting the error in the measurements. Selected bond lengths (Å): N(1)-Pd(1):2.021(2), O(1)-Pd(1): 2.0394(17), O(3)-Pd(1): 2.0300(17), O(5)-Pd(1):1.9969(17), Pd(1)-Pd(2): 3.0377(3), H(1)-O(8):1.98(1).

Furthermore, the synthesis of *bis-trans*-[piperidiny- $\kappa$ -NH]palladium(II) diacetate (**47**) previously reported by Storr *et al.* can also be performed in excellent yields upon addition of 2 equivalents of distilled piperidine to Pd(OAc)<sub>2</sub>.

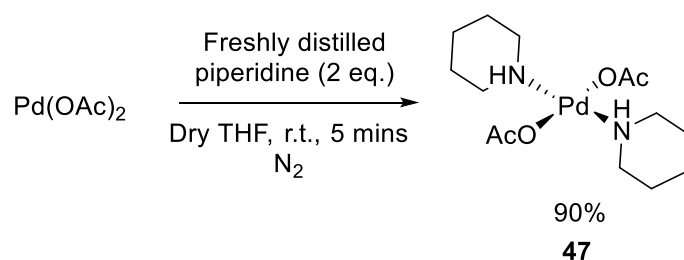
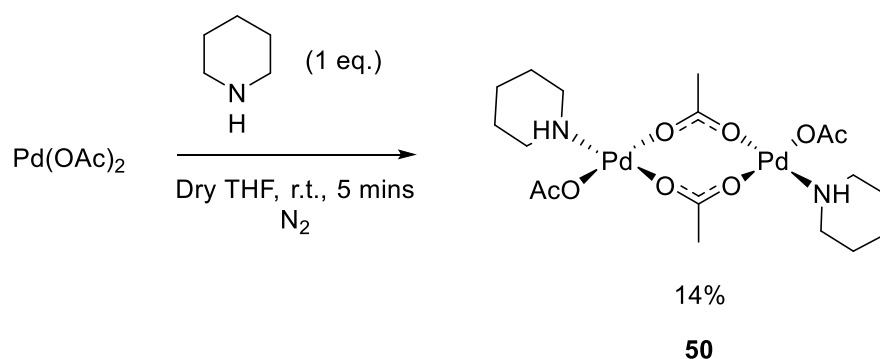


**Figure 20** Addition of piperidine (2 eq.) to  $Pd(OAc)_2$  yields the piperidine acetate monomer complex, **47**.

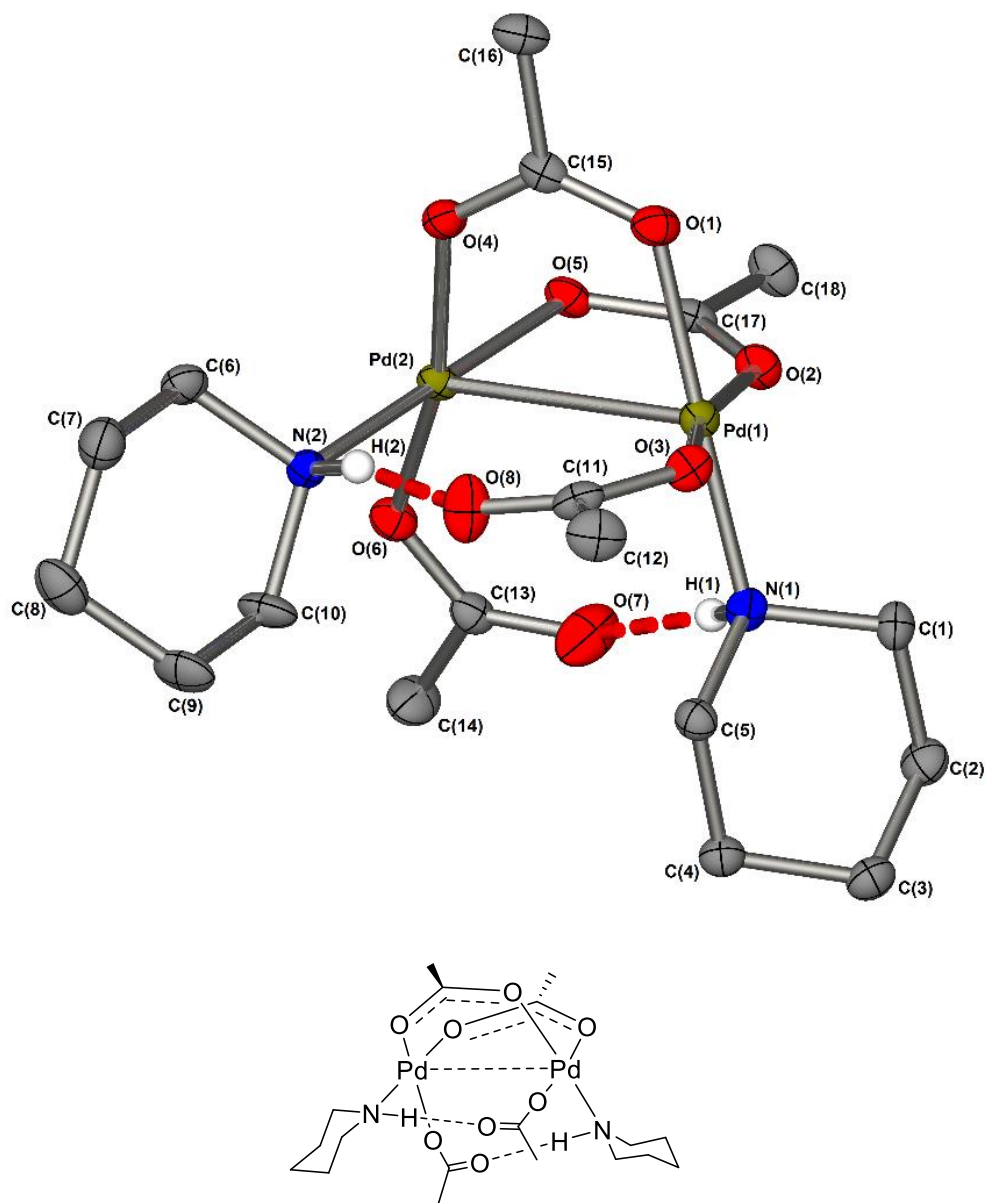
Again, the  $^1H$  NMR spectrum showed a deshielded N–H signal at 5.54 ppm which indicates significant hydrogen bonding character, which is also confirmed in the solid-state structure, as determined by X-ray diffraction by Storr *et al.*<sup>110</sup>



**Scheme 27** Addition of piperidine (1 eq.) to  $Pd(OAc)_2$  affords the piperidine acetate dimer complex, **50**.

The piperidine acetate Pd dimer complex **50** was also synthesised by gradual addition of 1 equivalent of piperidine to  $Pd(OAc)_2$ . However, as with **49**, despite complete conversion of  $Pd(OAc)_2$ , pure material was only isolated after successive recrystallisations and washes under inert atmosphere, resulting in a poor isolated yield of 14%. Comparing the  $^1H$  NMR data it is again evident that the N–H signal in the **50** is even more deshielded than that in the monomer, providing a signal at 7.00 ppm. Therefore it would be expected for significant hydrogen bonding character between the piperidinyl and acetate ligands across the two Pd centres to be present. Indeed upon obtaining the solid-state structure by single crystal X-ray diffraction this can be confirmed, as is displayed in Figure 21. Predictably the piperidine dimer compound **50** is similar in structure to **49**, with the distinctive clam-shell shapes found in many acetate bridged Pd dimer species.<sup>111</sup> This allows for intramolecular hydrogen bonding to occur between the acetate carbonyl and the piperidinyl N–H. It is also of note to mention the Pd–Pd interaction present in **49**, **50** and later, in **58**. This can be attributed to a true interaction, as in all three the Pd–Pd interatomic distances of 3.0377(3), 3.0389(5) and

3.0466(3), respectively, are all less than the sum of their individual van der Waals' radii (3.26 Å). The origin of this interaction, along with the ligand effects upon it are outlined later in section 2.3.

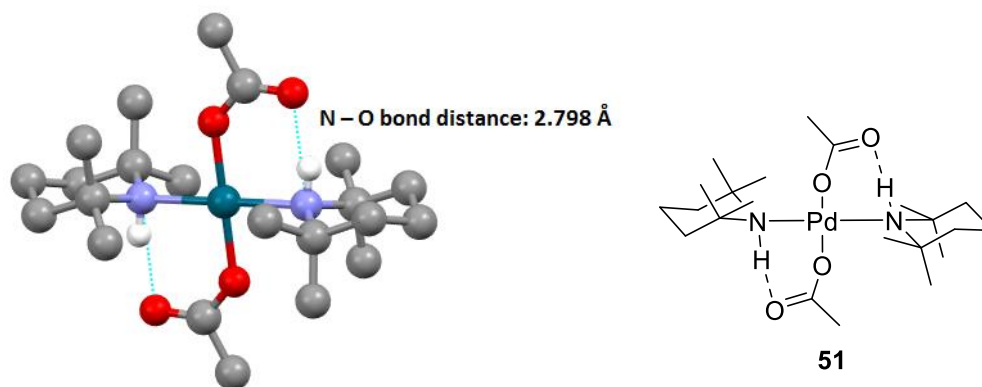


50

**Figure 21** Structure of 50, determined by X-ray diffraction; arbitrary numbering used. Selected hydrogen atoms removed for clarity. Thermal ellipsoids shown with a probability of 50%; numbers in parentheses are standard deviations from the measured value, denoting the error in the measurements. Selected bond lengths (Å): N(1)-Pd(1): 2.018(4), O(1)-Pd(1): 2.034(4), O(3)-Pd(1): 1.999(4), O(2)-Pd(1): 2.033(4), Pd(1)-Pd(2): 3.0389(5), H(1)-O(7):2.00(0).

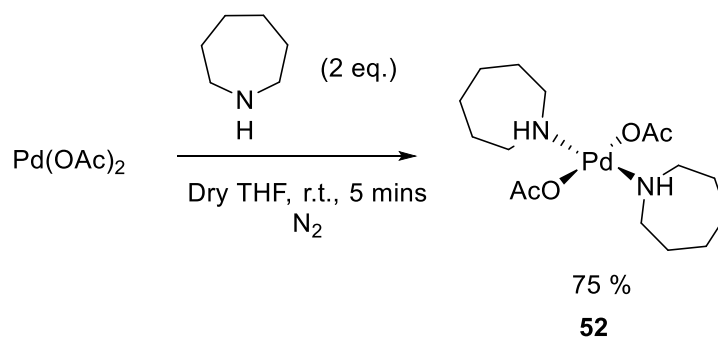
Boykin *et al.* state that “intramolecular hydrogen bonding may be a factor contributing to the stability of the complex”, however given that degradation of 47 in DMF resulted in the

formation of PdNPs along with reduction of the piperidine ligand to 2,3,4,5-tetrahydropyridine ( $\Delta^1$ -piperidine) it is possible that the decomposition of the complex may result from intramolecular deprotonation of the piperidine.<sup>112</sup> This implies that the intramolecular H-bonding may be the key to the instability of these compounds. Work published by Gaunt *et al.* discusses the role of Pd-amine complexes in the direct functionalisation of  $\text{CH}_3$  groups adjacent to a Pd-coordinated nitrogen.<sup>113</sup> They also report the crystal structures of a range of cyclic amine complexes with  $\text{Pd}(\text{OAc})_2$ , including *bis-trans*-[2,2,6,6-tetramethylpiperidinyl- $\kappa$ -NH]palladium(II) diacetate (**51**). In keeping with the similar structures displayed above, this complex also shows evidence for intramolecular hydrogen bonding between the acetates and the N–H groups of the 2,2,6,6-tetramethylpiperidine ligands.



**Figure 22** Crystal structure of *bis-trans*-[2,2,6,6-tetramethylpiperidinyl- $\kappa$ -NH]palladium(II) diacetate (**51**) displays hydrogen bonding character. Data obtained from Gaunt *et al. Nature*, 2014, 510, 129.

The azepane Pd complex (**52**) was made by addition of the freshly distilled amine directly to  $\text{Pd}(\text{OAc})_2$ , and provided the desired compound in a good 75% yield. No Pd black was formed in solution of dry solvent and the complex is air stable in the solid-state, however in wet solvent degradation to Pd black is rapid (Scheme 28).

Scheme 28. Synthesis of  $\text{Pd}(\text{OAc})_2[(\text{CH}_2)_6\text{NH}]_2$ .

The structure of **52** was confirmed by X-Ray diffraction of a single crystal (Figure 23) and in contrast to the compounds synthesised by Boykin *et al.*, no intramolecular hydrogen bond appears to be present between the amine N-H and the acetate groups. This corresponds directly to the comparatively shielded N-H signal at 5.96 ppm seen within the  $^1\text{H}$  NMR spectrum.

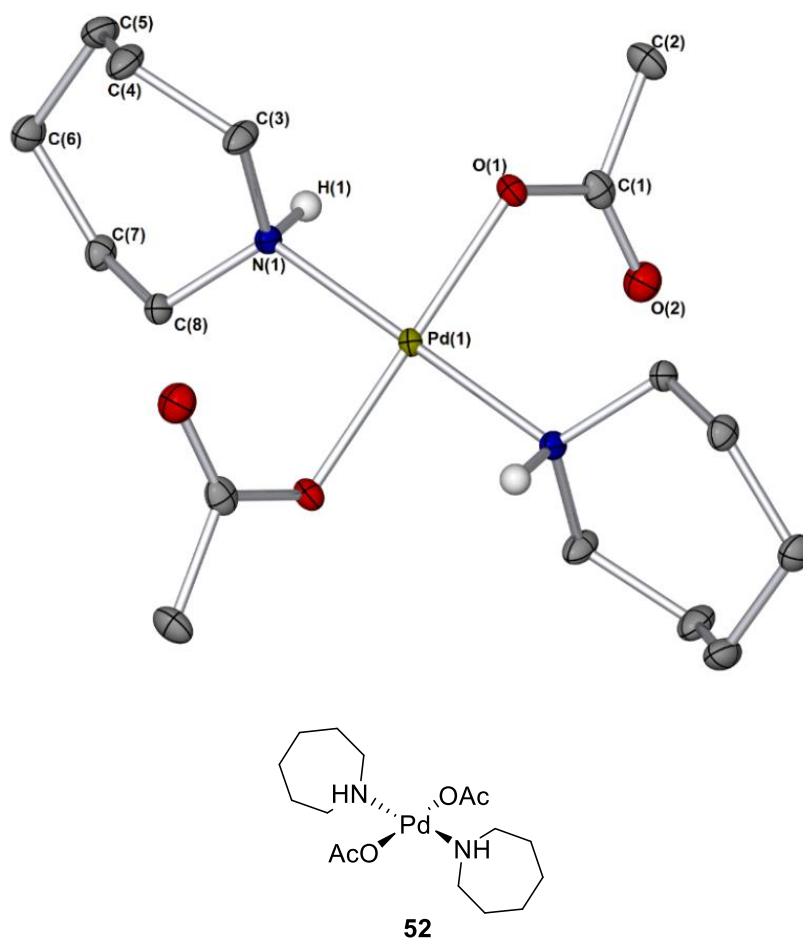
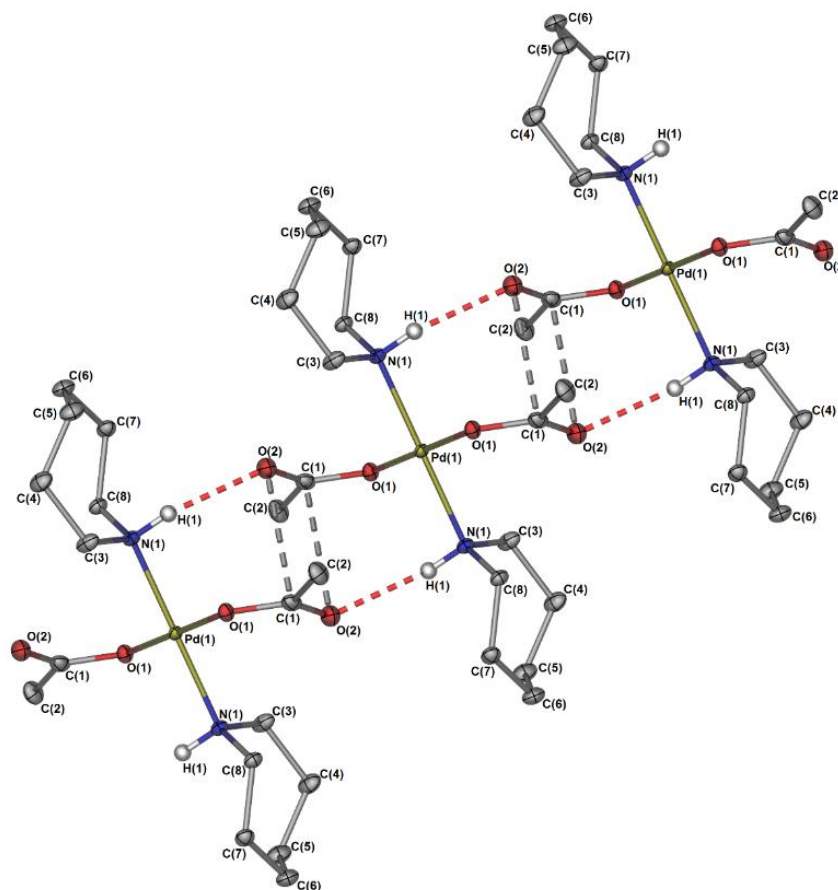


Figure 23. Structure of **52**, determined by X-ray diffraction; arbitrary numbering used. Selected hydrogen atoms removed for clarity. Thermal ellipsoids shown with a probability of

50%. Selected bond lengths (Å): N(1)-Pd(1): 2.0638(14), O(1)-Pd(1): 2.0050(12), C(1)-O(1): 1.286(2), C(1)-O(2): 1.236(2).

Expansion of the crystal packing reveals important structural intricacies, including carbonyl dipole-dipole interactions (Figure 24).



**Figure 24.** Extended lattice structure of 52, determined by X-ray diffraction; arbitrary numbering used. Selected hydrogen atoms removed for clarity. Thermal ellipsoids shown with a probability of 50%. Selected Hydrogen bond lengths and angles and Short-contact bond lengths calculated using Mercury: N(1)-H(1)⋯O(2): 2.972 Å, 158.93°, C(1)⋯O(2): 3.000 Å, C(1)-O(2)⋯C(1) 93.63°.

The dipole-dipole interaction strength between two dipoles varies dependent upon their relative orientation with each other and becomes a complicated affair in a fluid of freely rotating molecules. However when the two dipoles are in a fixed, parallel orientation (*i.e.* in a crystal) the potential energy of interaction per mole is:

$$V = - \left( \frac{\mu_1 \mu_2 (1 - 3 \cos^2 \theta)}{4\pi \epsilon_0 r^3} \right) N_A$$

**Equation 2.** Equation used to calculate the potential energy of a dipole-dipole interaction per mole. When  $\mu$  is the dipole moment in coulomb metres,  $\epsilon_0$  is the permittivity of free space,  $r$  is the distance between the two molecules and  $\theta$  is  $\approx 90^\circ$  according to Figure 25.

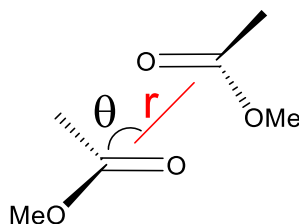


**Figure 25** The potential energy of dipole-dipole interaction can be calculated using their relative orientation and distance.

Substituting the dipole moment of methyl acetate as a model for the carbonyl groups (1.72 D,  $5.837 \times 10^{-30}$  C m),  $\theta = 93.63^\circ$  and the intermolecular distance of 3.000 Å (C(1)⋯O(2)) into Equation 2 it is therefore possible to calculate the strength of the carbonyl-carbonyl dipole interaction observed in Figure 24.<sup>114</sup>

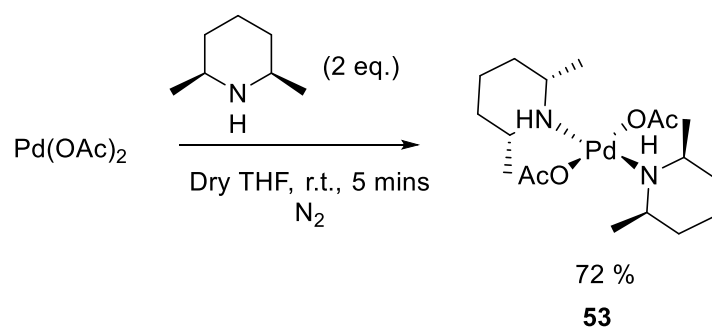
$$V = \left( \frac{(5.837 \times 10^{-30})^2 \times (1 - 3 \cos^2 93.63)}{4\pi \epsilon_0 \times (3.000 \times 10^{-10})^3} \right) \times 6.02214 \times 10^{23}$$

$$V = 6.747 \text{ kJmol}^{-1}$$

The value provided by Equation 2 is in the expected region for a strong dipole-dipole interaction.

Considering the effect of ring expansion upon intramolecular hydrogen bonding in **52**, it was therefore of interest to investigate the effect of increasing steric bulk around the coordinative nitrogen upon both solid state structure and its catalytic activity (as described in Chapter 5).

To this end, *cis*-2,6-dimethylpiperidine was employed as a ligand at Pd to afford the precatalyst **53** in a moderate 72% yield.



**Scheme 29** The synthesis of **53**.

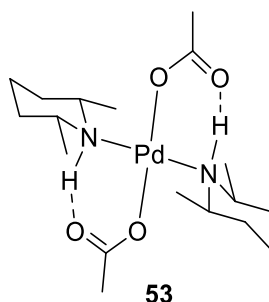
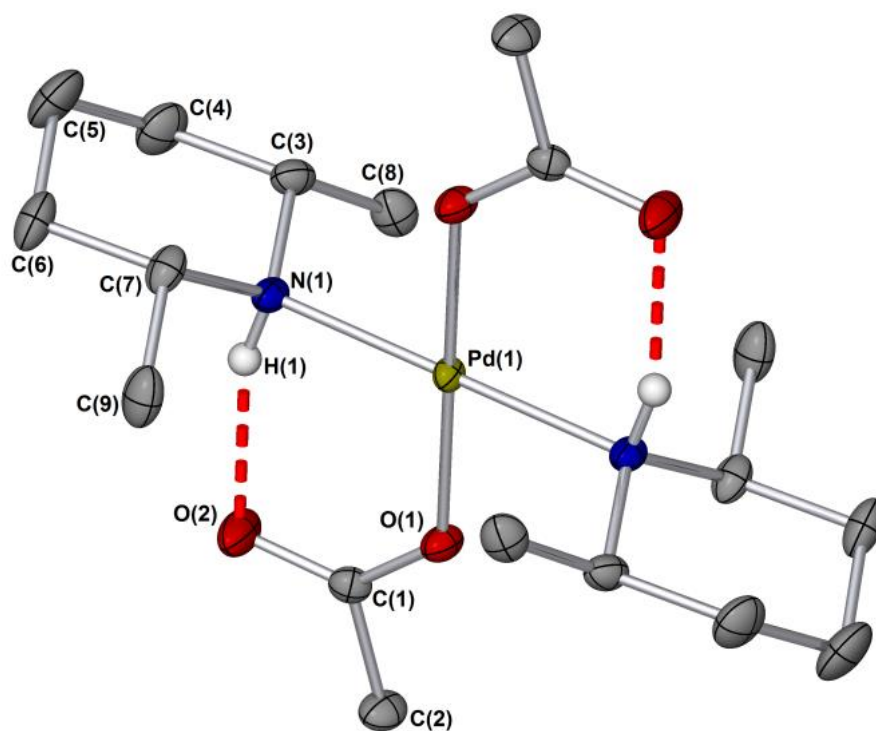
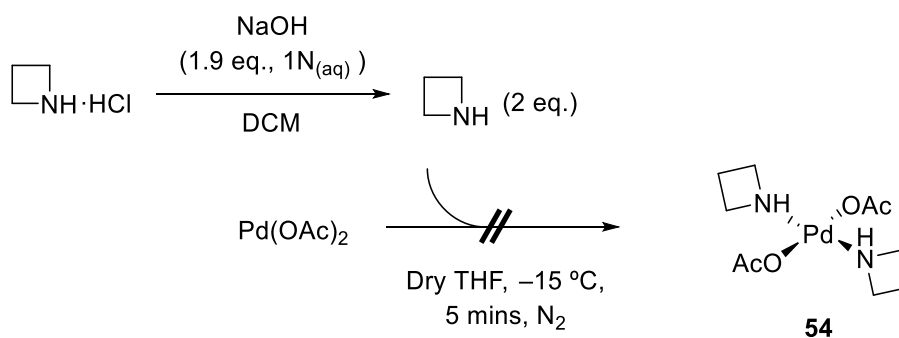


**Figure 26** Structure of **53**, determined by X-ray diffraction; arbitrary numbering used. Selected hydrogen atoms removed for clarity. Thermal ellipsoids shown with a probability of 50%. Selected bond lengths (Å): N(1)-Pd(1): 2.0696(18), O(1)-Pd(1): 2.0191(16), C(1)-O(1): 1.266(3), C(1)-O(2): 1.229(3), C(3)-N(1): 1.481(3).

The structure of **53** is in keeping with that determined for the structurally similar compound (**51**) synthesised by Gaunt *et al.*, again displaying strong hydrogen bonding interactions between the amine N–H and the acetate C=O. The signals corresponding to the N–H in the <sup>1</sup>H NMR spectra of **51** and **53** also appears at identical chemical shifts, 8.06 ppm, indicating very similar chemical environments at the amine centres.

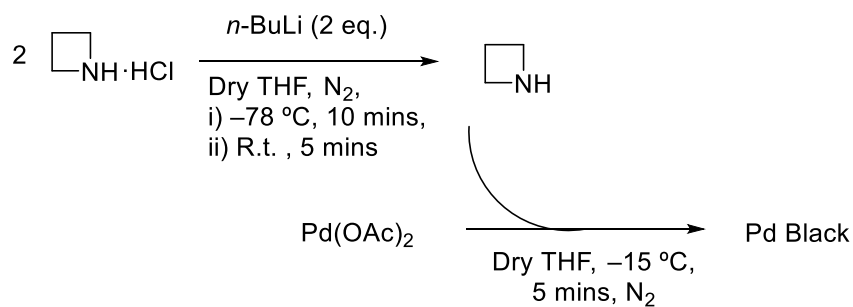
### 2.2.1. Attempted synthesis of azetidine Pd complex

Several attempts were made at synthesising the analogous azetidine compound from Pd(OAc)<sub>2</sub> and azetidine hydrochloride, however various complications have prevented isolation of the required compound. In order to synthesise compound **54**, the HCl salt of azetidine must first be neutralised *in situ* by reaction with a base, then added as a solution of approximate concentration to Pd(OAc)<sub>2</sub> in dry THF. Initial reactions were conducted using a deoxygenated, aqueous solution of 1N NaOH (Scheme 30). However due to the apparent incomplete neutralisation of the HCl salt the actual concentration of the azetidine solution added to the Pd(OAc)<sub>2</sub> was lower than expected, and upon the addition of the amine solution. Complete decomposition to Pd black was observed. No product was observed by <sup>1</sup>H NMR spectroscopy or by LIFDI MS.



Scheme 30 Attempted synthesis of **54**.

The neutralisation of the azetidine HCl salt was also attempted by precise addition of 1 equivalent of *n*-BuLi (with respect to azetidine hydrochloride), then addition of the solution of azetidine to Pd(OAc)<sub>2</sub>. However due to the insolubility of the azetidine salt in THF, there was incomplete neutralisation and upon addition of the solution to Pd(OAc)<sub>2</sub>, the immediate formation of Pd black occurred. Presumably, this was due to the presence of residual *n*-BuLi. No product was observed by <sup>1</sup>H NMR spectroscopy (Scheme 31).



Scheme 31 Attempting to neutralise azetidine hydrochloride with *n*-BuLi unfortunately resulted in the formation of Pd black.

### 2.3. The effect of increasing amine ligand size

Following the success of the synthesis of a series of mono- and dimeric Pd(OAc)<sub>2</sub>(HNR<sub>2</sub>)<sub>2</sub> complexes containing simple aliphatic amine ligands (**47**, **48**, **49**, **50**, **52** and **53**) it was also informative to investigate the structural effects of more complex and more sterically-demanding ligands upon the synthesis and catalytic efficiency of the precatalyst. The two ligands displayed in Figure 27 (**55**, **56**) were considered for their commercial availability, cost and interesting electronic character. It was also important to select a substrate which did not contain an  $\alpha$ -methylene group (as in 2,2,6,6-tetramethylpiperidine and 2,6-*cis*-dimethylpiperidine) as it has been shown that these are functionalisable at Pd under oxidative conditions.<sup>115</sup>

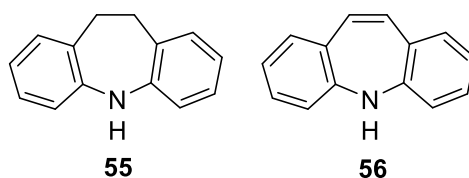
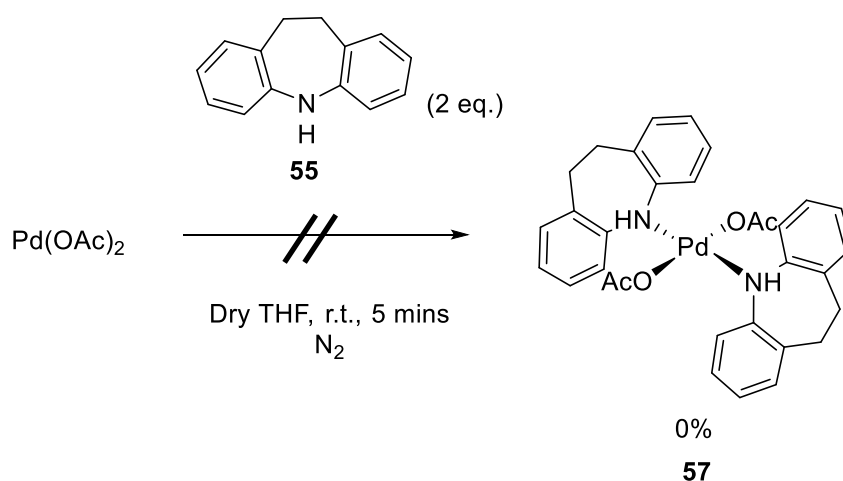


**Figure 27** Both iminodibenzyl (**55**) and dibenzazepine (**56**) were considered interesting potential ligands at Pd(OAc)<sub>2</sub>.

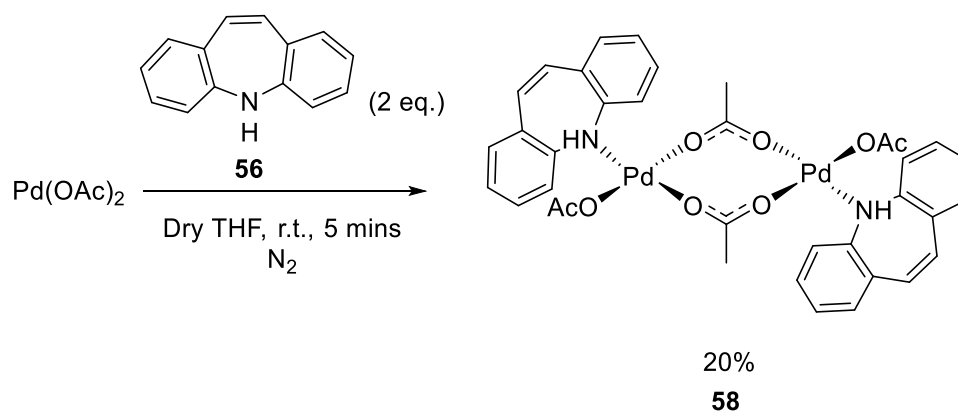
The attempted synthesis of the corresponding bisamino diacetate Pd complex, **57**, from **55** and Pd(OAc)<sub>2</sub> unfortunately resulted in complete lack of conversion of Pd(OAc)<sub>2</sub> to the desired product.



**Scheme 32** Attempted synthesis of **57**.

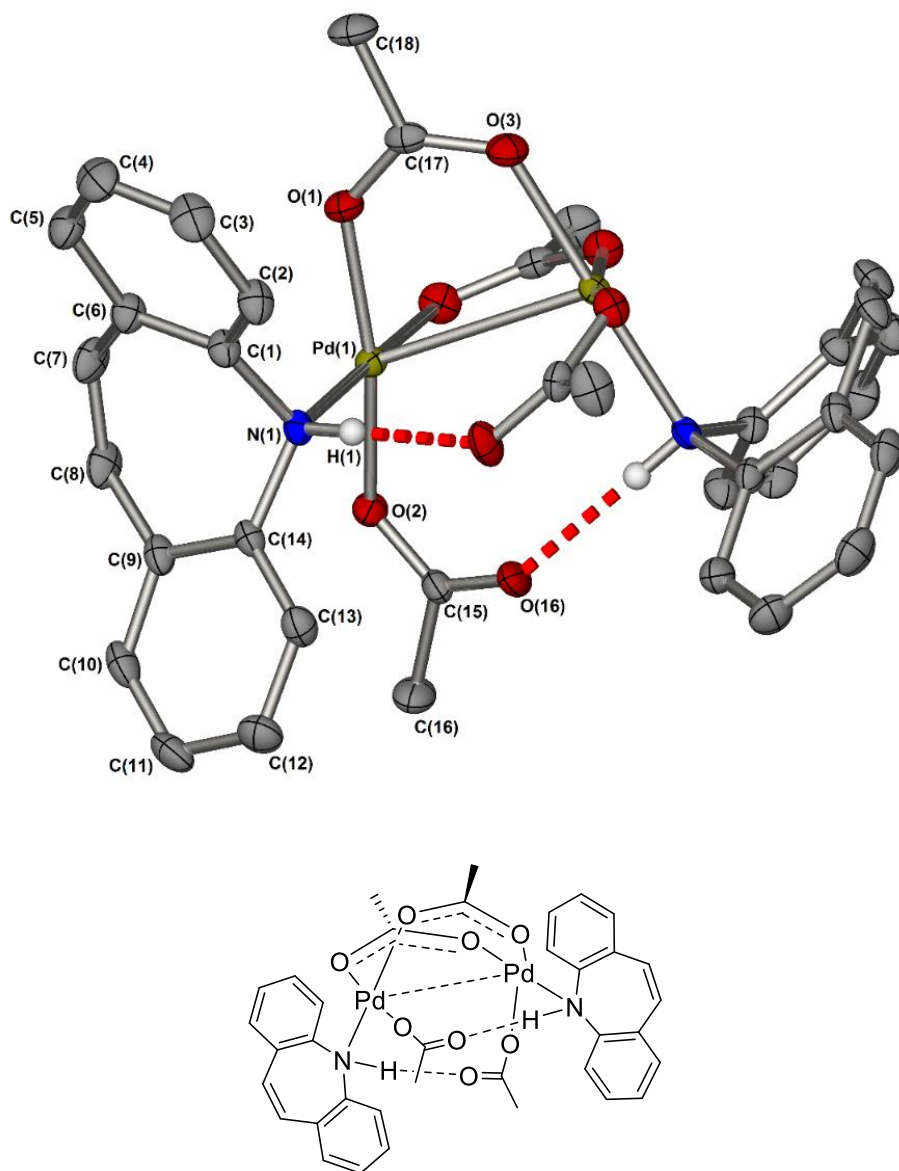
Treatment of Pd(OAc)<sub>2</sub> with two equivalents of dibenzazepine, **56**, pleasingly resulted in the 47% conversion of Pd(OAc)<sub>2</sub>. Despite the use of 2 equivalents of amine per Pd it was clear

that instead of the expected monomeric Pd complex, the dimeric complex (**58**) was isolated after recrystallisation in a poor 20% yield (Scheme 33).



**Scheme 33** Addition of **56** (2 eq.) to  $\text{Pd}(\text{OAc})_2$  resulted in the exclusive formation of the equivalent Pd dimer complex, **58**.

It was possible to confirm the structure of **58** by single crystal X-Ray diffraction and upon analysis of the solid-state structure (Figure 28) it is evident that even in the presence of a single **56** ligand per Pd centre it is already sterically crowded. Presumably the attempted addition of two equivalents of **56** to form the  $\text{Pd}(\text{OAc})_2(\text{HNR}_2)_2$  monomer is not sterically possible.



58

**Figure 28 Structure of 58, determined by X-ray diffraction; arbitrary numbering used. Selected hydrogen atoms and a molecule of pentane (antisolvent) have been removed for clarity. Thermal ellipsoids shown with a probability of 50%; numbers in parentheses are standard deviations from the measured value, denoting the error in the measurements. Selected bond lengths (Å): N(1)-Pd(1) 2.0757(15), Pd(1)-Pd(1) 3.0466(3), O(1)-Pd(1) 2.0147(12), O(2)-Pd(1) 1.9775(12), O(3) Pd(1) 2.0204(13), C(7)-C(8) 1.339(3), C(1)-N(1) 1.454(2).**

There is clear evidence for hydrogen bonding across the Pd dimer between the non-bridging acetate ligands and the N–H of the dibenzazepine in the x-ray diffraction and when compared with the significantly deshielded N–H <sup>1</sup>H NMR signal at 11.61 ppm this is corroborated. This value for the “N–H” is closer to the chemical shift expected of the O–H of a carboxylic acid (*i.e.* acetic acid: 11.53 ppm).<sup>113</sup> This strong hydrogen bond indicates that the valence electron

density around the <sup>1</sup>H in question is much decreased, and the N–H bond in question is therefore very long. The increased strength of this hydrogen bonding interaction could indicate increased hydrogen lability, resulting in easier N–H deprotonation by the non-bridging acetate. This would further facilitate the amine-assisted reduction of the Pd<sup>II</sup> centre and therefore complex decomposition, or put another way, propagation of PdNPs.

A recent publication from Musaev *et al.* highlights that computationally the dimeric stability and the strength of the Pd–Pd interaction of [(C<sup>^</sup>N)Pd<sup>II</sup>(OAc)]<sub>2</sub> complexes (such as **59**, right Figure 29) is dictated by the electronics of the C<sup>^</sup>N ligand, bridging and non-bridging acetate ligands.<sup>76</sup> It was also found that the ligand effects were antagonistic, so an increased Pd–Pd interaction strength resulted in a decreased Pd dimer stability. This can be explained by studying the idealised MO diagram for a Pd<sup>II</sup>–Pd<sup>II</sup> dimer (left, Figure 29). Mixing of the filled Pd<sup>II</sup>–Pd<sup>II</sup> dσ\* antibonding orbitals with the unoccupied Pd s and p<sub>z</sub> orbitals results in the formation of a hybridised orbital (middle, Figure 29) with less antibonding character. Thus, *via* the ligand σ–Pd dz<sup>2</sup> overlap, more electron donating ligands at Pd increase the energy of the dσ\* orbital, resulting in further mixing and an increased Pd<sup>II</sup>–Pd<sup>II</sup> interaction strength. *Vice versa*, electron withdrawing ligands were found to decrease the strength of this interaction. Experimental work by Green and co-workers also supports this hypothesis;<sup>116</sup> when the C<sup>^</sup>N ligand used was 2-*p*-tolylpyridine with bridging acetate ligands (R<sub>1</sub> = CH<sub>3</sub>, R<sub>2</sub> = CH<sub>3</sub>) the Pd–Pd distance was shorter than when the C<sup>^</sup>N ligand was 2-phenylpyridine with bridging TFA ligands (R<sub>1</sub> = H, R<sub>2</sub> = CF<sub>3</sub>).

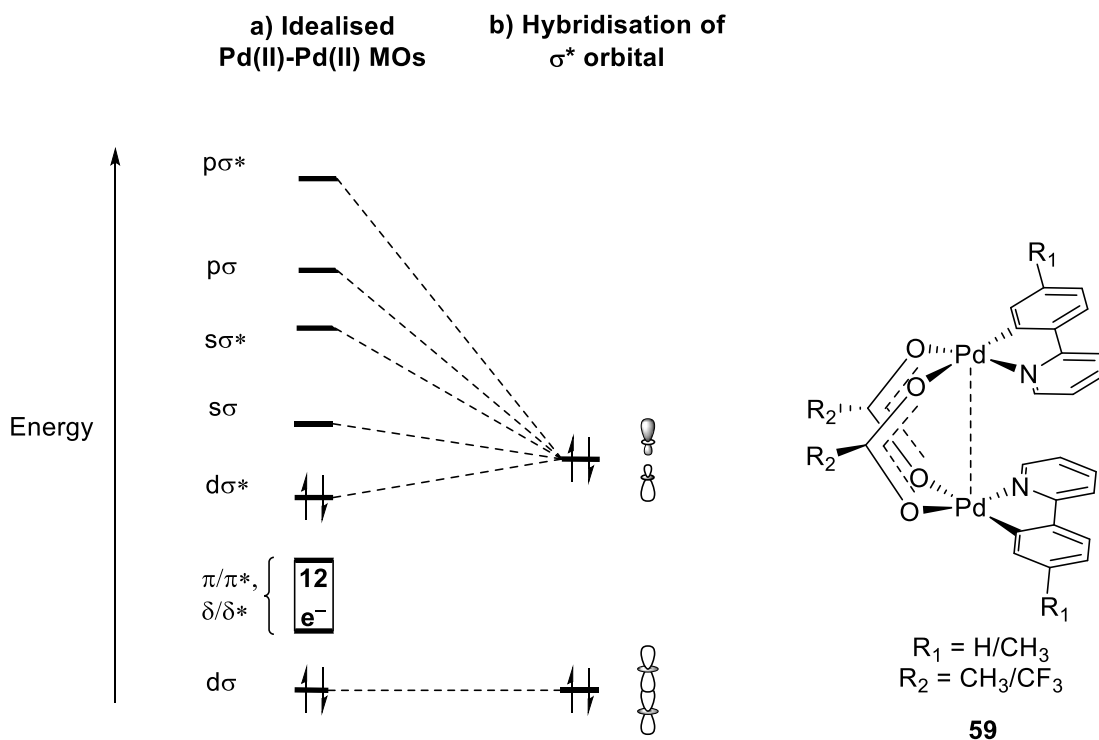


**Figure 29** Molecular orbital diagram for a  $\text{Pd}^{\text{II}}\text{-Pd}^{\text{II}}$  dimer of the type displayed.

Therefore based on the trends observed from interatomic distances, (Figure 30) it is possible to make some deductions about the electronic and steric effects of piperidine, pyrrolidine and **56** on the structure of their respective Pd acetate dimer complexes **49**, **50** and **58** from the X-ray diffraction structures.

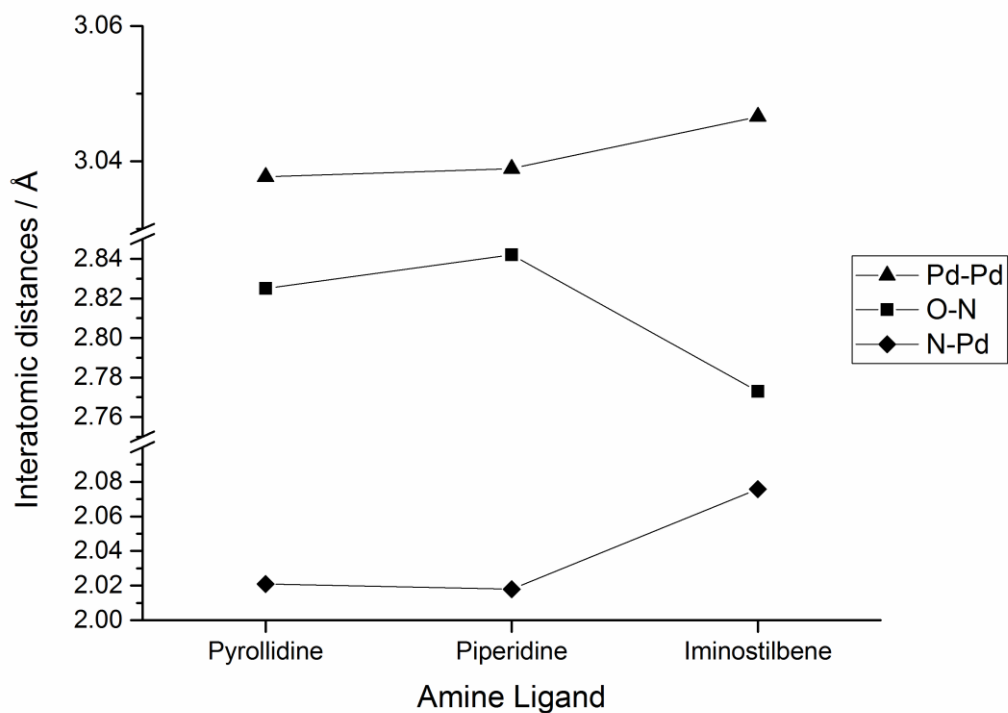


**Figure 30** Key interatomic distances in Pd dimers **49**, **50**, and **58**. O $\cdots$ N interatomic distances calculated using Mercury.

Figure 30 displays three key interatomic distances found within the structures of **49**, **50** and **58** and shows that there is little difference in the dimer structure when either pyrollidine or piperidine are ligands at  $\text{Pd}^{\text{II}}$ . A slight increase in O–N distance from pyrollidine to piperidine can be attributed to a weaker hydrogen bonding interaction. This is supported by a small decrease in  $^1\text{H}$  NMR chemical shift for these corresponding hydrogens from 7.03 to 7.00 ppm for **49** and **50** respectively, presumably due to a decrease in N–H acidity. Dibenzazepine has a more pronounced effect upon the overall structure of its Pd acetate dimer complex. Reduced electron density available to the  $n \rightarrow d\sigma$  dative bond due to  $\pi$  overlap between the nitrogen lone pair and the dibenzazepine aromatic system results in a weaker, longer bond to Pd. This results in the more acidic N–H being more susceptible to strong hydrogen bonding with the acetate carbonyl and a shorter N $\cdots$ O interatomic distance. Therefore, relative to **49** and **50** the weaker  $\sigma$  donor character ultimately results in lower electron density at each Pd centre, less mixing between  $d\sigma^*$  and the s and p orbitals (with increased antibonding character, Figure 29) and a longer Pd–Pd interaction.

Comparison of the solid-state structure of **58** with that of the ligands **55** and **56** (Figure 31) reveals a decrease in C–N–C bond angle upon coordination to Pd as the nitrogen tends towards a tetrahedral geometry, accentuating the concave face of the dibenzazepine ligand.

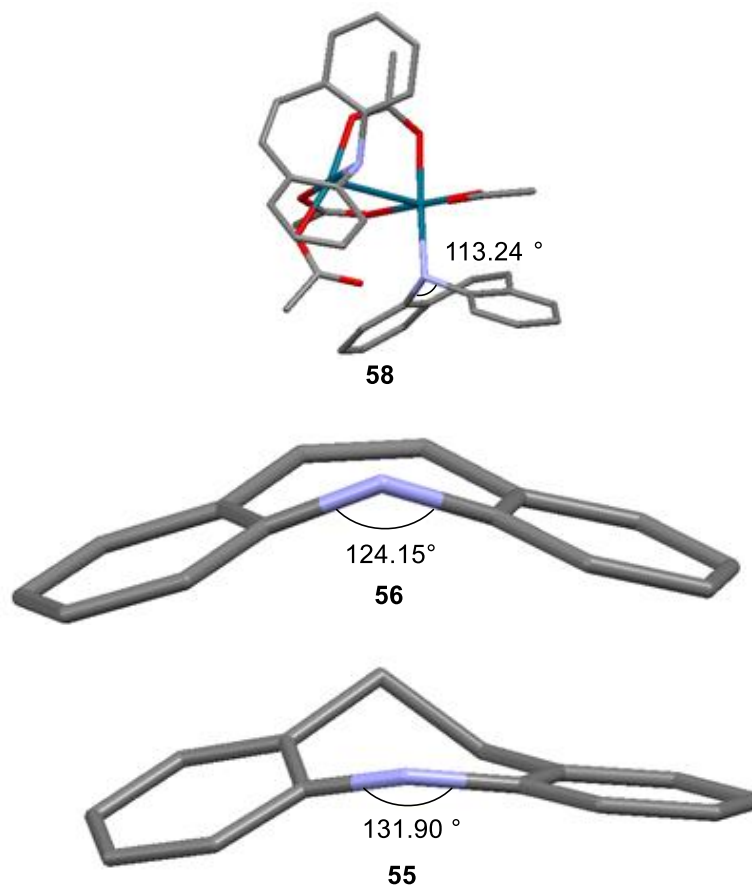


**Figure 31** Comparing C–N–C bond angles in the solid state structures of the free ligands **56** and **55** vs complex **58**. Images created in Mercury.

Inclusion of the *n*-pentane antisolvent molecule in Figure 32 shows how the concave dibenzazepine forms a hydrophobic pocket, in which the non-polar *n*-pentane molecule can aid crystallisation. The molecule of pentane in the unit cell is disordered, resulting in it being averaged over both positions and lacking the expected zig-zig structure.

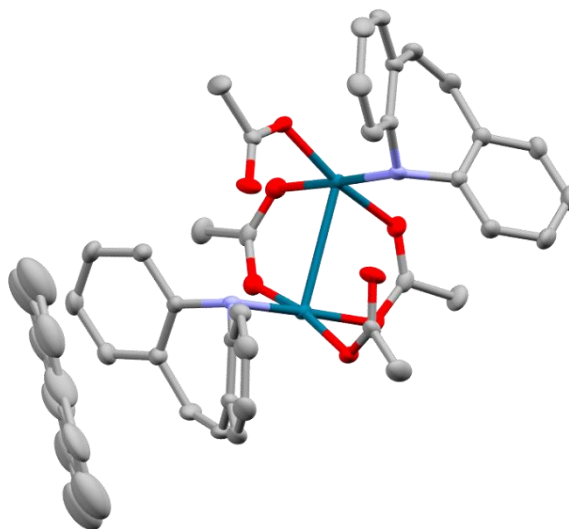
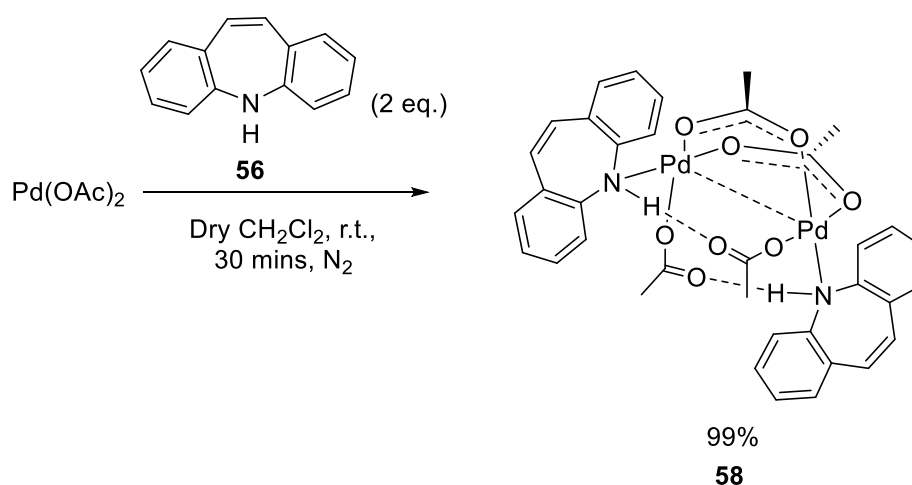


**Figure 32 Structure of 58, determined by X-ray diffraction, rotated to show molecule of pentane in hydrophobic solvent pocket. Hydrogen atoms have been removed for clarity. Thermal ellipsoids shown with a probability of 50%. Image created in Mercury.**

In light of NMR spectroscopic experiments on the mechanism and rate of aminolysis (Section 2.4) further optimisation for the synthesis of **58** was possible (Scheme 34). A massively improved yield of 99% was obtained by reduction of the amine equivalents from 2 *per* Pd to only 1 and by changing reaction solvent to dry, distilled dichloromethane. This change in solvent was crucial to allow for an increased reaction time to 30 minutes at room temperature with a diminished risk of product decomposition (as was observed in THF). It also allowed for immediate crude reaction mixture concentration (to *ca.* 33% original volume) before layering with dry pentane for purification by recrystallisation in the freezer (*ca.* -18 °C).



**Scheme 34 Optimised synthesis of 58.**

## 2.4. Mechanism of $Pd_3(OAc)_6$ Aminolysis

Recent work by Bedford *et al.* has shown that  $Pd_3(OAc)_6$  (top left, Figure 33), the major species in high purity palladium acetate,<sup>63-64, 67</sup> undergoes hydro- and alcoholysis as depicted below, in the presence of water and various alcohols respectively.<sup>68</sup>

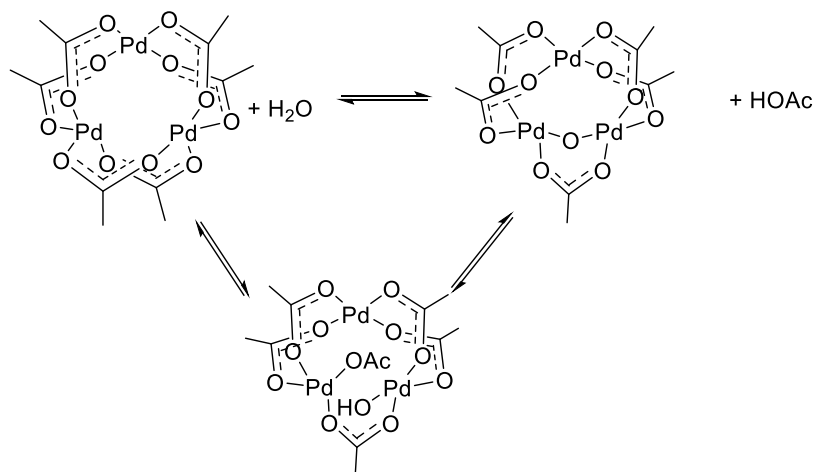


Figure 33 Hydrolysis of  $Pd_3(OAc)_6$ .

These findings not only draw into question the true identity of the active catalyst in countless Pd-catalysed reactions carried out under hydrous conditions or in the presence of an alcoholic solvent, but also may reveal the mechanism by which the  $Pd(OAc)_2(HNR_2)_2$  complexes presented in this chapter may be formed (Figure 34).

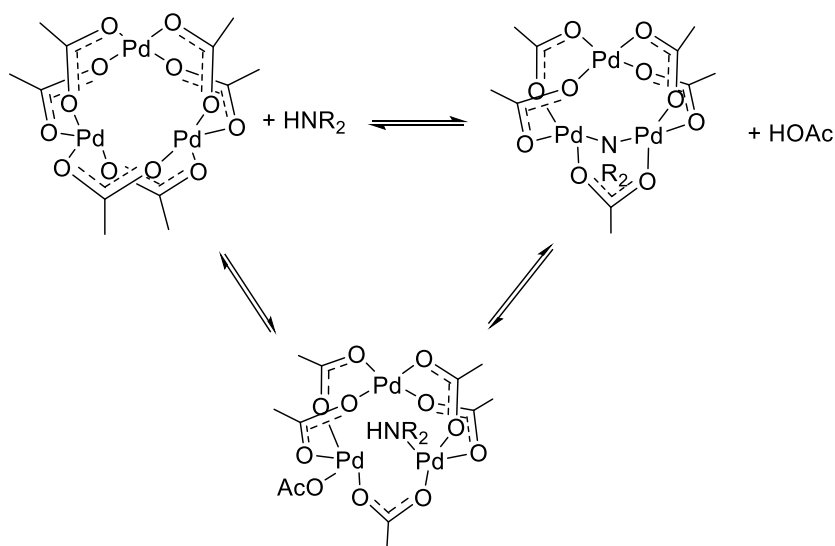
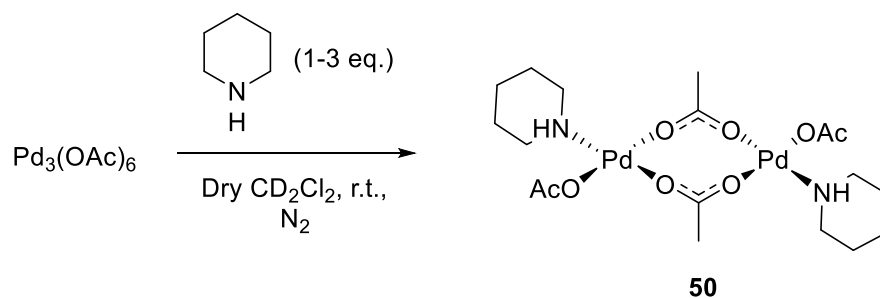
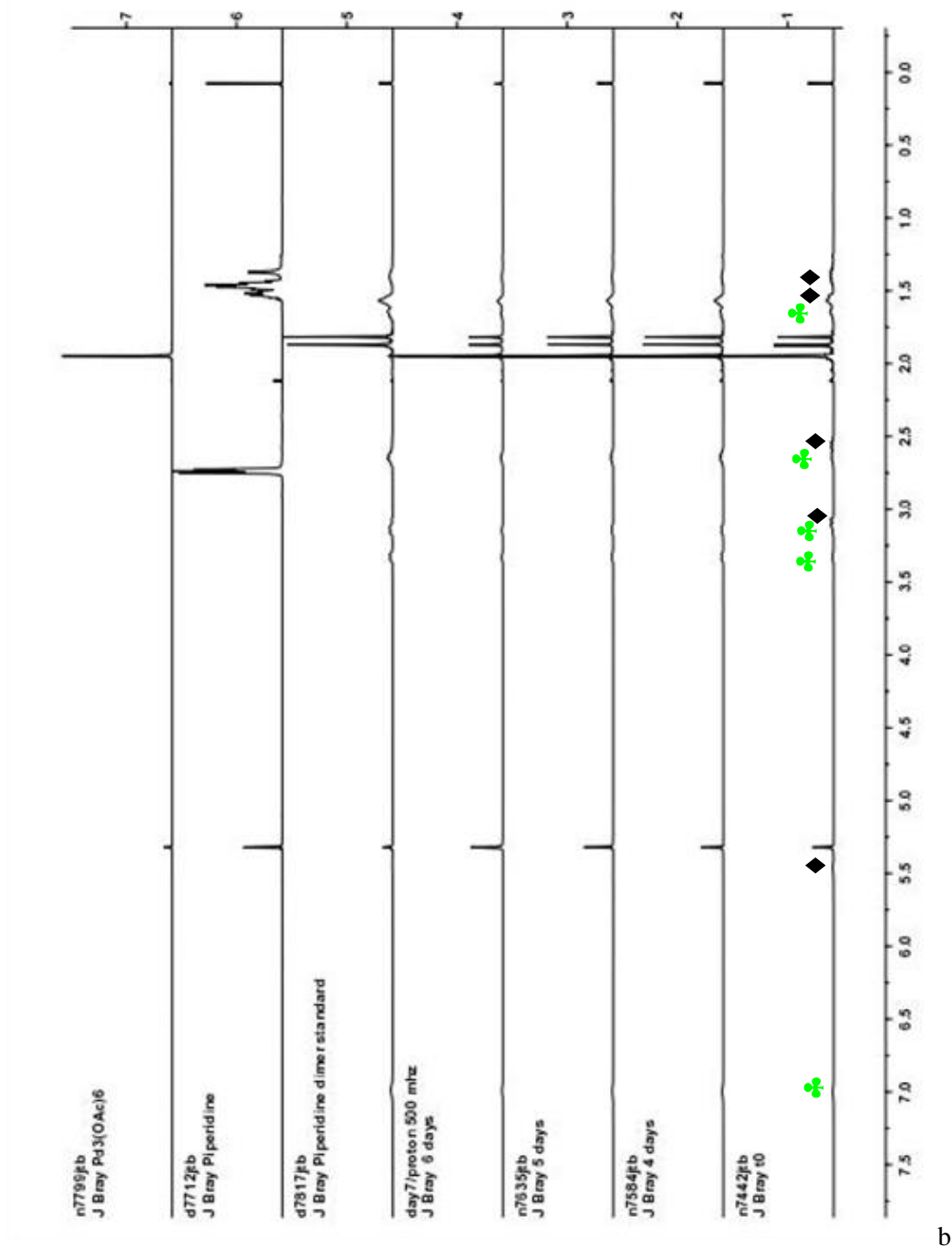


Figure 34 Postulated mechanism of  $Pd_3(OAc)_6$  aminolysis.

In light of this report, a brief study of the aminolysis of  $Pd_3(OAc)_6$  with piperidine was examined by  $^1H$  NMR spectroscopic analysis. Three separate experiments were carried out in a glove box where increasing equivalents of dry, distilled piperidine were added to  $Pd_3(OAc)_6$  in dry, distilled  $CD_2Cl_2$ . A comparative experiment was also carried out in THF- $d_8$ , but this resulted in extensive decomposition of the resultant complexes over a period of 1 hour.



**Scheme 35** Addition of differing equivalences of dry piperidine to  $Pd_3(OAc)_6$  will result in the formation of **50**, potentially *via* an observable aminolysis intermediate.



**Figure 35** Addition of dry piperidine (1 eq.) to  $\text{Pd}_3(\text{OAc})_6$  in  $\text{CD}_2\text{Cl}_2$  converts to **50** via **47**.  
 Reaction conditions: dry piperidine (1 eq.) added to  $\text{Pd}_3(\text{OAc})_6$  in  $\text{CD}_2\text{Cl}_2$  at room temperature. Black diamond: **47**; green club: **50**. 1) Immediately after addition of piperidine; 2) 4 days after addition; 3) 5 days after addition; 4) 6 days after addition; 5)  $^1\text{H}$  NMR spectrum of **50**; 6)  $^1\text{H}$  NMR spectrum of piperidine; 7)  $^1\text{H}$  NMR spectrum of  $\text{Pd}_3(\text{OAc})_6$ .

Upon addition of a single equivalent of piperidine to  $Pd_3(OAc)_6$  ( $\frac{1}{3}$  of an equivalent of piperidine per Pd) the formation of the dimer product **50** begins immediately at room temperature.

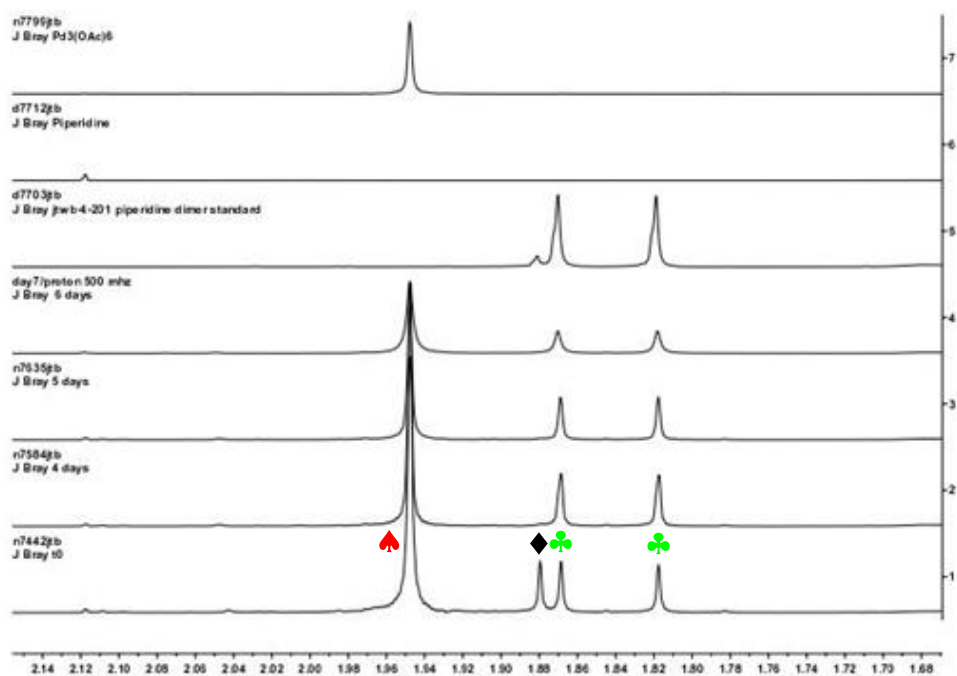
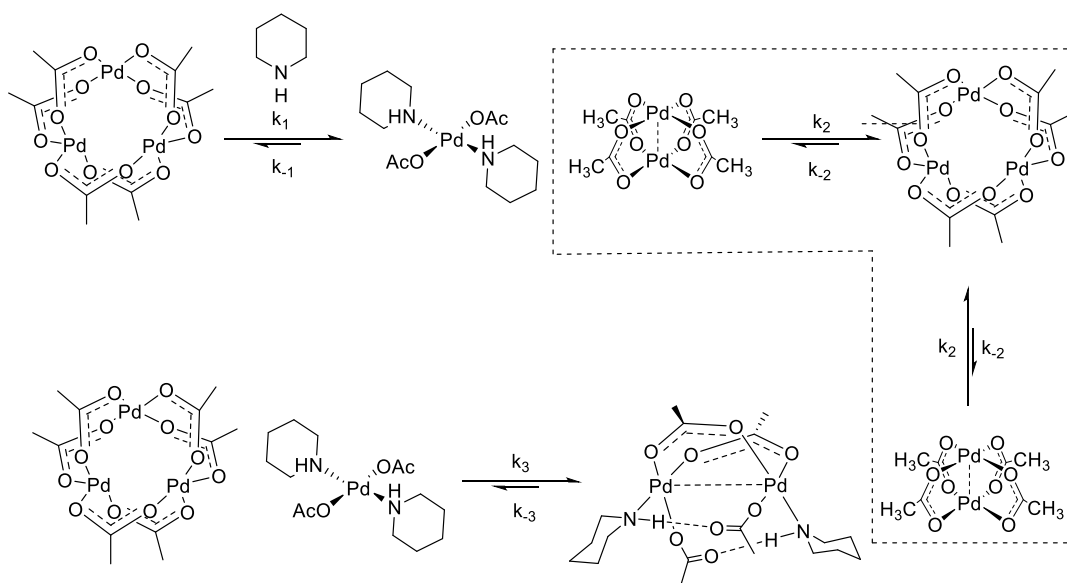


**Figure 36** Zoom of the characteristic acetate section of the spectra in Figure 35 reveals the formation of **47** (black diamond) along with the formation of the desired final product, **50** (green club) from  $Pd_3(OAc)_6$  (red spade) in the presence of piperidine. Reaction conditions: addition of dry piperidine (1 eq.) to  $Pd_3(OAc)_6$  in  $CD_2Cl_2$  at room temperature. 1) Immediately after addition of piperidine; 2) 4 days after addition; 3) 5 days after addition; 4) 6 days after addition; 5)  $^1H$  NMR spectrum of **50**; 6)  $^1H$  NMR spectrum of piperidine; 7)  $^1H$  NMR spectrum of  $Pd_3(OAc)_6$ .

It is important to note, however, that no free piperidine was observed at any point in the reaction, instead the formation of **47** occurs immediately after its addition. This experiment shows that after 4 days, the intermediate monomer complex has been completely converted to **50**. Presumably this occurs *via* aminolysis assisted removal of one molecule of “ $Pd(OAc)_2$ ” from all of the starting  $Pd_3(OAc)_6$  to form **47** and a molecule of  $Pd_2(OAc)_4$ . As is displayed in Scheme 36, the molecule of  $Pd_2(OAc)_4$  is in turn in equilibrium with the marginally more thermodynamically stable  $Pd_3(OAc)_6$ .<sup>76</sup> Presumably, no free piperidine is seen due to the initial high rate of aminolysis to form **47**. **47** is found to react with another molecule of  $Pd_3(OAc)_6$  to form **50** and another molecule of  $Pd_2(OAc)_4$  which, again, rapidly shifts back towards  $Pd_3(OAc)_6$ .



**Scheme 36 Mechanism of aminolysis of  $Pd_3(OAc)_6$  with piperidine to **50**. Where  $k_1 \approx k_2 > k_3 > k_{-1} \approx k_{-2} > k_{-3}$ .**

This complex equilibrium, involving the monomeric Pd complex **47** as the kinetic product clarifies the reason for the poor yields obtained in the synthesis of the dimeric Pd complexes **49** and **50** outlined in section 2.2. These reactions were left for a total of 5 minutes in THF at room temperature prior to removal of the solvent *in vacuo*. In the light of the mechanism detailed in Scheme 36 the formation of the dimeric Pd complexes is slow, so a reaction time as short as 5 minutes resulted in the contamination of the product with remaining  $Pd_3(OAc)_6$  and the monomeric Pd complexes, **47** and **48**.

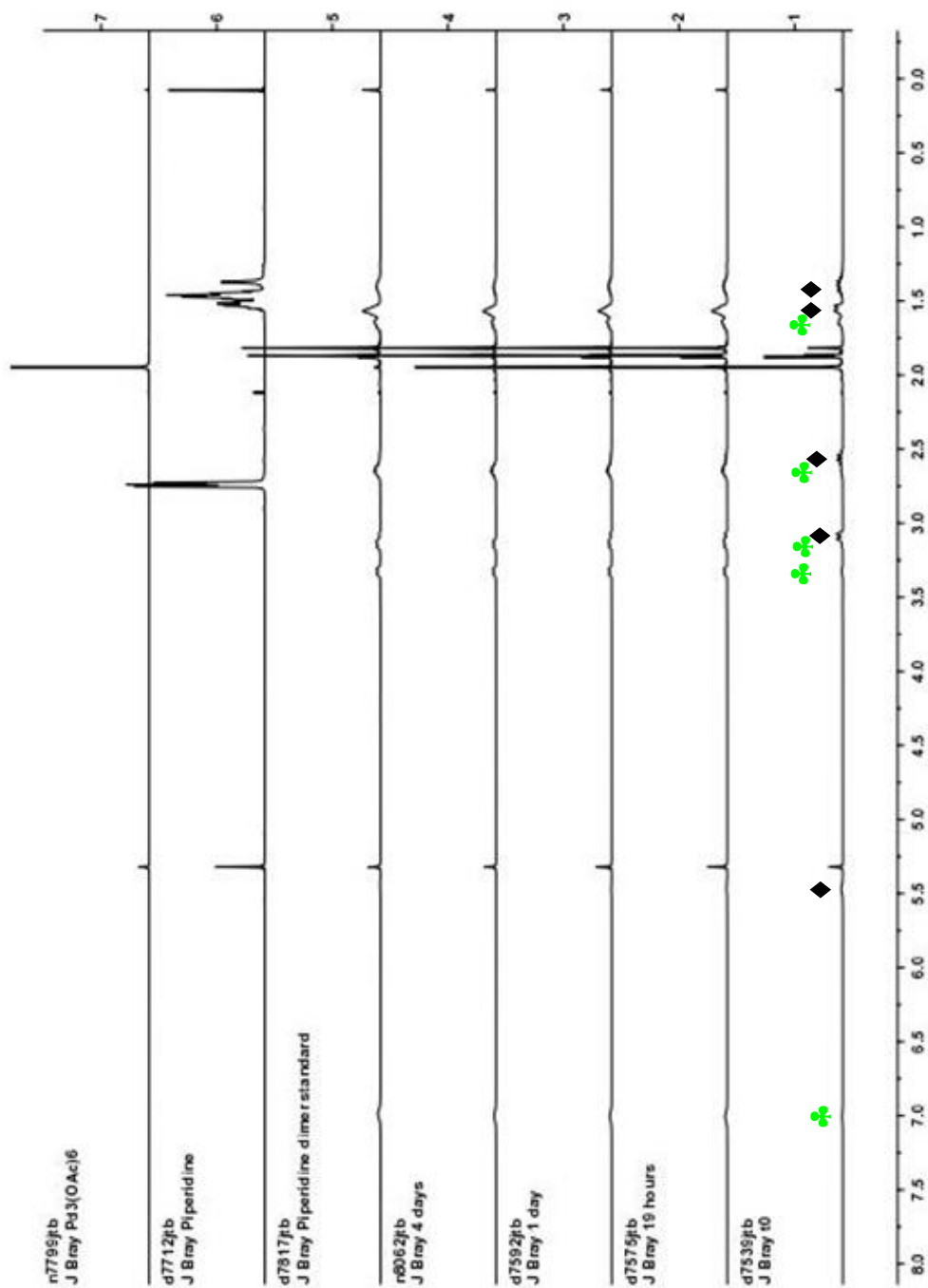


**Figure 37** Addition of dry piperidine (1 eq.) to  $\text{Pd}_3(\text{OAc})_6$  in  $\text{CD}_2\text{Cl}_2$  converts to **50** (green clubs) *via* **47** (black diamonds). Reaction conditions: dry piperidine (1 eq.) added to  $\text{Pd}_3(\text{OAc})_6$  in  $\text{CD}_2\text{Cl}_2$  at room temperature. 1) Immediately after addition of piperidine; 2) 19 hours after addition; 3) 1 day after addition; 4) 4 days after addition; 5)  $^1\text{H}$  NMR spectrum of **50**; 6)  $^1\text{H}$  NMR spectrum of piperidine; 7)  $^1\text{H}$  NMR spectrum of  $\text{Pd}_3(\text{OAc})_6$ .

Repeating the experiment, this time with two equivalents of piperidine ( $\frac{2}{3}$  of an equivalent per Pd) results in a similar outcome, with no free piperidine evident in solution immediately after addition, suggesting a fast initial reaction of the ligand with  $Pd_3(OAc)_6$ . Analysis of the whole reaction spectrum allows the observation of the rapid formation of **47** (denoted by the black diamonds) immediately after piperidine addition. All of the characteristic  $^1H$  NMR signals for **47** decreased over time, resulting in the exclusive formation of **50** (denoted by the green clubs) after 4 days.

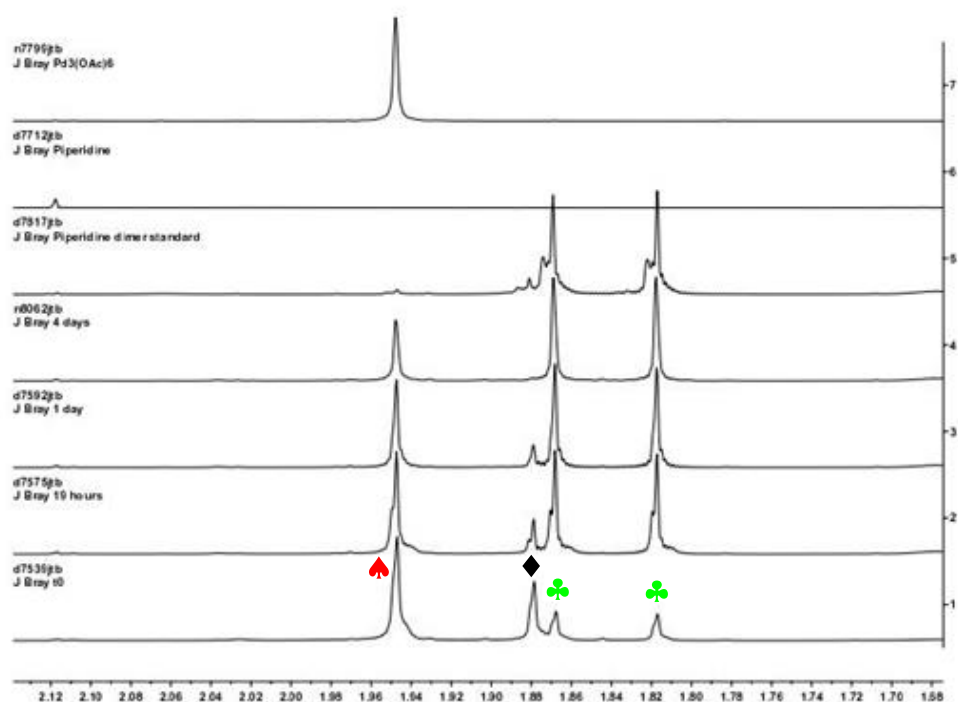


**Figure 38** Zoom of the characteristic acetate section of the spectra in Figure 37 reveals the formation of **47** (black diamond) along with the formation of the desired final product, **50** (green clubs) from  $Pd_3(OAc)_6$  (red spade) in the presence of piperidine. Reaction conditions: Addition of dry piperidine (2 eq.) to  $Pd_3(OAc)_6$  in  $CD_2Cl_2$  at room temperature. 1) Immediately after addition of piperidine; 2) 19 hours after addition; 3) 1 day after addition; 4) 4 days after addition; 5)  $^1H$  NMR spectrum of **50**; 6)  $^1H$  NMR spectrum of piperidine; 7)  $^1H$  NMR spectrum of  $Pd_3(OAc)_6$ .

Over a period of a further 19 hours the concentration of **47** decreases, with a low concentration of **47** still present after 1 day. After a reaction time of 4 days, all of the **47** has been consumed, converting into the final product, **50**. With the addition of 2 equivalents of piperidine, there is still incomplete consumption of  $Pd_3(OAc)_6$ , and at no point during the course of the reaction did a separate acetate peak appear corresponding to a separate  $Pd_2(OAc)_4$  dimer species. This supports the hypothesis that aminolysis occurs initially from the trimer species, and any  $Pd_2(OAc)_4$  formed from that reaction is in equilibrium with the

more stable  $\text{Pd}_3(\text{OAc})_6$ , causing it to convert back to the trimer at a rate which is not observable on the NMR timescale.



**Figure 39** Addition of dry piperidine (1 eq.) to  $\text{Pd}_3(\text{OAc})_6$  in  $\text{CD}_2\text{Cl}_2$  converts to **50** (green clubs) *via* **47** (black diamonds). Reaction conditions: dry piperidine (1 eq.) added to  $\text{Pd}_3(\text{OAc})_6$  in  $\text{CD}_2\text{Cl}_2$  at room temperature. 1) Immediately after addition of piperidine; 2) 3 minutes after addition; 3) 8 minutes after addition; 4) 14 minutes after addition; 5) 18 minutes after addition; 6) 7 hours after addition; 7) 19 hours after addition; 8) 43 hours after addition; 9)  $^1\text{H}$  NMR spectrum of **50**; 10)  $^1\text{H}$  NMR spectrum of piperidine; 11)  $^1\text{H}$  NMR spectrum of  $\text{Pd}_3(\text{OAc})_6$ .

Finally, upon addition of the full three equivalents of piperidine to  $\text{Pd}_3(\text{OAc})_6$  it is clear from Figure 40 that complete conversion of  $\text{Pd}_3(\text{OAc})_6$  to **50** occurs over a period of 43 hours, eventually resulting in the complete conversion of  $\text{Pd}_3(\text{OAc})_6$  to the final product with only a trace of **47**. Considering the  $^1\text{H}$  NMR spectrum at  $T_0$  (Figure 39), one singlet corresponding to the single acetate  $\text{CH}_3$  environment in **47** is present (at 1.88 ppm), four multiplets corresponding to the piperidinyaliphatic protons in **47** at 3.14, 2.54, 1.60 and 1.40 ppm and a broad triplet at 5.5 ppm consistent with a signal resulting from a Pd bound N–H involved in weak hydrogen bonding, as in **47**. As the reaction progresses, the growth of another species, **50**, becomes clearer: two singlets at 1.82 and 1.87 ppm corresponding to the terminal and bridging acetate  $\text{CH}_3$  environments; four broad multiplets corresponding to the piperidinyaliphatic protons at 3.35, 3.20, 2.70 and 1.60; a broad triplet at 7.0 ppm resulting from a Pd bound N–H involved in strong hydrogen bonding.

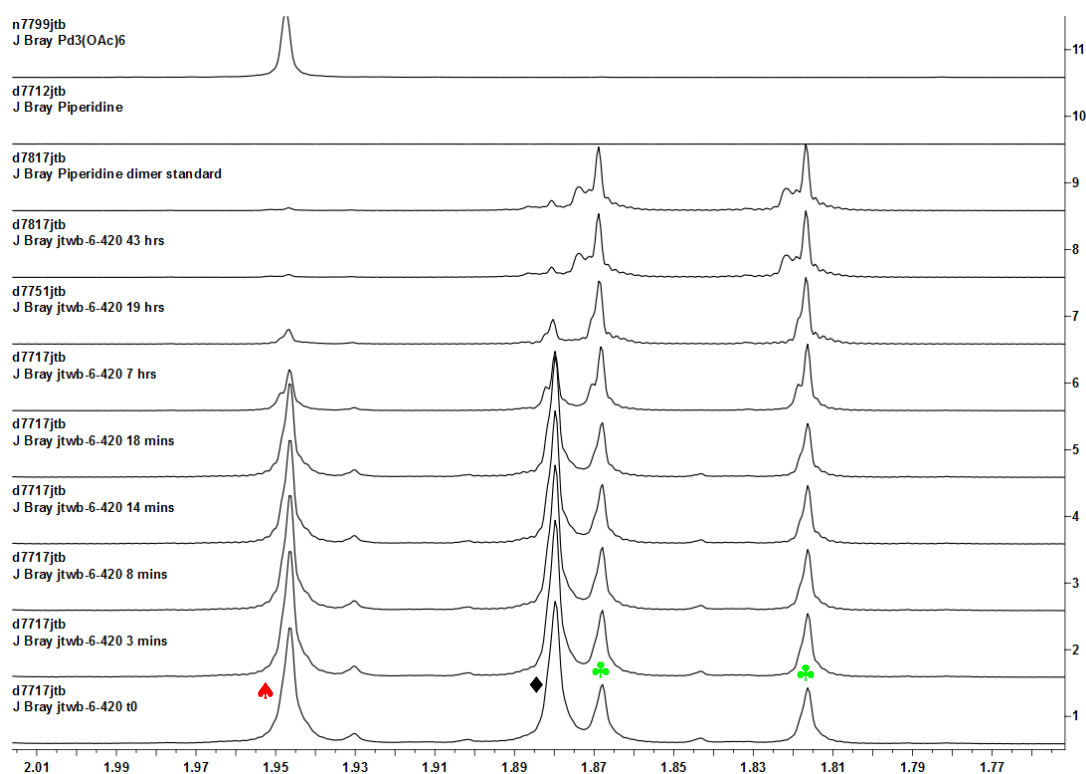


**Figure 40** Zoom of the characteristic acetate section of the spectra in Figure 37 reveals the presence of  $\text{Pd}_3(\text{OAc})_6$  (red spade) **47** (black diamond) along with the formation of the desired final product, **50** (green clubs). Reaction conditions: Addition of dry piperidine (3 eq.) to  $\text{Pd}_3(\text{OAc})_6$  in  $\text{CD}_2\text{Cl}_2$  at room temperature. 1) Immediately after addition of piperidine; 2) 3 minutes after addition; 3) 8 minutes after addition; 4) 14 minutes after addition; 5) 18 minutes after addition; 6) 7 hours after addition; 7) 19 hours after addition; 8) 43 hours after addition; 9)  $^1\text{H}$  NMR spectrum of **50**; 10)  $^1\text{H}$  NMR spectrum of piperidine; 11)  $^1\text{H}$  NMR spectrum of  $\text{Pd}_3(\text{OAc})_6$ .

These experiments build an important and revealing picture about the mechanism of formation of Pd<sub>2</sub>(OAc)<sub>4</sub>(HNR<sub>2</sub>) dimer complexes from Pd<sub>3</sub>(OAc)<sub>6</sub> (Scheme 36). It is apparent that under anhydrous conditions, upon treatment of Pd<sub>3</sub>(OAc)<sub>6</sub> with a cyclic secondary amine (such as piperidine) the kinetic product is the monomeric Pd(OAc)<sub>2</sub>(HNR<sub>2</sub>) species. Only after an extended period of time (up to two days later) does the reaction equilibrate to what is presumably the more thermodynamically stable [Pd(OAc)<sub>2</sub>(HNR<sub>2</sub>)]<sub>2</sub> dimer complex **50**. This results in an overall aminolysis mechanism consistent with that displayed in Scheme 36.

## 2.5. Conclusion

A series of monomeric Pd(OAc)<sub>2</sub>(HNR<sub>2</sub>)<sub>2</sub> and dimeric [Pd(OAc)<sub>2</sub>(HNR<sub>2</sub>)]<sub>2</sub> precatalysts have been synthesised in order for them to be examined in Pd catalysed arylocyanation reactions. Overall the yields of the monomeric Pd(OAc)<sub>2</sub>(HNR<sub>2</sub>)<sub>2</sub> complexes were higher, making them more promising catalysts to be applied to scale-up processes, and the isolated yields of **49** and **50** were unfortunately found to be purification limited. Application of the optimised conditions obtained by studying the addition of stoichiometric piperidine to Pd<sub>3</sub>(OAc)<sub>6</sub> allowed for the synthesis of the dimeric complex **58** in an excellent isolated yield. These stoichiometric studies into the mechanism of Pd<sub>3</sub>(OAc)<sub>6</sub> aminolysis by piperidine have revealed that **47** appears to be the kinetic product. However, when a single equivalent of amine per Pd centre is used, slow equilibration provides the thermodynamic product **50**, resulting from a series of equilibria as displayed in Scheme 36. This explains the low yields of **49** and **50** when short reaction times were used.

The high yielding synthesis of the monomeric Pd(OAc)<sub>2</sub>(HNR<sub>2</sub>)<sub>2</sub> complexes **48**, **47**, **52** and **53** along with **58** has allowed for extensive studies into their efficiencies as precatalysts in the Pd-catalysed (hetero)arylocyanation reaction, as is described in the remaining part of this thesis.

The solid-state structures of the monomeric and dimeric Pd complexes all exhibit acetate–NH intra- or intermolecular hydrogen bonding and further analysis and comparison of the structural and spectroscopic intricacies of **49**, **50** and **58**, shows that changing the amine ligand at Pd has a significant effect on the solid-state structure. Application of this knowledge may aid understanding of the active catalyst formed under reaction conditions and its mechanism of activation.

## Chapter 3: Identification and validation of a benchmark reaction for precatalyst screening in Pd-catalysed arylcyanations

### 3.1. Introduction

In order to screen the efficiency of Pd precatalysts in Pd-catalysed (hetero)arylcyanations a model reaction needed to be identified and validated. When choosing the substrate for investigation it was important for the molecule to be of biological (agrochemical and pharmacological) relevance and be a substrate with IR-active functionality – such as an embedded carbonyl – for study by *operando* IR spectroscopy (see Chapters 4 and 5). *N*-substituted-4-halogenated-6-methyl-2-pyridones and 4-halogenated-6-methyl-2-pyrones were therefore considered to be ideal candidates for initial screening. 2-Pyrones<sup>117</sup> and 2-pyridones<sup>118</sup> are present in a vast array of natural products, so are inherently bioactive. 3-Cyanopyridones also have a rich history of antimicrobial, antiviral<sup>119</sup> analgesic and anti-inflammatory<sup>120</sup> properties, and a number of which are commercially available.<sup>121</sup> Both 2-pyrones and 2-pyridones have been found to be readily compatible with Pd-catalysed cross-coupling<sup>3a, 122</sup> and C–H functionalisation chemistry.<sup>123</sup>

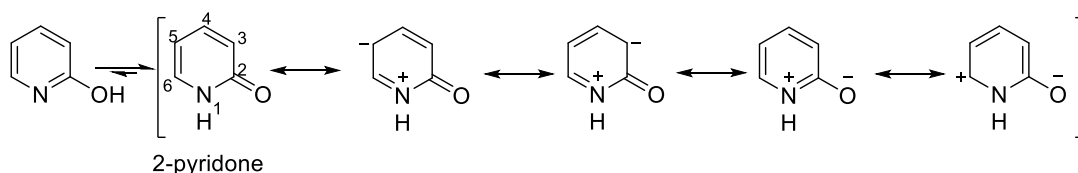


**Figure 41 Tautomers and resonance structures of a 2-pyridone.**

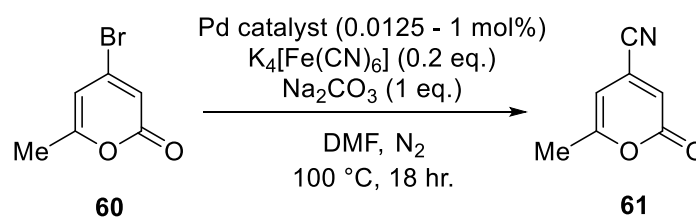
As displayed in Figure 41, positions 3 and 5 are inherently nucleophilic, whereas 4 and 6 are relatively electrophilic. Nucleophilic aromatic substitution is possible at the 4 and 6 positions if they are halogenated,<sup>124</sup> but this requires an adequate nucleophile such as a deprotonated amine. It is worthy of note here that the high stability of  $K_4[Fe(CN)_6]$  owing to the very strong  $\sigma$ -donor character of the  $^-CN$  ligand<sup>125</sup> means that free  $^-CN$  does not form in solution without an activating agent. In Pd-catalysed cyanation the  $^-CN$  is transferred to organic products *via* a transmetallation process from Fe to Pd, followed by reductive elimination.<sup>109</sup> Potassium hexacyanoferrate has been used as a nucleophilic cyanide source in the hydrocyanation of sulfonylimines and enones, but is reacted with benzoyl chloride to form benzoyl cyanide *in situ*.<sup>126</sup> This is further activated *via* nucleophilic attack from a strong nucleophile (*eg.*  $^-OH$  or

-OEt) to form a cyanohydrin – a precursor for the formation of HCN. The evidence for direct cyanation of 2-pyrones is limited in the literature, and there is no evidence of cyanopyrone synthesis *via* Pd-catalysis. Instead the use of the Rosenmund-von Braund reaction is prevalent for the installation of nitrile functionality in both pyrones<sup>127</sup> and pyridones.<sup>128</sup>

### 3.2. Attempted Cyanation of 4-Bromo-6-methyl-2-pyrone

PdNP precursors have been shown to act as effective catalysts in Pd-catalysed cyanation reactions, and may play a key part in the design of more efficient catalysts in these reactions.<sup>43</sup> In order to investigate the role of PdNPs in Pd-catalysed cyanation reactions, 4-bromo-6-methyl-2-pyrone (**60**) was initially chosen as a substrate for a benchmark reaction using the conditions developed by Beller *et al.*<sup>102a</sup>

An initial catalyst screen was carried out in the benchmark cyanation reaction shown in Scheme 37. The catalysts were chosen for being known PdNP precursors or presynthesised PdNPs. Complex **47**, *trans*-bromo(*N*-succinimidyl)bis(triphenylphosphine)palladium(II) (**59**),<sup>129</sup> Pd(OAc)<sub>2</sub> and presynthesised DMF stabilised PdNPs were all implemented in the reaction outlined in Scheme 37 at a range of catalyst loadings.<sup>5,110,130,19a</sup>



Scheme 37 Beller's conditions, used in the attempted Pd-catalysed cyanation of 4-Bromo-6-methyl-2-pyrone (**60**).

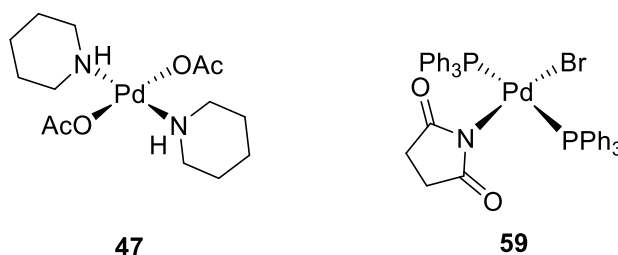


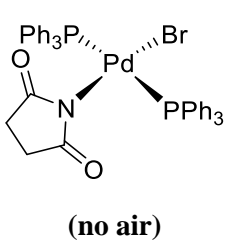
Figure 42 Left: *Bis-trans*-[piperidiny-κ-NH]Palladium(II) diacetate, Right: *trans*-bromo(*N*-succinimidyl)bis(triphenylphosphine)palladium(II).

**Table 1. Attempted optimisation of Pd-catalysed cyanation of 4-Bromo-6-methyl-2-pyrone (60).**

Cat. Loading (mol%)	Conversion <sup>b</sup> / %					
	62	63	62	63	62	63
0.0125	29	0	12	0	30	0
0.025	17	0	52	0	69	0
0.1	9	0	8	0	-	-
1	25	33	29	71	-	-

<sup>a</sup>Stopper removed for 5 seconds with no nitrogen flow with vigorous stirring, <sup>b</sup>Determined by <sup>1</sup>H NMR spectroscopy as a ratio of the signals 6.19 ppm (**60**) 6.32 ppm (**63**) and 6.23 ppm (**62**).

Table 2 Attempted optimisation of Pd-catalysed cyanation of 4-Bromo-6-methyl-2-pyrone (**60**).

	 <p>(no air)</p>	DMF NPs <sup>a</sup>			
Cat. Loading (mol%)	Conversion <sup>b</sup> / %				
	<b>62</b>	<b>63</b>	<b>62</b>	<b>63</b>	
0.0125	11	0	10	0	
0.025	7	0	9	0	
0.1	-	-	4	0	
1	20	0	3	5	

<sup>a</sup>Synthesised under air, <sup>b</sup>Determined by <sup>1</sup>H NMR spectroscopy as a ratio of the signals 6.19 ppm (**60**) 6.32 ppm (**63**) and 6.23 ppm (**62**).

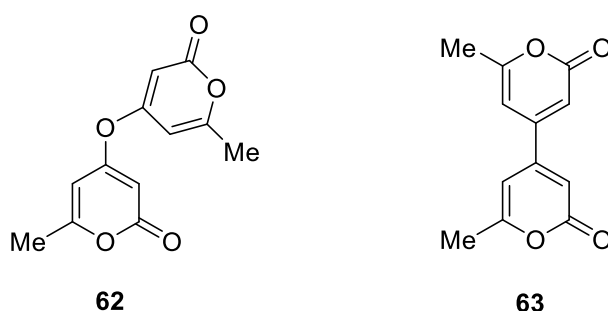
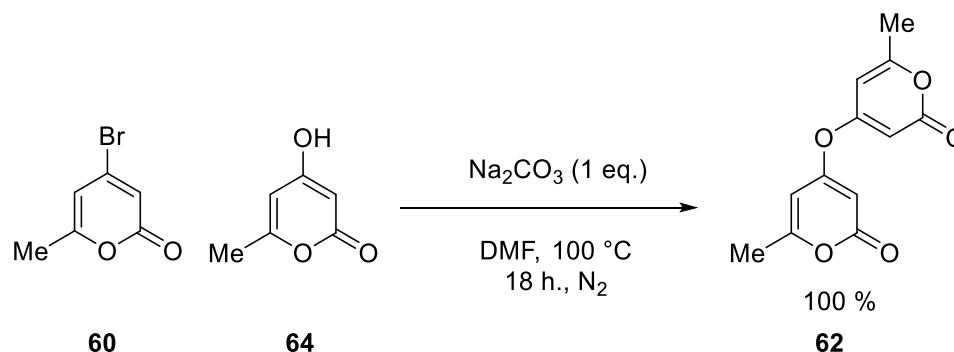


Figure 43. Actual products formed in attempted Pd-catalysed cyanation of 4-bromo-6-methyl-2-pyrone (**60**).

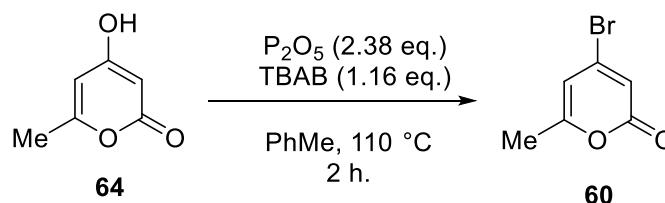
Upon attempting to synthesise 4-cyano-6-methyl-2-pyrone (**61**), it was found that instead the products formed were the homocoupling of **60** to give **63**, and the formation of the dipyronyl ether **62**. **62** can also be formed (following subsequent control experiments) from **60** and **64**

in the presence of 1 equivalent of  $\text{Na}_2\text{CO}_3$  in DMF in quantitative yield. Its synthesis has also been reported as a side product from the synthesis of 4-triflato-6-methyl-2-pyrone under similar reaction conditions.<sup>122b</sup>



Scheme 38 Synthesis of dipyronylether, **62**.

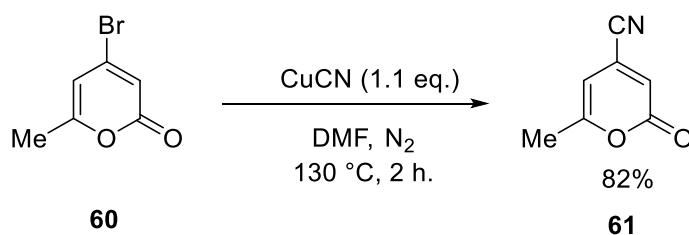
The formation of **62** either appears to be caused by trace amounts of **64** left over from the synthesis of **60** (Scheme 39) or by the hydrolysis of **60** under the reaction conditions.



Scheme 39 Bromination of 4-hydroxy-6-methyl-2-pyrone.<sup>131</sup>

The formation of the homocoupled product (**63**) proves that neither oxidative addition of Pd into the C—Br bond or reductive elimination are issues, thus suggesting that  $\text{K}_4[\text{Fe}(\text{CN})_6]$  was not a fast enough transmetallating agent to allow cyanation at the 4-position of the electron deficient 2-pyrone ring. This is most likely due to both the cyanide source's insolubility in the reaction solvent, resulting in a low concentration of  $\text{CN}^-$ , and the electron deficiency of the 2-pyrone. This is also consistent with literature reports of preferential dehalogenation of 3-bromo-2-pyrones under Pd-catalysis conditions.<sup>128</sup> This indicates that **60** is not a suitable for use as a model substrate, as the utilisation of  $\text{K}_4[\text{Fe}(\text{CN})_6]$  is key to achieving low Pd catalyst loadings.<sup>93-94</sup>

A Rosenmund-von Braun reaction was used to synthesise an analytical standard of 4-cyano-6-methyl-2-pyrone (**61**) in an 82% yield (Scheme 40).<sup>132,127</sup>



Scheme 40 Synthesis of 4-cyano-6-methyl-2-pyrone (**61**) via Rosenmund-von Braun reaction.

### 3.3. Cyanation of *N*-benzyl-4-bromo-6-methylpyrid-2-one.

Given the lack of success using **60** as a model substrate, it was necessary to carefully identify a different benchmark aryl halide substrate that would: (a) be suitably challenging (containing sensitive amide functionality); (b) provide a spectroscopic handle to monitor consumption by *in operando* real-time analysis (See Chapters 4 and 5); (c) be electron-deficient, providing a stern test for reductive elimination.<sup>109</sup> We also had in mind a chemical structure similar to interesting commercial targets such as olprinone and milrinone – 2-pyridinones possessing a Csp<sup>2</sup> nitrile substituent.<sup>73, 78, 121</sup>

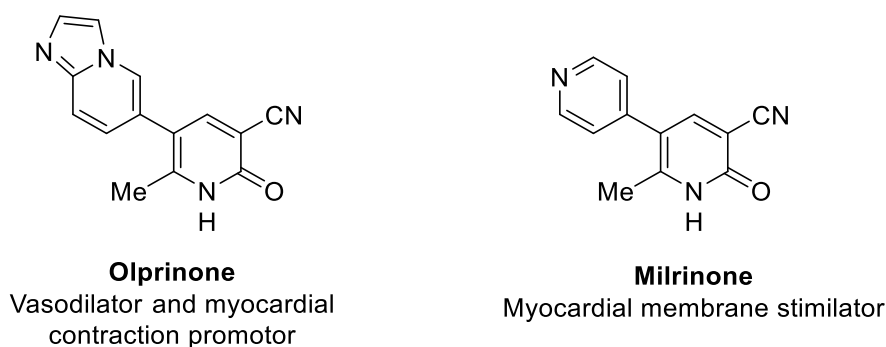


Figure 44 Nitrile-substituted 2-pyridinones are important chemical motifs within the fine chemical industry.

Following initial reaction screening (see Table 4), *N*-benzyl-4-bromo-6-methyl-2-pyridinone (**65**) was selected as a suitable substrate for further study.

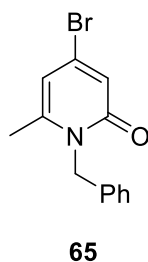
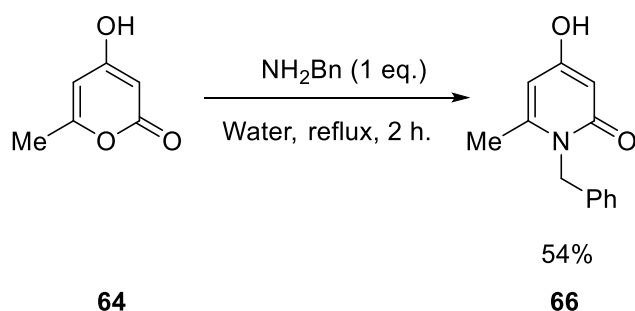


Figure 45 *N*-benzyl-4-bromo-6-methylpyrid-2-one (**65**).

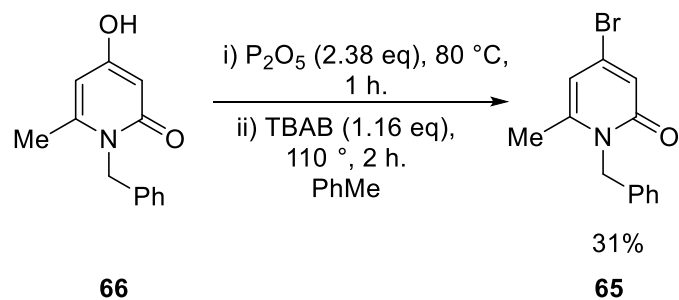
### 3.2.1. Synthesis of *N*-benzyl-4-bromo-6-methylpyrid-2-one

*N*-benzyl-4-hydroxy-6-methylpyrid-2-one (**66**) may be synthesised *via* a simple substitution reaction, by heating 4-hydroxy-6-methyl-2-pyrone (**64**) in water at reflux with benzylamine for two hours. This afforded the desired compound (**66**) in an adequate yield of 54% (Scheme 41).



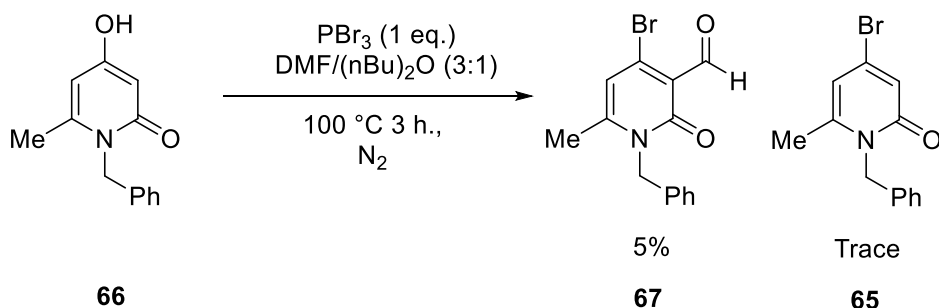
Scheme 41 Synthesis of *N*-benzyl-4-hydroxy-6-methylpyrid-2-one, **66**.

In the bromination of compound **66**, it was found that direct addition of both  $P_2O_5$  and TBAB (tetrabutyl ammonium bromide) to the 4-hydroxypyridone (**66**) under standard conditions (*i.e.* at the same time) afforded the desired compound **65** in a meagre yield of only 14%. However, pre-treatment of the hydroxyl compound with  $P_2O_5$  for 1 hour at 80 °C, followed by addition of TBAB and heating to reflux for a further two hours provided an improved, but still quite poor yield of 31% (Scheme 42).



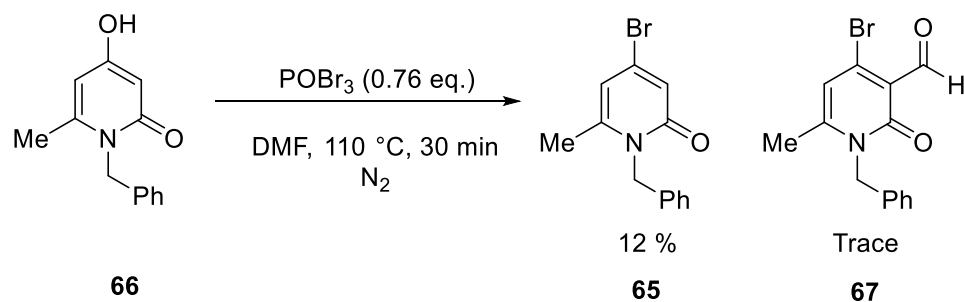
**Scheme 42** The improved synthesis of *N*-benzyl-4-bromo-6-methylpyrid-2-one, **65**.

Various routes towards compound **65** were attempted in order to obtain a higher yielding synthesis, however the best still proved to be an adaptation of the original, *vide infra*. Upon treating **66** with PBr<sub>3</sub> in DMF, the reaction mixture formed a thick orange mixture, which could only be mixed using a mechanical stirrer. It was found that the diagnostic signal for the proton at the 3-position (<sup>1</sup>H NMR) disappeared and was replaced by a signal in the aldehyde region, so instead of carrying out the straightforward bromodehydroxylation reaction, the major product formed was *N*-benzyl-3-formyl-4-bromo-6-methylpyrid-2-one (**67**) by a tandem bromination Vilsmeier-Haack formylation.<sup>133</sup>



**Scheme 43** Treatment of **66** with PBr<sub>3</sub> in DMF afforded the 3-formylated derivative **67**.

It was also found that treating **66** with POBr<sub>3</sub> provided the desired product **65** but in an unsatisfactory 12% yield along with trace of the undesired formylated side product, **67** (Scheme 44).<sup>134</sup>



**Scheme 44 Treatment of 66 with POBr<sub>3</sub>.**

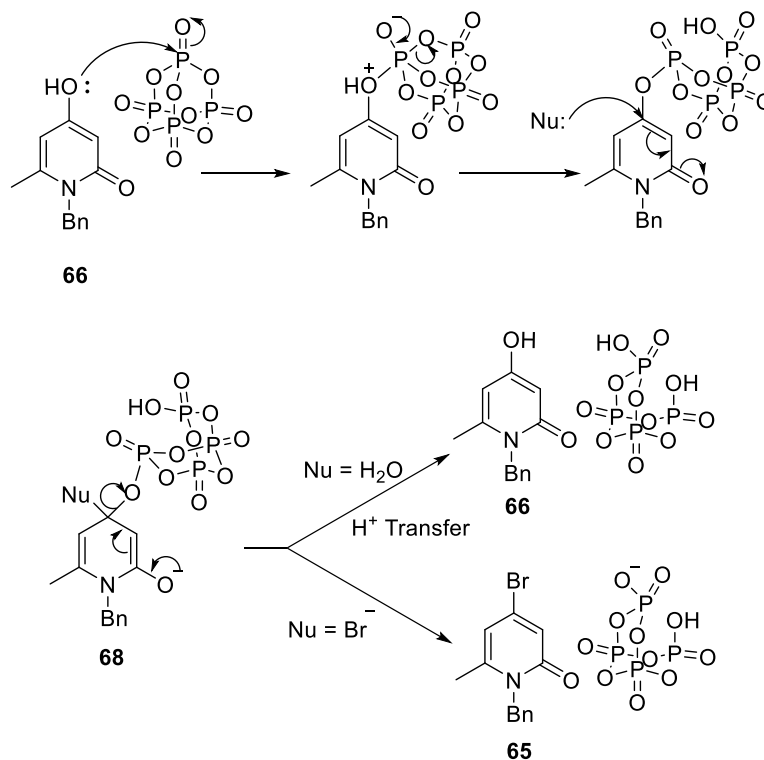
Finally, given the lack of success of other synthetic routes to **65** a small solvent and condition screen was carried out in order to optimise its synthesis *via* P<sub>2</sub>O<sub>5</sub> assisted bromodehydroxylation.

**Table 3 Optimisation of the synthesis of 65.**

Entry	Solvent	Temp (°C)	Time (h.)	Yield (%) <sup>a</sup>
1	Toluene	110	2	27 <sup>b</sup>
2	Dry toluene <sup>c</sup>	110	2	39 <sup>d</sup>
3	Toluene	110	20	12
4	Toluene	80	24	15
5	<i>p</i> -xylene	140	2	21
6	1,2-dichlorobenzene	180	2	8

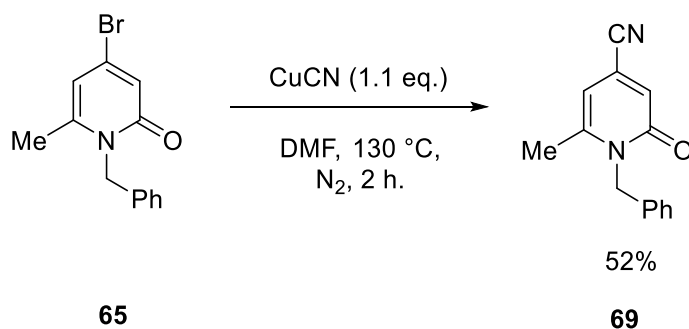
<sup>a</sup> Yield of isolated compound; <sup>b</sup> Average of 4 runs; <sup>c</sup> Reaction conducted under a flow of nitrogen; <sup>d</sup> Average of 7 runs ranging from 37% to 44% yield.

It is evident that from the examples provided, that neither temperature nor extending the reaction time beyond 2 hours in toluene have any significant positive effect on the yield (entries 1,3 and 4). Changing the solvent to high boiling 1,2-dichlorobenzene (as used by Kato *et al.*)<sup>131</sup> and heating to 180 °C (entry 6) led to complications during work up (emulsion formation) and isolation issues. Changing to the more practical *p*-xylene (entry 5) showed that with no isolation issues, after 2 hours of reaction at an increased temperature (140 °C) the reaction yield was still unimproved. However, conducting the experiment under dry, oxygen free conditions improved the yield to a more acceptable, and repeatable, 39% (entry 2). This was hypothesised to be due to the instability of the P<sub>4</sub>O<sub>10</sub>-alcohol adduct (**68**) towards nucleophilic addition reaction with water, as shown in Scheme 45.



**Scheme 45 Hypothesised mechanism for P<sub>4</sub>O<sub>10</sub> deactivation in the presence of water.**

A Rosenmund-von Braun reaction was used to synthesise an analytical standard of *N*-benzyl-4-cyano-6-methylpyridin-2-one (**69**) in a 52% yield (Scheme 46).<sup>132,127</sup>



**Scheme 46 Synthesis of *N*-benzyl-4-cyano-6-methylpyridin-2-one using Rosenmund-von Braun conditions.**

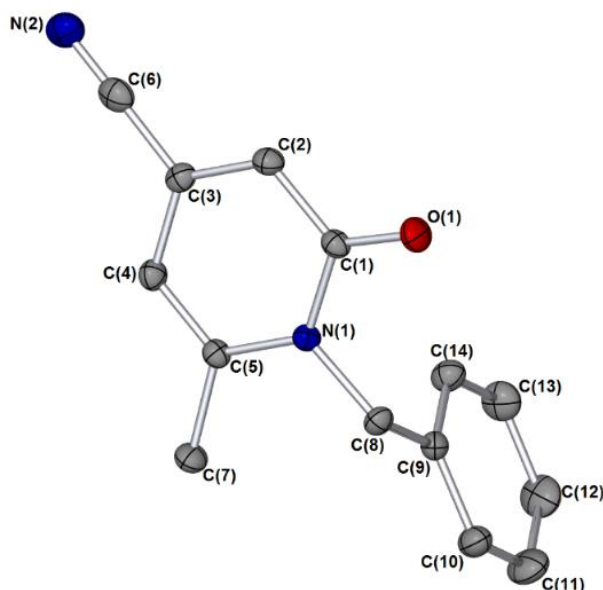
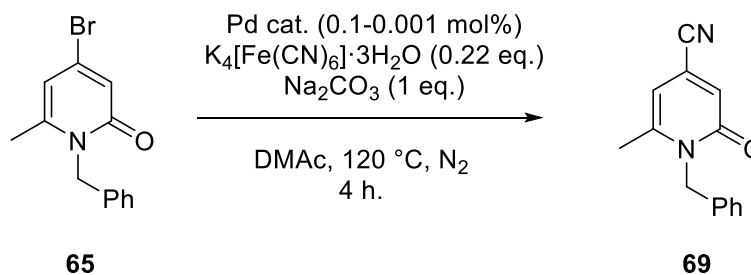


**Figure 46** The structure of *N*-benzyl-4-cyano-6-methylpyrid-2-one (**69**) as determined by X-ray diffraction; arbitrary numbering used. Hydrogen atoms removed for clarity. Thermal ellipsoids shown with a probability of 50%; numbers in parentheses are standard deviations from the measured value, denoting the error in the measurements. Selected bond lengths (Å): C(3)-C(6):1.431(3), C(6)-N(2): 1.150(3), C(1)-O(1): 1.2379(16), C(1)-N(1):1.4052(16), C(5)-N(1): 1.3811(16), C(8)-N(1):1.4717(17).

### 3.2.2. Investigating the effect of catalyst solution aging on reaction efficiency

Given the degradation issues associated with DMF (dimethylformamide) to give trace dimethylamine and CO<sup>135</sup> which could directly influence catalysis, the more stable DMAc (dimethylacetamide) solvent was selected for all subsequent studies with reactions run between 120-140 °C. *N*-Benzyl-4-bromo-6-methylpyrid-2-one (**65**) has proven to be a suitable substrate for this benchmark reaction. As the product of the cyanation reaction, **69** is easily isolated, contains IR-active amide functionality and the reaction rate is fast enough to provide adequate conversion after only 4 hours (42% with 0.1 mol% Pd(OAc)<sub>2</sub>). Some Pd-catalysed cyanation reactions on simple substituted bromoarenes with high catalyst loadings can require up to 20 hours to reach complete conversion.<sup>43, 102b</sup>



**Scheme 47** The benchmark reaction chosen for the initial screening of Pd precatalysts.

Initially four Pd catalyst solutions with different additives and aging were examined in the benchmark reaction. These catalyst solutions are shown in Table 4. Three of them (b, c, d) were aged for 16 h at 80 °C to promote the *in situ* formation of PdNPs.

**Table 4** The four different catalyst solutions screened in the benchmark reaction.

Catalysts			
<b>a</b>	<b>b</b>	<b>c</b>	<b>d</b>
Pd(OAc) <sub>2</sub> added as a fresh solution (2 mg ml <sup>-1</sup> ) in dry DMAc.	Pd(OAc) <sub>2</sub> heated at 80 °C in dry DMAc under N <sub>2</sub> for 16 hr. (1 mmol dm <sup>-3</sup> )	Pd(OAc) <sub>2</sub> , with wet piperidine (2 eq.) heated at 80 °C in dry DMAc under N <sub>2</sub> for 16 hr. (1 mmol dm <sup>-3</sup> )	Pd(OAc) <sub>2</sub> , with dry piperidine (2 eq. ) heated at 80 °C in dry DMAc under N <sub>2</sub> for 16 hr. (1 mmol dm <sup>-3</sup> )

The cyanation of **65** was carried out with each of **a**, **b**, **c** and **d** as catalysts over four different loadings, the results of which are shown in

Table 5 .

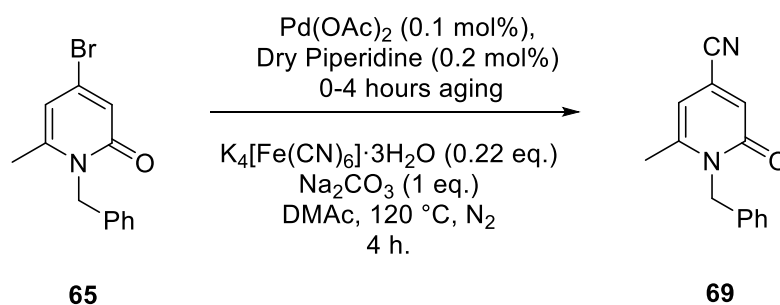
**Table 5 Product conversions from the benchmark reaction using the four catalyst solutions outlined in Table 4.**

Catalyst loading (mol%)	Conversions /% <sup>a</sup>			
	a	b	c	d
0.1	41	0	48	22
0.05	6	0	44	19
0.01	0	0	0	0
0.001	0	0	0	0

Reaction conditions: Catalyst (0.1-0.001 mol%),  $K_4[Fe(CN)_6] \cdot 3H_2O$  (0.22 eq.),  $Na_2CO_3$  (1 eq.), DMAc,  $N_2$ , 120 °C, 4 h.. <sup>a</sup>Determined by  $^1H$  NMR spectroscopy as a ratio between the signals at 6.80 ppm (**65**) and 6.85 ppm (**69**).

From these initial tests of catalytic activity piperidine appears to provide an improvement to the catalytic activity. Catalyst **c** provides a higher TON at 0.05 mol% than fresh  $Pd(OAc)_2$ , and provides only a small drop in conversion from 0.1 mol% to 0.05 mol%. Although catalyst **d** provided a poorer conversion at 0.1 mol% (22 %) than  $Pd(OAc)_2$ , again the addition of piperidine appears to stop the dramatic drop in conversion from 0.1 – 0.05 mol% observed with  $Pd(OAc)_2$ . Heating  $Pd(OAc)_2$  to 80 °C for 16 hours under  $N_2$  with no amine added (similar to the preparation of DMF stabilised nanoparticles reported by Obora *et al.*<sup>19a</sup>) formed Pd black and thus rendered it ineffective as a catalyst in the cyanation reaction.

Initially, an aging time of 16 hours was chosen based on previous aging experiments on **47** in DMF, however in order to assess the age at which the PdNPs formed are most active an aging experiment was required (Figure 47). A solution of  $Pd(OAc)_2$  (1 eq.) and piperidine (2 eq.) was heated to 80 °C, and aliquots were taken to be tested in the benchmark reaction (Scheme 48) at set intervals.



Scheme 48 Aliquots of the catalyst solution were taken at set intervals and used in the benchmark reaction.

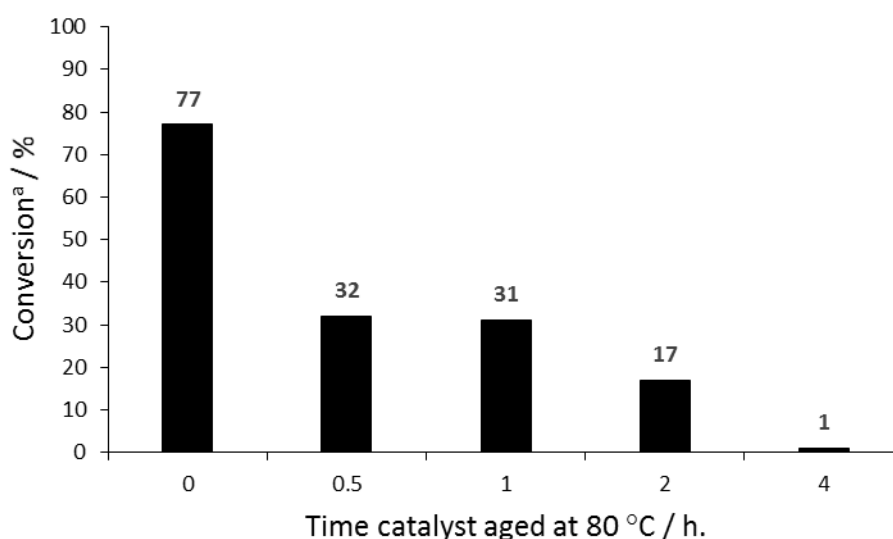


Figure 47 The effect of aging Pd(OAc)<sub>2</sub> (1 eq.) and piperidine (2 eq.) in DMAc at 80 °C upon the efficiency of the cyanation of 65. <sup>a</sup>Determined by <sup>1</sup>H NMR spectroscopy as a ratio between the signals at 6.80 ppm (65) and 6.85 ppm (69).

It is evident from these results that the point at which the Pd catalyst solution is most active (at 0.1 mol%) is immediately after addition of piperidine to the Pd(OAc)<sub>2</sub> in DMAc. The decrease in activity over 4 hours from 77-0% conversion shows that catalyst aging is unnecessary. This indicates that the catalyst species formed upon direct addition of the catalyst to the reaction, followed by heating to 120 °C (reaction mixture) is more active than that formed after prolonged heating at 80 °C. Presumably this is due to agglomeration of Pd to large, catalytically inactive aggregates, which is in keeping with many other studies.<sup>7</sup>

### 3.2.3. Cyanation of N-benzyl-4-bromo-6-methylpyrid-2-one using preformed Pd(OAc)<sub>2</sub>(HNR<sub>2</sub>)<sub>2</sub> complexes as catalysts.

A series of cyclic amine complexes have been synthesised (as discussed in Chapter 2), and screened as potential catalysts in the benchmark bromopyridone cyanation reaction. Due to their higher yielding and more reliable synthesis, it was decided that only the Pd monomers (Figure 48) were chosen as suitable catalysts. They were each screened in comparison with Pd(OAc)<sub>2</sub> and the *in situ* equivalent of **47**, which involves mixing Pd(OAc)<sub>2</sub> (1 eq.) and piperidine (2 eq.) in DMAc. The results of this screen are shown in

Table 6. Each catalyst, including Pd(OAc)<sub>2</sub> proved to be competent in the reaction at a loading of 0.1 mol%. A sharp cut off in catalytic activity occurred for **48** and **52** below 0.1 mol%, whereas **47** and **70** show medium activity at 0.05 mol%, providing conversions of 26% and 44% respectively. It is promising, however, to note that all of the Pd amine complexes show an increased activity over Pd(OAc)<sub>2</sub>. Under these reaction conditions and with this substrate, Pd(OAc)<sub>2</sub> does not act as an efficient catalyst below 0.1 mol% catalyst loading.

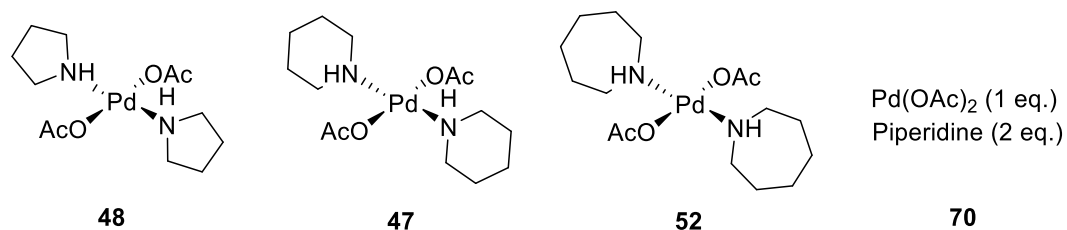
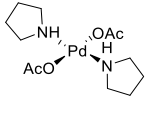
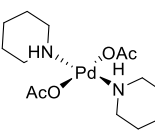
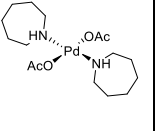


Figure 48 Four Pd precatalysts were screened in the benchmark cyanation reaction, **65** → **69**.

**Table 6** Conversions of the benchmark reaction 65 → 69 using the three monomeric, preformed Pd(OAc)<sub>2</sub>(HNR)<sub>2</sub> precatalysts after four hours reaction time, compared with *in situ* catalyst, 70, and Pd(OAc)<sub>2</sub>.

		Conversions <sup>a</sup> / %				
Cat. loading (mol %)	Pd conc. (ppm) <sup>b</sup>				Pd(OAc) <sub>2</sub> (1 eq.) Piperidine (2 eq.)	Pd(OAc) <sub>2</sub>
0.1	33.5	51	78 <sup>c</sup>	88	77	41
0.05	14.2	0	26 <sup>c</sup>	0 <sup>c</sup>	44	6
0.01	3.2	0	0 <sup>c</sup>	0	0 <sup>c</sup>	0
0.005	1.60	0	0	0	0	-
0.001	0.33	0	0	0	-	-

Reaction conditions: Catalyst solution (0.1-0.001 mol%), K<sub>4</sub>[Fe(CN)<sub>6</sub>]·3H<sub>2</sub>O (0.22 eq.), Na<sub>2</sub>CO<sub>3</sub> (1 eq.), DMAc, N<sub>2</sub>, 120 °C; <sup>a</sup> Determined by <sup>1</sup>H NMR spectroscopy; <sup>b</sup> Calculated as mol. ppm, with respect to solvent; <sup>c</sup> Average of two runs.

Recent publications by the Fairlamb group indicate that Pd catalyst concentration in C–H functionalisation reactions plays a key role in the formation of catalytically competent PdNPs. It was noted that almost every reaction outlined required a fairly high Pd concentration of 700 ppm, and led to PdNPs ranging from 2-7 nm in size.<sup>116</sup> It is clear that in the reactions detailed above the working concentration is substantially lower (a factor of 20). If PdNPs are indeed involved in this reaction mechanism, as later kinetic results suggest (see Chapter 4), understanding and exploiting the Pd concentration in cross-couplings will be critical in order to form a highly active catalyst system, with the ability to achieve high turnover numbers. It is also important to acknowledge that with such low Pd concentrations, with respect to those present in C–H functionalisations, under working reaction conditions any catalytically competent Pd cluster species will not exist beyond a single closed shell of Pd atoms (*i.e.* up to 13 atoms in an icosahedral cluster at lowest surface energy).<sup>136</sup> With this in mind, an optimisation of the reaction to lower catalyst loadings while maintaining a constant concentration of Pd was carried out (Table 7). According to these initial catalyst screens, the most promising catalyst at 0.1 mol% loading (33.5 ppm Pd) has been shown to be Pd(OAc)<sub>2</sub>(HNC<sub>6</sub>H<sub>12</sub>)<sub>2</sub> (**52**), providing a yield of 88% after only 4 hours. In an attempt to achieve efficient catalyst turn over at even lower loadings the benchmark reaction was carried out using **52** and the substrate/catalyst ratio decreased while maintaining a constant Pd concentration of 33.5 ppm. Normally, the precatalyst would be added as a stock solution of

a known concentration, separate from the rest of the reaction solvent. In order to ensure an accurate, and constant Pd concentration throughout all of the catalyst loadings screened (0.1-0.01 mol%), the entire reaction solvent was made up as a catalyst solution of 33.5 ppm Pd before its addition to the remaining reagents. At these low catalyst loadings, this is also desirable in order to improve the error involved with weighing out small amounts of catalyst. A larger quantity of catalyst stock solution and, critically, a higher reaction scale has therefore been employed in these reactions.

**Table 7 Maintaining the optimal Pd concentration of 33.5 ppm while using 52 as a catalyst in the arylocyanation of 65 allowed for improved catalytic activity.**

Scale (mg)	Substrate Conc. (M)	Cat. loading (mol%)	Yield (%) <sup>a</sup>	Conversion (%) <sup>b</sup>	Reaction Time (hr.)	TON	TOF (s <sup>-1</sup> )
500	0.36	0.1	33	41	4	330	0.023
250	0.36	0.1	38	50	4	380	0.024
500	1.2	0.025	60	64	20	2405	0.033
500	3.6	0.01	15	16	88	1500	0.005

Reaction conditions: Catalyst solution (0.1-0.01 mol%), K<sub>4</sub>[Fe(CN)<sub>6</sub>]·3H<sub>2</sub>O (0.22 eq.), Na<sub>2</sub>CO<sub>3</sub> (1 eq.), DMAc, N<sub>2</sub>, 120 °C; <sup>a</sup> Yield of isolated compound; <sup>b</sup> Determined by <sup>1</sup>H NMR spectroscopy.

Gratifyingly this study has provided improved catalyst activity at substantially lower Pd loadings, seemingly the effects of optimum catalyst concentration and decreased Pd/substrate ratio are complementary, allowing the catalyst TON to dramatically increase from 342 to over 2400 when a catalyst loading of 0.025 mol% was employed. Importantly, despite the increased reaction time of 20 hours, a substantially higher TOF of 0.033 s<sup>-1</sup> (compared with 0.024 s<sup>-1</sup>) has been achieved. Decreasing the loading further to 0.01 mol% still provides a promising (although diminished) 15% yield over 88 hours; the high TON reflects that the catalyst is still obviously effective at this low loading. Despite this, the decreased TOF (0.005 s<sup>-1</sup>) shows that with such a small amount of Pd, the catalyst efficacy is hampered. As discussed previously, with such a plethora of possible routes for catalyst poisoning to occur (Chapter 1), it is feasible that at higher Pd loadings these side reactions have a lower effect on catalyst efficacy. In order to achieve optimal catalyst TOF and TON with a catalyst loading at such a low level, the entirety of the Pd in solution needs to be catalytically competent, not tied up in a catalytic graveyard as Pd(CN)<sub>3</sub>X species.<sup>94a</sup> The turn-over frequencies quoted in Table 7 make the assumption that the catalyst is turning-over through the entire course of the reaction. With the current data, it is not possible to state if the catalyst

rapidly reached its end point, and then stopped or if the catalyst slowly continued to turn-over until the reaction was quenched by the user.

### 3.4. Conclusion

Upon screening the possibility of using 2-pyrone **60** as a model substrate in Pd catalysed arylocyanation reactions it was found that transmetalation of cyanide to this compound *via* Pd was too slow, presumably due to its latent electron deficiency.<sup>109</sup> Instead preferential homocoupling to form **63** was observed under the arylocyanation conditions. It was also found that the quantitative formation of **62** was possible upon reaction of **60** with **64** in the presence of Na<sub>2</sub>CO<sub>3</sub>. An authentic sample of **61** was synthesised using a Rosenmund-von Braund reaction but given the issues with the Pd-catalysed arylocyanation of **60** it was found to be an unsuitable candidate for a model substrate.

Changing the model substrate to the more electron rich 2-pyridone **65** yielded more success and a series of Pd precatalysts have been screened in its Pd-catalysed arylocyanation. Throughout this study it became apparent that an ideal benchmark reaction had been identified for this investigation. Pd(OAc)<sub>2</sub>(HNR<sub>2</sub>)<sub>2</sub> complexes have been shown to be adept precatalysts for this transformation, outperforming Pd(OAc)<sub>2</sub> and the *in situ* mixing of piperidine and Pd(OAc)<sub>2</sub>. The aging of the *in situ* precatalysts had a detrimental effect upon catalyst efficiency. *Bis-trans*-[piperidiny-κ-NH]palladium(II) diacetate (**47**) and *bis-trans*-[azepiny-κ-NH]palladium(II) diacetate (**52**) have been highlighted as being particularly promising precatalysts, and further investigations into the effects of catalyst loadings and concentrations have uncovered an increased catalytic efficiency upon maintaining a constant Pd concentration when decreasing catalyst loading.

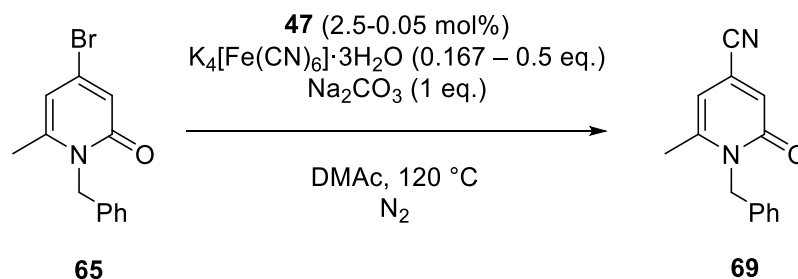
So far, promising TONs and TOFs have been achieved by both **47** and **52**, in order to truly understand the mode of catalysis, its efficiency and the processes involved in the formation of active Pd species in this arylocyanation reaction, a significant mechanistic study is required. In order to build a more complete picture of how the catalyst behaves and how to further improve the reaction efficiency, kinetic studies have been carried out using *in situ* infrared spectroscopy, as are detailed in Chapters 4 and 5.

## Chapter 4: Kinetic studies of the Pd(OAc)<sub>2</sub>(HNC<sub>5</sub>H<sub>10</sub>) catalysed cyanation of *N*-benzyl-4-bromo-6-methylpyrid-2-one by *in situ* infra-red spectroscopy under hydrous conditions

### 4.1. Introduction

Fourier transform infrared (FT-IR) spectroscopy is a technique used for the structural determination of chemical compounds and has been utilised to aid their characterisation ever since the mid-20<sup>th</sup> century.<sup>137</sup> Ever since the widespread availability of multinuclear NMR spectroscopy, FT-IR spectroscopy is most commonly used by organic chemists to identify and distinguish the presence of functional groups. However, the chemical environments surrounding these functional groups results in a unique infra-red spectrum for every compound – the fingerprint region (between 1450-500 cm<sup>-1</sup>) is unique to each species and corresponds to high energy bending and deformation absorbances. Given that FT-IR spectroscopy is such a powerful technique, the use of it *in situ* has also proven to be a valuable tool. It can be used to provide further mechanistic insight and to improve the methods of reaction optimisation and understanding of catalytic processes.<sup>138</sup> This tool not only provides information about reaction kinetics, but also opens the door to the characterisation of potential intermediates, side products and (most importantly for this case) how all these aspects can effect catalyst efficiency.

Frech *et al.* have previously published kinetic studies of Pd-catalysed cyanations using their Pd aminophosphine catalyst **26**, and provided kinetic evidence for the presence of PdNPs in cyanation reactions at low catalyst loadings (0.05 mol%).<sup>43</sup> Characteristic sigmoidal kinetic plots with noticeable induction periods were observed, suggesting the formation of catalytically relevant metal particles.<sup>106, 136</sup> These kinetic observations coupled with the judicious use of PdNP poisoning experiments<sup>108</sup> support the hypothesis that Pd-catalysed cyanations transpire through PdNPs or clusters. With these results in mind it was deemed sensible to investigate the relationship between reaction rate and catalyst loading (concentration) using our own potential PdNP precursors. As discussed previously (Chapter 1), it is typical for a reaction mediated by PdNPs to be impeded by a high catalyst loadings as a resultant of Pd aggregation, therefore the relationship between catalyst loading and reaction rate will be non-linear.



**Scheme 49** A series of kinetic experiments on the catalyst, **47**, were carried out using *in-situ* IR spectroscopy.

In order to prove the heterogeneity of a catalyst, the presence of sigmoidal kinetics which fit the Finke-Watzky 2-step mechanism (F-W 2-step mechanism) for catalyst activation, is the most compelling piece of evidence that one can acquire. Despite this, it is not possible to reach a definitive conclusion using only a single experimental method; a portfolio of evidence using different techniques must be acquired. A selection of these methods include transmission electron microscopy, mercury poisoning and CS<sub>2</sub> (or strong metal-ligand) poisoning, see Chapter 1, Section 1.1.1.

## 4.2. Kinetic Investigation using *in situ* React-IR spectroscopy

### 4.2.1. Monitoring the model cyanation reaction by React-IR

Primarily, it is important to note that all kinetic studies were carried out under Schlenk conditions but in an open system; the reaction mixture was open to a constant flow of nitrogen gas whilst the kinetic data was collected. To ensure all reactions were carried out at the required temperature ( $\pm ca.$  0.4 °C) all of the kinetic studies were constantly monitored using an external electronic thermometer. The *in situ* spectrometer measured one spectrum every minute. Analysis of the IR spectra of the product in the reaction solvent, DMAc, (Figure 49 and Figure 50) allowed for the determination that the peak corresponding to the nitrile stretch at 2237 cm<sup>-1</sup> as a suitable peak in the “solvent-window” to be selected to monitor the product’s formation throughout the reaction.

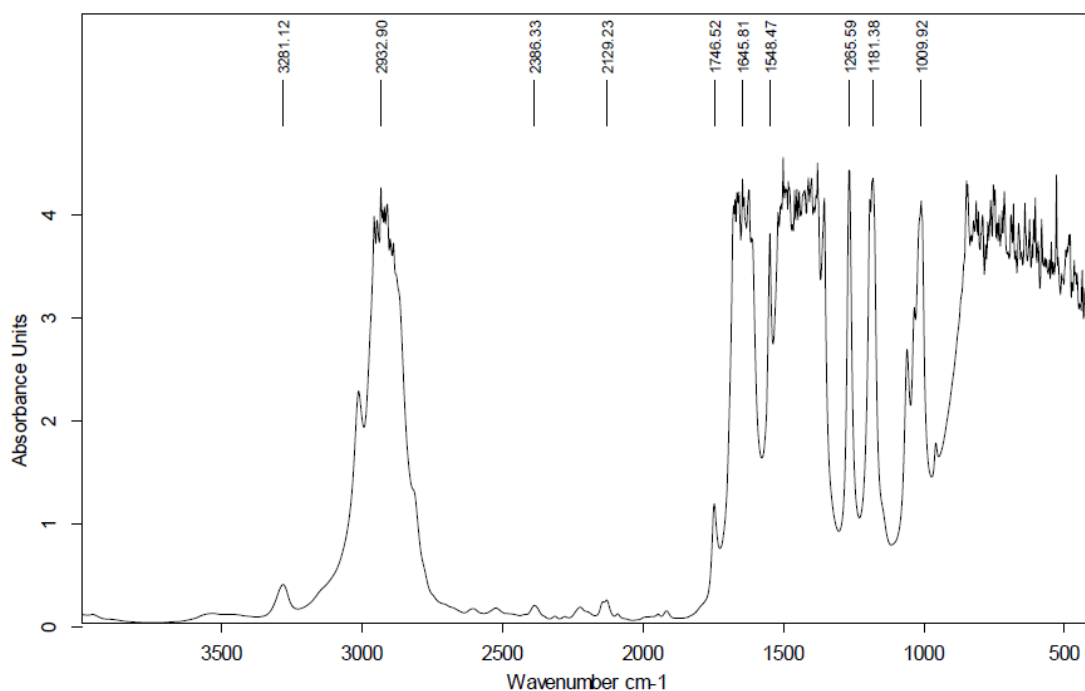


Figure 49 IR spectrum of DMAc.

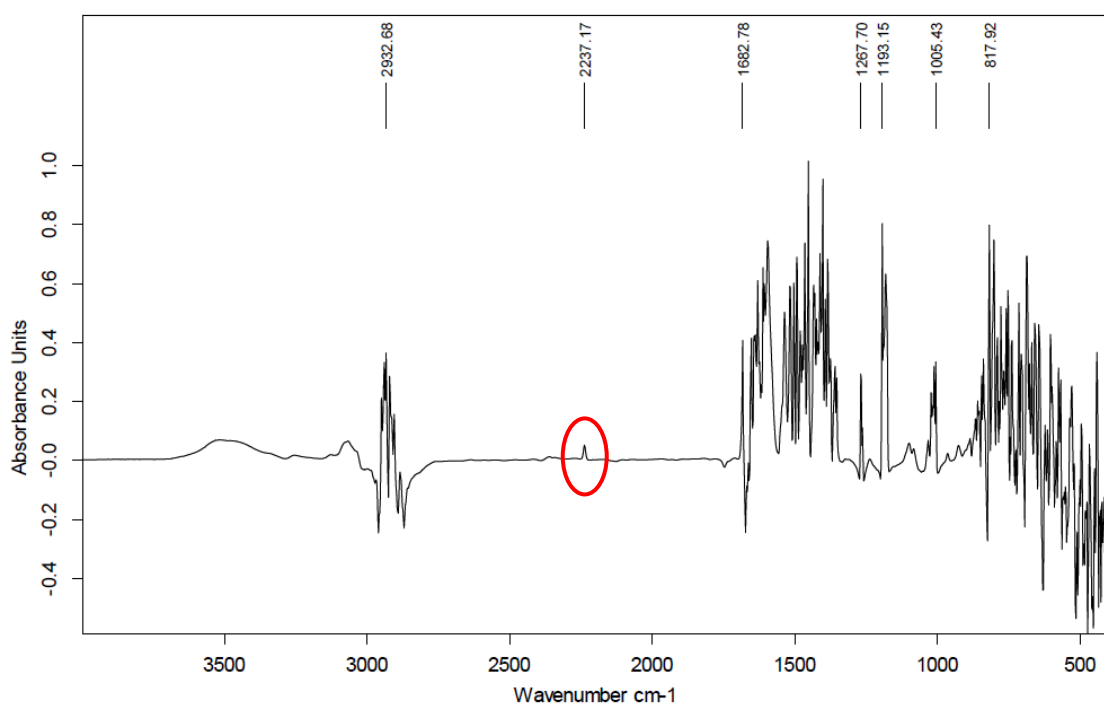


Figure 50 IR Spectrum of 69 in DMAc. The red circle highlights the IR absorbance corresponding to the nitrile C≡N stretching frequency of 69.

Initial study of the reaction kinetics under hydrous conditions, at 0.1 mol% catalyst loading, resulted in a promising reaction rate, a sigmoidal kinetic reaction profile and the appearance of a strong absorbance at 2045 cm<sup>-1</sup>.

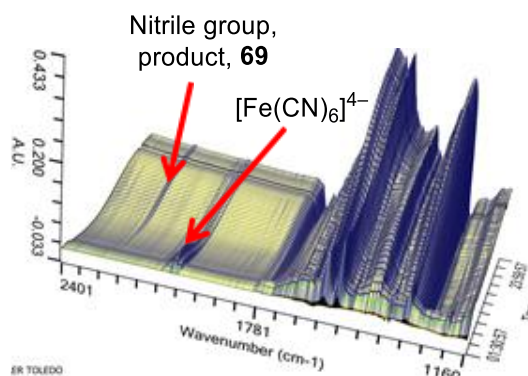


Figure 51 *In situ* IR spectra of the cyanation of 65. Reaction conditions: 47 (0.1 mol%),  $K_4[Fe(CN)_6] \cdot 3H_2O$  (0.22 eq.),  $Na_2CO_3$  (1 eq.), DMAc,  $N_2$ , 120 °C.

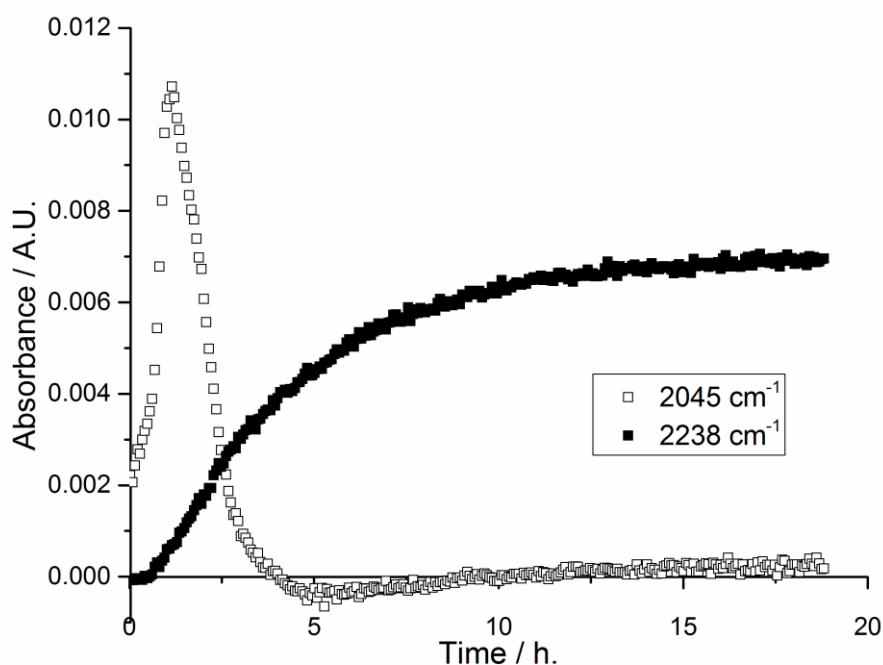
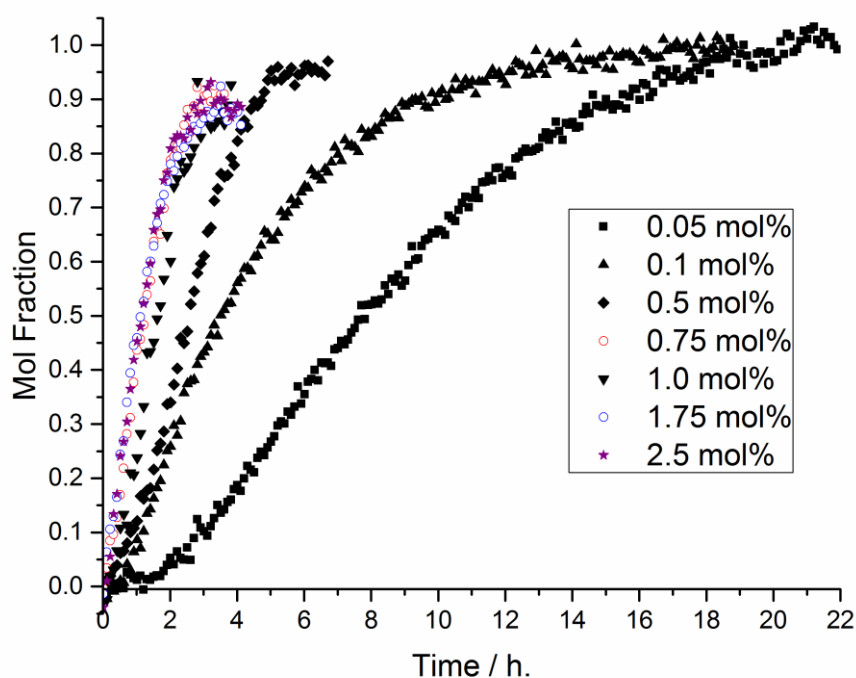


Figure 52 Raw data showing the time resolved formation of product ( $2238\text{ cm}^{-1}$ ) and solubilised  $[Fe(CN)_6]^{4-}$  ( $2045\text{ cm}^{-1}$ ), as characterised later. Reaction conditions: 47 (0.1 mol%),  $K_4[Fe(CN)_6] \cdot 3H_2O$  (0.22 eq.),  $Na_2CO_3$  (1 eq.), DMAc,  $N_2$ , 120 °C.

Figure 52 shows a short induction period and that after 12.5 hours the reaction has reached its end point. A strong, new absorbance at  $2045\text{ cm}^{-1}$  only grows in upon addition of the catalyst to initiate the reaction and has been characterised (as detailed in Section 4.4.1) as solubilised  $[Fe(CN)_6]^{4-}$ . The non-zero starting concentration for  $[Fe(CN)_6]^{4-}$  is a result of the stepwise addition of reagents,  $K_4[Fe(CN)_6]$  was added to the hot reaction solvent five minutes before the reaction initiation.

#### 4.2.2. Kinetic studies of the model cyanation reaction under hydrous conditions

Given the success of the initial studies a series of reactions were carried out using **47** as a catalyst with the loadings 0.05, 0.1, 0.5, 0.75, 1.0, 1.75 and 2.5 mol% (Figure 53). The raw values have been normalised by calculating the conversion of the reaction using a  $^1\text{H}$  NMR spectrum of the crude reaction mixture (no work-up). Sigmoidal kinetic plots were observed. This behaviour was particularly noticeable for reactions performed at low catalyst loadings, and are consistent with the findings of Frech *et al.*<sup>43</sup>



**Figure 53 Catalyst loading kinetic investigation of the cyanation of 65 under hydrous conditions. Reaction conditions: **47** (0.05 mol% - 2.5 mol%),  $\text{K}_4[\text{Fe}(\text{CN})_6]\cdot 3\text{H}_2\text{O}$  (0.22 eq.),  $\text{Na}_2\text{CO}_3$  (1 eq.), DMAc,  $\text{N}_2$ , 120 °C.**

Figure 54 shows that when the Pd precatalyst loading was dropped to 0.05 mol% of Pd catalyst, an even more significant induction period was seen. Inspection of the initial six hours of each kinetic trace (Figure 54) reveals that at induction periods of 40 minutes and upwards of 90 minutes were observed for catalyst loadings of 0.1 and 0.05 mol%, respectively. Crucially, this evidence indicates that mononuclear Pd as **47** appears to be incapable of carrying out effective catalysis under hydrous conditions; an activation step is therefore necessary. When a reaction is metal catalysed, sigmoidal kinetic profiles have been attributed in the literature to reactions which are catalysed at the surface of metal clusters which result from the autocatalytic formation of a catalytically active species from an inactive homogeneous precursor complex.<sup>33</sup> So far there appears to be good evidence to support the hypothesis that PdNPs are playing a key role in the Pd-catalysed cyanation mechanism,

especially when performed at low Pd loadings. However, this needs to be supported further with the application of a kinetic model and evidence for the catalytic relevance of metal cluster species under the reaction conditions.

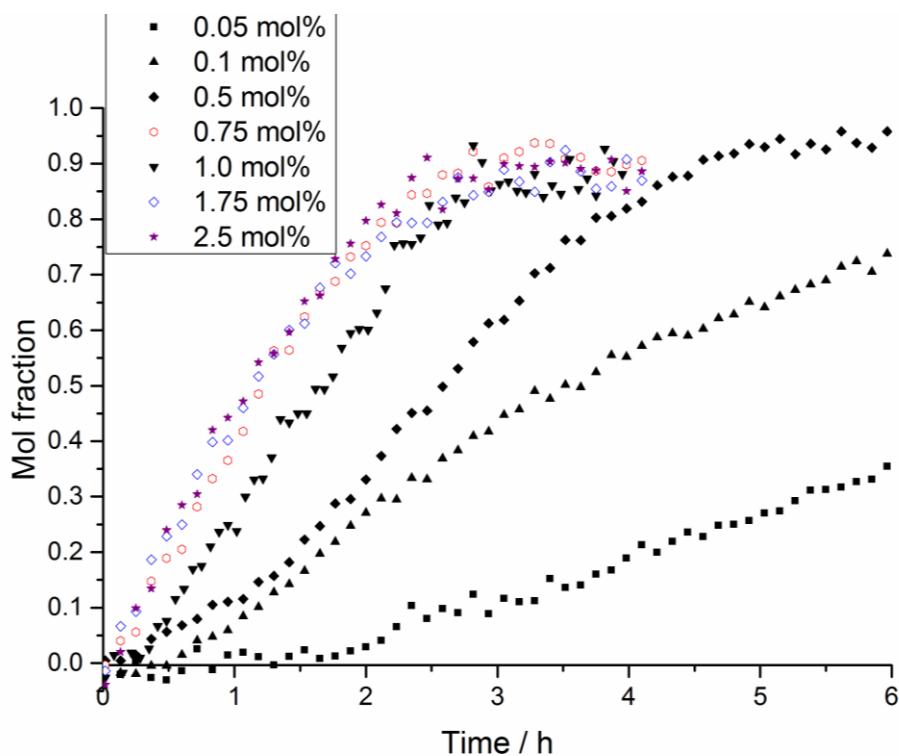


**Figure 54** The beginning of the kinetic plots displayed in Figure 53 enlarged to show induction periods. Reaction conditions: 47 (0.05 mol% - 2.5 mol%),  $K_4[Fe(CN)_6] \cdot 3H_2O$  (0.22 eq.),  $Na_2CO_3$  (1 eq.), DMAc,  $N_2$ , 120 °C.

Inspection of each of the kinetic plots can provide further information regarding the mechanism of catalysis. Calculating the  $k_{obs}$  for each of the catalyst loadings by creating plots of product concentration vs. time (Figure 55, for 0.05 mol%) allows for the rates of reaction with respect to catalyst concentration to be easily compared. In each case the  $k_{obs}$  values were obtained from the reactions at their peak rates.<sup>106</sup>

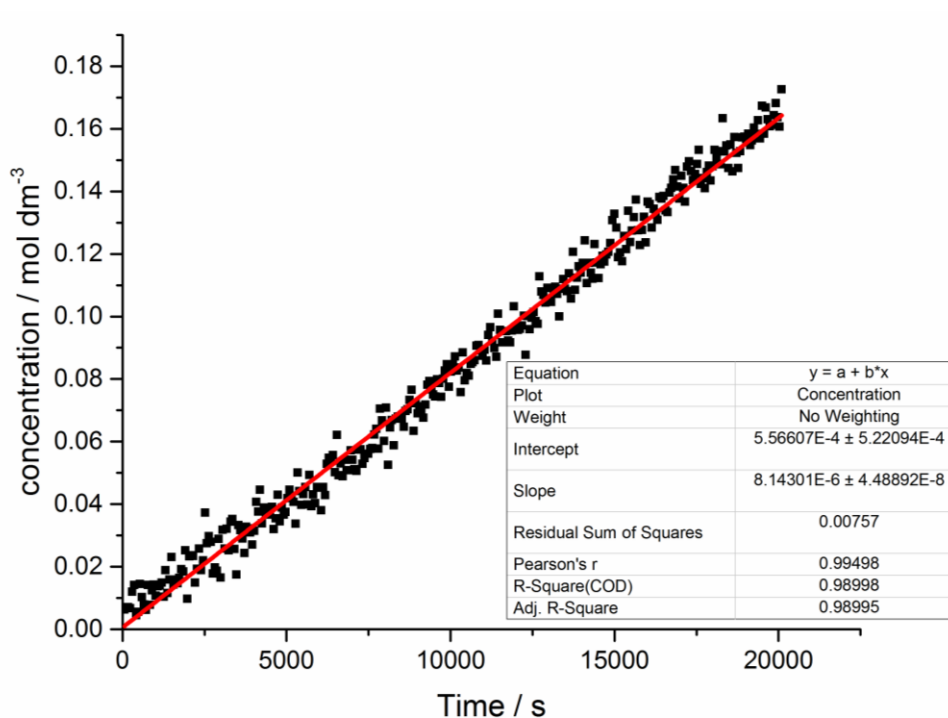


**Figure 55** A plot to calculate the observed rate constant,  $k_{\text{obs}}$ , obtained from the peak rate of reaction. Reaction conditions: 47 (0.05 mol%),  $\text{K}_4[\text{Fe}(\text{CN})_6] \cdot 3\text{H}_2\text{O}$  (0.22 eq.),  $\text{Na}_2\text{CO}_3$  (1 eq.), DMAc,  $\text{N}_2$ , 120 °C.

The complete collection of  $k_{\text{obs}}$  values and their errors, as determined by the linear fit, can be seen in Table 8. Despite the  $k_{\text{obs}}$  values providing a good insight into the effect of catalyst loading upon reaction rate, relative turn-over frequencies (TOF) under the working conditions also need to be considered. This is because TOF takes into account the relative abundance of catalyst in order for it to achieve the observed rate of reaction.

**Table 8** The effect of Pd catalyst loading on observed rate of reaction,  $k_{\text{obs}}$ , TON and TOF.

Entry	Catalyst loading (mol%)	[Catalyst] (mol dm <sup>-3</sup> )	$k_{\text{obs}}$ (mol dm <sup>-3</sup> s <sup>-1</sup> )	TON	TOF (s <sup>-1</sup> )
1	0.05	$1.80 \times 10^{-4}$	$8.14 \times 10^{-6} (\pm 4.49 \times 10^{-8})$	1960	0.0453
2	0.1	$3.60 \times 10^{-4}$	$1.87 \times 10^{-5} (\pm 1.57 \times 10^{-7})$	973	0.0519
3	0.5	$1.80 \times 10^{-3}$	$2.73 \times 10^{-5} (\pm 2.17 \times 10^{-7})$	137	0.0151
4	0.75	$2.69 \times 10^{-3}$	$4.32 \times 10^{-5} (\pm 4.94 \times 10^{-7})$	119	0.0161
5	1	$3.60 \times 10^{-3}$	$3.69 \times 10^{-5} (\pm 6.52 \times 10^{-7})$	65	0.0103
6	1.75	$6.28 \times 10^{-3}$	$4.06 \times 10^{-5} (\pm 6.49 \times 10^{-7})$	49	0.00647
7	2.5	$8.99 \times 10^{-3}$	$4.13 \times 10^{-5} (\pm 5.30 \times 10^{-7})$	29	0.00460

Despite the large induction period and lower  $k_{\text{obs}}$  value observed with 0.05 mol% catalyst loading, after the Pd catalyst reaches its most active phase it is stable. With such a low loading

and concentration, the catalyst is turned-over rapidly (TOF:  $0.0453 \text{ s}^{-1}$ , see Table 8, entry 1) for over twelve hours until reaction completion, little catalyst degradation is evident here. When the catalyst loading was increased to 0.1 mol% (entry 2) a higher TOF of  $0.0519 \text{ s}^{-1}$  was achieved. This indicates that at this concentration and Pd:substrate ratio the catalyst turns over at its most efficiently. However, upon increasing the catalyst loading and concentration further to 0.5 mol% and above, the catalyst TOF suffers a significant decrease (Figure 56). The lower TOF resulting from the increased Pd concentration can be attributed to less catalytically active sites per moles of Pd, suggesting the presence of larger, less catalytically active Pd clusters at higher concentrations. Increased TON and TOF upon decreasing catalyst loading has also been attributed to catalyst degradation by aggregation in Sonogashira reactions: Fairlamb *et al.* report higher TOFs at 0.001 mol% than at 0.01 mol%<sup>21</sup> catalyst loadings and a significant decrease in catalyst activity above that catalyst concentration. A similar outcome was reported by De Vries *et al.* where higher yields were obtained in a Heck<sup>7-8</sup> reaction at 0.02 and 0.08 mol% Pd catalyst loadings than at 0.00125 and 1.28 mol%.

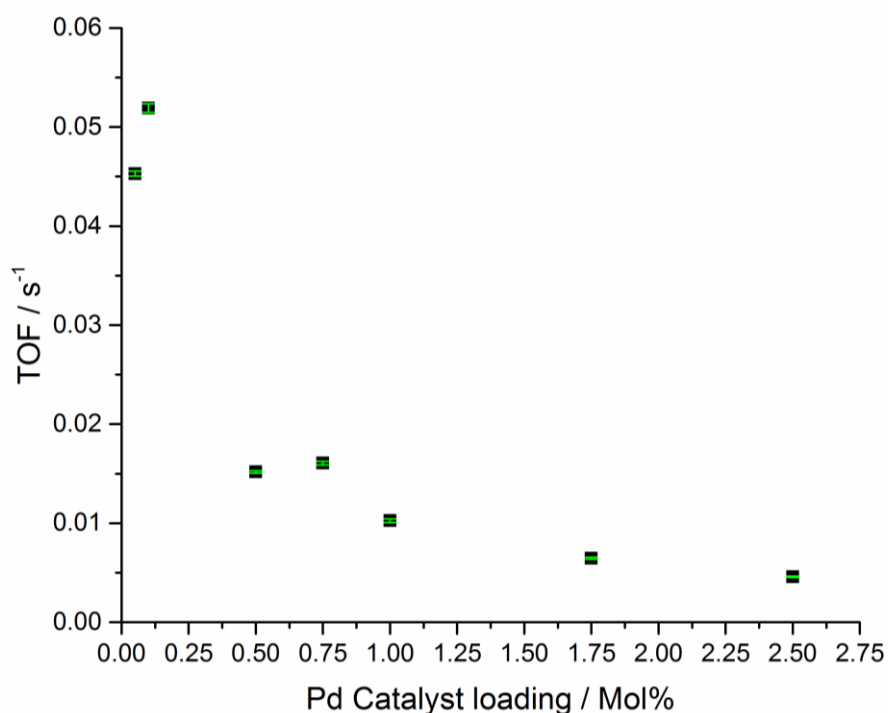


**Figure 56** A graph to show TOF vs Pd catalyst (47) loading. The TOFs of each of the different precatalyst loadings was measured as a gradient of  $\text{TON s}^{-1}$  for the straight line section of the kinetic profiles. Reaction conditions: 47 (0.05 mol% - 2.5 mol%),  $\text{K}_4[\text{Fe}(\text{CN})_6] \cdot 3\text{H}_2\text{O}$  (0.22 eq.),  $\text{Na}_2\text{CO}_3$  (1 eq.), DMAc,  $\text{N}_2$ ,  $120 \text{ }^\circ\text{C}$ .

An optimum TOF was found at 0.1 mol% ( $[\text{Pd}] = 3.6 \times 10^{-4} \text{ mol dm}^{-3}$ ), and by reducing the catalyst loading further to 0.05 mol% ( $[\text{Pd}] = 1.80 \times 10^{-4} \text{ mol dm}^{-3}$ ) a small drop in TOF was observed. By constructing a plot of  $k_{\text{obs}}$  vs catalyst concentration (Figure 57), it was possible to determine that there is not a positive linear relationship; *i.e.* the rate of reaction is not first

order with respect to the concentration of Pd catalyst. This is not the expected outcome for a reaction undergoing homogeneous catalysis, a non-linear relationship between  $k_{\text{obs}}$  and catalyst concentration is indicative of a process involving higher-order catalyst species.

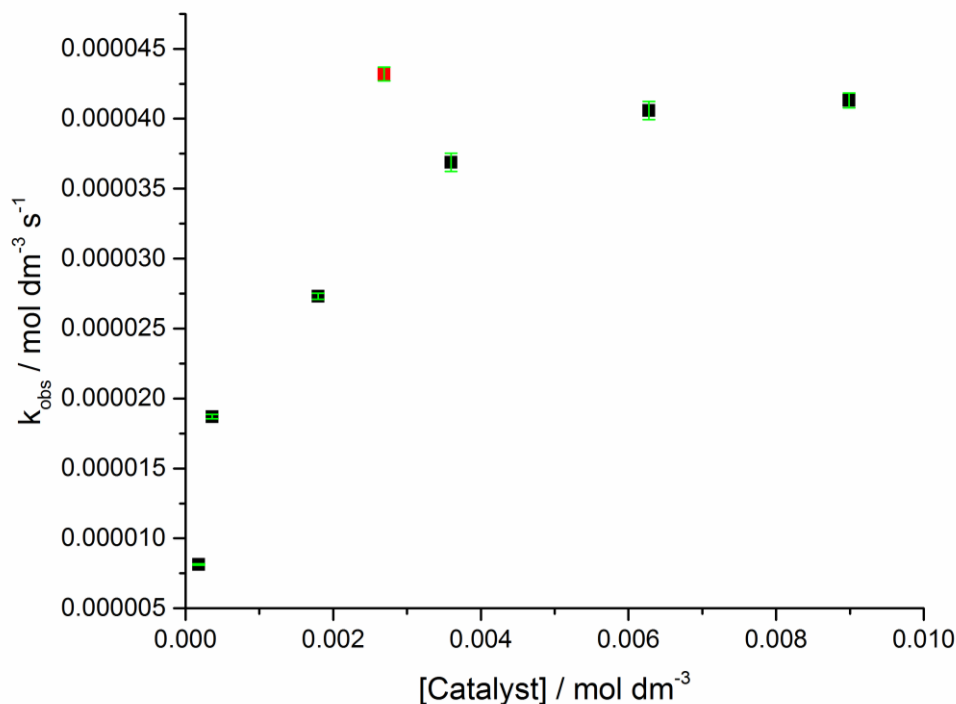


**Figure 57** A plot of  $k_{\text{obs}}$  vs. [Pd] shows there is not a linear relationship between reaction rate and catalyst loading. It also reveals that the  $k_{\text{obs}}$  obtained for 0.0027 mol dm<sup>-3</sup>/0.75 mol% is an anomaly (highlighted in red). Reaction conditions: 47 (0.05 mol% - 2.5 mol%), K<sub>4</sub>[Fe(CN)<sub>6</sub>]·3H<sub>2</sub>O (0.22 eq.), Na<sub>2</sub>CO<sub>3</sub> (1 eq.), DMAc, N<sub>2</sub>, 120 °C.

The non-linear relationship between reaction rate and catalyst concentration is representative of the fact that not all of the Pd in the reaction system is capable (or involved) in the catalytic cycle. There have been multiple reports in the literature of Pd catalysed reactions involving an off cycle dimeric species in the reaction mechanism acting as a Pd reservoir resulting in an order of 0.5 with respect to Pd.<sup>38</sup> A higher nuclearity of Pd species in the catalytic cycle would therefore result not only in a non-linear rate-catalyst loading relationship, but also in an order with respect to Pd of a value lower than 0.5.

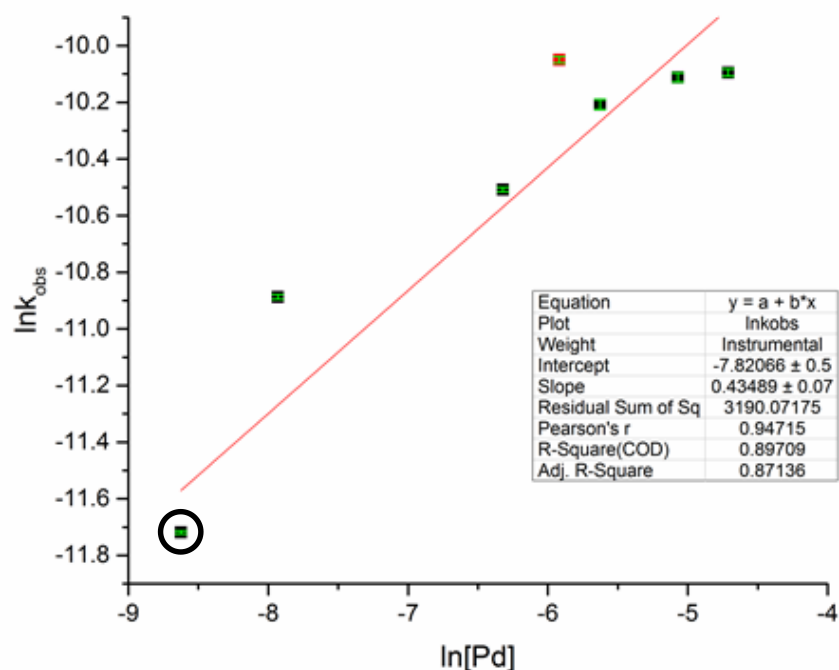


**Figure 58** Calculating the order with respect to Pd *via* the differential method provides a value of 0.435 ( $\pm 0.076$ ). One anomalous point has been highlighted in red, as explained in Figure 57. The point within the bold black circle (0.05 mol%,  $1.80 \times 10^{-4}$  mol dm $^{-3}$ ) also appears to be off the expected linear trend.

A partial order of 0.435 ( $\pm 0.07$ ) is obtained when the differential method is used (displayed in Figure 58) and the data point for 0.05 mol% Pd catalyst loading, ( $[Pd] = 1.80 \times 10^{-4}$  mol dm $^{-3}$ ) is included within the data plot. This results in a large error during the attempted linear fit and may suggest (along with the decrease in TOF shown in Figure 56) that at this lower  $[Pd]$  and catalyst loading a different mechanism may become more prevalent. With this in mind, it is clear that the order obtained from Figure 58 is therefore not representative of the reaction mechanism operating under the majority of reaction conditions. Recalculating the order of reaction with respect to Pd *via* the differential method while considering the two points for catalyst loadings of 0.75 mol% ( $[Pd] = 2.69 \times 10^{-3}$  mol dm $^{-3}$ ) and 0.05 mol% ( $[Pd] = 1.80 \times 10^{-4}$  mol dm $^{-3}$ ) as anomalous or uncharacteristic of the reaction mechanism, respectively, gives Figure 59.

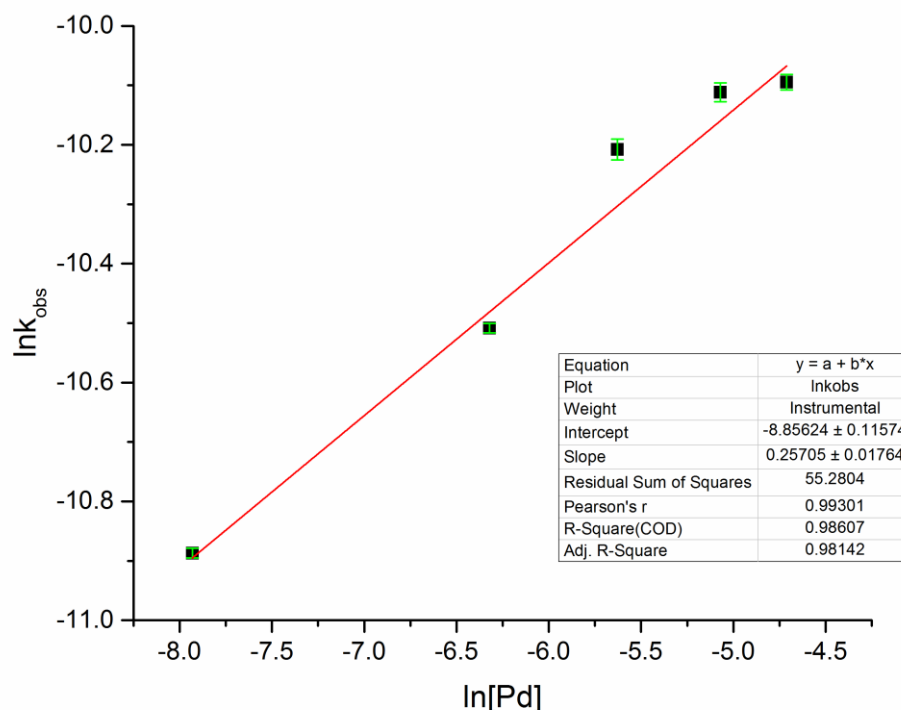


**Figure 59** Calculating the order with respect to Pd via the differential method provides a value of  $0.257 (\pm 0.02)$ .

The order with respect to Pd obtained by the differential method of five concentrations of Pd catalyst has been calculated as  $0.26 (\pm 0.02)$ . This partial order is representative of a complex, multistep reaction mechanism<sup>139</sup> and implies that higher order Pd species (*i.e.* potentially with a nuclearity of 4) are catalytically competent. It has previously been reported by Finke *et al.* that slight variations of reaction conditions can instigate the change in active catalyst species formed from the *in situ* reduction of  $[\text{RhCp}^*\text{Cl}_2]_2$  in hydrogenation reactions;  $\text{Rh}_1$ ,  $\text{Rh}_4$  (sub-nanometer clusters, as detected by XAFS and MS) and  $\text{Rh}_{(n)}$  (heterogeneous particles) all have been shown to be catalytically competent species under slightly different reaction concentrations, pressures and temperatures.<sup>140</sup>

### 4.3. Tests for the presence of heterogeneous catalysis.

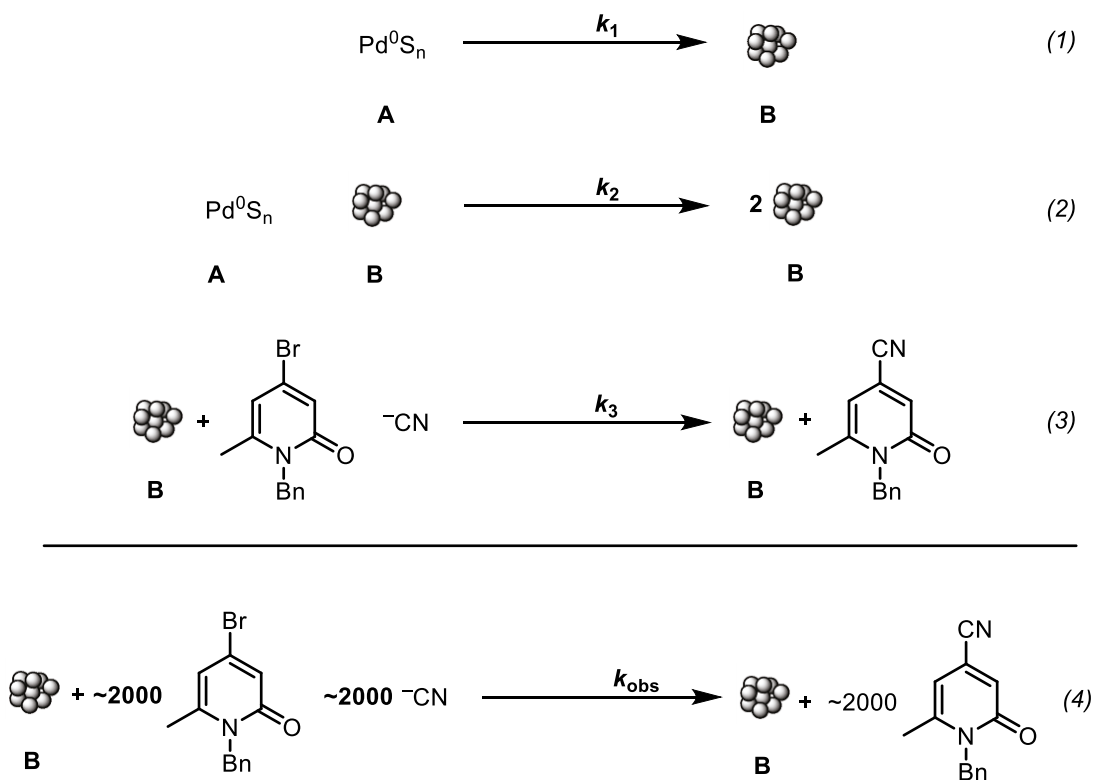
#### 4.3.1. Finke-Watzky analysis of sigmoidal kinetic plots.

The sigmoidal kinetic traces obtained coupled with the non-linear relationship between catalyst concentration and  $\ln k_{\text{obs}}$  is convincing evidence to support the hypothesis that this Pd-catalysed cyanation reaction only proceeds after the *in situ* formation of PdNPs when using  $\text{K}_4[\text{Fe}(\text{CN})_6] \cdot 3\text{H}_2\text{O}$  as a cyanating agent, and **47** as a catalyst. However, in order to

further support this hypothesis, a mathematical analysis of these sigmoidal plots would be vigilant. As discussed in Chapter 1 Finke and Watzky provided a convincing, quantitative mechanistic explanation for the shape of similar kinetic plots seen in the Ir(0)<sub>~300</sub> nanocluster-catalysed hydrogenation of cyclohexene.

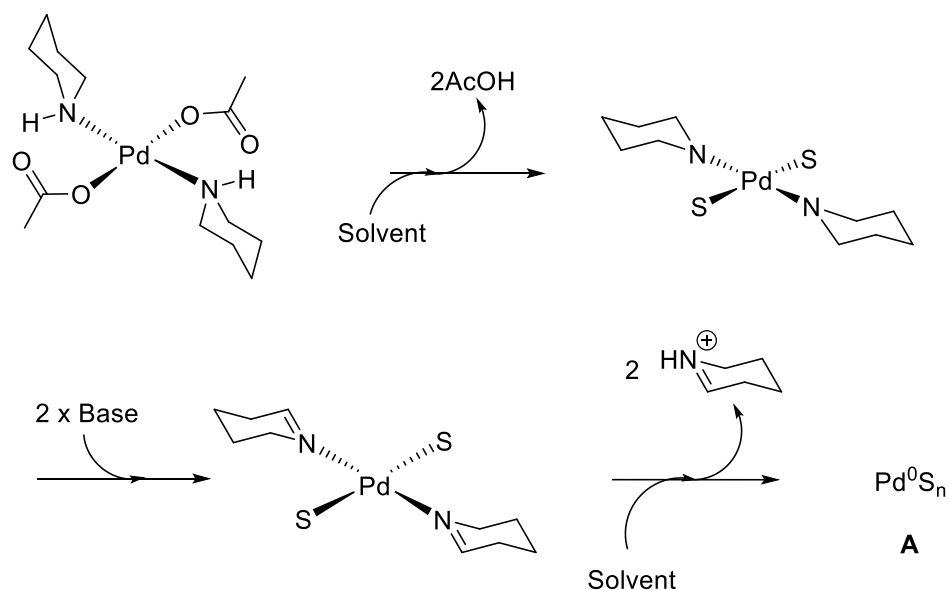
Under Finke and Watzky's published conditions this distinguishing catalytic behaviour is explained by the slow formation of the catalytically active species (**B**) via two key elementary steps as described in Scheme 50. Reaction (1), is a slow nucleation step and dictates the rate at which the active catalyst (**B**) can be formed, outlining it as rate determining.<sup>106</sup> This proposed mechanism therefore includes the key rate constants  $k_1$  and  $k_2$ , used in the integrated rate equation for the 2-step, Finke-Watzky nucleation and autocatalytic growth mechanism (referred to from here-on as the F-W 2-step mechanism).

Finke and Watzke state that if a reaction is autocatalytic in its formation of the active catalyst (**B**), then the rate constants  $k_1$  and  $k_2$  can be determined experimentally from the overall reaction kinetics. Here it is key to recognise that the kinetic profile of the reaction is a result of a pseudoelementary mechanistic step.<sup>67</sup> This pseudoelementary step (Reaction (4), Scheme 50) is comprised of a sum of 3 elementary steps, each with individual rate constants, detailed below. This means that the overall reaction (in the case of this work, a Pd-catalysed cyanation) acts as a "reporter" reaction to determine the two rate constants ( $k_1$ ,  $k_2$ ) involved in catalyst activation.



**Scheme 50 The Finke-Watzky nucleation and autocatalytic growth mechanism.**  
 Provided  $k_3 \gg k_2 > k_1$  it is possible to calculate the values of  $k_1$  and  $k_2$  using the kinetics for the summative pseudoelementary step (4).

Scheme 51 details a suggested mechanism for the formation of species **A**, the precursor for the active catalyst **B**, by a CMD/AMLA-6 type internal deprotonation. The existence of the acetate-N-H hydrogen bond has been confirmed by X-ray crystal diffraction in similar complexes, as discussed elsewhere (Chapter 2) and the presence of homopiperidine has been detected by MS upon decomposition of **47** in previous studies.<sup>110</sup> The metal nanoparticles formed from it under reaction conditions for the C-H arylation of 2'-deoxyadenosine with stoichiometric  $\text{Cu}^{\text{I}}$  have been characterized as small (*ca.* 1.5 nm) DMF-stabilized spherical truncated icosahedra containing a (111) surface.<sup>20</sup>



**Scheme 51** Suggested mechanism for the formation of catalytic precursor, “A”. S = DMAc

Due to the rate-determining step of the overall reaction being the formation of the catalyst **B**, it is possible to obtain kinetic information ( $k_1$  and  $k_2$ ) by determining that  $+\delta[\mathbf{B}]/\delta t$  and therefore  $-\delta[\mathbf{A}]/\delta t$  is directly related to  $+\delta[\text{ArCN}]/\delta t$  and therefore  $-\delta[\text{ArBr}]/\delta t$ . A full derivation of the integrated analytical expression below is provided by Finke and Watzke.<sup>106</sup>

$$[A]_t = \frac{\frac{k_1}{k_2} + [A]_0}{1 + \frac{k_1}{k_2[A]_0} \times e^{(k_1+k_2[A]_0)t}}$$

**Equation 3** The integrated rate equation for the 2-step, Finke-Watzky nucleation and autocatalytic growth mechanism.

In order to investigate the possibility of the F-W 2-step mechanism being present in this catalyst system, when the catalyst loadings display significant induction periods (*i.e.* 0.1 and 0.05 mol%) this equation was employed in the nonlinear least-squares fitting of the concentration *vs.* time data. All data treatments were devised after careful incorporation of the protocol provided by Kemmer and Keller<sup>141</sup> for non-linear least-squares data fitting with the integrated rate equation for the 2-step, Finke-Watzky nucleation and autocatalytic growth mechanism (Equation 1).<sup>33</sup> This provided the curvefits *vide infra*.

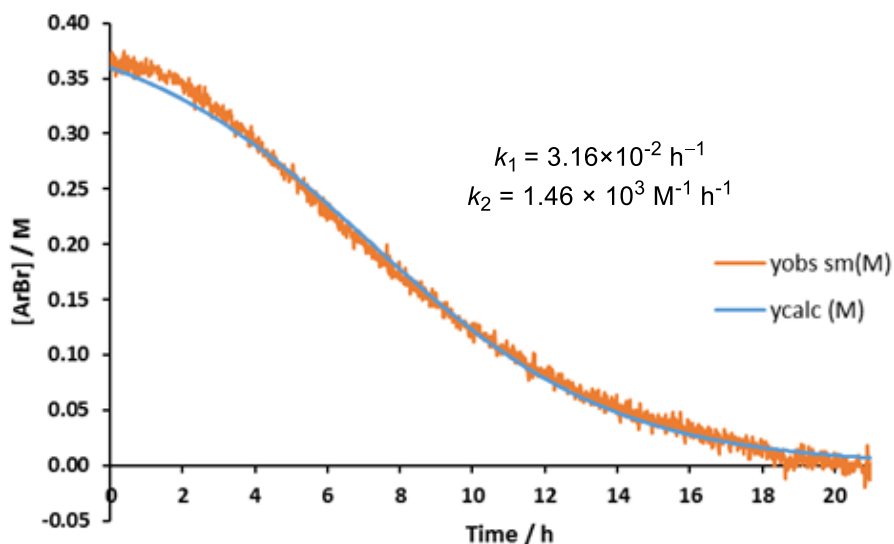


Figure 60 Concentration vs. time curve and data fit to the F-W 2-step mechanism for 0.05 mol% catalyst loading. The resultant rate constant  $k_2$  has been corrected by using a stoichiometry factor of 2000.  $k_1$  confidence intervals: 95% =  $2.4 \times 10^{-2} - 4.1 \times 10^{-2} \text{ h}^{-1}$ ; 99% =  $2.15 \times 10^{-2} - 4.5 \times 10^{-2} \text{ h}^{-1}$ .  $k_2$  confidence intervals: 95% =  $1.2 \times 10^3 - 1.74 \times 10^3 \text{ M}^{-1} \text{ h}^{-1}$ ; 99% =  $1.12 \times 10^3 - 1.84 \times 10^3 \text{ M}^{-1} \text{ h}^{-1}$ .

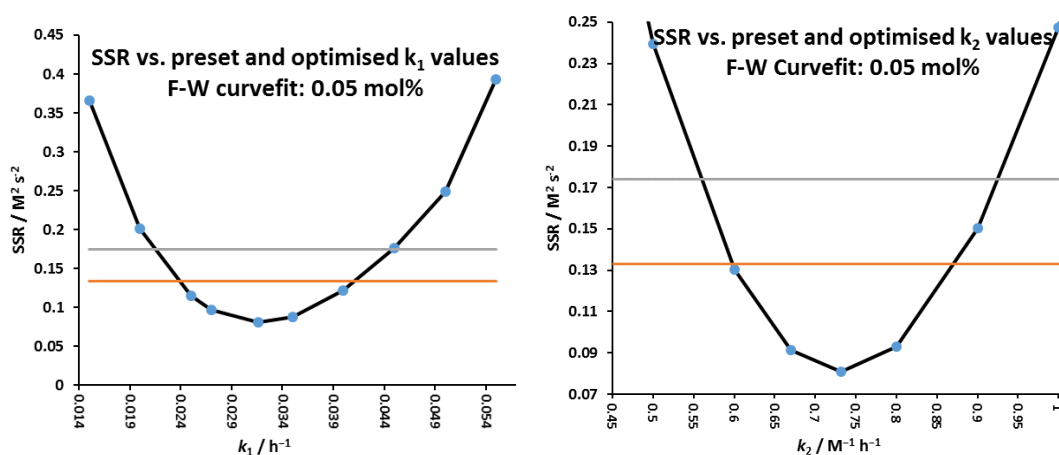
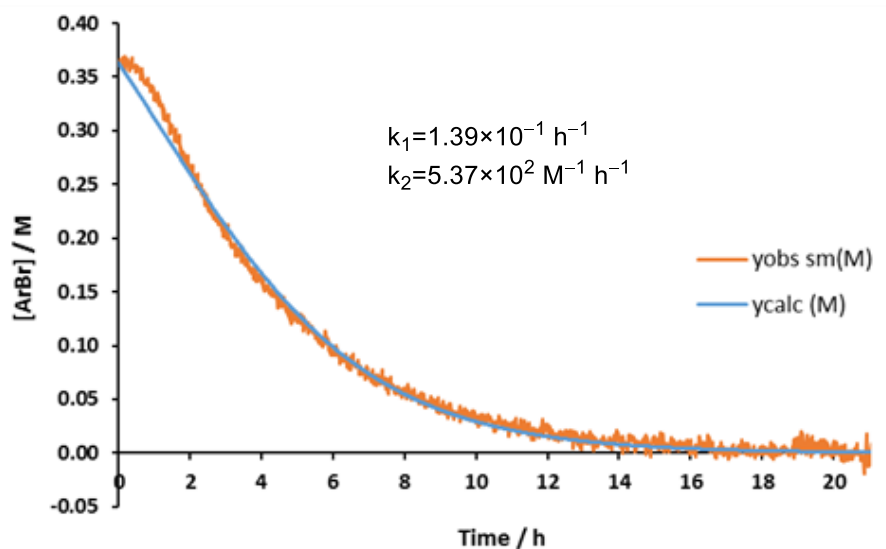
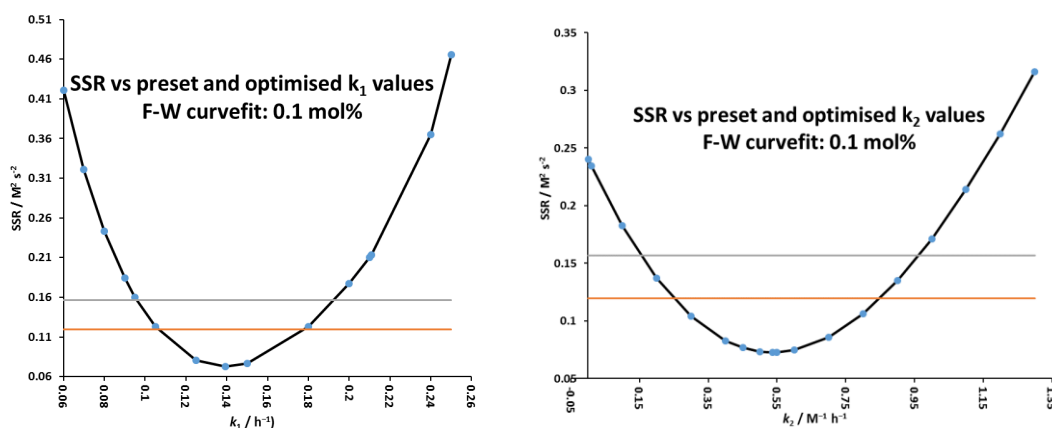


Figure 61 Visual representations of the 95% (brown line) and 99% (grey line) confidence limits for  $k_1$  (left) and  $k_2$  (right) for the F-W 2-step curvefit displayed in Figure 60.



**Figure 62** Concentration vs. time curve and data fit to the F-W 2-step mechanism for 0.1 mol% catalyst loading. The resultant rate constant  $k_2$  has been corrected by using a stoichiometry factor of 1000.  $k_1$  confidence intervals: 95% =  $1.06 \times 10^{-1} - 1.78 \times 10^{-1} \text{ h}^{-1}$ ; 99% =  $9.6 \times 10^{-2} - 1.92 \times 10^{-1} \text{ h}^{-1}$ .  $k_2$  confidence intervals: 95% =  $2.5 \times 10^2 - 8.50 \times 10^2 \text{ M}^{-1} \text{ h}^{-1}$ ; 99% =  $1.56 \times 10^2 - 9.6 \times 10^2 \text{ M}^{-1} \text{ h}^{-1}$ .



**Figure 63** Visual representations of the 95% (brown line) and 99% (grey line) confidence limits for the limits for  $k_1$  (left) and  $k_2$  (right) for the F-W 2-step curvefit displayed in Figure 62.

It is difficult to reliably correlate the relationship between increased induction period and decreased value of  $k_1$  with only the two values from 0.05 and 0.1 mol% ( $3.16 \times 10^{-2} \text{ h}^{-1}$  and  $1.39 \times 10^{-1} \text{ h}^{-1}$  respectively). However comparison with other literature values published by Finke and Watzke reveals that the two are directly linked. According to the confidence intervals obtained by manual confidence assessment using Fisher's  $F$  distribution, the curvefit for 0.05 mol% provides considerably more precise values of  $k_1$  and  $k_2$  than the curvefit for 0.1 mol%.<sup>141</sup> This implies that as catalyst concentrations increase (above and including  $3.6 \times 10^{-4} \text{ mol dm}^{-3}$ /0.1 mol%) the mechanism deviates from the F-W 2-step mechanism further. This can be rationalised by the raised concentration of Pd in solution leading to a much faster nucleation step ( $k_1$ ). It is important to remember here that in order

for the F-W 2-step mechanism to be valid, the rate of continuous nucleation must be *much* lower than both the rate of catalyst formation ( $k_2$ ) by autocatalytic surface growth, and the overall rate of reaction ( $k_{\text{obs}}$ ). Instead, it would be sensible to suggest that under these conditions, Pd may be above its critical agglomeration concentration. This means that autocatalysis has a limited effect upon the rate of active catalyst (**B**) formation, so the F-W 2-step mechanism is an unsuitable model to apply.

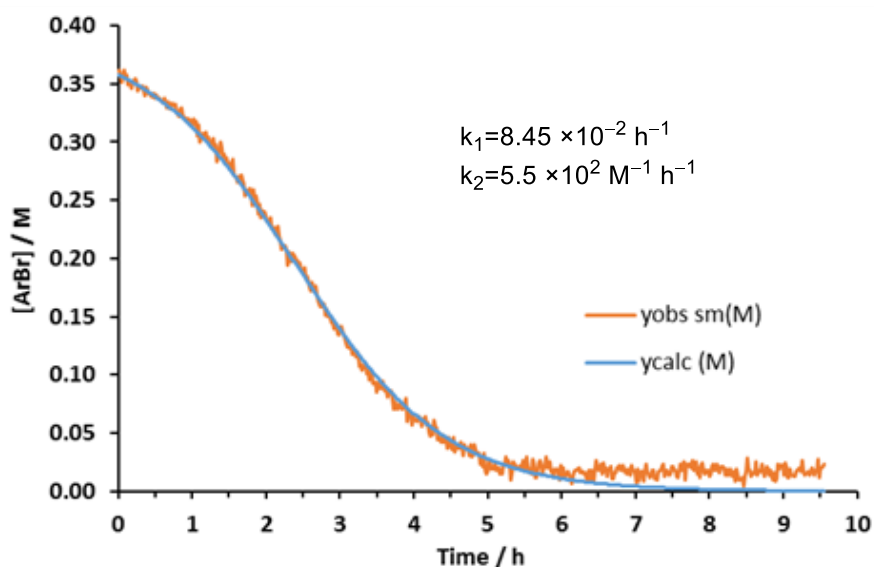


**Figure 64** Concentration vs. time curve and data fit to the F-W 2-step mechanism for 0.5 mol% catalyst loading. The resultant rate constant  $k_2$  has been corrected by using a stoichiometry factor of 200.  $k_1$  confidence intervals: 95% = 0.05 – 0.13  $\text{h}^{-1}$ ; 99% = 0.04 – 0.15  $\text{h}^{-1}$ .  $k_2$  confidence intervals: 95% = 360 – 670  $\text{M}^{-1} \text{h}^{-1}$ ; 99% = 320 – 720  $\times 10^2 \text{M}^{-1} \text{h}^{-1}$ .

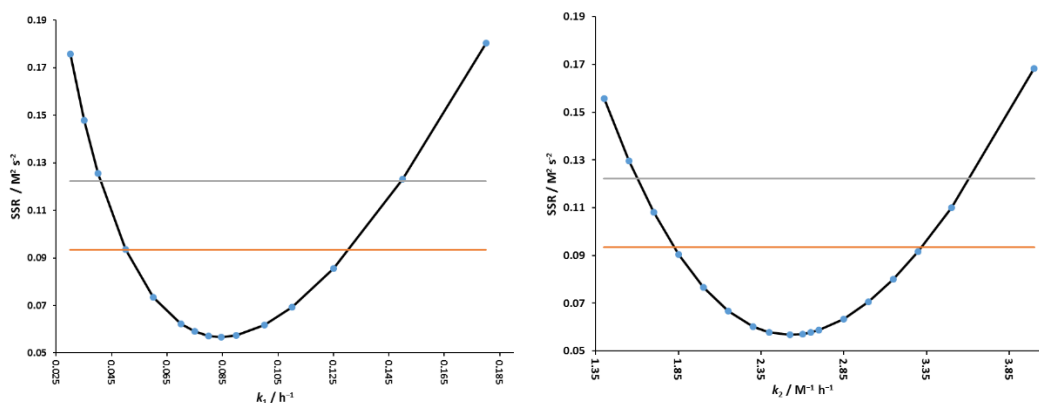


**Figure 65** Visual representations of the 95% (brown line) and 99% (grey line) confidence limits for the limits for  $k_1$  (left) and  $k_2$  (right) for the F-W 2-step curvefit displayed in Figure 64.

Analysis of the quality of the curvefit upon increasing the catalyst concentration to  $1.8 \times 10^{-3} \text{mol dm}^{-3} / 0.5 \text{mol\%}$  reveals that despite the kinetic traces appearing to be a good candidate for the F-W 2-step mechanism (sigmoidal reaction profile, Figure 64) further investigation

reveals that the 95% confidence limits of both  $k_1$  and  $k_2$  are too wide. (Figure 65) and is representative of a poor fit to the kinetic model.

In contrast, at lower Pd concentration ( $1.8 \times 10^{-4}$  mol dm<sup>-3</sup>/0.05 mol%) the curvefit displayed in Figure 60 is good, providing narrow 95% confidence intervals for both  $k_1$  and  $k_2$  ( $3.16 \times 10^{-2}$  h<sup>-1</sup> and  $1.46 \times 10^3$  M<sup>-1</sup> h<sup>-1</sup>, respectively) suggesting that the F-W 2-step mechanism provides a reasonable fit to explain the shape of the kinetic data obtained. Despite this, slight deviations away from the expected rate of catalyst formation are seen. A series of reasons for this are possible: i) the rate of formation of “A” is limited by the initial degradation of the molecular catalyst which, in this kinetic fitting model, is not taken into account and therefore not been assigned a separate rate constant ii) The F-W 2-step mechanism was designed around the Ir(0)<sub>-300</sub> nanocluster catalysed hydrogenation of cyclohexene. Although the mechanism for the initial reduction of the precatalyst, **47**, is as-yet unproven, it is likely to be instigated by increased reaction temperature rather than an external reductant, as shown in Scheme 51.

Increasing the catalyst loading to 1.0 and 2.5 mol% and Pd concentration to  $3.6 \times 10^{-3}$  and  $9.0 \times 10^{-3}$  mol dm<sup>-3</sup> causes further deviation from the F-W 2-step mechanism.

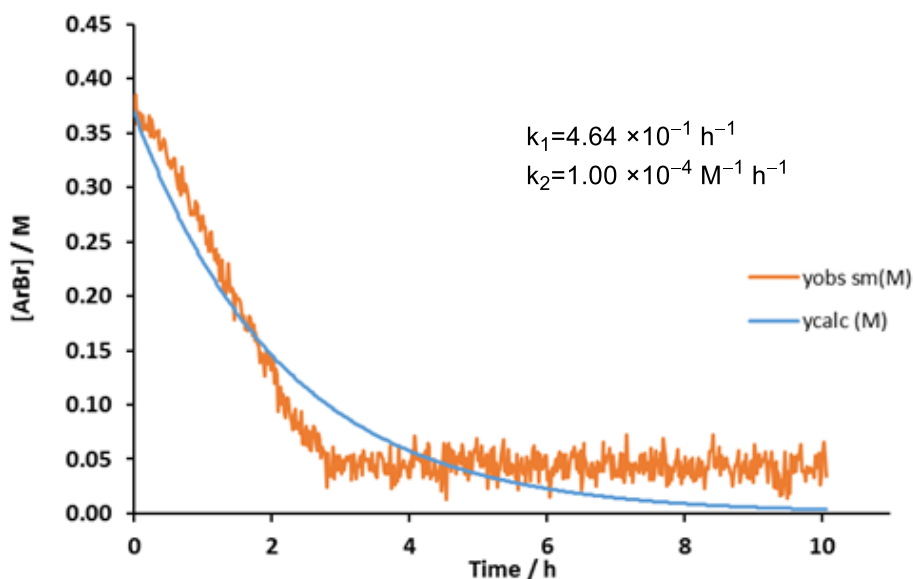


**Figure 66** Concentration vs. time curve and attempted data fit to the F-W 2-step mechanism for 1.0 mol% catalyst loading. The resultant rate constant  $k_2$  has been corrected by using a stoichiometry factor of 100.  $k_1$  confidence intervals: 95% =  $6.0 \times 10^{-2} - 6.2 \times 10^{-1} \text{ hr}^{-1}$ ; 99% =  $2.0 \times 10^{-2} - 7.3 \times 10^{-1} \text{ hr}^{-1}$ .  $k_2$  confidence intervals: 95% = N/A; 99%: N/A.

Although it is evident simply from inspection that the F-W 2-step mechanism does not provide an adequate fit to the experimental data shown in Figure 66, this is further supported by the large 95% and 99% confidence intervals for  $k_1$  and the inability to calculate the confidence intervals for  $k_2$  (Figure 67).

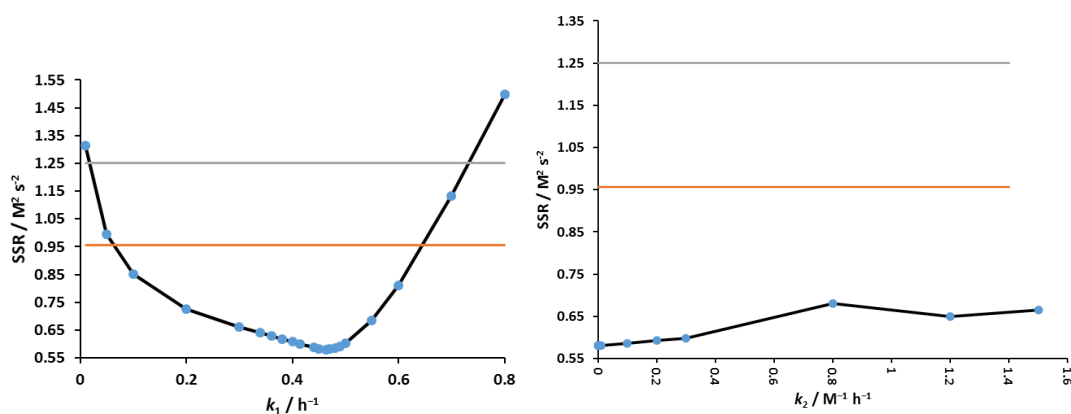


**Figure 67** Visual representations of the 95% (brown line) and 99% (grey line) confidence limits for the limits for  $k_1$  (left) and  $k_2$  (right) for the attempted F-W 2-step curvefit displayed in Figure 66.

As displayed in Figure 67, upon attempting to calculate the 95% and 99% confidence limits of  $k_1$  (left), the visual representation shows a very wide, asymmetric distribution of  $k_1$  values with a range of fixed  $k_2$  values. Applying this method to obtain the 95% and 99% confidence

limits for  $k_2$  (right), resulted in a flat line rather than the required inverse bell curve required to obtain the values. It was therefore impossible to obtain meaningful 99% confidence limits for  $k_2$ . Extending this approach further to the kinetic profile of the reaction at 2.5 mol% catalyst loading shows that, again, the F-W 2-step mechanism fails to provide an adequate curvefit.

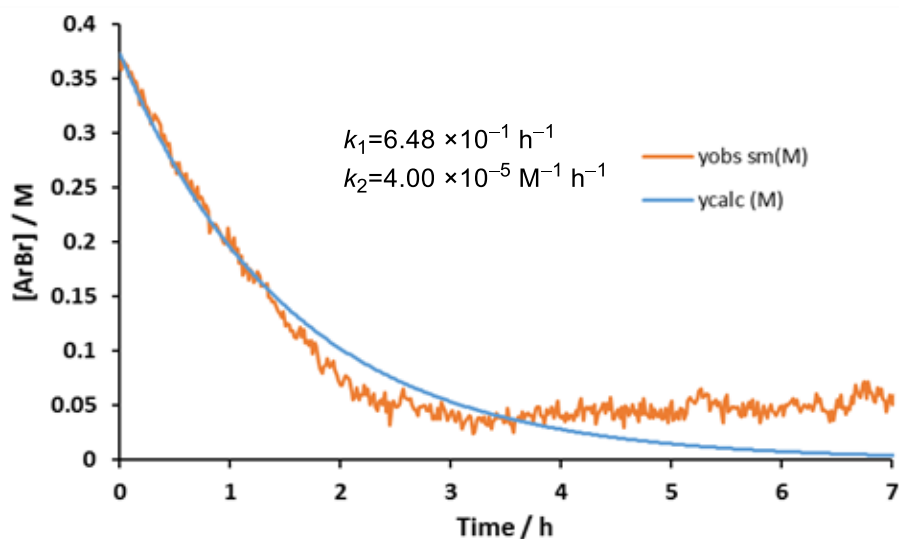


**Figure 68** Concentration vs. time curve and attempted data fit to the F-W 2-step mechanism for 2.5 mol% catalyst loading. The resultant rate constant  $k_2$  has been corrected by using a stoichiometry factor of 40.  $k_1$  confidence intervals: 95% =  $2.8 \times 10^{-1} - 8.8 \times 10^{-1} \text{ hr}^{-1}$ ; 99% =  $1.5 \times 10^{-1} - 9.5 \times 10^{-1} \text{ hr}^{-1}$ .  $k_2$  confidence intervals: 95% = N/A; 99%: N/A.

As before, upon attempting to fit the autocatalysis kinetic model to the curve displayed in Figure 68, inspection shows a poor fit. Figure 69 supports this by showing a wide, asymmetric distribution of  $k_1$  values at fixed  $k_2$  intervals, and little change in  $k_2$  at different  $k_1$  values, as shown by the flat line.

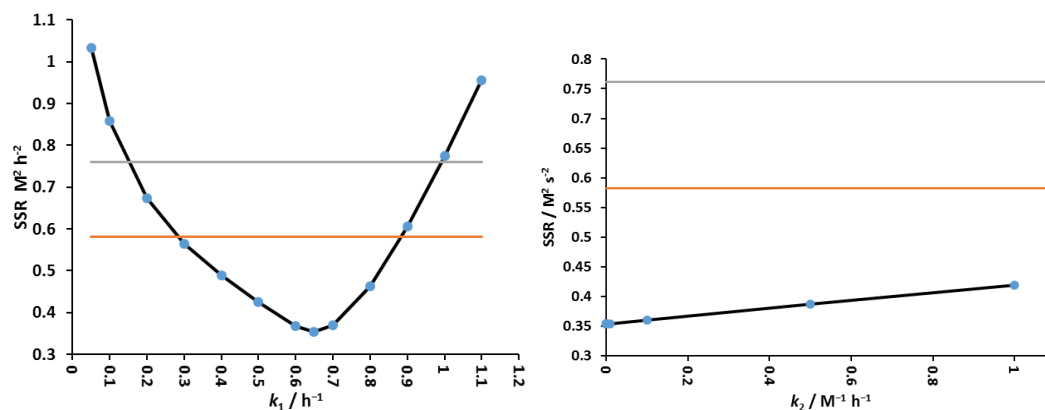


**Figure 69** Visual representations of the 95% (brown line) and 99% (grey line) confidence limits for the limits for  $k_1$  (left) and  $k_2$  (right) for the attempted F-W 2-step curvefit displayed in Figure 68.

Analysis of the kinetic data from several viewpoints has allowed for a more complete mechanistic picture to be constructed. The non-linear relationship between  $k_{\text{obs}}$  and catalyst loading (shown in Figure 57) shows that the increase in reaction rate is not directly proportional to the catalyst concentration, as would be expected in a reaction catalysed by a homogeneous Pd species. Indeed the evidence provided in Figure 59 of an order of 0.26 ( $\pm 0.02$ ) with respect to Pd between the catalyst loadings of 0.1 and 2.5 mol% shows that each time the [Pd] was doubled the rate increased by a factor of  $\sqrt[4]{n-1}$ . It is also apparent that a) the drop in TOF upon decreasing the Pd catalyst loading from 0.1 to 0.05 mol% (in contrast with the increase in TOF when decreasing Pd catalyst loading from 2.5 to 0.1 mol%) and b) the poorer fit of the kinetic data above 0.1 mol% Pd catalyst loading to the F-W 2-step model may denote a change in the nature of the catalytic species. This change is facilitated by a decreased Pd concentration and catalyst-substrate ratio. The high quality data fit of reactions with low Pd concentrations (0.05 mol%,  $1.80 \times 10^{-4}$  mol dm<sup>-3</sup>) with the F-W 2-step mechanism further supports the hypothesis that under these conditions, surface/cluster catalysis is occurring.

With the evidence given thus far it is plausible to suggest that at all catalyst loadings tested whilst under hydrous conditions – in the presence of  $\text{K}_4[\text{Fe}(\text{CN})_6] \cdot 3\text{H}_2\text{O}$  – PdNPs are likely to be present and catalytically relevant. It is expected that under these working reaction conditions that any catalytically competent Pd cluster species will not exist beyond a single closed shell of Pd atoms (*i.e.* up to 13 atoms in an icosahedral cluster at lowest surface energy) and of the structure type **83**, discussed in Chapter 5.<sup>136</sup>

### Mercury poisoning test

In order to further test the presence of surface catalysis it was possible to carry out a  $\text{Hg}^0$  poisoning experiment. The addition of  $\text{Hg}^0$  to a metal-catalysed reaction to establish the occurrence of heterogeneous catalysis is a well-established and widely used test.<sup>77, 80, 142</sup> Although the prevention of catalysis by formation of a catalyst- $\text{Hg}^0$  amalgam provides good evidence for the presence of catalytically active nanoclusters, it is not conclusive and has various complications involved. In order to ensure effective contact between  $\text{Hg}^0$  and the entire reaction system, a large excess must be used with respect to the catalyst (200 eq.) and the reaction mixture must be stirred efficiently. In addition to this,  $\text{Hg}^0$  may engage in unwanted side reactions with arylhalides, *i.e.* organomercurial formation<sup>143</sup> and their cross-coupling *via* Pd,<sup>144</sup> so reaction conversions have to be calculated with care. In this case it was possible to observe that the reaction had stopped and no further side-reactions occurred by monitoring the change of both starting material (C=O stretch at  $1727\text{ cm}^{-1}$ ) and product (C≡N stretch at  $2238\text{ cm}^{-1}$ ) by IR spectroscopic analysis and by the absence of any other incriminating species in the  $^1\text{H}$  NMR spectrum of the crude reaction mixture.

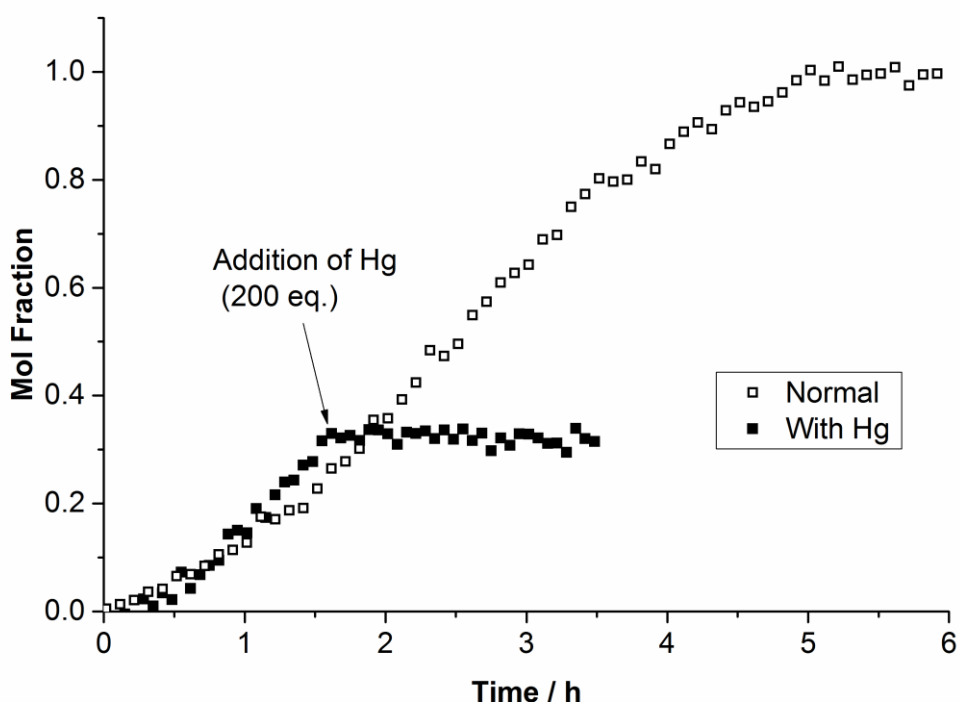


**Figure 70 Mercury drop test experiment. Reaction conditions: **47** (0.5 mol%),  $\text{K}_4[\text{Fe}(\text{CN})_6]\cdot 3\text{H}_2\text{O}$  (0.22 eq.),  $\text{Na}_2\text{CO}_3$  (1 eq.),  $\text{N}_2$ ,  $120\text{ }^\circ\text{C}$ , DMAc. Hg (200 eq. with respect to Pd) added with vigorous stirring after 93 mins.**

To carry out the Hg poisoning experiment Hg (200-fold excess relative to Pd) was added to the vigorously stirred cyanation reaction of **65** catalysed by **47** (0.5 mol%), whilst the

catalyst was achieving its highest TOF after 93 minutes. Upon addition of Hg, the cyanation reaction came to a complete halt, providing a positive outcome for the presence of catalytically active Pd nanoclusters (Figure 70).

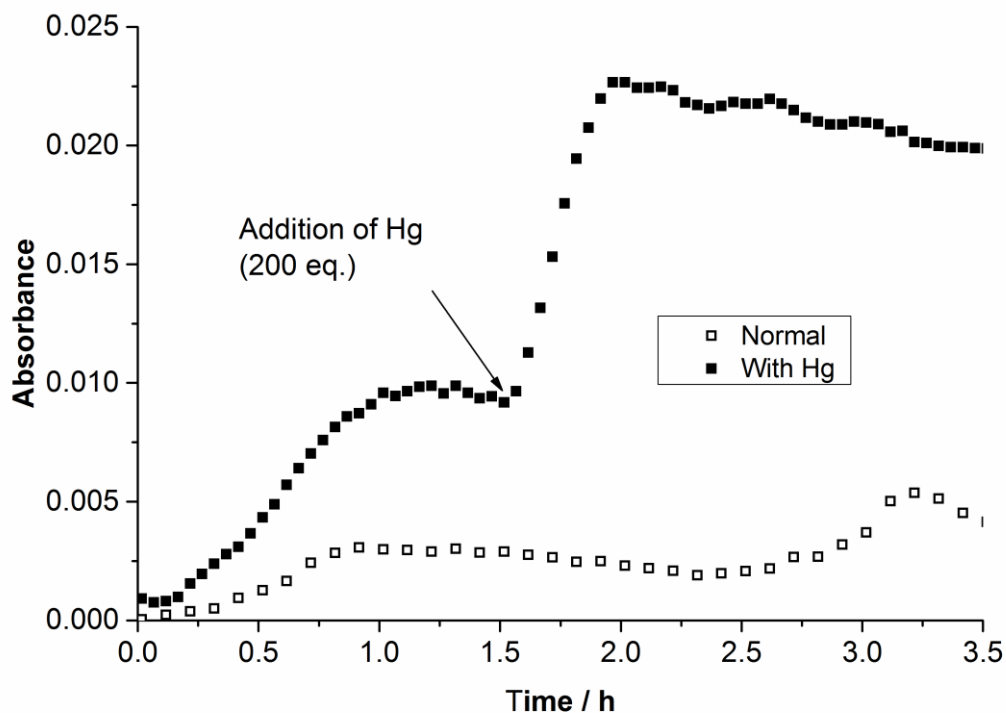


**Figure 71** Dissolution profile of “[Fe(CN)<sub>6</sub>]<sup>4-</sup>” (followed by monitoring IR absorbance at 2045 cm<sup>-1</sup>) under normal conditions and during Hg poisoning experiment. Reaction conditions: 47 (0.5 mol%), K<sub>4</sub>[Fe(CN)<sub>6</sub>·3H<sub>2</sub>O (0.22 eq.), Na<sub>2</sub>CO<sub>3</sub> (1 eq.), N<sub>2</sub>, 120 °C, DMAc. Hg (200 eq. with respect to Pd) added with vigorous stirring after 93 mins.

Comparison of the effect of Hg on the cyanation reaction with respect to the concentration of “[Fe(CN)<sub>6</sub>]<sup>4-</sup>” in solution (Figure 71) shows that as the rate of catalysis increases under normal conditions (in the absence of Hg), after *ca.* 1 hour this rate competes with the rate of dissolution of “[Fe(CN)<sub>6</sub>]<sup>4-</sup>”. At this point “[Fe(CN)<sub>6</sub>]<sup>4-</sup>” appears to reach a steady state, drip feeding <sup>-</sup>CN into the reaction mixture by a solubility dictated equilibrium. However, upon quenching the reaction with Hg, a sharp increase in concentration of “[Fe(CN)<sub>6</sub>]<sup>4-</sup>” occurs after all the catalytically competent Pd is sequestered. At two hours, “[Fe(CN)<sub>6</sub>]<sup>4-</sup>” reaches the solubility limit, the gradual decrease from here on is more than likely caused by its slow precipitation, as observed in Figure 77. This shows that in the presence of Hg, there is no catalytically competent Pd present to facilitate transmetalation of <sup>-</sup>CN, and therefore maintain a steady-state concentration of “[Fe(CN)<sub>6</sub>]<sup>4-</sup>”.

#### 4.4. Studying the absorbance at 2045 cm<sup>-1</sup>

Throughout the kinetic studies it was found that a series of peaks at *ca.* 2045  $\text{cm}^{-1}$  grew in immediately after catalyst addition as was first shown in Figure 52, which then disappeared throughout the course of the reaction as the product was formed.

#### 4.4.1. Characterisation of the species responsible for the absorbance

The peak at 2045  $\text{cm}^{-1}$  was initially hypothesised as belonging to belong to free  $\text{CN}^-$ . In order to probe this hypothesis an experiment where KCN (equimolar to equivalent  $\text{CN}^-$  available in the reaction mixture from  $\text{K}_4[\text{Fe}(\text{CN})_6]\cdot 3\text{H}_2\text{O}$ ) was added to DMAc at 120 °C and studied by ReactIR. (Figure 73)

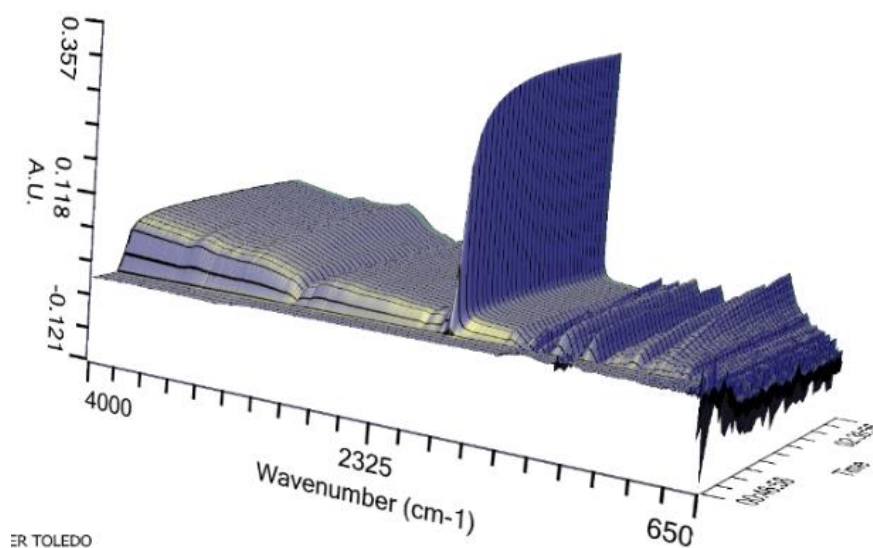
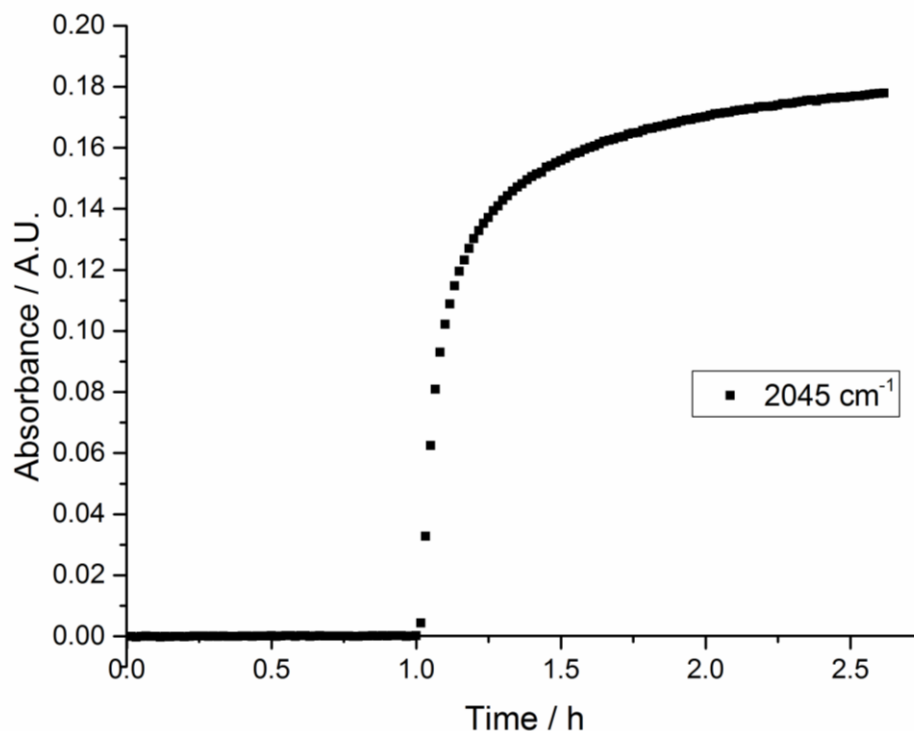


Figure 72 3D *in situ* IR spectra of KCN in DMAc at 120 °C.



**Figure 73** Time resolved dissolution of KCN in DMAc at 120 °C, monitored at 2045 cm<sup>-1</sup>.

It was evident from the curve displayed in Figure 73 that although the species present under working conditions provides an absorption at the same energy (2045 cm<sup>-1</sup>), the single absorbance peak of KCN contrasts with the species observed under working conditions, which contains multiple absorbance frequencies between 2040 and 2056 cm<sup>-1</sup>. This evidence supports that the functional group observed is likely to be a metal cyanide, but not free <sup>-</sup>CN.

In order to better understand the rate of formation of this “intermediate” species in the absence of Pd, a control reaction was performed under standard reaction conditions, but without the addition of a Pd catalyst. It was found that the rate of growth of the absorbance at 2045 cm<sup>-1</sup> was significantly higher, and no product was formed (Figure 74, Figure 75).

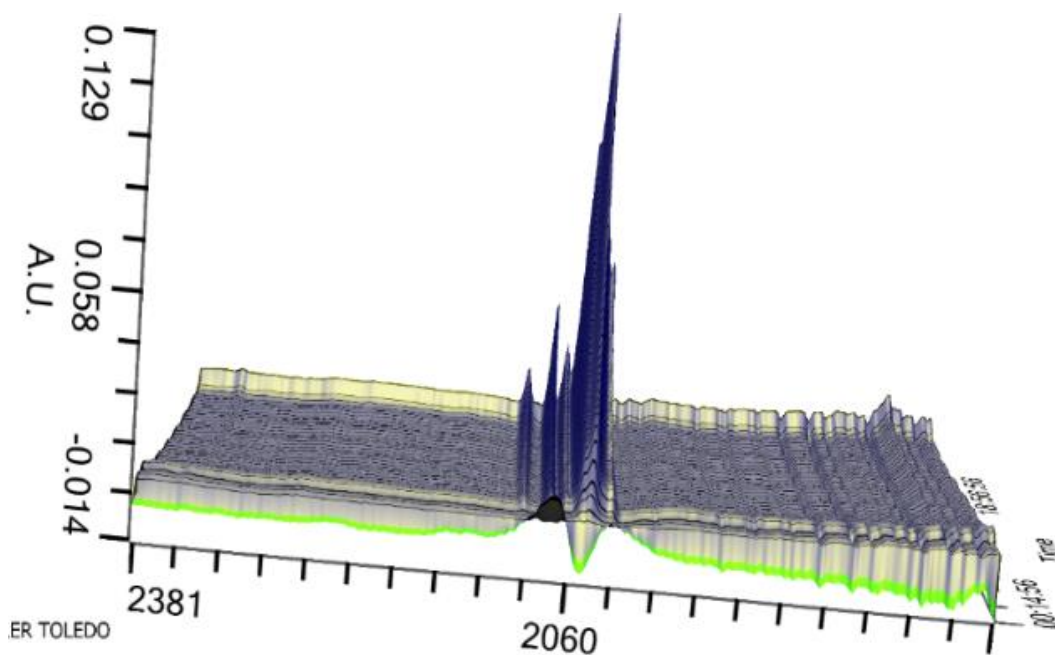


Figure 74 *In situ* IR spectrum of  $K_4[Fe(CN)_6] \cdot 3H_2O$ ,  $Na_2CO_3$  and **65** in DMAc at 120 °C.

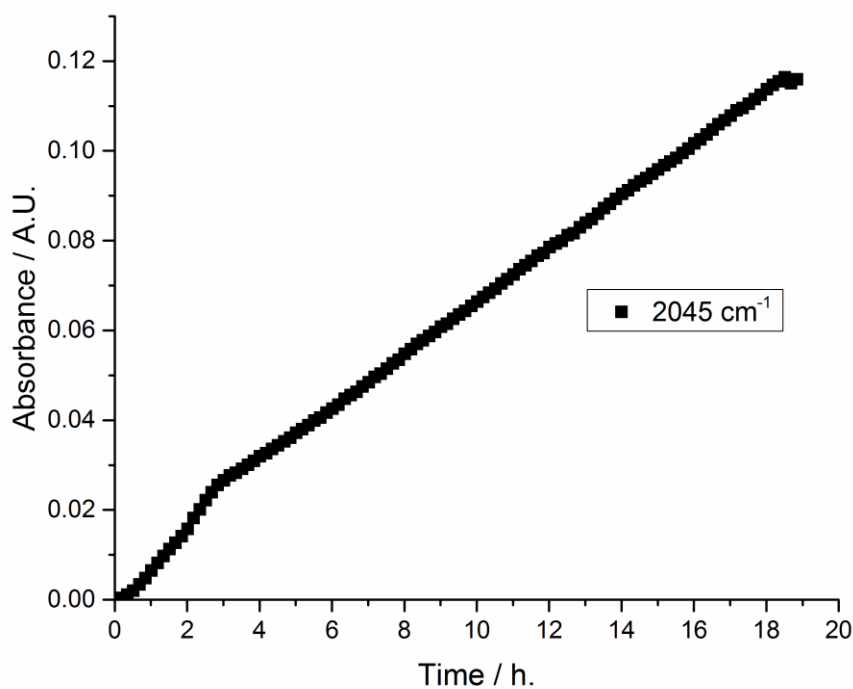
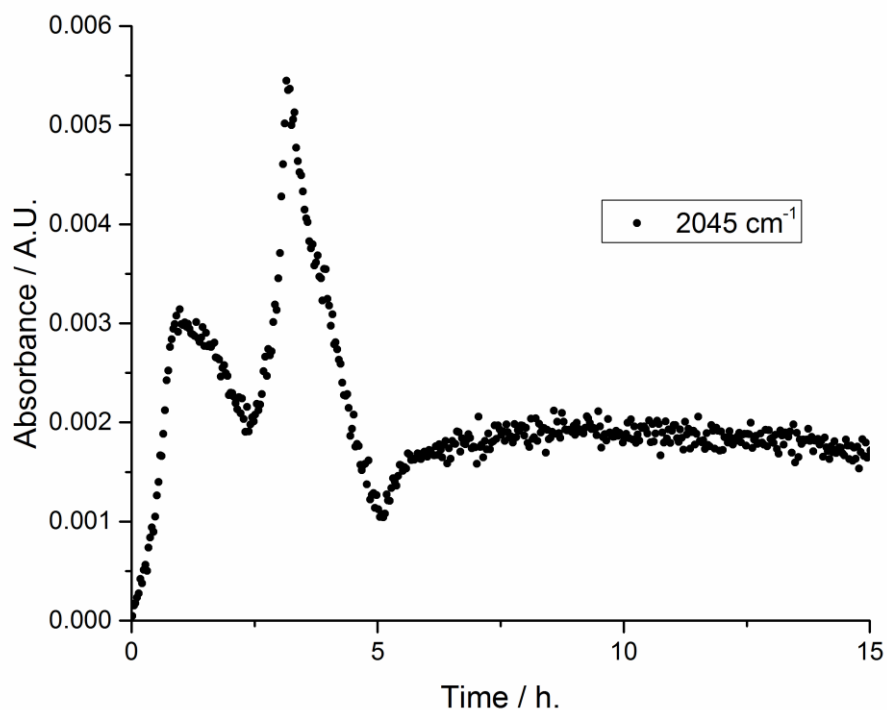


Figure 75 Time resolved study of the absorbance at  $2045\text{ cm}^{-1}$ . Reaction conditions: **65** (1 eq.),  $K_4[Fe(CN)_6] \cdot 3H_2O$  (0.22 eq.),  $Na_2CO_3$  (1 eq.),  $N_2$ , 120 °C, DMAc.

The experiment outlined in Figure 74 and Figure 75 does not provide full characterisation of the species corresponding to the absorbance at  $2045\text{ cm}^{-1}$ , it is clear however that it has a role in the reaction, as its reaction profile differs significantly under reaction conditions in the presence (Figure 76) and absence of a catalyst.



**Figure 76** Time resolved study of the absorbance at  $2045\text{ cm}^{-1}$ . Reaction conditions: **47** (0.5 mol%),  $\text{K}_4[\text{Fe}(\text{CN})_6]\cdot 3\text{H}_2\text{O}$  (0.22 eq.),  $\text{Na}_2\text{CO}_3$  (1 eq.),  $\text{N}_2$ ,  $120\text{ }^\circ\text{C}$ , **DMAc**.

These lower absorbance values indicate a lower concentration of the species in solution in the presence of Pd. This therefore further supports the hypothesis of it corresponding to a metal cyanide species (presumably Fe), where the concentration is controlled under standard reaction conditions (*i.e.* in the presence of Pd) at steady-state *via* transmetallation to Pd and consumption in a productive catalytic cycle.

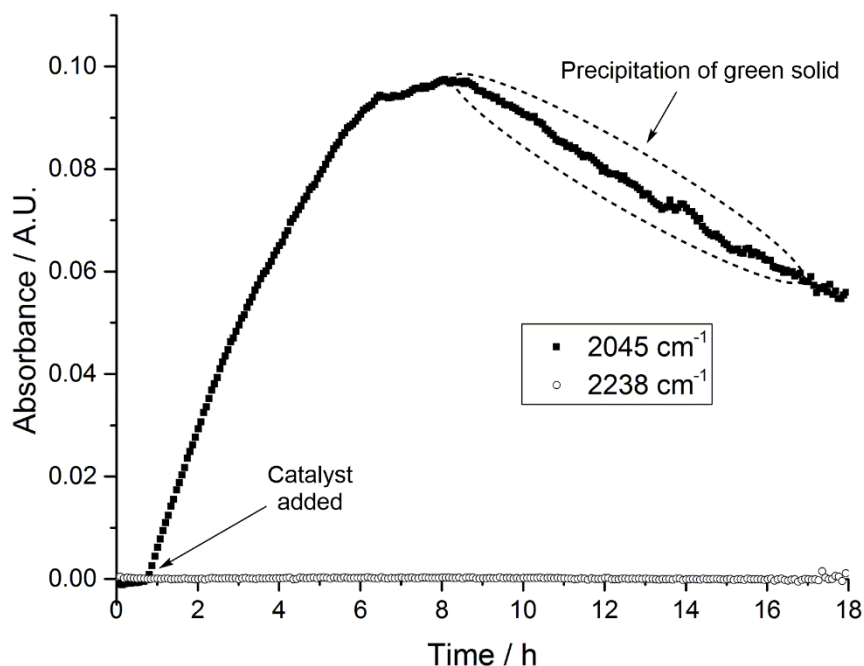


**Figure 77** Raw absorbance data showing the metal cyanide and product (**69**) absorbances at  $2045\text{ cm}^{-1}$  and  $2238\text{ cm}^{-1}$  respectively under anhydrous reaction conditions in the absence of  $\text{Na}_2\text{CO}_3$ . Reaction conditions: **47** (0.05 mol%), **65** (1 eq.),  $\text{K}_4[\text{Fe}(\text{CN})_6]$  (0.22 eq.),  $\text{N}_2$ ,  $120\text{ }^\circ\text{C}$ , DMAc.

It has been hypothesised by Buchwald *et al.* that the role of  $\text{Na}_2\text{CO}_3$  in the cyanation reaction is important to aid transmetallation of  $\text{CN}^-$  from  $[\text{Fe}(\text{CN})_6]^{4-}$  to Pd.<sup>107</sup> In a series of experiments devised to test this theory (outlined in full in Section 5.6) it was found that by performing the reaction under anhydrous conditions (using  $\text{K}_4[\text{Fe}(\text{CN})_6]$  as a cyanating agent) with 0.05 mol% catalyst loading but in the absence of  $\text{Na}_2\text{CO}_3$ , no product was formed. Figure 77 shows the raw absorbance data for the formation of the intermediate cyanide species ( $2045\text{ cm}^{-1}$ ) immediately following addition of **47**, after 8 hours the strength of the absorbance began to decrease. This was concomitant with the precipitation of a green solid.

When the ATR-IR spectrum of the green precipitate (Figure 78, Figure 79) was compared with the ATR-IR spectrum of  $\text{K}_4[\text{Fe}(\text{CN})_6]$ , (Figure 80, Figure 81) it was evident that the species responsible for the absorbance at  $2045\text{ cm}^{-1}$ , under working conditions, corresponded to solubilised  $[\text{Fe}(\text{CN})_6]^{4-}$ .

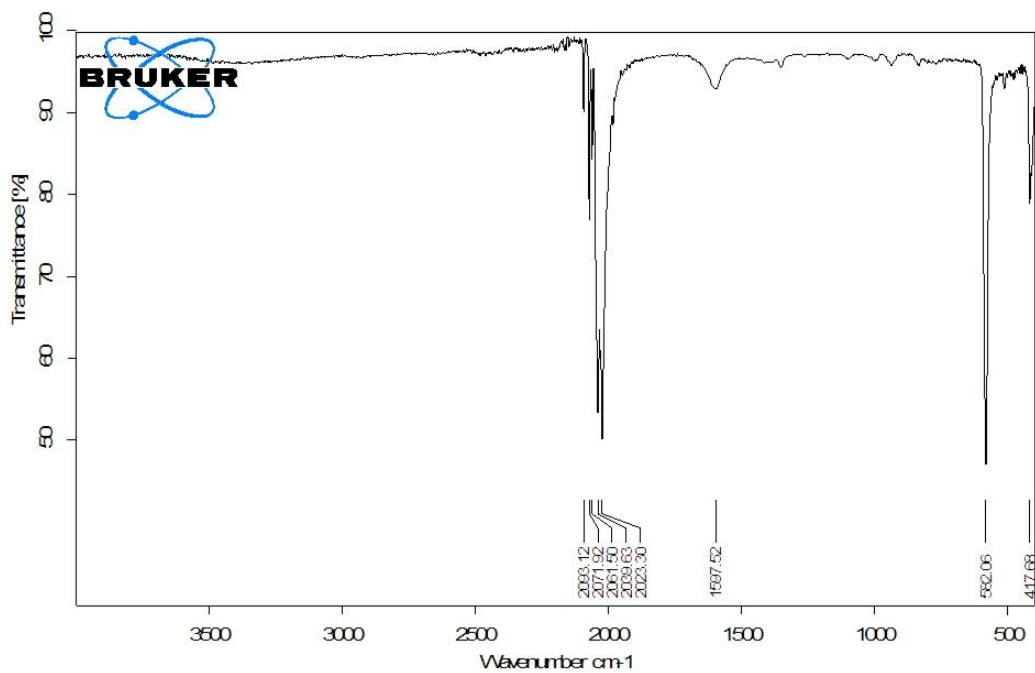


Figure 78 ATR-IR spectrum of green precipitate formed after 8 hours under reaction conditions but in the absence of  $\text{Na}_2\text{CO}_3$ . Reaction conditions: **47** (0.05 mol%), **65** (1 eq.),  $\text{K}_4[\text{Fe}(\text{CN})_6]$  (0.22 eq.), DMAc,  $\text{N}_2$ , 120 °C.

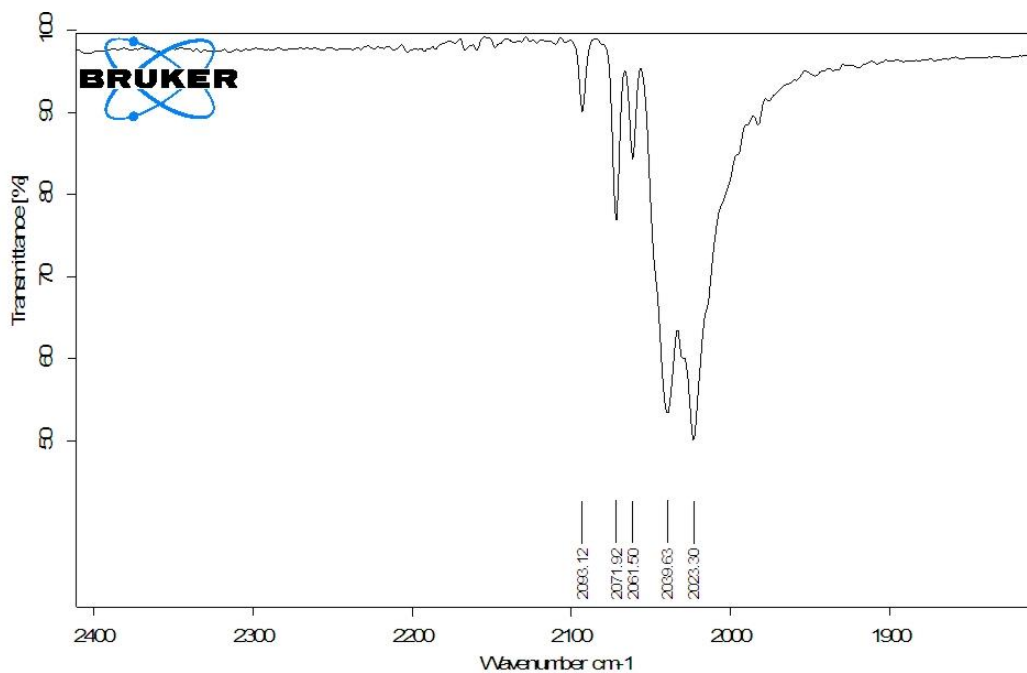


Figure 79 Expanded section of IR-region between 1800-2400  $\text{cm}^{-1}$  of the ATR-IR spectrum shown in Figure 78.

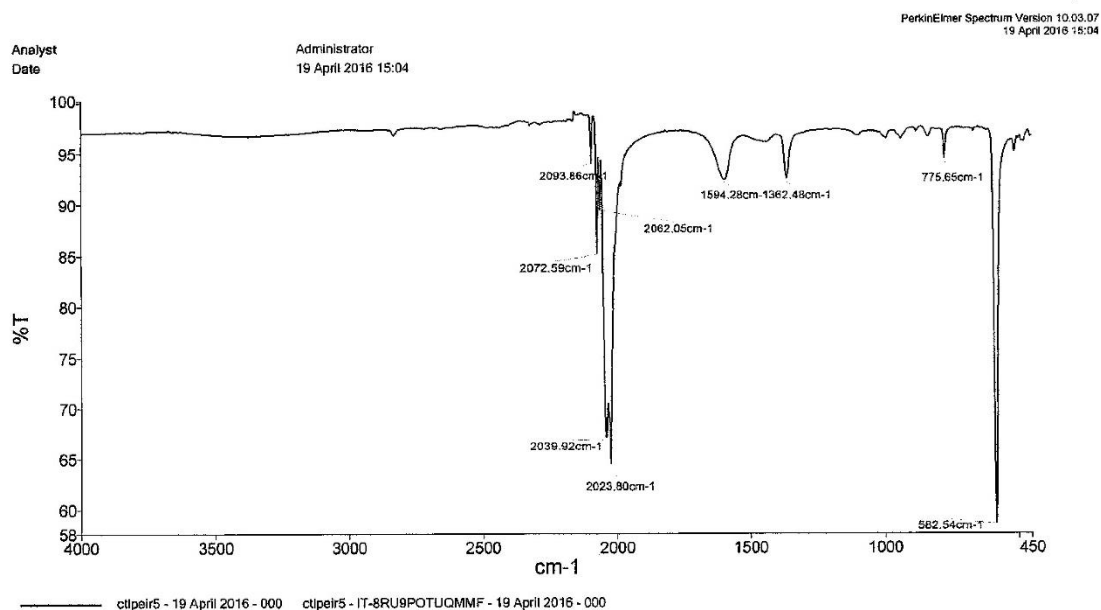


Figure 80 ATR-IR spectrum of  $K_4[Fe(CN)_6]$ .

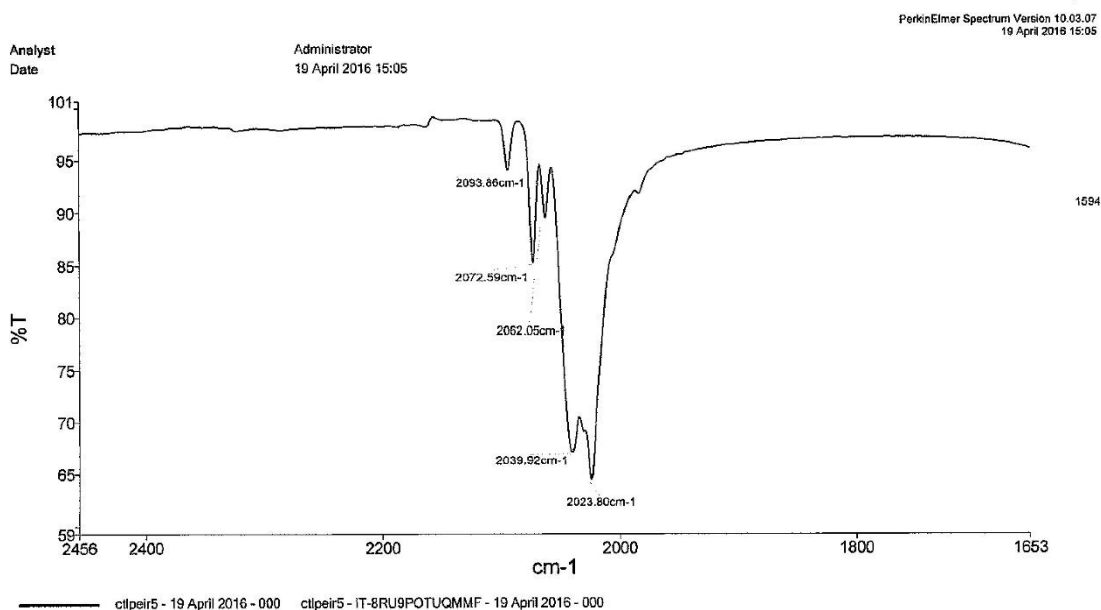
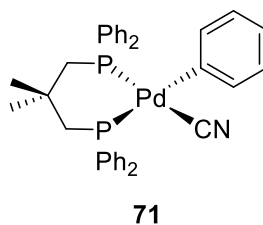


Figure 81 Expanded section of IR-region between 1800-2400  $cm^{-1}$  of the ATR-IR spectrum shown in Figure 80.

#### 4.4.2. Investigating concentration effects of $[Fe(CN)_6]^{4-}$ on catalysis

Now, given the confirmation of the identity of the absorbance at 2045  $cm^{-1}$  as  $[Fe(CN)_6]^{4-}$ , it is possible to investigate the effect of reaction conditions upon the concentration of  $[Fe(CN)_6]^{4-}$ . ReactIR allows for the real-time, qualitative correlation of catalyst loading with  $[Fe(CN)_6]^{4-}$  concentration. At catalyst loadings from 0.05 mol% to 2.5 mol% it was noted

that there was a consistent trend where metal cyanide concentration in solution began to increase immediately after the addition of Pd, followed by a decrease as the reaction reached its optimum rate. However upon further inspection of the kinetic traces, Figure 83, a marked difference is evident between the two lowest catalyst loadings, 0.1 and 0.05 mol%, from the rest (Figure 83). Although the characteristic initial increase of  $[\text{Fe}(\text{CN})_6]^{4-}$  is present, it is much less pronounced when the catalyst loadings are  $> 0.1$  mol%. This can be attributed to the increased rate of transmetalation observed at higher catalyst loadings. Any catalyst decomposition attributed to cyanide poisoning would be expected to have significant effects on the reaction rates of those performed at very low catalyst loadings, however even in the presence of high  $[\text{Fe}(\text{CN})_6]^{4-}$  concentrations (at 0.05 mol%) efficient catalyst turn over still occurred. It has been shown that in the presence of  $\text{PPh}_3$  the rate constants at Pd for  $\text{I}^-/\text{CN}$  exchange,  $\text{PPh}_3^-/\text{CN}$  exchange and  $\text{Ph}-\text{CN}$  reductive elimination decrease in the order  $k_{\text{I}/\text{CN}} > k_{\text{PPh}_3/\text{CN}} \geq k_{\text{RE}} \times 100$ .<sup>93</sup> This coupled with the fact that stoichiometric studies indicate that reductive elimination occurs exclusively from the tricoordinate complex  $[\text{Pd}(\text{Ar})(\text{CN})_2]^-$  or from complexes such as **71**, (Figure 82) means that in the absence of phosphine, predissociation of a cyanide group is required from  $[\text{Pd}(\text{Ar})(\text{CN})_3]^{2-}$  before reductive elimination can occur. Given that this process is very unfavourable if catalyst poisoning is present, the absence of catalyst deactivation at low catalyst loadings therefore shows that no cyanide catalyst poisoning occurred under these conditions.



**Figure 82** Hartwig *et al.* showed that formation of  $\text{ArCN}$  from complexes such as **71** was remarkably fast (first order rate constant =  $11 \times 10^{-4} \text{ s}^{-1}$ ) at room temperature.<sup>109</sup>

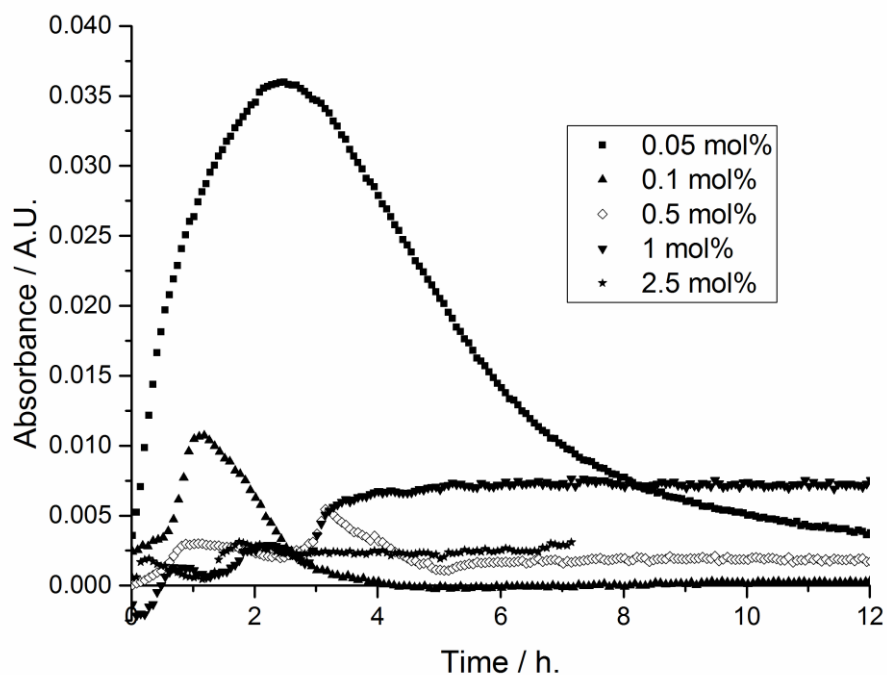


**Figure 83** Monitoring the change in absorbance at  $2045\text{ cm}^{-1}$  allows a qualitative insight into the amount of  $[\text{Fe}(\text{CN})_6]^{4-}$  in solution throughout the course of the reaction when carried out with differing 47 catalyst loadings. Reaction conditions: 47 (0.05 – 2.5 mol%),  $\text{K}_4[\text{Fe}(\text{CN})_6]\cdot 3\text{H}_2\text{O}$  (0.22 eq.),  $\text{Na}_2\text{CO}_3$  (1 eq.),  $\text{N}_2$ ,  $120\text{ }^\circ\text{C}$ , DMAc.

At a low Pd loading of 0.05 mol%, it is clear that despite increased concentrations of “ $^- \text{CN}$ ”, Pd is still capable of acting with very high efficiency, achieving TONs of 1960 and TOFs comparable with other concentrations ( $0.0453\text{ s}^{-1}$ ). This dispel the myth that “high  $[\text{CN}^-]$  causes extensive catalyst poisoning” and (provided this reaction is catalysed by PdNPs, as our kinetic results suggest) is supportive evidence for Frech’s claim that heterogeneous Pd is somewhat immune to cyanide poisoning from  $\text{K}_4[\text{Fe}(\text{CN})_6]$ . It is therefore clear from these studies that correctly balancing the concentration of both Pd and cyanide is essential to achieving the most active catalyst system. In light of this, further kinetic experiments were carried out in order to study the effect of changing cyanide equivalences (Figure 84).

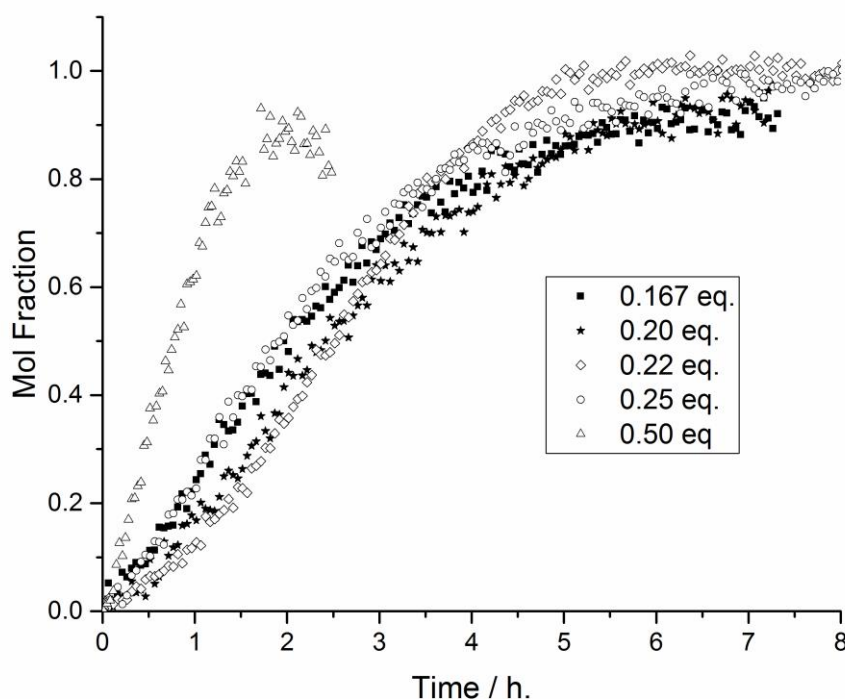


**Figure 84** Varying equivalence of  $\text{K}_4[\text{Fe}(\text{CN})_6]\cdot 3\text{H}_2\text{O}$  has little effect on reaction rate, until a vast excess of “ $\text{CN}^-$ ” is added. Reaction conditions: **47** (0.5 mol%),  $\text{K}_4[\text{Fe}(\text{CN})_6]\cdot 3\text{H}_2\text{O}$  (0.167 – 0.5 eq.),  $\text{Na}_2\text{CO}_3$  (1 eq.),  $\text{N}_2$ , 120 °C, DMAc.

By varying the number of equivalents of  $\text{K}_4[\text{Fe}(\text{CN})_6]\cdot 3\text{H}_2\text{O}$  (Figure 84) it is clear that in the presence of 0.167 equivalents of (exactly 1 equivalent of  $\text{CN}^-$  per equivalent of substrate) all six cyanides are released from Fe, facilitating complete conversion. Interestingly, the rate of reaction does not appear to be affected by which equivalent of  $\text{CN}^-$  is removed from the Fe centre. It would be expected that upon removal of each equivalent of  $\text{CN}^-$  that the strength of both L–M  $\sigma$ -donation and subsequently M–L  $\pi$ -back bonding to the remaining cyanide ligands to increase, thus making them incrementally more difficult to remove.<sup>145</sup> The efficiency with which transmetalation occurs does not appear to be affected by increased Fe–CN bond strength under these conditions.

In summary, varying the equivalences of  $\text{K}_4[\text{Fe}(\text{CN})_6]\cdot 3\text{H}_2\text{O}$  has little effect upon reaction rate, overall yield or the concentration of  $[\text{Fe}(\text{CN})_6]^{4-}$  in solution (Figure 85) until 0.5 eq. of  $\text{K}_4[\text{Fe}(\text{CN})_6]\cdot 3\text{H}_2\text{O}$  is added, providing a vast excess (3 eq.) of  $\text{CN}^-$ . This appears to further confirm that increased cyanide concentration has limited detrimental effect on catalyst efficiency under these conditions, in fact when a large excess is used it dramatically increases the rate of reaction. It is of note that at both 0.167 and 0.5 eq. of  $\text{K}_4[\text{Fe}(\text{CN})_6]\cdot 3\text{H}_2\text{O}$ , the overall TON is decreased slightly; with both reactions reached reaction completion at 88% conversion, rather than quantitative, as observed in the presence of 0.22 eq. of

$\text{K}_4[\text{Fe}(\text{CN})_6]\cdot 3\text{H}_2\text{O}$ . When the reaction equivalents of  $\text{K}_4[\text{Fe}(\text{CN})_6]\cdot 3\text{H}_2\text{O}$  is increased from 0.25 to 0.5, the improved in reaction rate is accompanied by a dramatic increase in  $[\text{Fe}(\text{CN})_6]^{4-}$  concentration (Figure 85).

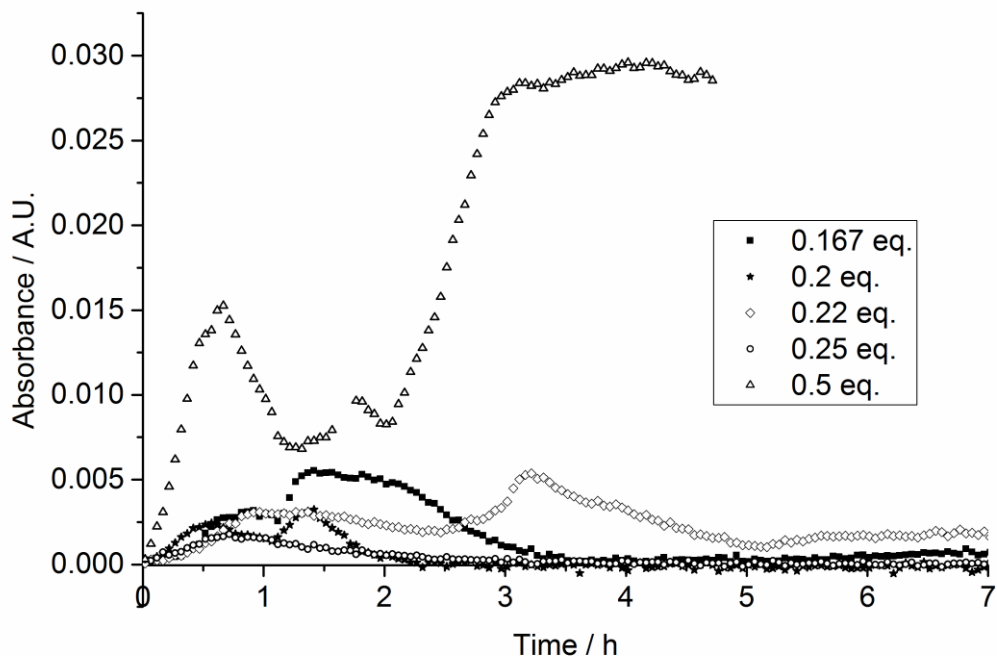


**Figure 85** Real time analysis of  $[\text{Fe}(\text{CN})_6]^{4-}$  (at  $2045\text{ cm}^{-1}$ ) upon variation of  $\text{K}_4[\text{Fe}(\text{CN})_6]\cdot 3\text{H}_2\text{O}$  equivalents. Reaction conditions: **47** (0.5 mol%),  $\text{K}_4[\text{Fe}(\text{CN})_6]\cdot 3\text{H}_2\text{O}$  (0.167 – 0.5 eq.),  $\text{Na}_2\text{CO}_3$  (1 eq.),  $\text{N}_2$ ,  $120\text{ }^\circ\text{C}$ , DMac.

Inspection of Figure 85 allows a qualitative viewpoint on the concentration of  $[\text{Fe}(\text{CN})_6]^{4-}$  in solution throughout the course of the reactions, and it is clear to see that there is little difference between 0.167 – 0.25 eq. of  $\text{K}_4[\text{Fe}(\text{CN})_6]\cdot 3\text{H}_2\text{O}$ . However when the equivalence is increased to 0.5, the  $[\text{Fe}(\text{CN})_6]^{4-}$  concentration is considerably higher throughout the course of reaction. For 0.167 – 0.25 eq., after reaction completion, the majority of  $\text{K}_4[\text{Fe}(\text{CN})_6]\cdot 3\text{H}_2\text{O}$  has also been consumed by the reaction, so its concentration in solution drops to a steady, low level. However if every equivalent of cyanide is utilised from each molecule of  $[\text{Fe}(\text{CN})_6]^{4-}$ , when 0.5 eq. was used there would still be 2.12 equivalents of  $\text{K}_4[\text{Fe}(\text{CN})_6]\cdot 3\text{H}_2\text{O}$  present after reaction completion (88% conversion). Figure 85 shows that after 2 hours (reaction completion)  $[\text{Fe}(\text{CN})_6]^{4-}$  continues to dissolve until the mixture appears to reach saturation point after 3 hours.

#### 4.5. Conclusions

When  $\text{K}_4[\text{Fe}(\text{CN})_6]\cdot 3\text{H}_2\text{O}$  is used as a cyanating agent and **47** as a precatalyst, kinetic evidence suggests that the reaction proceeds *via* heterogeneous catalysis. This hypothesis has been tested and supported using multiple complementary methods including non-linear curve

fitting using the Finke-Watzky 2-step mechanism.<sup>33</sup> When catalyst loadings and concentrations were low (0.05 mol%,  $1.80 \times 10^{-4}$  mol dm<sup>-3</sup> and 0.1 mol%,  $3.6 \times 10^{-4}$  mol dm<sup>-3</sup>) the quality of fit of the sigmoidal reaction profiles was good. However, above 0.1 mol% the data fit was poor, suggesting a change in the nature of the active catalyst when the Pd catalyst concentrations are above  $3.6 \times 10^{-4}$  mol dm<sup>-3</sup>.

It was also determined that decreasing Pd catalyst loadings from 2.5 to 0.1 mol% resulted in a dramatic increase in TOF, but upon decreasing from 0.1 to 0.05 mol%, the TOF was reduced. This is consistent with previous reports for reactions shown to be catalysed by PdNPs.<sup>7-8, 21</sup> This drop in TOF and  $k_{\text{obs}}$  is also coherent with the change in catalytic species insinuated by the Finke-Watzky analysis. The order of reaction with respect to Pd between the catalyst loadings 0.1 mol% and 2.5 mol% was calculated as 0.26 ( $\pm 0.02$ ), indicating the role of a small Pd cluster species as the active catalyst. This has been tentatively assigned to a structure type discussed further in Section 5.4.

Under the reaction conditions screened **47** is a competent catalyst, providing excellent yields for the arylcyanation of **65** with catalyst loadings as low as 0.05 mol%.

The characterisation of solubilised  $[\text{Fe}(\text{CN})_6]^{4-}$  as the absorbance at  $2045 \text{ cm}^{-1}$  has allowed for an unprecedented insight into the relationship between the rate of reaction and the concentration of hexacyanoferrate in solution. When the number of equivalents of  $\text{K}_4[\text{Fe}(\text{CN})_6] \cdot 3\text{H}_2\text{O}$  was increased to 0.5 from the usual 0.22 there was a small increase in the rate of reaction at the detriment of the catalyst TON. However, little change in the reaction rate was observed between 0.167 and 0.25 eq. of  $\text{K}_4[\text{Fe}(\text{CN})_6] \cdot 3\text{H}_2\text{O}$ . Upon decreasing Pd catalyst loadings below 0.1 mol%, the rate of transmetalation was found to be lower than the rate of solubilisation of  $\text{K}_4[\text{Fe}(\text{CN})_6] \cdot 3\text{H}_2\text{O}$ , leading to an increased concentration  $\text{K}_4[\text{Fe}(\text{CN})_6] \cdot 3\text{H}_2\text{O}$ .

These experiments focussed on measuring the catalytic efficacy of **47** and determination of the nature of the active Pd catalyst in arylcyanation reactions when under hydrous conditions. The results thus far are promising, and further investigation of  $\text{Pd}(\text{OAc})_2(\text{HNR}_2)_2$  complexes as precatalysts in arylcyanation reactions under anhydrous conditions has also been carried out, as detailed in Chapter 5.

## Chapter 5: Kinetic studies of the Pd(OAc)<sub>2</sub>(HNR<sub>2</sub>)<sub>2</sub> catalysed cyanation of *N*-benzyl-4-bromo-6-methylpyrid-2-one by *in situ* infrared spectroscopy under anhydrous conditions.

### 5.1 Screening of *trans*-Pd(OAc)<sub>2</sub>(HNR<sub>2</sub>)<sub>2</sub> precatalysts in an anhydrous, model Pd catalysed arylcyanation

Five monomeric Pd bisacetate, bisamine complexes (**48**, **47**, **52**, **51**, **53**) containing different sized secondary amine ligands, as outlined in Chapter 2, are shown in Figure 86. Their catalytic efficiencies were analysed under anhydrous conditions in the benchmark Pd catalysed arylcyanation reaction developed in Chapter 3, Scheme 52.

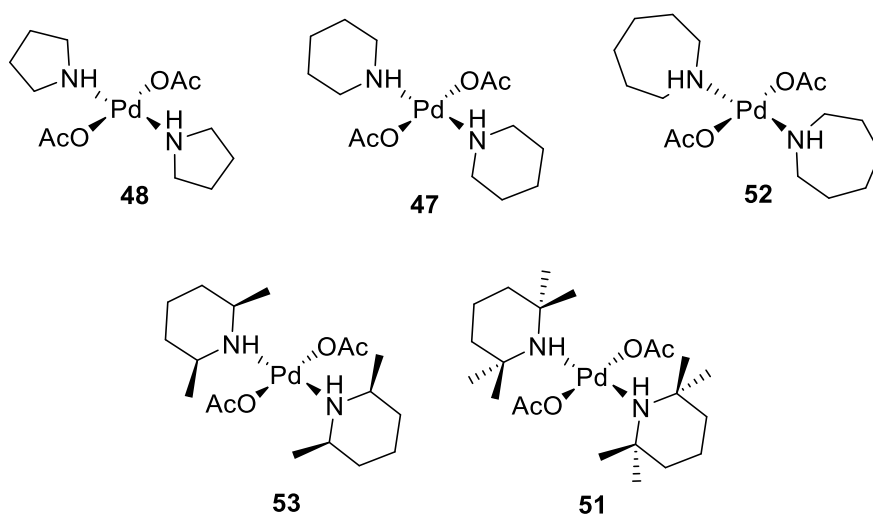
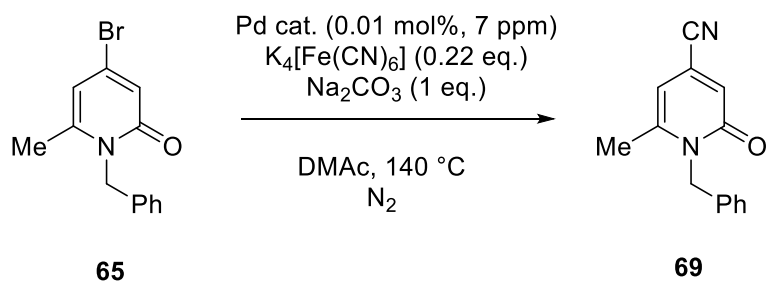


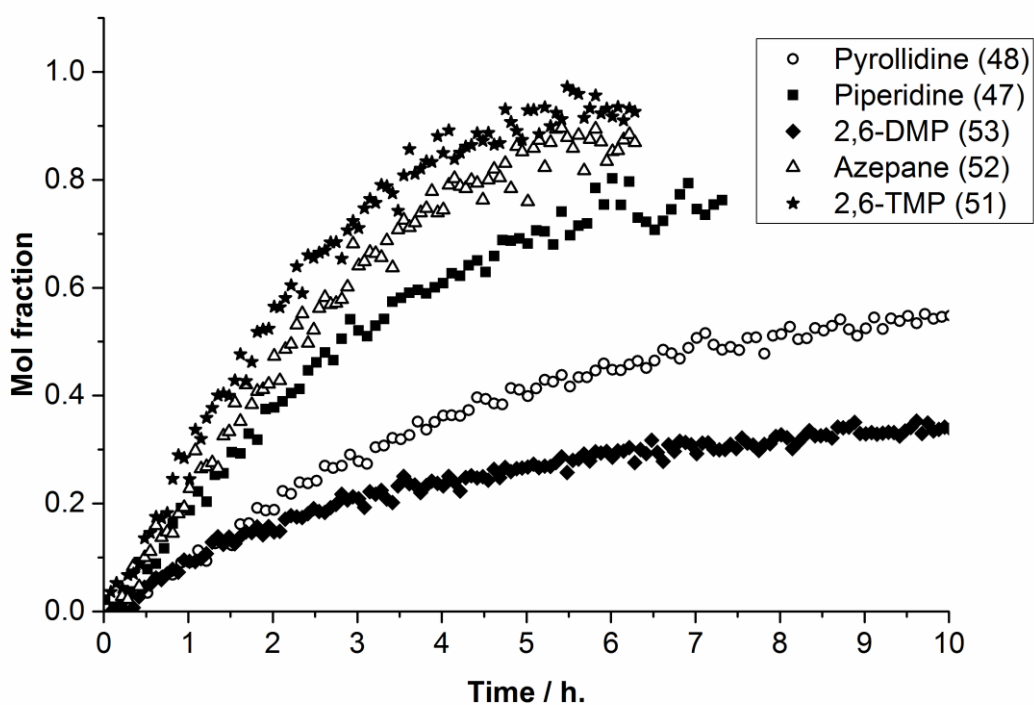
Figure 86 A series of *trans*-Pd(OAc)<sub>2</sub>(HNR<sub>2</sub>)<sub>2</sub> precatalysts.



**Scheme 52** The benchmark reaction developed for kinetic analysis of catalytic efficiency using *in situ* infrared spectroscopy.

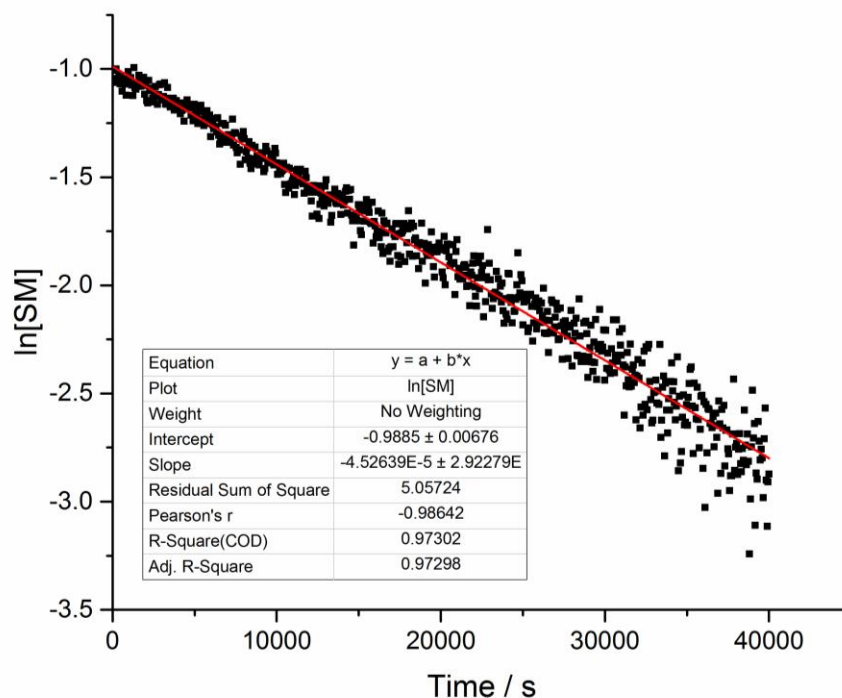
Previous work (Chapter 4) has shown that under arylcyanation conditions using  $\text{K}_4[\text{Fe}(\text{CN})_6] \cdot 3\text{H}_2\text{O}$  as a cyanide source results in kinetic behaviour characteristic of a reaction proceeding *via* heterogeneous catalysis following the activation of a homogeneous precatalyst.

Figure 87 shows a comparison of kinetic traces for the five  $\text{trans-Pd}(\text{OAc})_2(\text{HNR}_2)_2$  precatalysts using ultra-low loadings of Pd (0.01 mol%) at a Pd concentration of 72  $\mu\text{M}$ . The anhydrous salt  $\text{K}_4[\text{Fe}(\text{CN})_6]$  was formed by heating  $\text{K}_4[\text{Fe}(\text{CN})_6] \cdot 3\text{H}_2\text{O}$  to 80  $^\circ\text{C}$  under high vacuum (at least 0.1 mmHg) until the pressure remained stable – this typically took *ca.* 3 hours.



**Figure 87** Comparison of precatalyst activity in the cyanation of *N*-benzyl-4-bromo-6-methyl-2-pyridinone (**65**). Reaction conditions: Precatalyst (0.01 mol%, 72  $\mu$ M),  $K_4[Fe(CN)_6]$  (0.22 eq.),  $Na_2CO_3$  (1 eq.), DMAc,  $N_2$ , 140  $^\circ$ C.

The most noticeable trait about the reaction profiles shown in Figure 87 was their change in shape from sigmoidal, as was found when using  $K_4[Fe(CN)_6] \cdot 3H_2O$  as a cyanide source, to exponential growth, as would be expected of a first order reaction. A simple plot of  $\ln[\mathbf{65}]$  vs. time provided a straight line with a good quality linear fit, confirming this hypothesis.<sup>146</sup>



**Figure 88** Plotting ln[65] vs time (initial 40000 s) for the arylocyanation of 65 catalysed by precatalyst 47 provides a straight line with a good quality linear fit.

This dramatic change in reaction profile can only be attributed to a change in mechanism of catalysis. The complete lack of induction period even at very low catalyst loadings and concentrations (0.005 mol%, 36  $\mu$ M Pd, Figure 90) show that precatalyst activation (*i.e.* reduction of Pd<sup>II</sup> to catalytically active Pd<sup>0</sup> species) was incredibly fast. It also indicated that under anhydrous conditions, the formation of the active catalyst does not transpire *via* the Finke-Watzky 2-step autocatalytic surface growth mechanism. Despite this, work in chapter 4 showed that it is plausible for the precatalyst 47 to form multinuclear, catalytically active Pd species in the absence of the F-W 2 step mechanism. However, given i) the propensity of *trans*-Pd(OAc)<sub>2</sub>(HNR<sub>2</sub>)<sub>2</sub> complexes to thermally degrade; ii) the precedent for the formation of PdNPs from 47 under anhydrous conditions in C–H functionalisation reactions;<sup>110</sup> iii) previous reports of heterogeneous catalysis from homogeneous Pd precatalysts in arylocyanation reactions under anhydrous conditions;<sup>43</sup> the role of higher order Pd species as active catalyst species was still deemed plausible.

The best precatalysts under the reaction conditions were found to be 52 and 51 containing the azepane and 2,2,6,6-TMP ligands. The piperidine-derived precatalyst, 47, exhibited comparable activity up to 50% conversion to product and continued on to 75% within the same time frame. The pyrrolidine-derived precatalyst 48 was considerably less active than either 52, 51 or 47. Instead, 48 provided only 50% conversion after 10 hours. By comparison with all other precatalysts tested, the *cis*-2,6-dimethylpiperidine-derived precatalyst 53 was

poor and suffered from significant catalyst deactivation after 2 h. (ca. 15% conversion). This resulted in a total conversion of only 35% after 10 hours.

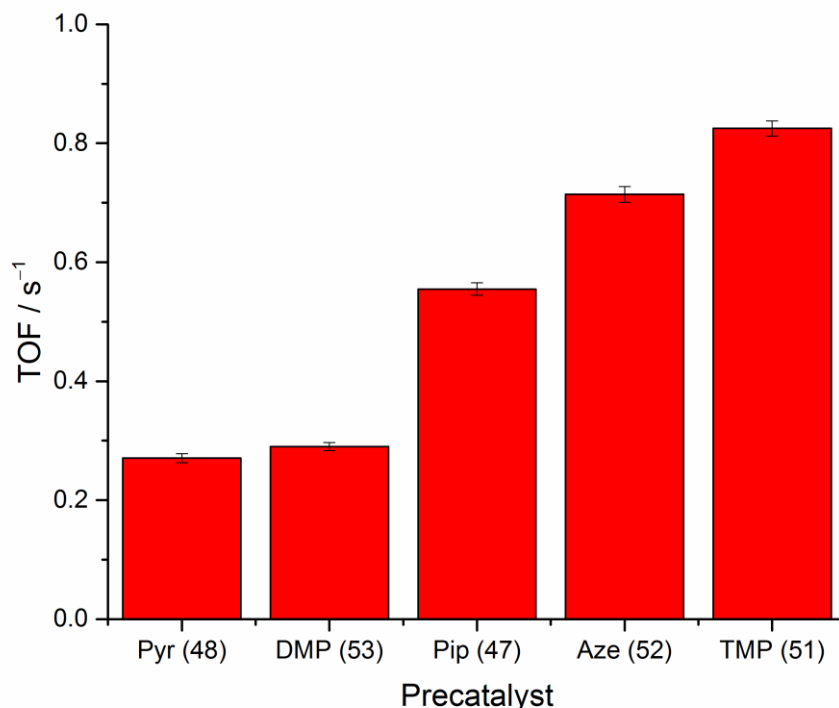


**Figure 89** The TOFs of each of the different precatalyst was measured as a gradient of TON s<sup>-1</sup> for an initial period of 5400 seconds (1.5 h).<sup>147</sup> Reaction conditions: Precatalyst (0.01 mol%, 72 μM), K<sub>4</sub>[Fe(CN)<sub>6</sub>] (0.22 eq.), Na<sub>2</sub>CO<sub>3</sub> (1 eq.), DMAc, N<sub>2</sub>, 140 °C.

By comparing the TOFs of each of the precatalysts a more accurate representation of their catalytic efficiency is shown in Figure 89. The TOF's for each of the precatalysts were measured as a gradient of TON s<sup>-1</sup> for the first 1.5 hours of reaction. This was due to it being the only period of time when all catalysts were performing at their optimum rates. By analysing the catalytic performances in this way it was possible to not only distinguish their efficiencies by the overall reaction profile (*i.e.* the overall conversion, reaction time period and features such as catalyst deactivation) but also by using a quantitative measure of the rate of catalyst turn over. As discussed by Kozuch and Martin<sup>147</sup> the TOFs for each precatalyst were calculated using the gradient of TON *vs* time. Analysis *via* this method also allowed for the errors in this measurement to be calculated using the quality of the linear fit. Accurate TOFs allow the reader to distinguish differences between the precatalysts which by simply studying Figure 87 would not have been apparent. Figure 89 shows that despite the poor overall performance of **53** shown in Figure 87, at optimum rate it achieved a higher turnover frequency than **48**. This is again apparent when comparing the TOFs of **52** and **47**, where despite **47** not quite reaching the same TON as **52** their optimum rates of catalysis were

comparable. Precatalyst **51** achieved the highest performance by each analysis. Despite this increased activity, in a trade-off between the relative precatalyst efficacies, price and ease of synthesis it was deemed that from an industrial perspective **47** was the most suitable candidate for further study.

## 5.2 Concentration effects on catalyst performance

In continuation of the kinetic studies, efforts were focused on precatalyst **47**. As a precatalyst, **47**: (a) exhibits good activity for the reaction of **65** → **69**, performing well at lower catalyst loadings than reported by Weissman *et al.* under comparable conditions on other substrates;<sup>102b</sup> (b) is the most straight-forward and cheapest to prepare within the series; (c) the Pd nanoparticles derived from it have been characterized in the direct arylation of 2'-deoxyadenosine (spherical truncated icosahedral Pd nanoparticles containing a 111 surface)<sup>41</sup>; d) it has already displayed high reactivity in Pd catalysed cyanation reactions under hydrous conditions in Chapter 4.

Further investigation into the effect of temperature and catalyst loading showed that at slightly increased catalyst loadings (0.05 mol%, 180 μM Pd) **47** still performed as an effective precatalyst when the temperature was decreased to 120 °C. It is also worth noting that doubling this catalyst loading to 0.1 mol% (360 μM Pd) did not result in a doubled initial rate (Figure 90). When performing the reaction at very low catalyst loadings (0.01 – 0.005 mol%) it was necessary to increase the reaction temperature to 140 °C. When the catalyst loading was decreased to 0.005 mol%, doubling the reaction concentration with respect to substrate to maintain a consistent Pd concentration of 36 μM was found to achieve noteworthy conversion after 14 hours.

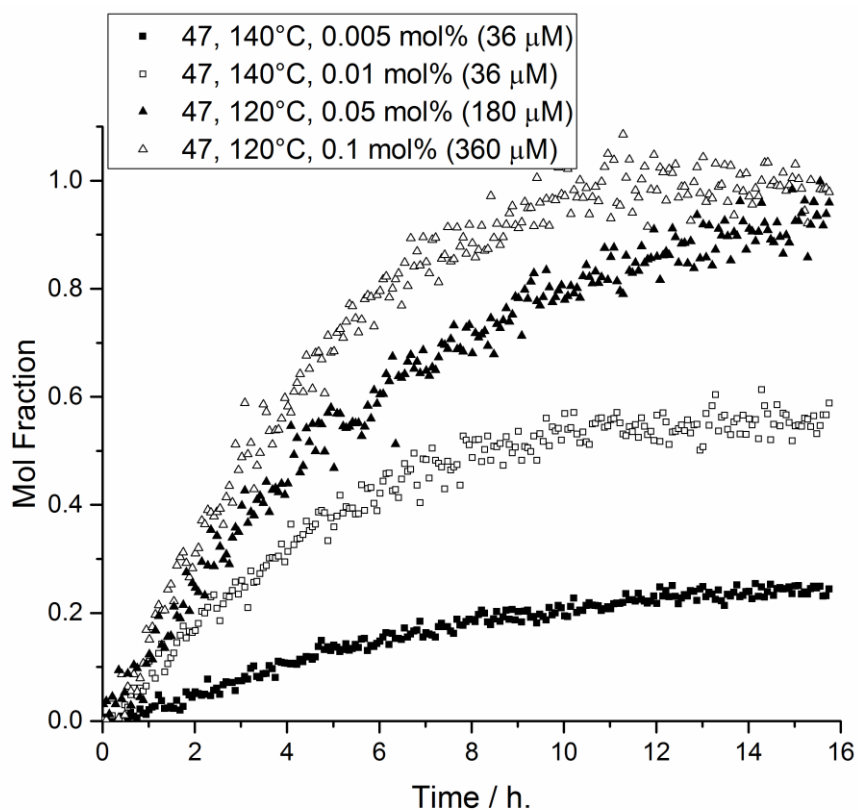


**Figure 90** Reaction profiles for the reaction  $65 \rightarrow 69$  at different precatalyst **47** loadings and temperatures under anhydrous conditions. Reaction conditions: Precatalyst **47** (0.005 – 0.1 mol%, 36 – 360  $\mu\text{M}$  Pd),  $\text{K}_4[\text{Fe}(\text{CN})_6]$  (0.22 eq.),  $\text{Na}_2\text{CO}_3$  (1 eq.), DMAC,  $\text{N}_2$ , 120–140  $^\circ\text{C}$ .

Given that it was possible to partially negate the effect of halving reaction precatalyst loading by doubling the reaction concentration, this effect was investigated further. Work within the Fairlamb group has shown that Pd concentration could be critical in delivering catalytically active PdNPs in C–H functionalisation reactions.<sup>116</sup> Despite the role of PdNPs having been reported in many Pd-catalysed cross-coupling reactions, the effect of Pd concentration on catalytic behaviour, rather than the Pd:substrate ratio, is unfortunately somewhat limited within the literature.

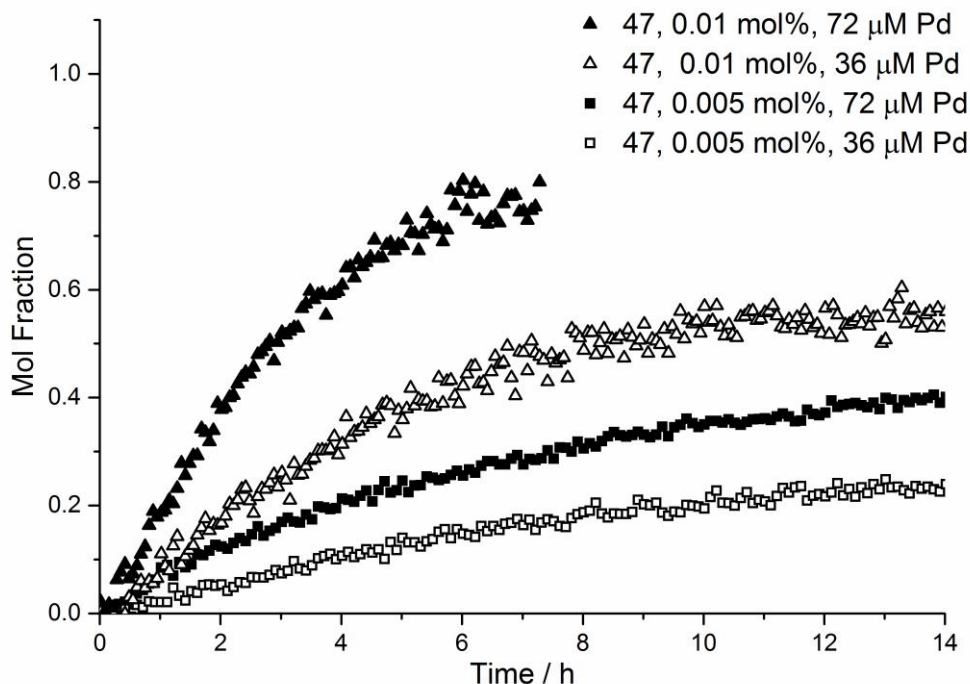


**Figure 91** Reaction profile for reaction 65  $\rightarrow$  69 with increased [Pd] and reaction concentrations while maintaining constant catalyst loadings under anhydrous conditions. Reaction conditions: Precatalyst 47 (0.005 or 0.01 mol%, 36 or 72  $\mu\text{M}$  Pd),  $\text{K}_4[\text{Fe}(\text{CN})_6]$  (0.22 eq.),  $\text{Na}_2\text{CO}_3$  (1 eq.), DMAc,  $\text{N}_2$ , 140  $^\circ\text{C}$ .

It was found that by increasing Pd concentration while maintaining constant catalyst loading (at 0.01 and 0.005 mol%) the catalyst efficiency of **47** was increased (Figure 91). The key values extrapolated from the traces shown in Figure 91 are listed in Table 9. At a Pd concentration of 72  $\mu\text{M}$ , and precatalyst loading of 0.01 mol% the reaction proceeded to 77% conversion after 6 hours at 140  $^\circ\text{C}$ . This resulted in a TON of 7700 (Entry 2). A decreased 52% conversion when the [Pd] was reduced to 36  $\mu\text{M}$ , at the same precatalyst loading: TON = 5200 (Entry 1). Although decreasing the precatalyst loadings while maintaining a constant [Pd] results in lower final conversions it is worthy of note that their catalyst efficiencies are still comparable. Comparable TONs were recorded for 0.01 mol% (72  $\mu\text{M}$ , Entry 2) and 0.005 mol% (72  $\mu\text{M}$ , Entry 4).

**Table 9** Values calculated from the kinetic traces displayed in Figure 91. Catalyst TOFs were measured as a gradient of TON  $s^{-1}$  for an initial period of 11,880 seconds (3.3 h.) Reaction conditions: Precatalyst 47 (0.005 or 0.01 mol%, 36 or 72  $\mu$ M),  $K_4[Fe(CN)_6]$  (0.22 eq.),  $Na_2CO_3$  (1 eq.), DMAc,  $N_2$ , 140  $^{\circ}C$ .

Entry	Precatalyst loading / mol%	[Pd] / $\mu$ M	TON	TOF / $s^{-1}$	Reaction Time / h.
1	0.01	36	5300	0.278 $\pm$ 0.00506	10
2	0.01	72	7700	0.527 $\pm$ 0.00473	6
3	0.005	36	5200	0.145 $\pm$ 0.00518	15
4	0.005	72	7600	0.329 $\pm$ 0.00495	15

As before, qualitative comparison of the reaction profiles does not reveal the full story of catalyst efficiency. In order to complete the picture, the conditions needed to be compared quantitatively using experimentally determined TOFs. The TOFs and their errors were calculated using the gradient of TON *vs* time for during the period where the reactions were at their peak rates. In this instance, this was for the first 3.3 hours. The results of these measurements are displayed graphically in Figure 92.

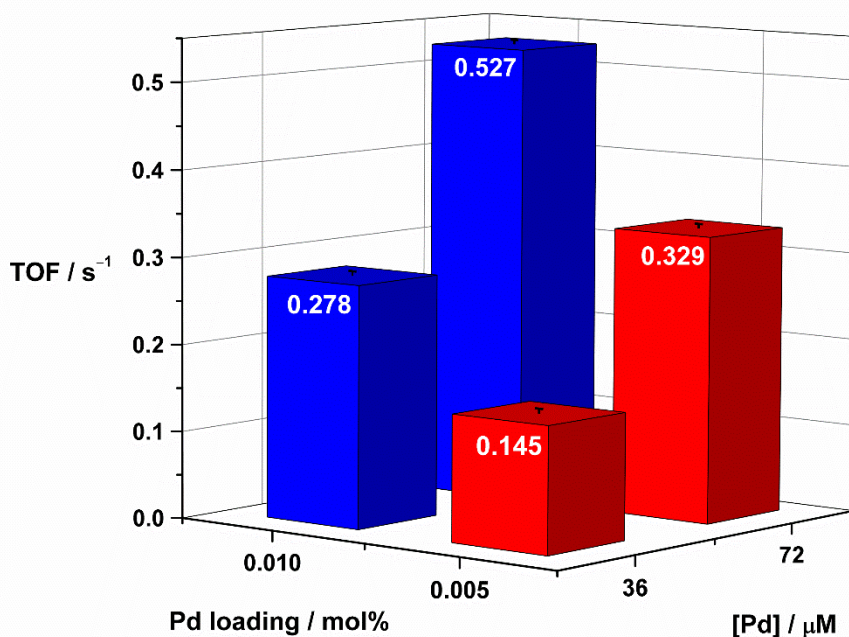


**Figure 92** Effect of [Pd] on catalyst TOFs in the cyanation of **65** under anhydrous conditions. The TOF was measured as a gradient of TON s<sup>-1</sup> for an initial period of 1.2x10<sup>4</sup> seconds (3.3 h.). Precatalyst used: **47**, other reaction conditions: K<sub>4</sub>[Fe(CN)<sub>6</sub>] (0.22 eq.), Na<sub>2</sub>CO<sub>3</sub> (1 eq.), DMAc, N<sub>2</sub>, 140 °C.

Comparison of the results in Figure 92 and the reaction profiles shown in Figure 91 shows that higher catalyst loadings were able to achieve higher conversions with comparable TON and TOFs. Under more dilute concentrations of Pd (36 μM), doubling the catalyst loading from 0.005 mol% to 0.01 mol% resulted in a TOF slightly higher than double the previous value, a similar result was measured upon maintaining a constant catalyst loading (0.005 mol%) but doubling the Pd concentration from 36 μM to 72 μM (entry 4, Table 9). The slightly lower value of TOF at 0.005 mol%, 36 μM Pd may be attributed to partial catalyst deactivation due to the presence of trace impurities when operating at such low catalyst loadings as 0.005 mol%. As would be expected in the presence of homogeneous catalysis, performing the reactions at double concentrations (72 μM Pd) a catalyst loading of 0.01 mol% (entry 2, Table 9) yielded a TOF four times larger than when performed at 0.005 mol% and 36 μM. When utilised at this optimum catalyst loading and concentration (0.01 mol%, 72 μM), precatalyst **47** was capable of reaching a TOF of 0.527 s<sup>-1</sup> and TON of 7700. These are the conditions under which all of the different precatalyst were screened in Figure 87.

### 5.3 Substrate screening

Following the kinetic work detailed above, the optimised reaction system was tested on a range of (hetero)aryl bromides, the successfully cyanated substrates are outlined below (Figure 93).

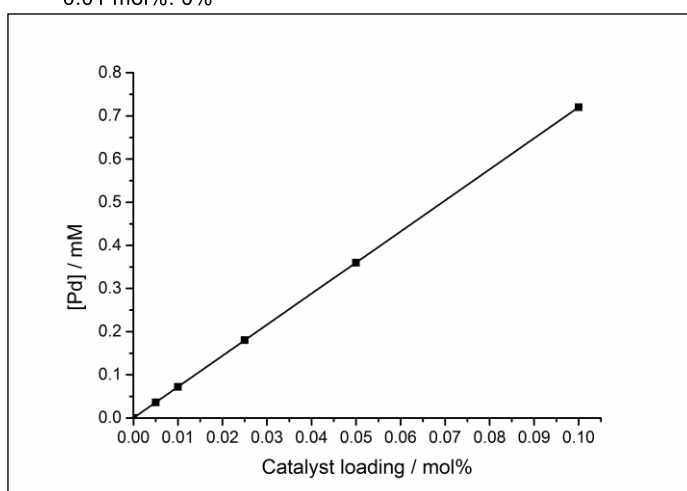
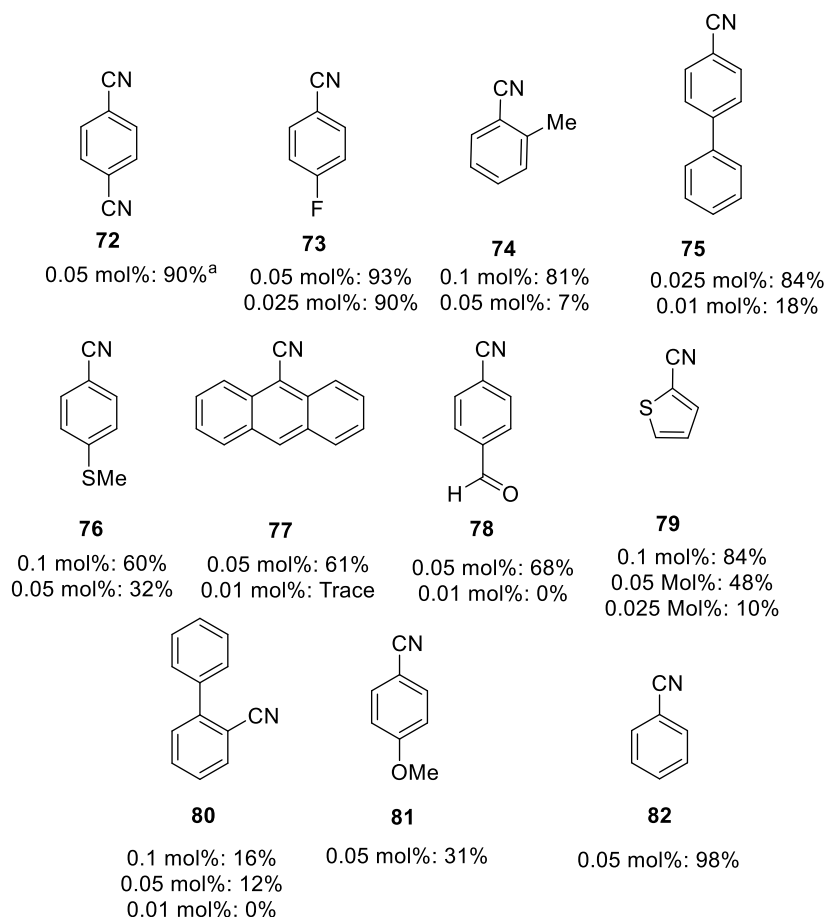


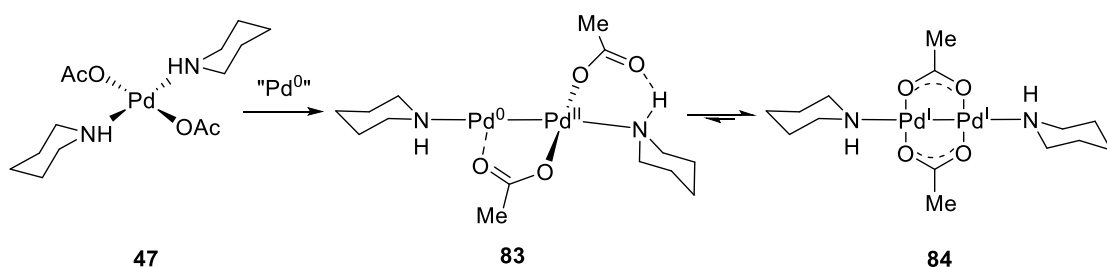
**Figure 93** Reaction conditions: ArBr (1 eq., 1.4 mmol), **47** (0.01-0.1 mol%),  $K_4[Fe(CN)_6]$  (0.22 eq.),  $Na_2CO_3$  (1 eq.), DMAc (2 ml),  $N_2$ , 140 °C, 16 h. <sup>a</sup> Using  $K_4[Fe(CN)_6]$  (0.44 eq. with respect

to 1,4-dibromobenzene). Inset graph shows the catalyst loading-Pd concentration ( $\mu\text{M}$ ) relationship under substrate screen conditions.

A range of catalyst loadings and concentrations were utilised in an attempt to optimise reaction yields. Electron poor coupling partners provided the best results, with 4-fluorobromobenzene achieving 90% yield with a catalyst loading of only 0.025 mol% (180  $\mu\text{M}$ ). Likewise, **72** was provided in 90% yield with a catalyst loading of 0.05 mol% (360  $\mu\text{M}$ ) in the presence of 0.44 eq. of  $\text{K}_4[\text{Fe}(\text{CN})_6]$ ; no monocyanted product was isolated from the reaction mixture. Both **77** and **78** were isolated in good yields in the presence of 0.05 mol% **47**, however further reducing the catalyst loadings to 0.01 mol% resulted in no catalyst turn over. Interestingly, increased steric bulk around the position of cross-coupling had a substantial detrimental effect on product yields. In order to achieve acceptable yields Pd precatalyst loadings and concentrations had to be increased to 0.1 mol% ( $[\text{Pd}] = 720 \mu\text{M}$ ) when attempting to cyanate 2-methylbromobenzene to give **74**. Similarly, only meagre yields were observed when increased catalyst loadings were attempted in the synthesis of **80**. Sulphur was tolerated in both **76** and **79** when catalyst loadings were increased to 0.1 mol%, but in the presence of the strongly electron donating 4-methoxy group, low yields were observed at 0.05 mol% catalyst loading in the synthesis of **81**. For the exhaustive conditions screened in an attempt to cyanate aryl chlorides please see Appendix 2.

#### 5.4 DFT studies into the structure of the active catalyst

In an attempt to understand the nature of the catalytically active species formed from precatalyst **47** under working conditions, computational work using DFT methods was carried out.



**Scheme 53** Autocatalytic growth of higher order  $\text{Pd}_n$  clusters, exemplified here for  $n = 2$ : Computational calculations (DFT methods in Gaussian09: wb97xd/dgdzvp-def2tzv) show that **83** and **84** are energetically feasible species, with **84** being *ca.* 15.4 kcal mol<sup>-1</sup> lower in energy – an accessible barrier for the aryl cyanation reaction conditions). Calculations performed by Prof. Ian Fairlamb.

It was revealed that under reducing conditions Pd can form higher order species by addition of Pd<sup>0</sup> to **47** to give small Pd clusters, exemplified as **83** and **84** (Scheme 53) here for a dinuclear Pd species. We expect that Pd<sub>3</sub>-Pd<sub>8</sub> clusters are accessible under the reaction conditions. Computational calculations using DFT methods confirm the feasibility of **83** and **84**. Interestingly, the lowest energy arrangement of such a species is the unique Pd<sup>I</sup>-Pd<sup>I</sup> dimer structure **84**, while we expect **83** to be accessible energetically under the aryl cyanation reaction conditions.

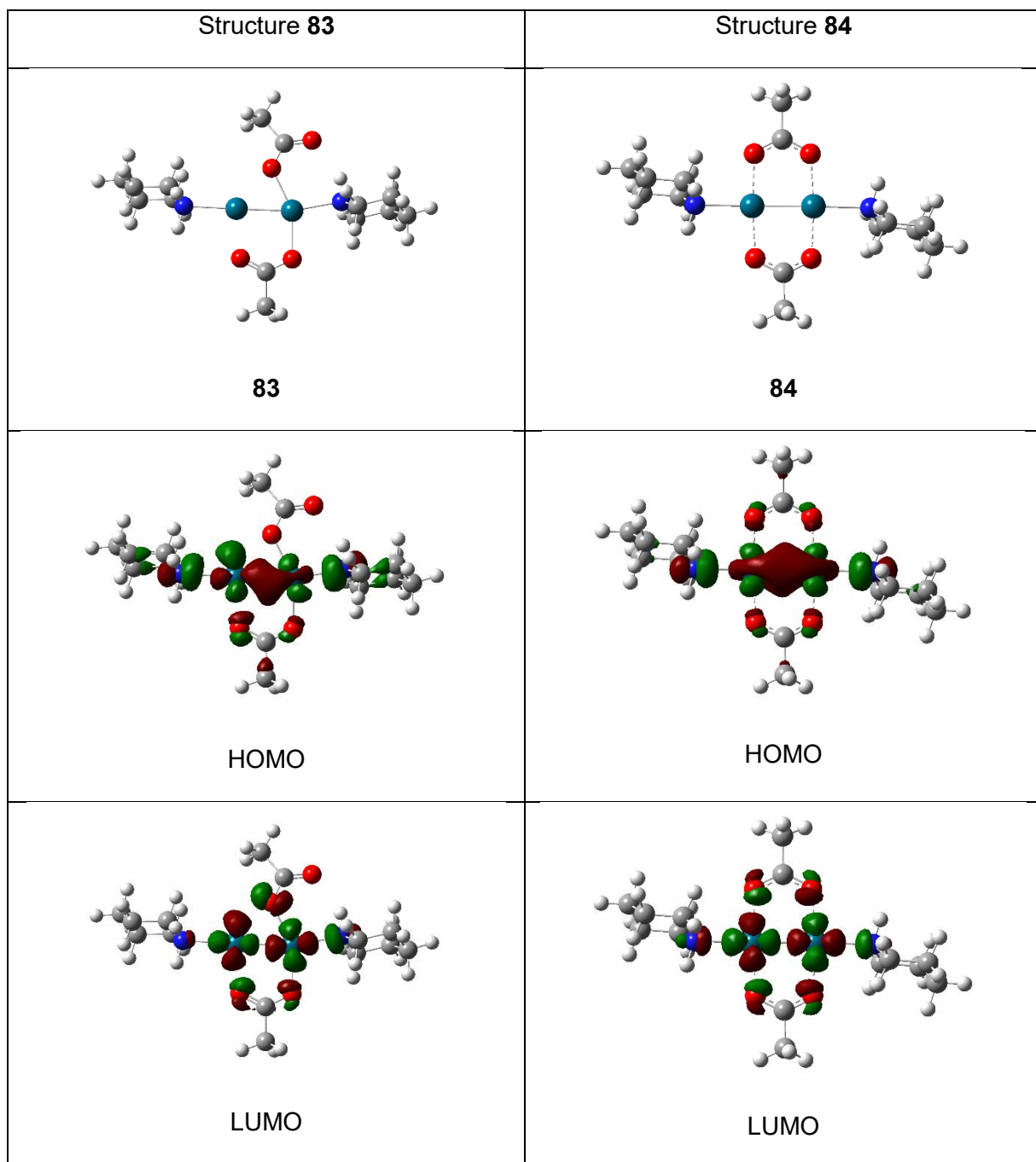


**Figure 94** Frontier molecular orbitals for **83** and **84**. Calculations performed by Prof. Ian Fairlamb.

The calculated frontier molecular orbitals for structures **83** and **84** show that the HOMO resides primarily on the Pd<sup>0</sup> in **83**, suggesting that the right-hand side Pd<sup>II</sup>(OAc)<sub>2</sub>-piperidine group is acting like a pseudo-ligand for Pd<sup>0</sup>. An analogy can be drawn here between a commonly proposed catalyst species Pd-[L], where L is sterically and electronically tuned, and Pd-[Pd<sub>n</sub>L<sub>o</sub>X<sub>p</sub>] (with varying n, o and p), proposed here as the catalyst species that can be tuned for high catalytic activity in arylcyanation chemistry (Figure 95).

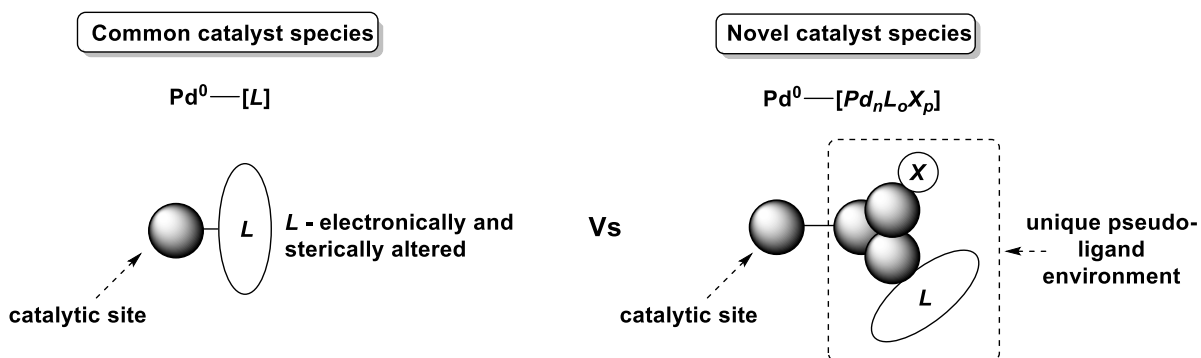


**Figure 95** Structural analogy of **83**,  $\text{Pd}^0\text{---}[\text{Pd}_n\text{L}_o\text{X}_p]$ , with a  $\text{Pd}\text{---}[\text{L}]$ .

We expect that the number of Pd atoms and ligand (L) and halide/pseudohalide (X) environment affects catalytic activity and efficacy in a profound and distinct manner. The precise catalyst structure is expected to be controlled by Pd concentration, ligand/halide ratios, solvent, substrates and products, in addition to global reaction conditions. It would also be expected that tuning the electronic and steric influence of L may have a profound effect upon the activity of the catalytic site.

### 5.5 Effect of increased amine ligand size on catalysis

In Chapter 2, it was highlighted that changing the amine ligand from simple, cyclic, aliphatic amines such as pyrrolidine and piperidine to dibenzazepine had a pronounced effect on the solid-state structures of the Pd dimer complexes **49**, **50** and **58**. Not only does **58** show interesting structural differences from the other complexes, it was also possible to synthesise in excellent yields, making it possible to test as a catalyst in the arylocyanations of **65**. It is important to note here that precatalyst **58** contains two atoms of Pd *per* molecule, therefore the catalyst loadings calculated with respect to the amount of complex **58** required have to be calculated as half the amount of Pd required, *i.e.* in this instance 0.005 mol% of **58** provides 0.01 mol% of Pd.

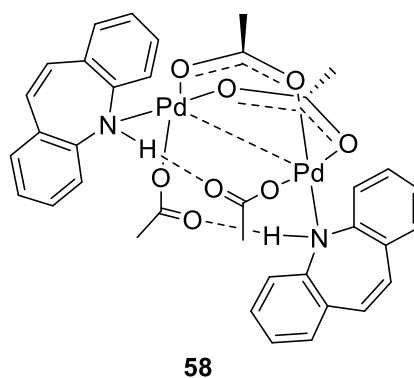


**Figure 96** The dimeric complex **58** was tested as a precatalyst in the arylocyanation of **65**.

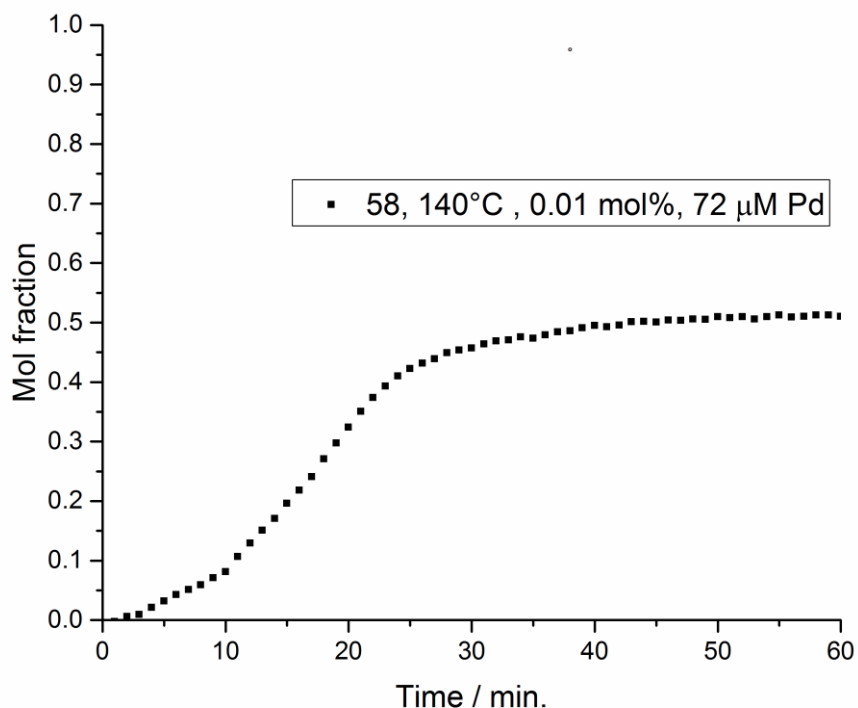


**Figure 97** Reaction profile for **65** → **69** using **58** as a precatalyst. Reaction conditions: Precatalyst **58** (0.005 mol%, Pd concentration = 72 μM),  $K_4[Fe(CN)_6]$  (0.22 eq.),  $Na_2CO_3$  (1 eq.), DMAc,  $N_2$ , 140 °C.

Examination of precatalyst **58** under the optimised cyanation conditions used to screen the other  $Pd(OAc)_2(HNR_2)_2$  precatalysts (shown in Figure 87) reveals promising catalytic activity (Figure 97). Precatalyst **58** was capable of achieving a yield of 50% within only 30 minutes of reaction initiation. Despite reaching a lower total TON (5000) than **47** (7700), direct comparison in Figure 98 between the relative rates of catalysis for **47** and **58** shows how much faster **58** was. Interestingly, precatalyst **58** was not only faster but the reaction profile also appeared to be a sigmoid, reminiscent of the profiles observed for this cyanation reaction under hydrous conditions (Chapter 4).

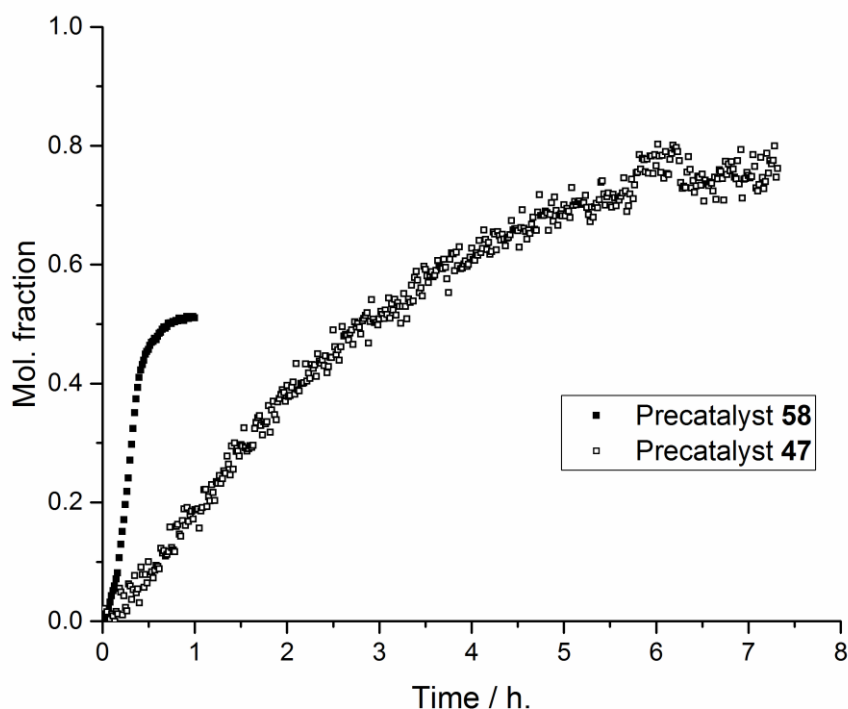


**Figure 98** Direct comparison for the reaction profiles of the cyanation of **65** with piperidine (**47**) or dibenzazepine (**58**) as ligands at Pd shows their relative rates. Catalyst loadings: with precatalyst **47** (0.01 mol%, Pd conc = 72  $\mu\text{M}$ ); with precatalyst **58** (0.005 mol%, Pd conc = 72  $\mu\text{M}$ ). Other conditions:  $\text{K}_4[\text{Fe}(\text{CN})_6]$  (0.22 eq.),  $\text{Na}_2\text{CO}_3$  (1 eq.), DMAc,  $\text{N}_2$ , 140  $^\circ\text{C}$ .

The TOF of precatalyst **58** was extrapolated from this data by measuring the gradient of TON vs time (s) for its most active period of catalysis, between 20-40 minutes. When compared with the previously tested, monomeric Pd precatalysts **48**, **47**, **52**, **53** and **54**, a ligand effect on the rate of catalysis is evident. Given the higher TOF achieved, it appears that the dibenzazepine ligand facilitated the formation of the most active catalyst species.

The TOF for precatalyst **58** is significantly higher than the other, monomeric precatalysts (Figure 99). The larger error in this measurement is due to only 20 data points being used in the TON  $\text{s}^{-1}$  plot; for all the other precatalysts, 90 data points were used.

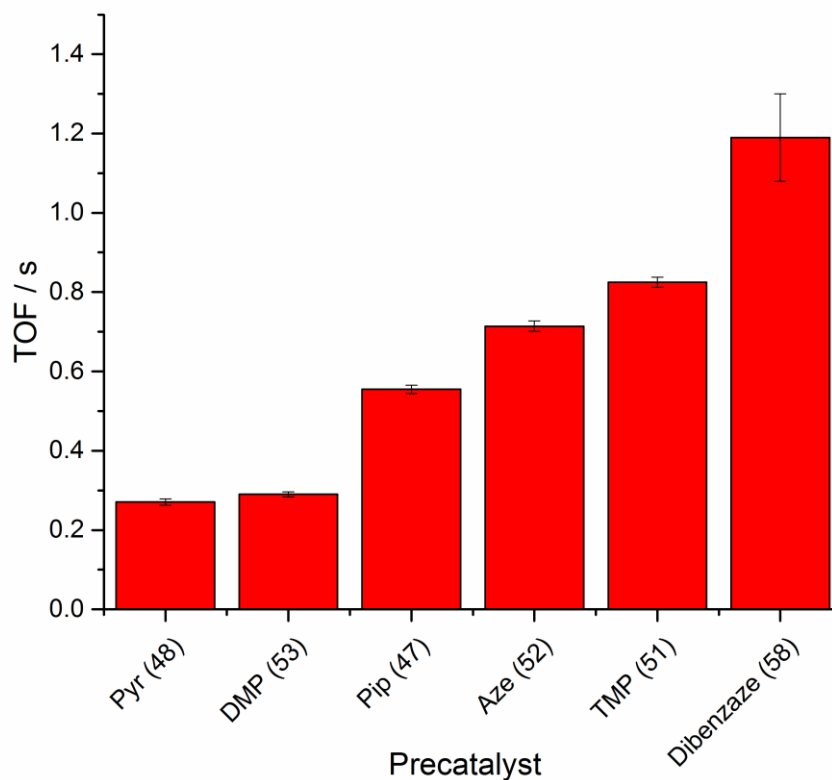


**Figure 99** The TOFs of each of the different precatalysts was measured as a gradient of  $\text{TON s}^{-1}$  for an initial period of 5400 seconds (1.5 h.), except from 58 which was for the most active period from 1200-2400 (20-40 minutes). Catalyst loadings: with precatalyst 58 (0.005 mol%, Pd conc = 72  $\mu\text{M}$ ); with all other precatalysts: (0.01 mol%, Pd conc = 72  $\mu\text{M}$ ) Other conditions:  $\text{K}_4[\text{Fe}(\text{CN})_6]$  (0.22 eq.),  $\text{Na}_2\text{CO}_3$  (1 eq.), DMAc,  $\text{N}_2$ , 140 °C.

This increased activity is hypothesised to be due to the fact that as a dimer there may be a lower barrier to the formation of catalytically active species such as **83**. As stated in section 5.4, altering L ligands on the right hand side of **83** would have a pronounced effect upon the electronic character of the active site. The analogous structures of the species **83** and **84** with dibenzazepine ligands are shown in Figure 100.

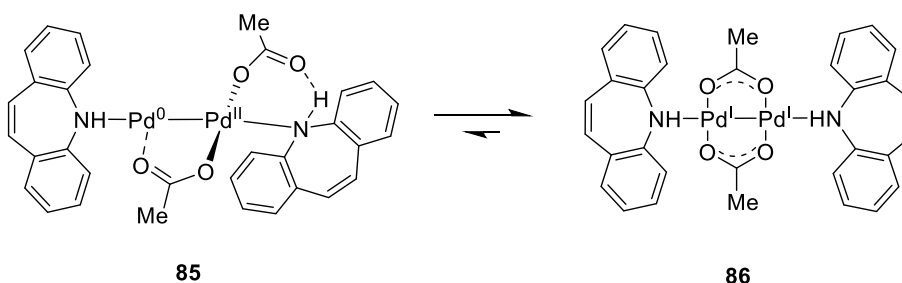


**Figure 100** Hypothetical structures for the active catalyst species formed under cyanation conditions from **58**.

Indeed, the solid-state structure of **58** shows that the coordinative nitrogen in benzazepine is a poorer  $\sigma$ -donor to Pd and a stronger hydrogen bond donor than the comparable aliphatic ligands (piperidine and pyrrolidine). Presumably, this would result in an enriched electron density on the Pd<sup>II</sup> centre; this is likely to reduce the amount of electron density donated into the Pd<sup>0</sup>–Pd<sup>II</sup> bond by the Pd<sup>0</sup> centre, in turn increasing the orbital coefficient at that reactive centre. This feature could result in more facile C–Br (or even C–Cl) oxidative addition at Pd and increased catalytic efficiency.

In light of this insight, further computational work into the effect of dibenzazepine on the structure and bonding in **85** and **86** proves appealing and could prove crucial in the design of future, analogous precatalysts.

## 5.6 Role of Na<sub>2</sub>CO<sub>3</sub>

### 5.6.1 Varying Na<sub>2</sub>CO<sub>3</sub> equivalences

Despite there being no role for a base in the mechanism for Pd-catalysed arylcyanation reactions, inorganic carbonates are ubiquitous in their use as an additive in arylcyanations employing potassium hexacyanoferrate(II) as a cyanide source.<sup>94b, 107-108</sup> The development of methodologies where an additive is not required appears to have only occurred in two instances, one where PdNPs impregnated in a molecular cage were used as a catalyst<sup>106</sup> and the other where PdNPs are impregnated on a CuO support.<sup>105</sup> Unfortunately despite this progression, no attempt was made in either case to discern the reason for the reaction working in the absence of an additive. Given that additives have always been reported as necessary when using a heterogeneous Pd catalyst in arylcyanations before, it seems likely that the reader can attribute the unique reactivity of these catalysts to the structure of the dendritic molecular cage scaffold (a subsection of which is displayed in Figure 101) or the CuO support.

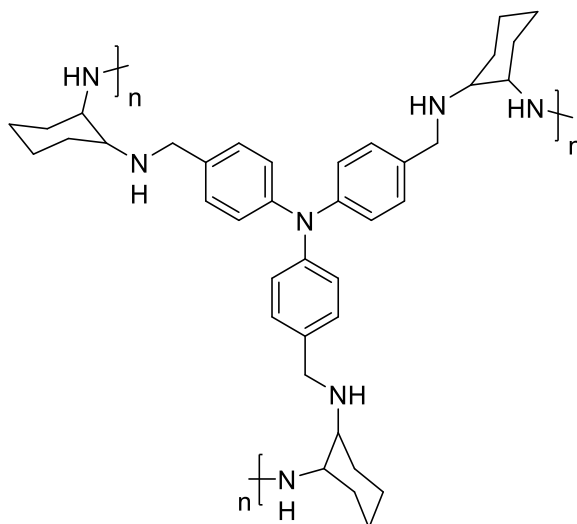
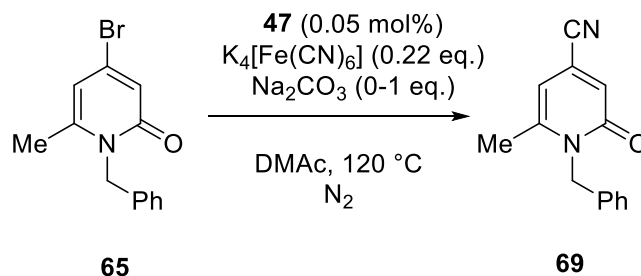


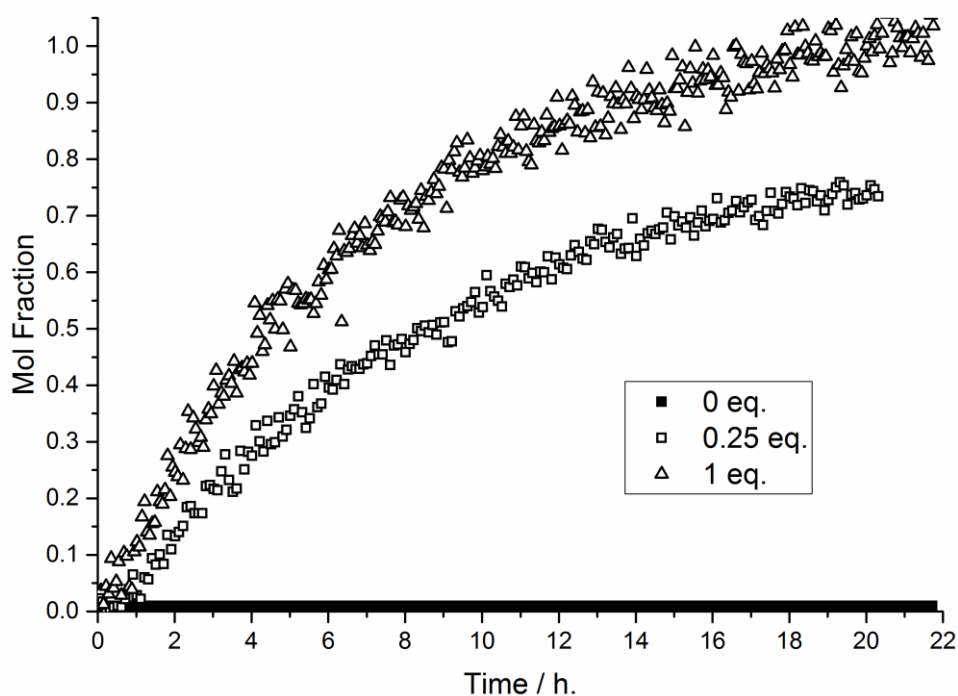
**Figure 101** One unit of the molecular cage substructure used to support PdNPs capable of catalysing arylcyanations in the absence of additives.<sup>106</sup>

The attempts made in the current study to discern the role of the most common additive in Pd-catalysed arylcyanations using hexacyanoferrate as a cyanide source are shown henceforth. All experiments from here on in this chapter were carried out using **47** as a precatalyst in order maintain consistency with previous mechanistic studies.



**Scheme 54** Reaction conditions to study effects of alternative  $\text{Na}_2\text{CO}_3$  equivalences in the cyanation of **65**.

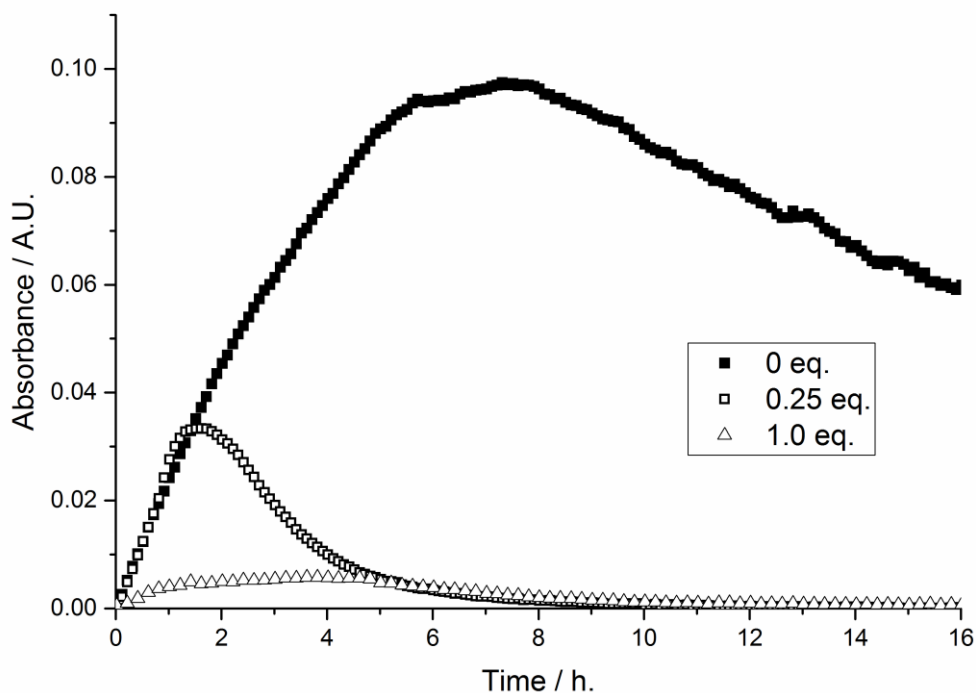
It was reported by Buchwald and co-workers that under their conditions published for the Pd-catalysed arylcyanation of aryl chlorides in the presence of bulky, bidentate phosphines that only catalytic  $\text{NaOAc}$  (0.25 eq.) was required to achieve maximum conversions.<sup>107</sup> In light of this, the model reaction (Scheme 54) converting **65** to **69** in the presence of  $\text{K}_4[\text{Fe}(\text{CN})_6]$  was tested in the absence, and presence of 0.25 eq. of  $\text{Na}_2\text{CO}_3$ , to compare with standard conditions. The kinetic traces shown in Figure 102 show that it was possible for  $\text{Na}_2\text{CO}_3$  to work in a catalytic role, with only 0.25 equivalents aiding an overall conversion of *ca.* 70%. It is evident however that in the complete absence of an additive, no catalysis occurred; no product was formed under these conditions, even after 21 hours.



**Figure 102** Reaction profiles for reaction 65 → 69 with varied  $\text{Na}_2\text{CO}_3$  equivalences. Reaction conditions: Precatalyst 47 (0.05 mol%, 180  $\mu\text{M}$ ),  $\text{K}_4[\text{Fe}(\text{CN})_6]$  (0.22 eq.),  $\text{Na}_2\text{CO}_3$  (0 – 1 eq.), DMAc,  $\text{N}_2$ , 120 °C.

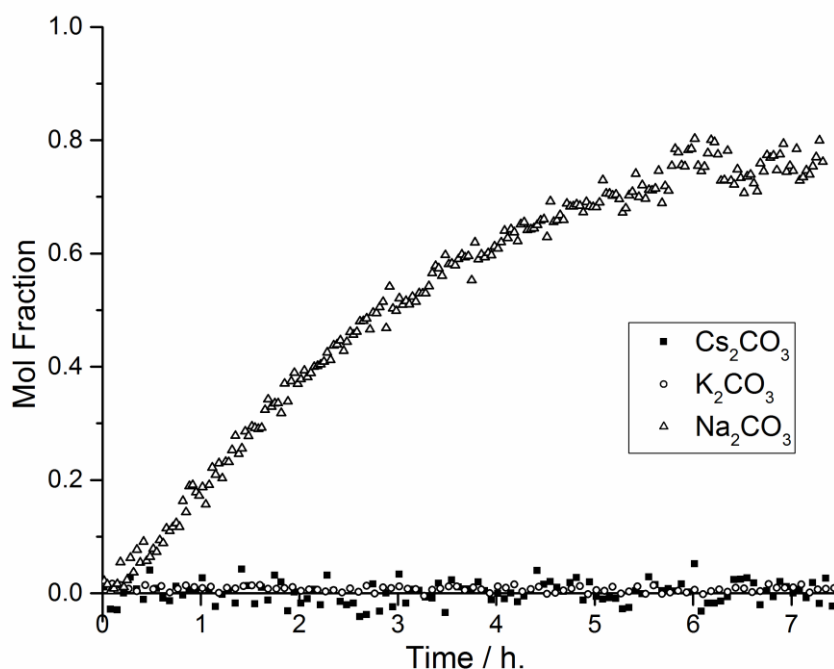
Despite  $\text{Na}_2\text{CO}_3$  having performed capably at only 0.25 equivalents, these conditions were still outcompeted with a full equivalent. It was possible to study the effect of differing  $\text{Na}_2\text{CO}_3$  equivalences upon the concentration of  $[\text{Fe}(\text{CN})_6]^{4-}$  by following the absorbance present at 2045  $\text{cm}^{-1}$  (for information regarding the characterisation of this species, see Chapter 4). Doing so for the Pd-catalysed arylcyanations displayed in Figure 102, sheds some light on the role of the additive.

Figure 102 displays that when a full equivalent of  $\text{Na}_2\text{CO}_3$  was used the reaction reached completion after 20 hours, along with a achieving a faster reaction rate than when performed with only 0.25 equivalents. When compared with Figure 103, the corresponding traces show that the decreased rate of catalysis throughout the reaction performed with 0.25 equivalents of  $\text{Na}_2\text{CO}_3$  came hand-in-hand with an increased concentration of  $[\text{Fe}(\text{CN})_6]^{4-}$ . In the complete absence of  $\text{Na}_2\text{CO}_3$ , the concentration of  $[\text{Fe}(\text{CN})_6]^{4-}$  continued to increase over a period of 7 hours until it decreased due its precipitation. The initial rate of solvation of  $[\text{Fe}(\text{CN})_6]^{4-}$  either in the absence of, or the presence of 0.25 eq. of  $\text{Na}_2\text{CO}_3$  were the same, but when the reaction was under conditions facilitating more rapid catalysis this dropped. This evidence supports speculative statements made by Buchwald *et al.* regarding the role of the additive as assisting transmetallation of  $^-\text{CN}$  from Fe to Pd.<sup>107</sup>



**Figure 103**  $[\text{Fe}(\text{CN})_6]$  ( $2045 \text{ cm}^{-1}$ ) traces with varied  $\text{Na}_2\text{CO}_3$  equivalences. Reaction conditions: Precatalyst 47 (0.05 mol%, 180  $\mu\text{M}$ ),  $\text{K}_4[\text{Fe}(\text{CN})_6]$  (0.22 eq.),  $\text{Na}_2\text{CO}_3$  (0 – 1 eq.), DMAc,  $\text{N}_2$ , 120  $^\circ\text{C}$ .

Given the apparent importance of  $\text{Na}_2\text{CO}_3$  in the system to facilitate transmetalation, it was still unclear as to the role of both the anionic and the cationic portions of the salt. In an attempt to unravel these intricacies, both  $\text{K}_2\text{CO}_3$  and  $\text{Cs}_2\text{CO}_3$  were tested as alternative additives in the Pd-catalysed cyanation of **65** under optimised conditions (see Section 5.2). It is clear in Figure 104 that under these optimised conditions neither  $\text{Cs}_2\text{CO}_3$  nor  $\text{K}_2\text{CO}_3$  facilitated the catalytic turnover of Pd, even after a reaction time of 14 hours.



**Figure 104** Reaction profiles for formation of cyanopyridone with different carbonate additives. Reaction conditions: Precatalyst 47 (0.01 mol%, 72  $\mu\text{M}$ ),  $\text{K}_4[\text{Fe}(\text{CN})_6]$  (0.22 eq.),  $\text{X}_2\text{CO}_3$  (1 eq.), DMAc,  $\text{N}_2$ , 140  $^\circ\text{C}$ .

The exact reason for this complete reaction shut-down was not entirely clear, but it was apparent that the cationic counterion of the additive is crucial to the mechanism by which the reaction transpires. Given that larger alkali metal counterions have lower solvation enthalpies, the inhibition of catalysis in the presence of  $\text{K}^+$  and  $\text{Cs}^+$  may have been due to the solvation of the alkali metal carbonates. Studying the  $[\text{Fe}(\text{CN})_6]^{4-}$  traces displayed in Figure 105 showed that in the presence of  $\text{Na}^+$  a normal trend was observed: the initial solvation of  $[\text{Fe}(\text{CN})_6]^{4-}$  followed by its consumption by catalysis. However, when  $\text{K}^+$  was employed,  $[\text{Fe}(\text{CN})_6]^{4-}$  was still solubilised but not consumed by the formation of **69**. In the presence of  $\text{Cs}^+$ , there was very little solvation of  $[\text{Fe}(\text{CN})_6]^{4-}$  at all initially, however over a period of 6 hours its concentration did increase. Interestingly the concentration of  $[\text{Fe}(\text{CN})_6]^{4-}$  appeared to decrease upon the addition of  $\text{Cs}_2\text{CO}_3$ ; this may be attributed to the counterion exchange between it and  $\text{K}_4[\text{Fe}(\text{CN})_6]$  resulting in a less soluble salt. It is possible that partial counterion exchange may have occurred in all three systems and that  $\text{Na}^+$  provided the optimal solubility conditions for effective catalysis to occur.<sup>148</sup>

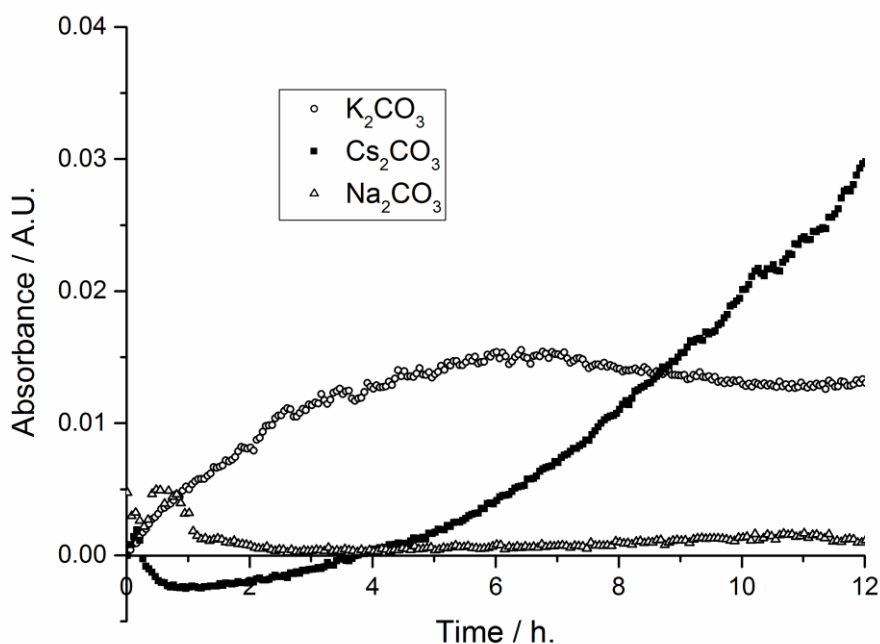
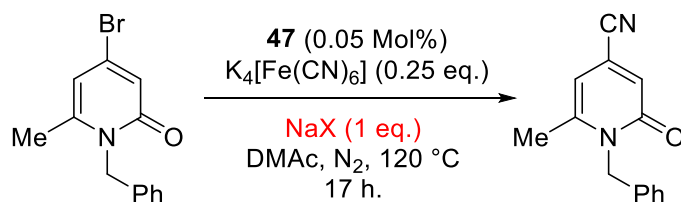


Figure 105  $[\text{Fe}(\text{CN})_6]^{4-}$  traces in the attempted cyanation of **65** with different carbonate additives, shown in Figure 104. Reaction conditions: Precatalyst **47** (0.01 mol%, 72  $\mu\text{M}$ ),  $\text{K}_4[\text{Fe}(\text{CN})_6]$  (0.22 eq.),  $\text{X}_2\text{CO}_3$  (1 eq.), DMAc,  $\text{N}_2$ , 140  $^\circ\text{C}$ .

### 5.6.2 Testing the role of $\text{Na}^+$ in a counterion exchange process

Following the hypothesis that  $\text{Na}^+$  may be involved in important counterion exchange processes with  $\text{K}_4[\text{Fe}(\text{CN})_6]$ , such as the formation of  $\text{KNa}[\text{Fe}(\text{CN})_6]^{2-}$  ion triplets,<sup>148a</sup> a simple non-kinetic study using alkali metal-halogen salts as additives instead of alkali metal carbonates was carried out. It was of interest to establish the relative importance of both  $\text{Na}^+$  and  $\text{CO}_3^{2-}$  in the catalytic process.



Scheme 55 Reaction conditions under which the effects of three NaX salts as additives were tested in the cyanation of **65** using precatalyst **47**.

The other reaction conditions (catalyst loading, reaction temperature and length) were chosen because under standard conditions, in the presence of  $\text{Na}_2\text{CO}_3$  (1 eq.), these would result in the quantitative conversion of **65** into **69**.

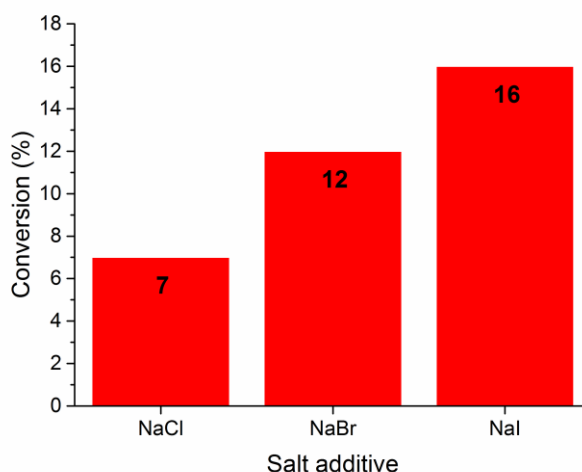


**Figure 106 Replacing  $\text{Na}_2\text{CO}_3$  with sodium halide salts still resulted in partial conversion of starting material. Reaction conditions: **47** (0.05 mol%, 180  $\mu\text{M}$ ),  $\text{K}_4[\text{Fe}(\text{CN})_6]$  (0.22 eq.),  $\text{NaX}$  (1 eq.), DMAc,  $\text{N}_2$ , 120  $^\circ\text{C}$ , 17 h..**

Surprisingly, all three alkali metal halide salts facilitated partial conversion of **65** to **69**. The percentage conversion increased as the strength of ionic pairing decreased and may be due to the increased solubility of the salts in the organic solvent, DMAc. These results confirm the importance of using an additive which contains a  $\text{Na}^+$  counterion which appears to participate in counterion swapping with  $\text{K}_4[\text{Fe}(\text{CN})_6]$ . Comparison of these decreased conversions with the results when using  $\text{Na}_2\text{CO}_3$  also confirmed the importance for the role of the carbonate anion in assisting transmetallation of  $^-\text{CN}$  from Fe to Pd. The halogen anions were capable of achieving the process but with a much lower efficiency.

Buchwald *et al.* reported that when using 0.5 eq. of  $\text{K}_4[\text{Fe}(\text{CN})_6]$  in the presence of NaOAc for the arylation of aryl and heteroarylchlorides, when each reaction reached completion the mixtures would turn dark blue. They later characterised the compound giving rise to this colour as “Prussian blue” ( $\text{Fe}_4[\text{Fe}(\text{CN})_6]_3$ ) using powder X-Ray diffraction.<sup>107</sup> Presumably, this occurs due to the reaction of  $\text{K}_4[\text{Fe}(\text{CN})_6]$  with  $\text{Fe}^{\text{III}}$  formed under reaction conditions; Prussian blue is made by reacting an  $\text{Fe}^{\text{III}}$  salt (normally  $\text{FeCl}_3$ ) with  $\text{K}_4[\text{Fe}^{\text{II}}(\text{CN})_6]$ .<sup>149</sup> Normally, under the reaction conditions employed by this researcher the reaction mixtures at completion were black, however when using NaX additives the reaction mixtures at completion were varying colours: red in the presence of NaCl; dark blue in the presence of NaBr; green in the presence of NaI.



**Figure 107** The three reactions reached different conversions at reaction completion and gave different coloured solutions. This was presumably due to the formation of varying  $K_xNa_y[Fe(CN)_z]$  species through counterion swapping and consumption of starting material.

These colour differences were likely caused by different Fe cyanide complexes and Fe oxidation states observed at varying stages of reaction progression. Tentatively, these may be associated with known coloured hexacyanoferrate complexes. Red may be attributed to the symmetry disallowed, spin-allowed d-d transition present in  $K_3[Fe^{III}(CN)_6]$  (Prussian red); blue may be attributed to the intervalence charge transfer band between  $Fe^{II}$  and  $Fe^{III}$  in  $KFe^{III}[Fe^{II}(CN)_6]$  or  $Fe^{III}_4[Fe^{II}(CN)_6]_3$  (“soluble” Prussian blue and Prussian blue respectively); green has been characterised in the past as a different linkage isomer of  $K_4[Fe(CN)_6]$ .<sup>148b</sup> However, given the progression of understanding regarding the structure and bonding of transition metal complexes in the past 100 years, a green colour seemed more likely to result from a mixture of Prussian blue and yellow  $K_4[Fe(CN)_6]$ . The weak yellow colour seen from  $K_4[Fe(CN)_6]$  is the result of a symmetry disallowed d-d transition.

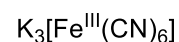
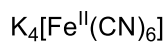
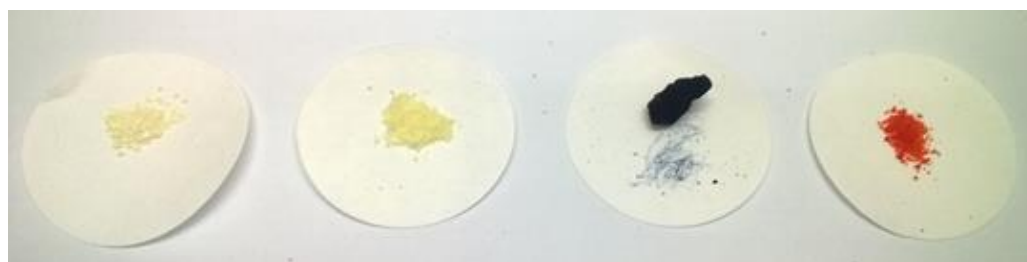
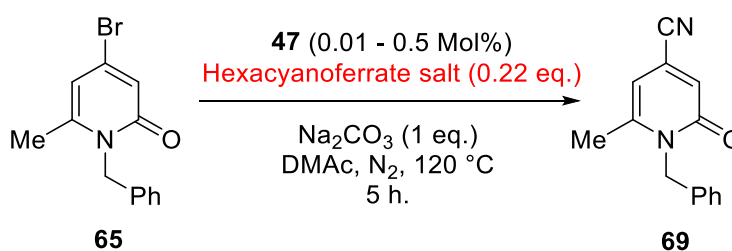


**Figure 108** The appearances of these four hexacyanoferrate complexes are distinct due to their differing electronic and molecular structures.

Given the possible presence of each of these different hexacyanoferrate salts in the incomplete cyanation reactions, along with the role of  $\text{Na}^+$  in counterion swapping, it was considered beneficial to investigate their potentials as cyanide sources in discrete Pd catalysed arylcyanations reactions.

### 5.7 Investigating other hexacyanoferrate salts as cyanide sources



**Scheme 56** Reaction conditions used to test alternative hexacyanoferrates as cyanide sources in the cyanation of **65**.

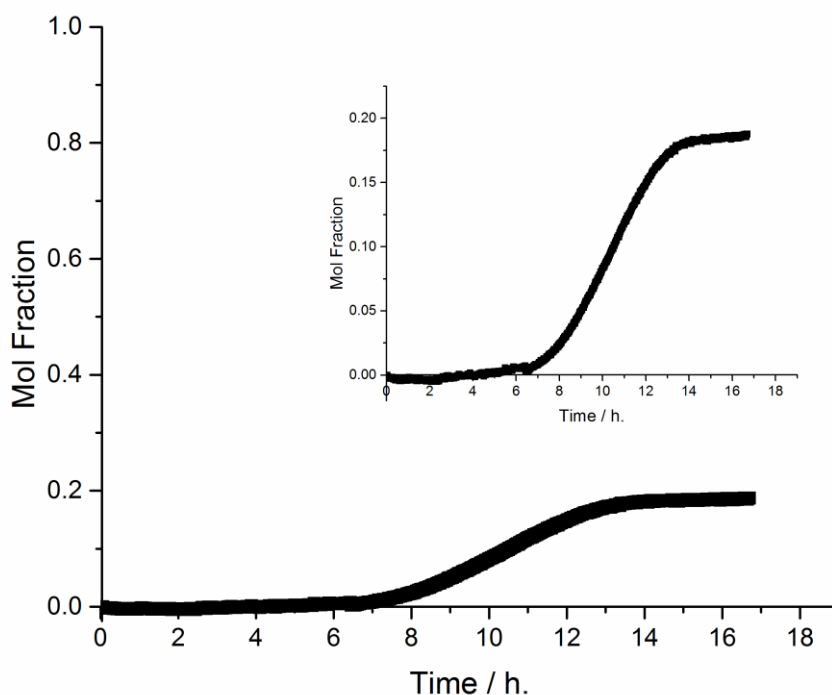
The reaction conditions were selected for this study because under normal conditions, *i.e.* when using  $\text{K}_4[\text{Fe}(\text{CN})_6]$  at 0.05 mol%, these would result in 50% conversion of **65** into **69** after 5 hours. This way, it was possible to screen a range of hexacyanoferrates and distinguish any improvements or deteriorations in reaction efficiency without the requirement of a full kinetic study.

**Table 10 Variation of the cyanide source.**

Entry no.	Cyanide source <sup>a</sup>	Catalyst loading (mol%)	Conversion (%) <sup>b</sup>
1	KFe <sup>III</sup> [Fe <sup>II</sup> (CN) <sub>6</sub> ]	0.5	0, 0 <sup>c</sup>
2	K <sub>3</sub> [Fe <sup>III</sup> (CN) <sub>6</sub> ]	0.5	53
4	Na <sub>4</sub> [Fe <sup>II</sup> (CN) <sub>6</sub> ] <sup>d</sup>	0.01	16
5	Na <sub>4</sub> [Fe <sup>II</sup> (CN) <sub>6</sub> ] $\cdot$ 10H <sub>2</sub> O	0.05	0
6	Na <sub>4</sub> [Fe <sup>II</sup> (CN) <sub>6</sub> ] <sup>d</sup>	0.05	50
7	Na <sub>4</sub> [Fe <sup>II</sup> (CN) <sub>6</sub> ] <sup>d</sup>	0.05	0 <sup>e</sup>
8	Na <sub>4</sub> [Fe <sup>II</sup> (CN) <sub>6</sub> ] <sup>d</sup>	0.1	0 <sup>e</sup>

<sup>a</sup> Reaction conditions: Precatalyst **47** (0.01-0.5 mol%), “[Fe(CN)<sub>6</sub>]<sup>-</sup>” (0.22 eq.), Na<sub>2</sub>CO<sub>3</sub> (1 eq.), DMAc, N<sub>2</sub>, 120 °C, 5 h. <sup>b</sup> Determined by <sup>1</sup>H NMR spectroscopic analysis. <sup>c</sup> Reaction performed with 10 vol% degassed H<sub>2</sub>O in DMAc to aid KFe[Fe(CN)<sub>6</sub>] solubility. <sup>d</sup> The anhydrous compound was formed simply by heating Na<sub>4</sub>[Fe(CN)<sub>6</sub>] $\cdot$ 10H<sub>2</sub>O to 80 °C under high vacuum (at least 0.1 mmHg) until the pressure remained stable. <sup>e</sup> Without Na<sub>2</sub>CO<sub>3</sub>.

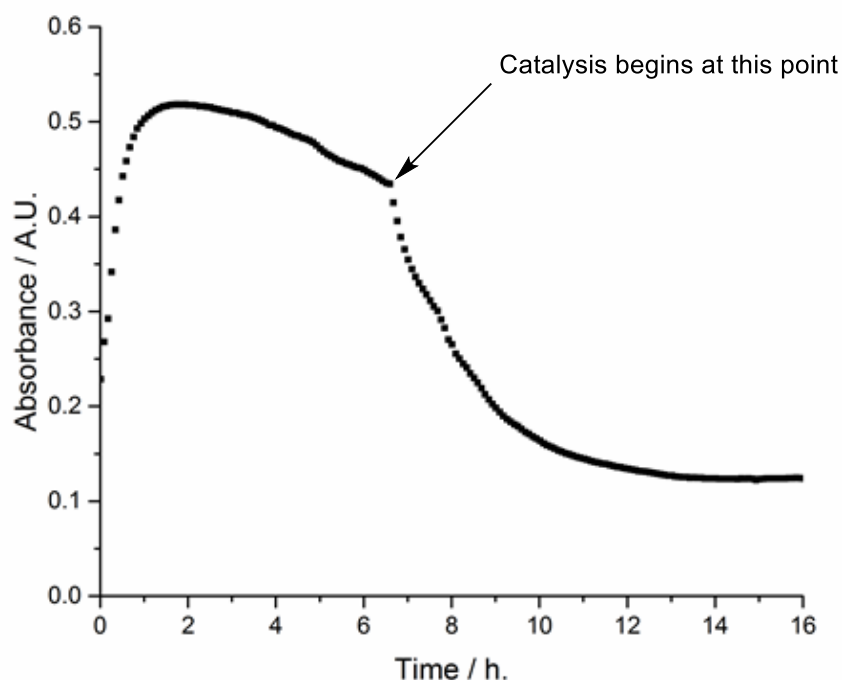
As reported by Buchwald *et al.* Prussian blue was found to be incapable as a <sup>-</sup>CN source. In an attempt to assist its solubility in the reaction mixture in DMAc, the reaction (entry 1) was repeated in the presence of 10 vol% degassed water but was found to have no effect. Interestingly, when K<sub>3</sub>[Fe<sup>III</sup>(CN)<sub>6</sub>] (entry 2) was used as a cyanide source, a commendable 53% conversion to **69** was achieved, validating further study (Figure 111). Substituting K<sub>4</sub>[Fe(CN)<sub>6</sub>] for Na<sub>4</sub>[Fe<sup>II</sup>(CN)<sub>6</sub>] both in the presence (entries 4 and 6) and absence (entries 7 and 8) of Na<sub>2</sub>CO<sub>3</sub> strengthened the hypothesis for Na<sup>+</sup> playing a role in counterion swapping. These also confirmed the requirement for the presence of carbonate to expedite transmetallation. The kinetics of the reaction carried out under the conditions used in entry 4 were studied by ReactIR (Figure 109). Using the commercially available Na<sub>4</sub>[Fe<sup>II</sup>(CN)<sub>6</sub>] $\cdot$ 10H<sub>2</sub>O (entry 5) resulted in no conversion to product after 5 hours.



**Figure 109** Reaction profile when  $\text{Na}_4[\text{Fe}(\text{CN})_6]$  was used as a cyanide source and **47** as a precatalyst in the cyanation of **65**. Reaction conditions:  $\text{Na}_4[\text{Fe}(\text{CN})_6]$  (0.22 eq.),  $\text{Na}_2\text{CO}_3$  (1 eq.), precatalyst **47** (0.01 mol%, 72  $\mu\text{M}$ ), DMAc,  $\text{N}_2$ , 120  $^\circ\text{C}$ . Inset graph shows enlargement of reaction profile up to 20 % conversion.

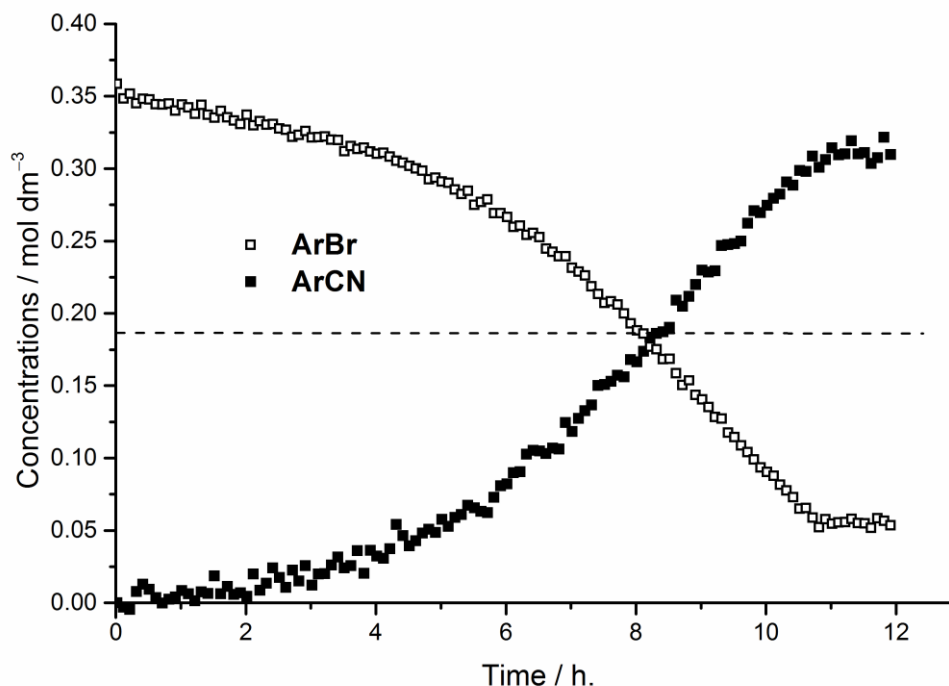
The reaction profile shown in Figure 109 when the cyanation reaction was performed using  $\text{Na}_4[\text{Fe}(\text{CN})_6]$  showed an induction period of 7 hours before catalysis began. Such a pronounced sigmoidal reaction is indicative of a reaction catalysed by the surface of a nanoparticulate catalyst grown *via* the Finke-Watzky 2-step mechanism.<sup>31, 33</sup> By following the  $[\text{Fe}(\text{CN})_6]^{4-}$  absorbance, as expected  $\text{Na}_4[\text{Fe}(\text{CN})_6]$  was much more soluble in hot DMAc than  $\text{K}_4[\text{Fe}(\text{CN})_6]$  (Figure 110). When using  $\text{Na}_4[\text{Fe}(\text{CN})_6]$ , the absorption corresponding to  $[\text{Fe}(\text{CN})_6]^{4-}$  appeared at 2061  $\text{cm}^{-1}$  due to different solvation and ion pairing effects.<sup>148a</sup> Contrary to what was usually observed (the majority of  $[\text{Fe}(\text{CN})_6]^{4-}$  solvation occurring upon addition of Pd, as in Figure 103) a large portion of  $\text{Na}_4[\text{Fe}(\text{CN})_6]$  was already in solution before the addition of the precatalyst. When conducting experiments on the ReactIR the modular addition of reagents to the reaction vessel is required, meaning that the  $\text{Na}_4[\text{Fe}(\text{CN})_6]$  had been stirred in DMAc at 120  $^\circ\text{C}$  for at least 5 minutes prior to the addition of the precatalyst. This may be a contributing factor as to why the reaction profile in the presence  $\text{Na}_4[\text{Fe}(\text{CN})_6]$  as a cyanating agent of did not reflect the result displayed in

Table 10 (Entry 4, 16% conversion after 5 hours).



**Figure 110** The trend of the hexacyanoferrate absorbance (at  $2061\text{ cm}^{-1}$ ) when using  $\text{Na}_4[\text{Fe}(\text{CN})_6]$  as a cyanide source. Reaction conditions:  $\text{Na}_4[\text{Fe}(\text{CN})_6]$  (0.22 eq.),  $\text{Na}_2\text{CO}_3$  (1 eq.), precatalyst 47 (0.01 mol%,  $72\text{ }\mu\text{M}$ ), DMAc,  $\text{N}_2$ ,  $120\text{ }^\circ\text{C}$ .

A reason for the extended induction period may be due to the formation of catalytically inactive  $\text{Pd}^{\text{II}}$  cyanide salts in the presence of high concentrations of  $[\text{Fe}(\text{CN})_6]^{4-}$ .<sup>43</sup> Catalysis only occurred after a long period of slow continuous nucleation of available  $\text{Pd}^0$ , followed by a rapid increase in rate, attributed to fast autocatalytic surface growth.<sup>33</sup> The point at which efficient catalysis started to occur (*ca.* 6.5 hours) is evident in Figure 110 as a sharp decrease in  $[\text{Fe}(\text{CN})_6]^{4-}$  concentration.



**Figure 111** Reaction profile for reaction  $65 \rightarrow 69$  using Prussian red ( $K_3[Fe(CN)_6]$ ) as a cyanating agent. Dotted line indicates the point at which the concentration of starting material and product are equal. Reaction conditions: Precatalyst **47** (0.5 mol%, 1.8 mM),  $K_3[Fe(CN)_6]$  (0.22 eq.),  $Na_2CO_3$  (1 eq.), DMAc,  $N_2$ , 120 °C.

Subsequent kinetic analysis of  $K_3[Fe(CN)_6]$  as a cyanating agent, using 0.5 mol% **47** showed that the reaction proceeded by an alternative reaction mechanism. This displayed neither clear hetero- nor homogeneous catalytic behaviour (Figure 111). As the consumption of **65** and formation of **69** were almost completely symmetrical, thus concomitant with each other, there were no stoichiometric organic intermediates present in the catalytic cycle. For this type of reaction profile to occur, the mechanism must have involved the slow *in situ* formation of catalytic quantities of a key intermediate, meaning that this was an autoinductive process, in keeping with that seen in other reaction systems reported by Blackmond and co-workers.<sup>35</sup>

## 5.8 Conclusions

A range of *trans*- $Pd(OAc)_2(HNR_2)_2$  precatalysts have been shown to be catalytically competent in the Pd catalysed arylcyanation of **65**. In direct contrast to the sigmoidal kinetic traces observed under hydrous conditions, product formation was shown to proceed *via* exponential growth highlighting the absence of precatalyst activation by the F-W 2-step mechanism. Kinetic analysis of the processes by *operando* infrared spectroscopy has allowed for the distinction of catalytic efficiencies of the precatalysts tested. **51** and **52** were found to be the most efficient, however **47** was also very competent at low catalyst loadings. Given the ease and relative low price of its synthesis **47** was found to be the most financially viable

for use in a scaled up process. Under these optimised conditions **47** has been shown to be capable of cyanating a range of (hetero)aryl bromides at low catalyst loadings.

Computational work has revealed the structure of a potential active catalyst, **83**, formed *via* the autocatalytic addition of Pd<sup>0</sup> to **47** and formation of a unique Pd<sup>0</sup>-Pd<sup>II</sup> dimer species. Such a species may be the foundation for the growth of small (3-8 atoms) clusters.

Utilisation of the dimeric Pd amine complex **58** in the arylcyanation of **65** revealed a dramatic increase in catalytic activity. Providing a more facile route to species such as **85** while tuning both the electronic and steric environment around the active site therefore may increase the scope and efficacy of Pd catalysts in cross-coupling reactions in the future.

Further to the effects of amine ligands on the rates of arylcyanation chemistry, the mechanistic role of both Na<sup>+</sup> and CO<sub>2</sub><sup>2-</sup> have been confirmed as assisting the optimum solubility of the [Fe(CN)<sub>6</sub>]<sup>4-</sup> anion *via* ion pairing and facilitating transmetallation, respectively. While KFe<sup>III</sup>[Fe<sup>II</sup>(CN)<sub>6</sub>] proved to be incompetent as a cyanide source, K<sub>3</sub>[Fe(CN)<sub>6</sub>] proved otherwise and at 0.5 mol% catalyst loading resulted in the efficient arylcyanation of **65**, albeit in a surprising change of mechanism to an autoinductive process.

## Chapter 6: Conclusions and Future Work

### 6.1. Conclusions

The work described within this thesis has explored the design, synthesis and use of amine containing Pd<sup>II</sup> precatalysts in Pd-catalysed arylocyanation reactions. A series of Pd(OAc)<sub>2</sub>(HNR<sub>2</sub>)<sub>2</sub> precatalysts have been synthesised and their mechanism of formation from Pd<sub>3</sub>(OAc)<sub>6</sub> revealed. Further to this, an adapted preparation for the synthesis of a sterically encumbered [Pd(OAc)<sub>2</sub>(HNR<sub>2</sub>)]<sub>2</sub> dimer precatalyst (**58**) in excellent yield was developed. Structural analysis by single crystal X-Ray diffraction showed strong inter- or intramolecular hydrogen bonding interactions in all monomeric and dimeric precatalysts. Comparison of the structural and spectroscopic intricacies of **49**, **50** and **58** with established literature regarding Pd–Pd interactions in Pd<sup>II</sup> dimers rationalised the structural changes observed upon variation of the amine ligand at Pd.

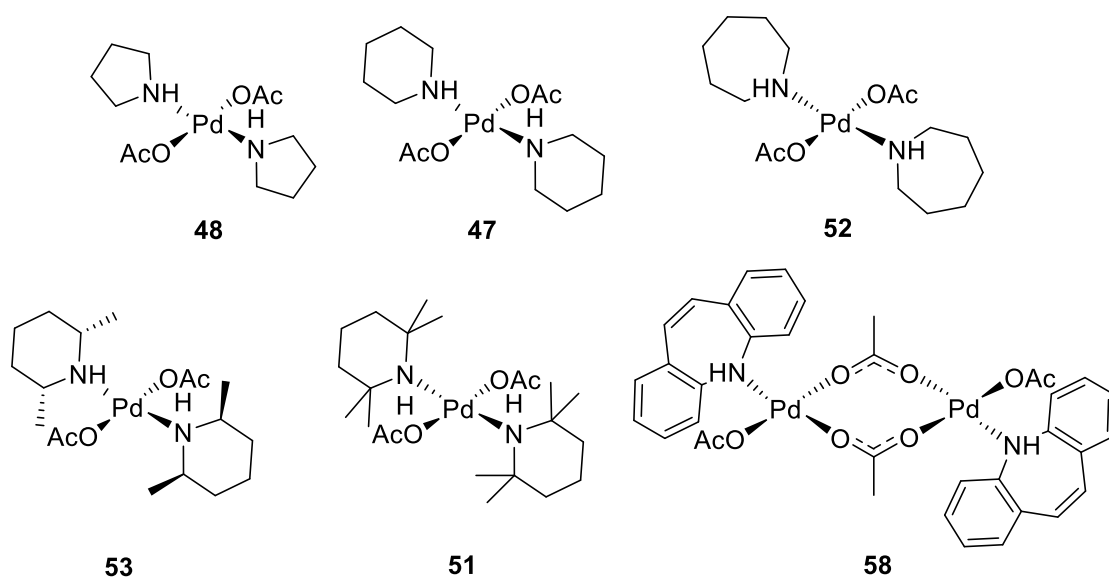


**Figure 112** Six Pd<sup>II</sup> amine complexes investigated as precatalysts in the arylocyanation of **65** during this study.

The utility of *in situ* infrared spectroscopy allowed for the kinetic investigation of the model arylocyanation reaction when using **47** as a precatalyst under hydrous and anhydrous conditions. In the presence of the cyanating agent K<sub>4</sub>[Fe(CN)<sub>6</sub>]·3H<sub>2</sub>O, at low precatalyst loadings (0.05 mol% 17.5 ppm) sigmoidal reaction profiles were characterised as proceeding *via* the Finke-Watzky 2-step slow nucleation and autocatalytic growth mechanism by non-linear, sum of least squares data fitting. As Pd precatalyst loadings were increased (0.1–2.5 mol% 35–875 ppm) the precatalyst activation mechanism was found to deviate further from

the F-W 2-step mechanism. Despite this, a non-linear relationship between Pd concentration and reaction rate and catalyst TOF was found at these higher Pd loadings and concentrations. The order with respect to Pd was found to be 0.26 ( $\pm 0.02$ ) under these reaction conditions and this in conjunction with a positive result from a  $\text{Hg}^0$  additive test provides evidence for the presence of catalytically active multinuclear Pd species.

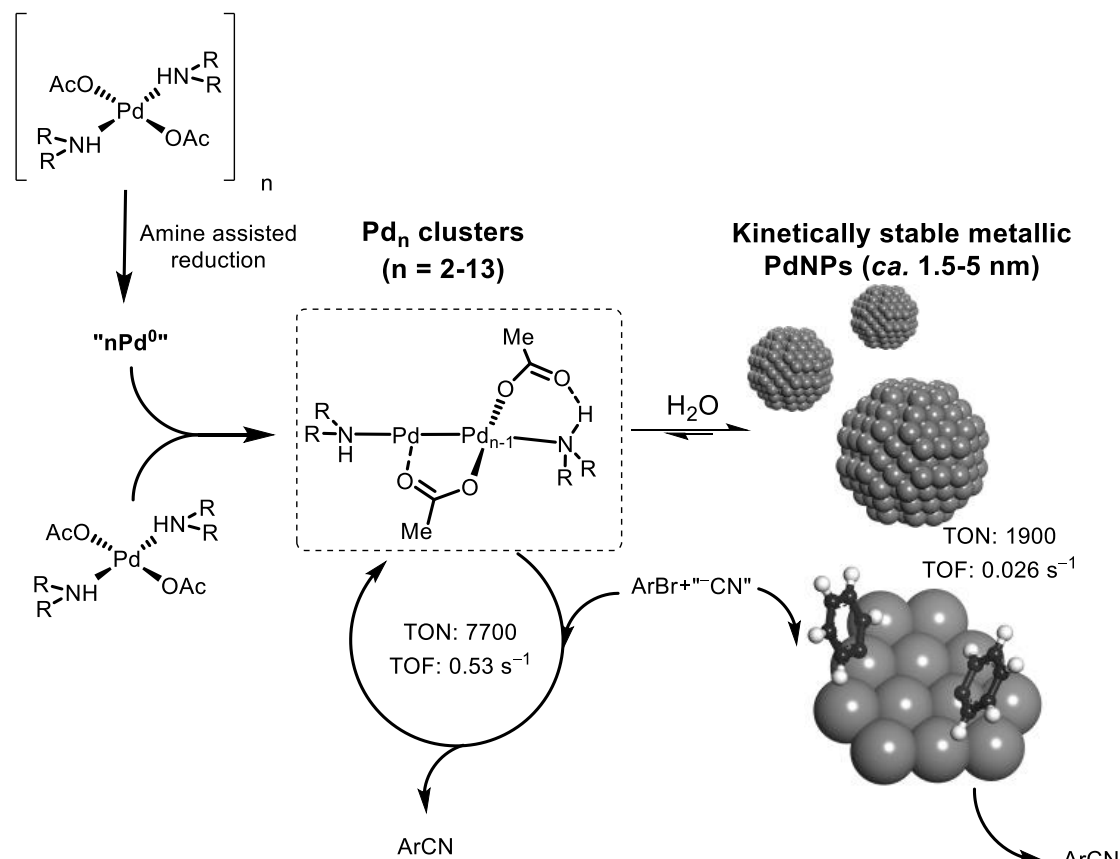


**Figure 113** The nature of the active catalyst formed from precatalysts such as **47** in Pd-catalysed arylocyanation reactions is dependent upon Pd concentration, catalyst:substrate ratio and the presence of water.

Further to this mechanistic investigation, upon kinetic analysis of the same reaction under anhydrous conditions, *i.e.* when utilising  $\text{K}_4[\text{Fe}(\text{CN})_6]$  as the cyanating agent, a dramatic change of kinetic profile for product formation from sigmoidal to exponential growth was observed. This highlighted the absence of precatalyst activation by the F-W 2-step mechanism under anhydrous conditions. The catalytic efficiencies of the precatalysts shown in Figure 112 have been quantitatively analysed at 0.01 mol% Pd precatalyst loading and a concentration of  $72 \mu\text{mol dm}^{-3}$  (7 ppm). A range of efficiencies was observed across the precatalyst series, but despite **51** and **52** being found to be the most proficient, **47** was also found to operate at a comparable efficiency.

A synergistic effect of both optimum catalyst loadings and concentration has been revealed, showing that at 0.01 mol% a Pd concentration of 72  $\mu\text{mol}$  (7 ppm) provided the highest catalytic efficiency. The increased reaction efficiency under these optimum reaction conditions has been tentatively attributed to an active catalyst species of type **83** (Figure 113). Under these optimised conditions precatalyst **47** has been shown to be capable of cyanating a range of (hetero)arylbromides at low catalyst loadings. Following preliminary kinetic studies the sterically encumbered dimer precatalyst **58** was found to operate at much higher TOFs than the monomeric  $\text{Pd}(\text{OAc})_2(\text{HNR}_2)_2$  precatalysts, albeit at the detriment of TON.

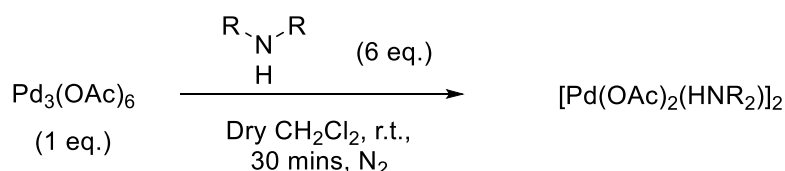
In light of previous literature examples, the kinetic data presented here is complementary to that reported by Frech *et al.*,<sup>43</sup> with strong evidence for the role of higher order Pd species in the mechanism of Pd catalysed arylcyanation reactions using  $\text{K}_4[\text{Fe}(\text{CN})_6]$  or  $\text{K}_4[\text{Fe}(\text{CN})_6]\cdot 3\text{H}_2\text{O}$ . The precatalysts reported within this thesis have shown the capability to operate at catalyst loadings as low as 0.005 mol% in arylcyanation reactions when at a Pd concentration of 72  $\mu\text{M}$ , 7 ppm while achieving TONs higher than that reported under similar conditions when using the PdNP precursor complex, **26** developed by Frech *et al.*<sup>43</sup> or  $\text{Pd}(\text{OAc})_2$  as demonstrated by Beller *et al.*<sup>102a</sup> and Weissman *et al.*<sup>102b</sup>

The kinetic analysis of the Pd-catalysed arylcyanation reaction by *in situ* infrared spectroscopy has also allowed for the role of  $\text{CO}_2^{2-}$  to be established as facilitating transmetallation from Fe to Pd, and for additive counterions (such as  $\text{Na}^+$ ) as assisting the optimum solubility of the  $[\text{Fe}(\text{CN})_6]^{4-}$  anion *via* ion-pairing. The observation of solubilised  $[\text{Fe}(\text{CN})_6]^{4-}$  enabled for an unprecedented insight into the relationship between the rate of reaction and the concentration of hexacyanoferrate in solution. This further supports the literature precedent for limited heterogeneous Pd catalyst poisoning in the presence of  $\text{K}_4[\text{Fe}(\text{CN})_6]$  and  $\text{K}_4[\text{Fe}(\text{CN})_6]\cdot 3\text{H}_2\text{O}$ .

## 6.2. Future work

### 6.2.1. Use of $[\text{Pd}(\text{OAc})_2(\text{HNR}_2)]_2$ precatalysts in Pd-catalysed arylcyanation reactions

Whilst the preliminary studies into the catalytic activity of **58** show promise, it would be of interest to investigate the reason for improved catalyst efficiency. Work within this thesis has shown that  $[\text{Pd}(\text{OAc})_2(\text{HNR}_2)]_2$  complexes can be synthesised by the addition of a single equivalent of a secondary amine per Pd to  $\text{Pd}_3(\text{OAc})_6$ . The synthesis of **49** and **50** were found to be low yielding. However it has been shown that aminolysis of  $\text{Pd}_3(\text{OAc})_6$  with piperidine forms the thermodynamic product, **50**, *via* **47** as a kinetic product. Application of this information resulted in the successful, high yielding synthesis of **58**. It would therefore be possible to extend the scope of this methodology, if the synthesis of **49** and **50** were improved by the same method.



**Scheme 57** Using the optimised conditions used in the synthesis of **58** a range of dimeric  $[\text{Pd}(\text{OAc})_2(\text{HNR}_2)]_2$  precatalysts could be synthesised.

Given the improved TOF achieved upon using **58** as a precatalyst it is still unclear as to whether this improved efficiency is due to structural effects increasing the activity of the active catalyst, or whether it is due to the increased ease of access to species such as **83** and **84** from a dimeric precatalyst. The improved synthesis of **49** and **50** would allow for their activities to be directly compared with their monomeric equivalents, **48** and **47**. Any further improvement to catalytic activity resulting from structural manipulation rather than simply monomer/dimer effects would therefore become evident.

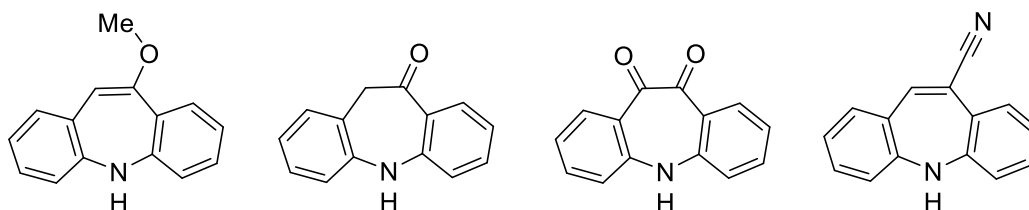


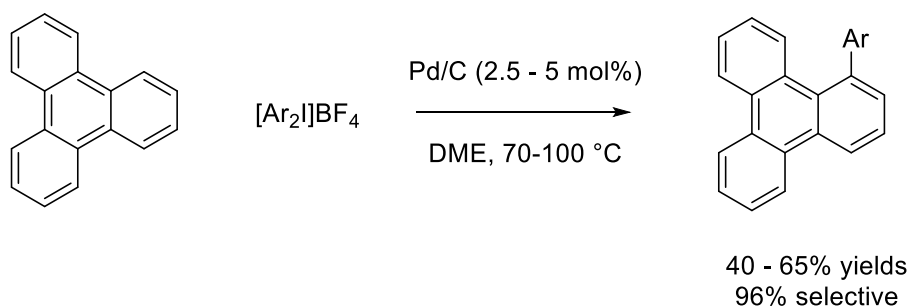
**Figure 114** Potential substituted dibenzazepine ligands.

Ligand electronics have been shown to have significant effects on the solid state structures of **49**, **50** and **58** (see Section 2.3).<sup>76</sup> Upon deconvolution of a monomer/dimer effect on catalyst efficiency, it may be possible to further take advantage of ligand electronic influences on precatalyst capability *via* the fine-tuning of electron density on the active site of catalysis on **85**. The synthesis of the dimer complexes with the ligands shown in Figure 114,<sup>150</sup> their solid-state structural analysis and catalytic testing in a model cross-coupling reaction, coupled with *in silico* studies on the effect of substituents on the HOMO and LUMOs of the active catalyst species could result in establishing a structure-activity relationship.

## 6.2.2. Investigation of “heterogeneity triggers” in Pd-catalysed cross-couplings and C–H functionalisation reactions

Within this thesis it is reported that water and Pd concentration can affect the mechanism of precatalyst activation, catalysis and therefore catalyst efficiency. This has been attributed to the more facile formation of catalytically active PdNPs or small multinuclear Pd clusters under specific reaction conditions. The use of small variations of conditions to access different phases of catalysis, *i.e.* homogeneous *vs* small cluster *vs* nanoparticulate, has been utilised previously in the study of Rh-catalysed hydrogenation reactions.<sup>140</sup>

Reports from the Glorius group have shown the utility of widely available, poorly characterised Pd/C catalysts in the highly regioselective C–H functionalisation of both heteroarenes<sup>12a, 151</sup> and unreactive, polycyclic arenes (Scheme 58).<sup>152</sup>



**Scheme 58** Glorius *et al.* report the highly regioselective C–H arylation of polyaromatics by Pd/C.<sup>152</sup>

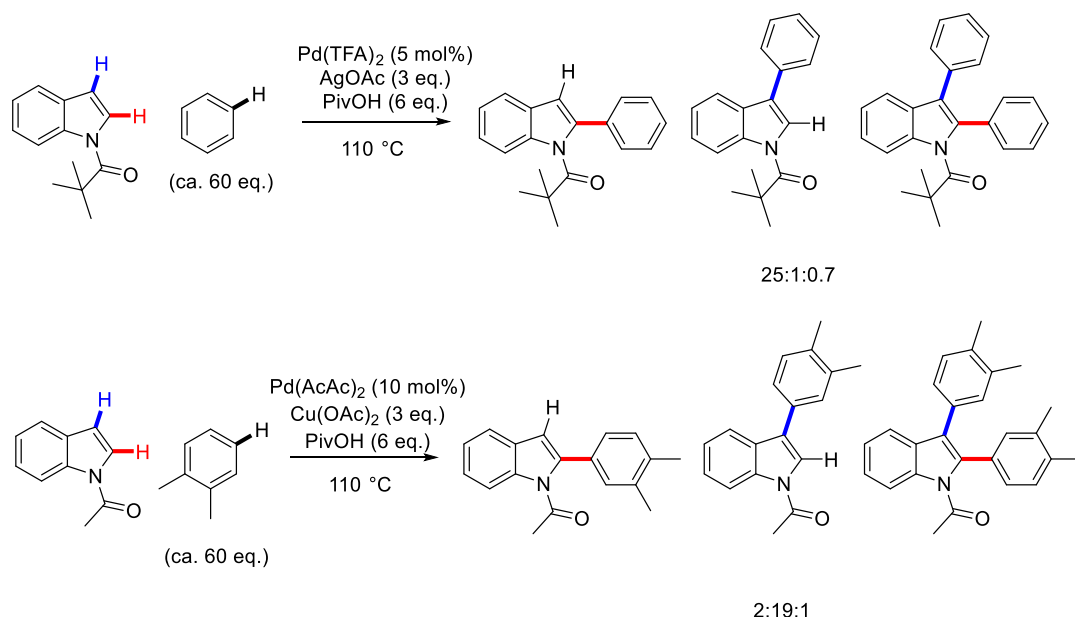
Despite their mild reaction conditions and display of novel reactivity, little insight into the true nature of the active catalyst has so far been provided. Very little structural characterisation of the Pd/C catalysts was carried out. It is possible therefore that a better mechanistic understanding of such catalytic processes would allow for more experimentally informed decisions regarding Pd precatalyst choice. This in-turn should result in higher

catalytic efficiency and lower catalyst loadings. Subsequent studies within this group have highlighted the importance of observing reaction kinetics to evaluate the most suitable Pd precatalysts for such transformations along with characterising their behaviour as sources of “homogeneous” or “heterogeneous” Pd.<sup>153</sup>

Water has been revealed within this study to act as a “heterogeneity trigger” from homogeneous Pd precatalysts in cross-coupling processes. The judicious control of Pd concentration in hand with Pd catalyst loading has allowed for further catalytic optimisation. The application of this knowledge to reactions such as that shown in Scheme 58 may result in a greater understanding of the nature of the active catalyst species and provide higher catalyst efficiency. Application of such “heterogeneity triggers” to Pd precatalysts under the reaction conditions displayed in Scheme 58 could result in the formation of PdNPs capable of comparable transformations at higher efficiencies.

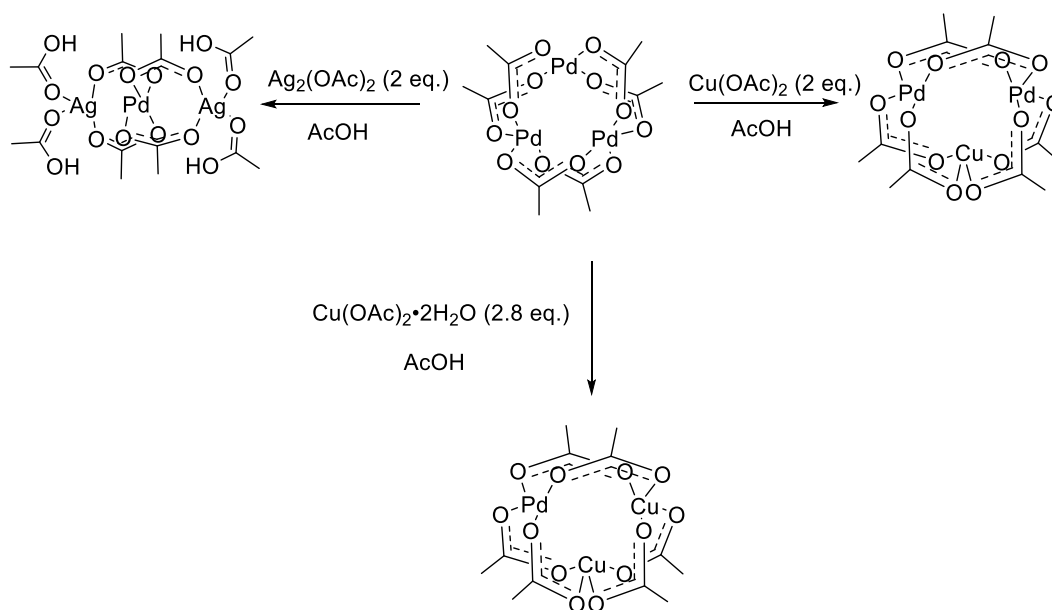
### **6.2.3. Use of mixed-metal clusters and use in Pd-catalysed cross-couplings and C–H functionalisation reactions**

Throughout the course of the studies within this thesis, the broad subject area within the Fairlamb group, supervision of project students along with discussions with Ian Fairlamb have highlighted the potential role of mixed-metal clusters as precatalysts for C–H functionalisation processes. The increasing requirement for the minimisation of waste production and concise chemical synthesis has led to the development of a vast array of greener Pd-catalysed C–C bond formation methodologies. Direct arylation provides an elegant alternative route towards the synthesis of biaryl motifs by surpassing the requirement for wasteful prefunctionalisation, as required for traditional cross-couplings.<sup>154</sup> However, the direct coupling of two C–H bonds provides substantial regiochemical challenges in substrates with multiple C–H bonds available for functionalisation. While the utilisation of coordinating directing groups can facilitate regioselectivity, few instances of regioselective direct arylation in the absence of directing groups have been achieved.<sup>155</sup> While the use of stoichiometric Cu<sup>II</sup> or Ag<sup>I</sup> salts as oxidants in direct arylation chemistry is widespread, Fagnou *et al.* uncovered an intriguing regiochemical switch in the direct arylation of indoles at C2/C3 (Scheme 59) as a function of the metal oxidant used.<sup>156</sup>



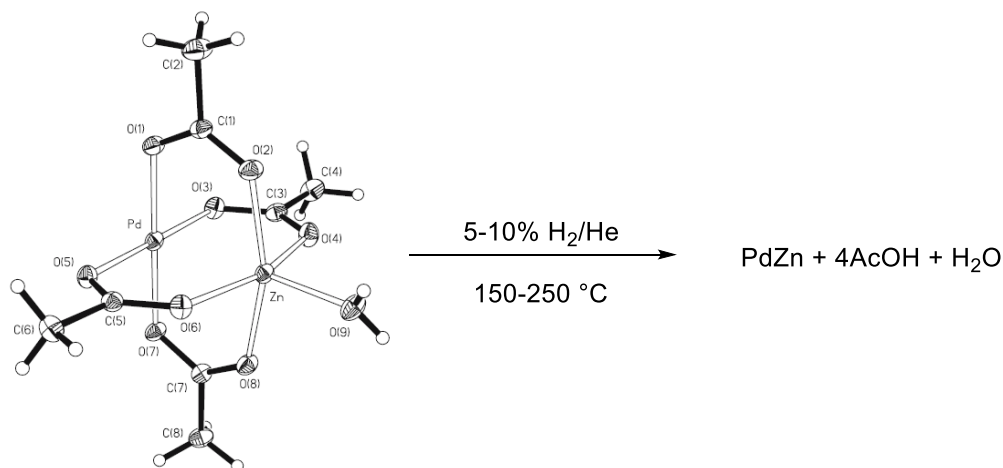
**Scheme 59** Switch in the regioselectivity of the direct arylation of *N*-protected indole in the presence of differing terminal oxidants.<sup>156</sup>

While the mechanism by which this dramatic switch in regiochemistry proceeds is as yet unknown it has been postulated that heterodimetallic Pd<sup>II</sup>-Cu/Ag clusters may play an integral role in the catalytic cycle, with the metal cations influencing the regiochemical outcome of the reaction. A vast array of heterodimetallic Pd<sup>II</sup>-M acetate clusters have been reported to form under acidic conditions (Scheme 60),<sup>58b, 157</sup> and interestingly their syntheses have been found to be catalysed by the presence of substoichiometric amounts of water.<sup>158</sup> In addition, Pd<sup>II</sup>-rare earth metal acetate complexes have also been shown to undergo facile total acetate-pivalate metathesis.<sup>159</sup> The synthesis of the Pd<sup>II</sup>-Cu<sup>II</sup> and Pd<sup>II</sup>-Ag<sup>I</sup> acetate clusters for use as catalysts directly in these direct arylation reactions would not only provide important evidence for the mechanism of regioselectivity, but also help to open a niche for these relatively catalytically unexplored complexes. The further application of these precatalysts, coupled with mechanistic investigation will expand the scope of Pd-heterometallic cooperative catalysis to more recent examples developed in the Fairlamb group.<sup>110, 160</sup>



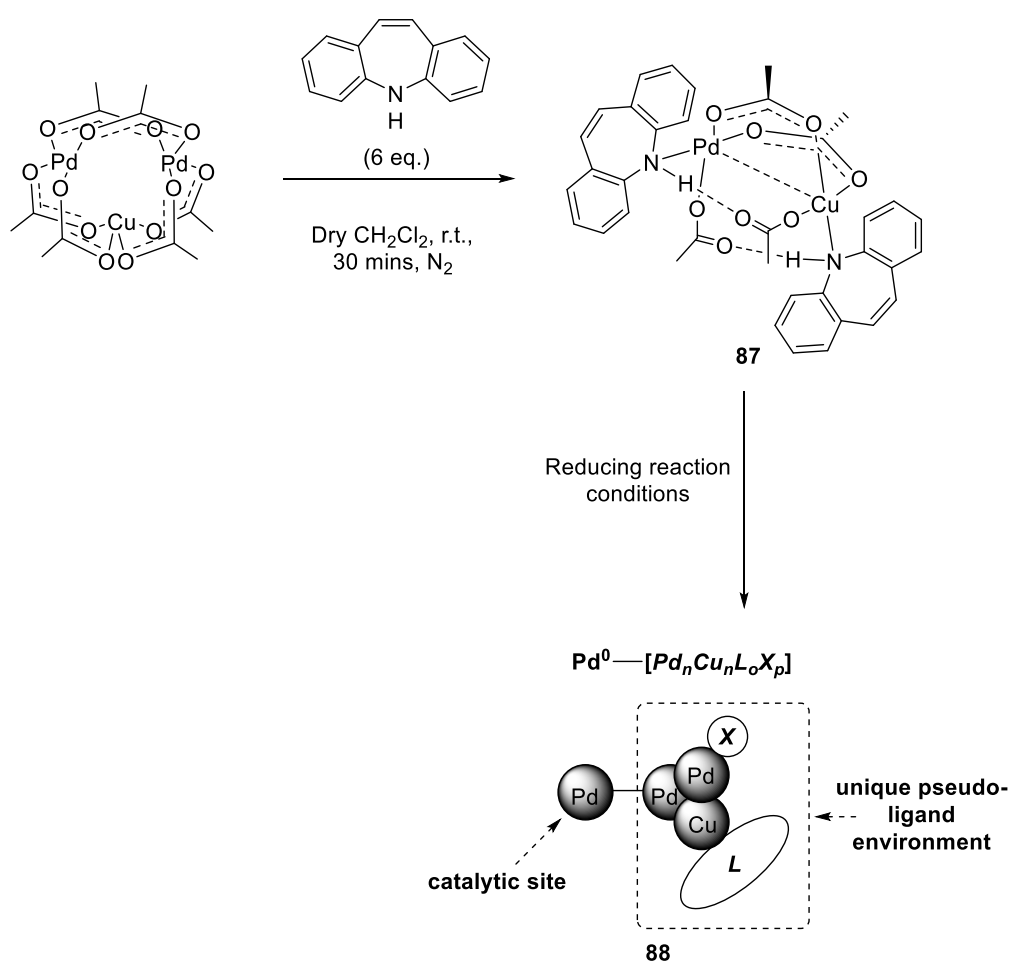
**Scheme 60** Synthesis of heterodimetallic Pd-Cu/Ag acetate clusters.<sup>161</sup>

While there is a surplus of literature supporting the role of homogenous Pd in direct arylation chemistry, there is significant evidence for PdNPs as competent catalysts in cross-coupling<sup>10</sup> and C–H functionalisation reactions.<sup>116, 162</sup> Further to this, heterogeneous Pd catalysts have also been shown to display superior selectivity in C–H functionalisation processes.<sup>12, 151-153</sup> Given the established speciation of  $\text{Pd}_3(\text{OAc})_6$  to catalytically competent PdNPs under aqueous Suzuki-Miyaura cross-coupling conditions (see Section 1.2.2 of this thesis for an in depth discussion of this)<sup>40, 68, 70a, 74, 76</sup> and that heterodimetallic  $\text{Pd}^{\text{II}}\text{-Zn}^{\text{II}}$  acetate clusters are convenient precursors to well-defined Pd–Zn alloy NPs by reduction with  $\text{H}_2$ , it is feasible that other heterodimetallic carboxylates (Cu/Ag) are also competent NP precursors.<sup>157f</sup> Whether these complexes will form alloy NPs *in situ* under simple reducing conditions or upon the addition of catalytic water remains unclear and will require further experimentation.



**Scheme 61** The reduction of Pd(II)-Zn(II) acetate clusters under H<sub>2</sub> provides well defined PdZn alloy nps.<sup>157f</sup> Adapted with permission from *Catal. Lett.* 2006, 112, 155-161. Copyright of Springer.

If the heterodimetallic Pd-Cu clusters were found to be catalytically active, further control over the formation of defined nanoparticulate alloys from them could be introduced *via* amine assisted metal reduction. Given the precedent set within this thesis for the role of Pd(OAc)<sub>2</sub>(HNR<sub>2</sub>)<sub>2</sub> and [Pd(OAc)<sub>2</sub>(HNR<sub>2</sub>)]<sub>2</sub> as precursors for the formation of highly catalytically active small Pd clusters of type **83**, the synthesis and application of mixed metal complexes of the type **87** could provide access to heterodimetallic analogues of type **88** (Scheme 62).



**Scheme 62** The synthesis of Pd(OAc)<sub>2</sub>(HNR<sub>2</sub>)Cu(OAc)<sub>2</sub>(HNR<sub>2</sub>) complexes, and use as precursors for catalysts of type **88**.

Tuning the electronics of the active catalytic site in **88** by the introduction of heterometals could reveal completely unprecedented reactivities and contribute to the expanding area of nanoalloy catalysis.<sup>163</sup>

## Chapter 7: Experimental Section

### 7.1. General Experimental Techniques

#### Solvents and Reagents

Commercially sourced reagents were purchased from Sigma Aldrich, Alfa Aesar, Acros or Fluorochem and used as received unless otherwise noted. Dry ether (diethyl ether), THF, CH<sub>2</sub>Cl<sub>2</sub>, hexane, toluene and acetonitrile were obtained dry from a Pure Solv MD-7 solvent machine and stored under nitrogen. Ether and THF were also degassed by bubbling nitrogen gas through the solvent with sonication for at least 30 minutes. Piperidine was distilled from KOH under a nitrogen atmosphere and stored in an ampoule wrapped in aluminium foil under nitrogen. Pyrrolidine, azepane, 2,6-*cis* dimethylpiperidine and 2,2,6,6-tetramethylpiperidine were all freshly purified prior to use *via* short path distillation. Dry DMF and DMAc were obtained from Acros, degassed by bubbling with nitrogen gas through the solvent with sonication and stored in ampoules under nitrogen while over activated 4Å molecular. Petrol refers to the fraction of petroleum ether boiling in the range 40-60 °C. Schlenk techniques (high vacuum, liquid nitrogen trap on a standard in-house built dual line). Room temperature upper and lower limits are stated as 13-25 °C, but typically 21 °C was recorded. Brine refers to a saturated aqueous solution of NaCl.

#### Chromatography

Thin layer chromatography (TLC) was carried out using Merck 5554 aluminium backed silica plates (silica gel 60 F254) and spots were visualized using UV light (at 254 nm). Where necessary, plates were stained and heated with one of potassium permanganate, anisaldehyde or vanillin as appropriate. Retention factors (R<sub>f</sub>) are reported in parentheses along with the solvent system used. Flash column chromatography was performed according to the method reported by W. C. Still *et al.* using Fluorochem 60 Å silica gel (particle size 40–63 µm) and a solvent system as reported in the text.

## Nuclear Magnetic Resonance Spectroscopy

NMR spectra were obtained in the solvent indicated, using a JEOL ECX400 or JEOL ECS400 spectrometer (400 MHz, 101 MHz and 376 MHz for  $^1\text{H}$ ,  $^{13}\text{C}$  and  $^{19}\text{F}$ , respectively). Chemical shifts are reported in parts per million and were referenced to the residual undeuterated solvent of the deuterated solvent used ( $\text{CHCl}_3$   $\delta_{\text{H}} = 7.26$  ppm;  $\delta_{\text{C}} = 77.16$  ( $\text{CDCl}_3$ ),  $\text{CDHCl}_2$   $\delta_{\text{H}} = 5.31$  and  $\delta_{\text{C}} = 54.0$  ( $\text{CD}_2\text{Cl}_2$ ). Spectra were typically run at a temperature of 298 K. All  $^{13}\text{C}$  NMR spectra were obtained with  $^1\text{H}$  decoupling. NMR spectra were processed using MestReNova software (versions 5.3, 7.03 and 8.1) as required and were exported as .TIF files in and inserted directly into the document. Multiplicities are described as singlet (s), doublet (d), triplet (t), quartet (q), quintet (quin), multiplet (m), apparent (app.) and broad (br). The coupling constants ( $J$ ) have been quoted to  $\pm 0.1$  Hz.  $^1\text{H}$  NMR chemical shifts are quoted to 2 decimal places;  $^{13}\text{C}$  and  $^{19}\text{F}$  NMR chemical shifts are quoted to 1 decimal place. Numbers were rounded to the nearest value, e.g.  $1.237 \approx 1.24$ ,  $1.232 \approx 1.23$ . Copies of  $^1\text{H}$  and  $^{13}\text{C}$  NMR spectra for all compounds are given in appendix 7.

## Infrared Spectroscopy

Infrared spectra were obtained using either a Unicam Research Series FTIR (KBr-IR) or a Bruker ALPHA-Platinum FTIR Spectrometer with a platinum-diamond ATR sampling module, in a NaCl window solution cell. All cyanation kinetics and complimentary studies were followed using a Mettler Toledo React-IR spectrometer with a silicon probe and K6 conduit/R4 (mirror arm) and MCT detector. IR spectra are taken in real-time every 60 seconds between  $4000$  and  $649\text{ cm}^{-1}$ , with a spectral resolution of  $4\text{ cm}^{-1}$ . All reaction temperatures were measured independently from the heating bath using a TENMA 72-7715 electronic thermometer and thermocouple to ensure accurate reaction temperature regulation.

## Mass Spectrometry

Electrospray ionisation (ESI) mass spectrometry was performed on a Bruker Daltronics micrOTOF spectrometer. Electron impact (EI), atmospheric pressure chemical ionisation (APCI) and liquid induction field desorption ionisation (LIFDI) mass spectrometry were carried out using a Waters GCT Premier MS Agilent 7890A GC. Mass spectral data is quoted as the  $m/z$  ratio. Mass to charge ratios ( $m/z$ ) are reported in Daltons. High resolution mass spectra are reported with  $<5$  ppm error (ESI) or  $<20$  ppm error (LIFDI). For clarity, LIFDI data are reported for  $^{106}\text{Pd}$ , the most abundant natural isotope of Pd.

## Melting points

Melting points were recorded using a Stuart digital SMP3 machine with a using a temperature ramp rate of 5 °C min<sup>-1</sup>.

## Elemental Analysis

Elemental analysis was carried out using an Exeter Analytical CE-440 Elemental Analyser, with the percentages reported as an average of two runs.

## X-Ray Crystallography

Diffraction data were collected at 110 K on an Agilent SuperNova diffractometer with Mo K $\alpha$  radiation ( $\lambda = 0.71073 \text{ \AA}$ ). Data collection, unit cell determination and frame integration were carried out with CrysAlisPro. Absorption corrections were applied using face indexing and the ABSPACK absorption correction software within CrysAlisPro. Structures were solved and refined using Olex2<Dolomanov, 2009 #261> implementing SHELX algorithms and the Superflip<sup>164</sup> structure solution program. Structures were solved by charge flipping, Patterson or direct methods and refined with the ShelXL<sup>165</sup> package using full-matrix least squares minimisation. All non-hydrogen atoms were refined anisotropically. Tables of crystallographic data are given in Appendix 3.

## 7.2. Manual treatment of kinetic data

### 7.2.1. Treatment of kinetic data for Finke-Watzky nucleation and autocatalytic growth mechanism by nonlinear sum of least-squares curvefitting

All data treatments were devised after careful incorporation of the protocol provided by Kemmer and Keller for nonlinear least-squares data fitting<sup>141</sup> with the integrated rate equation for the 2-step, Finke-Watzky nucleation and autocatalytic growth mechanism (Equation 1).<sup>33</sup>

$$[A]_t = \frac{\frac{k_1}{k_2} + [A]_0}{1 + \frac{k_1}{k_2[A]_0} \times e^{(k_1+k_2[A]_0)t}}$$

**Equation 4. The integrated rate equation for the 2-step, Finke-Watzky nucleation and autocatalytic growth mechanism.**

Figure 115 shows a screenshot of the spreadsheet, with formulae shown, used to calculate each curvefit. Where:  $k_1$  (cell B1) is the calculated rate of nucleation;  $k_2$  (cell B2) is the calculated rate of catalytic surface growth; corrected  $k_2$  (cell B3) is the calculated rate of autocatalytic surface growth corrected to include the correct catalyst : substrate ratio; X (column C) is the time of reaction progression in hours;  $Y_{\text{obs}}$  (column E) is the concentration of starting material, calculated from the known concentration of product in column D;  $Y_{\text{calc}}$  (column F) is the calculated concentration of starting material according to Equation 1;  $\delta^2$  (column G) is the square residual between  $Y_{\text{obs}}$  and  $Y_{\text{calc}}$ .

In order to calculate a sum of least squares fit, Excel Solver must be used to optimise the Sum of Square Residuals (SSR) (**Set Target Cell**, B4), to the **Value of: 0, Subject To The Constraints**, B2>0.000001. The adjustable parameters in this instance are  $k_1$  and  $k_2$  and can be set in Solver by defining the field “By Changing Cells” as cells B1 and B2. By setting the SSR to 0 rather than minimum, this reduces the likelihood of Solver getting stuck in a local minima. However when using experimental data it is often very unlikely for this to reduce to zero and causes Solver to open an error window stating that a solution was unable to be found; this error message can be ignored.

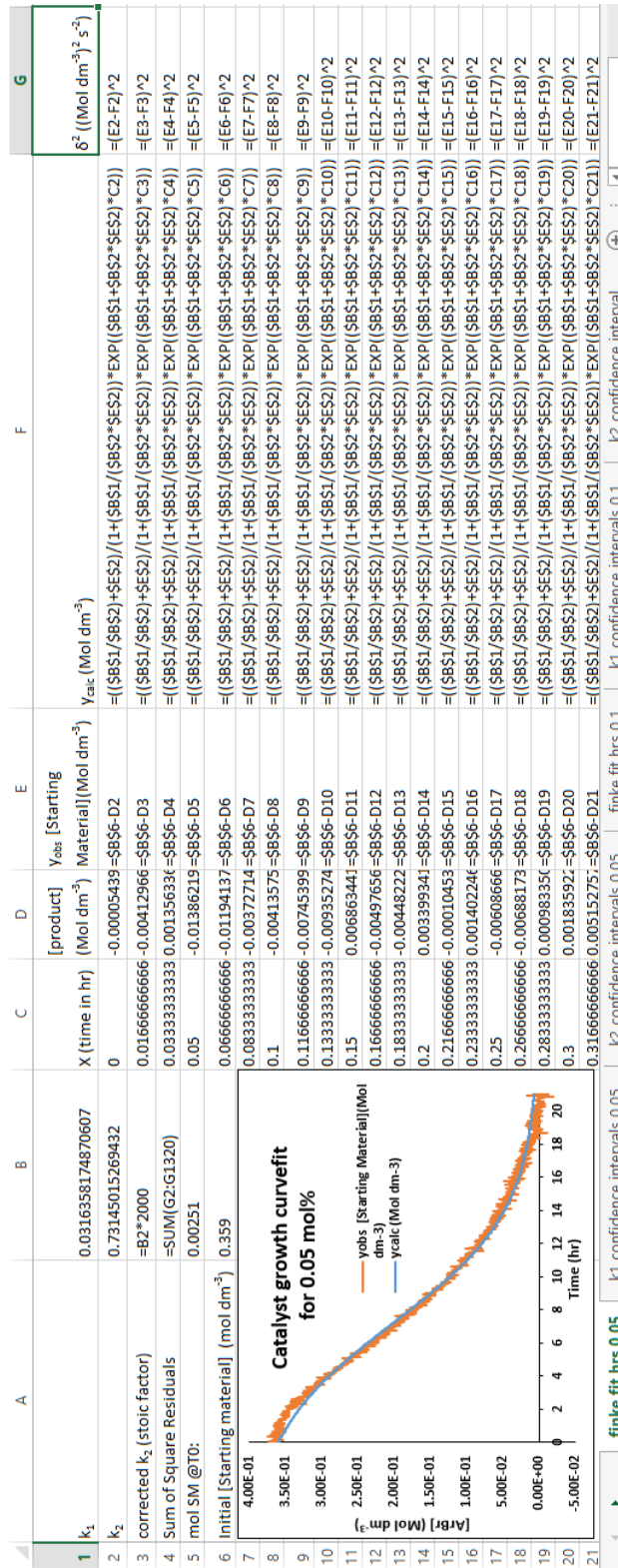
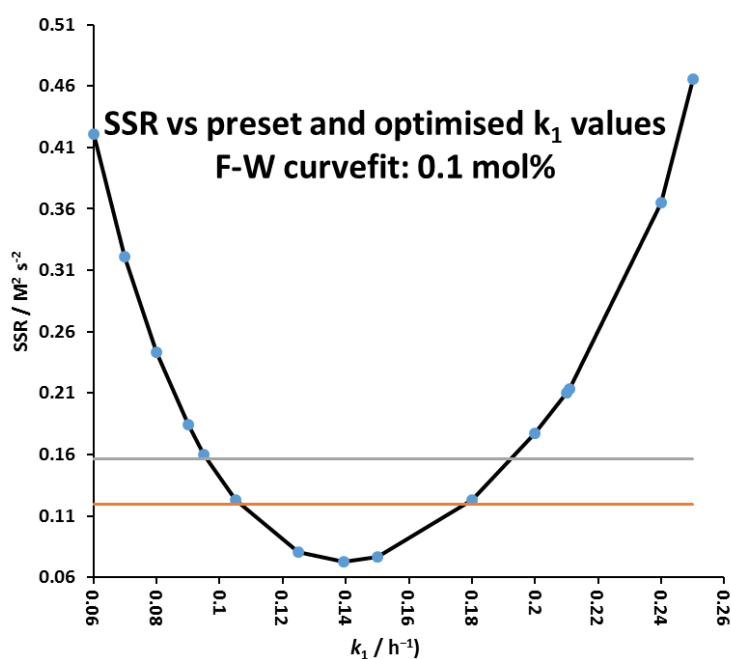


Figure 115 By incorporating Equation 1 into a nonlinear least-squares data fit, a suitable F-W 2-step mechanism curvefit can be achieved using Excel Solver for the consumption of starting material using 0.05 mol% 47 and  $K_4[Fe(CN)_6] \cdot 3H_2O$

### 7.2.2. Curvefit confidence interval calculations

Approximate curvefit confidence limits of 95 and 99% were calculated using Fisher's  $F$  distribution as described by Kemmer and Keller on optimised curvefits, prior to interval assessments.<sup>141</sup> All curvefit confidence interval assessments were calculated in Excel, manually using the protocol provided by Kemmer and Keller. This was performed by fixing one adjustable parameter at time to values close to but different from the optimal solution, then allowing solver to only optimise the other variable. This effects the SSR value, and therefore the quality of the data fit (*i.e.* the larger the SSR, the poorer the data fit). The quality of the initial curvefit is therefore reflected by the range in which the SSR is most effected; the *narrower* the range in which the data provides a good fit, the better the initial fit. A narrow range is graphically represented with steep sides and a narrow minima (of the previously optimised variable value) as is displayed by the graph shape in Figure 116.



**Figure 116 Visual representation of the 95% (brown line) and 99% (grey line) confidence limits for the limits for  $k_1$  for the F-W 2-step curvefit for a precatalyst (47) loading of 0.1 mol%.**

If a wide range of possible values for the variable in question provide an SSR value below the predetermined confidence limits, this is indicative of a poor initial data fit. This therefore causes an abnormal, wide sloping graph shape without a sharp minima (which may or may not be the previously optimised variable value) as is displayed by the graph shape in Figure 117.

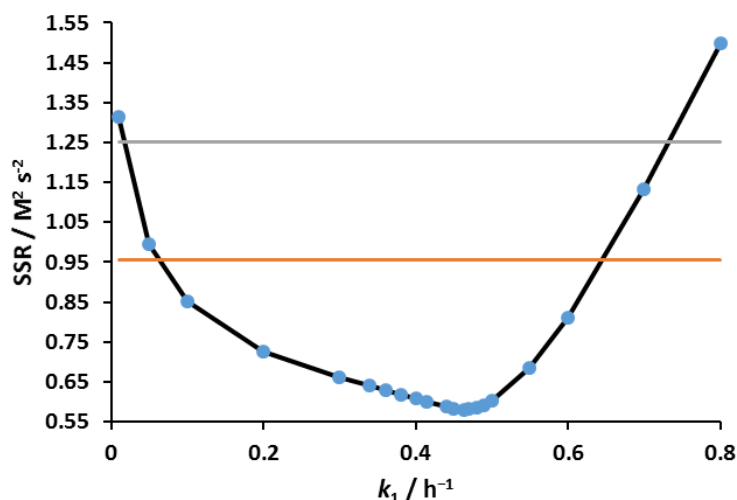


Figure 117 Visual representations of the 95% (brown line) and 99% (grey line) confidence limits for the limits for  $k_1$  for the attempted F-W 2-step curvefit.

### 7.3. General procedures

#### 7.3.1. General procedure A: React-IR kinetic studies of Pd-catalysed cyanations

An annotated picture of the experimental set up is displayed in Figure 118.

An oven dried, 100 ml three necked round bottomed flask equipped with a small stirrer bar was attached to the React-IR, then backfilled with nitrogen three times. At all points of the experiment hereafter, the reaction vessel was open to a steady flow of  $N_2$ . In parallel, a small oven dried Schlenk tube was charged with catalyst (10 mg.) and backfilled with nitrogen three times.

After backfilling the round bottomed flask with dry  $N_2$ , a background spectrum was collected and dry, degassed DMAc added (6 ml). At this point a reference spectrum was recorded with stirring. After sequence initiation, the reaction was stirred at room temperature for 5 minutes, before being heated to reaction temperature (as monitored by the internal thermocouple) by being placed in a silicon oil bath set to an appropriate level above the desired reaction temperature. After the reaction mixture reached the correct temperature, the solvent was stirred for a further five minutes and a spectrum used as a reference. To the hot solvent was then added the  $Na_2CO_3$  (0.25 – 1 eq., freshly ground in a pestle and mortar) and was stirred for a further 5 minutes. After the system reached equilibrium, the cyanating agent ( $K_4[Fe(CN)_6] \cdot 3H_2O$  or  $K_4[Fe(CN)_6]$ , 0.167 – 0.5 eq., freshly ground in a pestle and mortar) was added and stirred for 5 minutes. A  $\nu$ -spectrum was then selected as a second reference. To

the mixture was then added *N*-Benzyl-4-Bromo-6-methylpyridin-2-one (700 mg, 2.51 mmol, 1 eq.), and the sides of the flask rinsed with dry, degassed DMAc (0.5-1 ml, adding the appropriate amount to make the *final total reaction volume* up to 7 ml) *via* a septum. The reaction mixture was then stirred for 5 minutes, to allow for temperature equilibration back to the desired reaction temperature and dissolution of the substrate. During this time the appropriate amount of dry, degassed DMAc was added to the small Schlenk containing the precatalyst to make a stock solution. All catalyst stock solutions were made to a concentration of 25 mmol dm<sup>-3</sup> prior to their addition to reaction mixtures. After the reaction mixture had achieved a constant temperature and immediately after complete dissolution of the catalyst, the reaction was initiated by addition of an appropriate quantity of catalyst stock solution using a syringe to the round bottomed flask *via* a septum.

The reaction progress was monitored by measuring the increase in absorbance at 2238 cm<sup>-1</sup>, corresponding to the product's nitrile stretch. After the absorbance at 2238 cm<sup>-1</sup> had reached a constant value (indicating reaction completion) the experiment was stopped and the reaction mixture allowed to *cool to room temperature*. *Important safety note: exposure of arylcyanation reaction mixtures to water (via atmospheric air) COULD result in the formation of a small quantity of HCN gas.*<sup>93-94, 107</sup> *It is therefore imperative that any arylcyanation reaction mixtures should be allowed to cool fully, and any manipulation should be carried out in a fume cupboard with appropriate PPE.* Once the mixture had cooled, the final conversion of each reaction was measured by direct <sup>1</sup>H NMR of the crude reaction mixture. An aliquot of the reaction mixture was filtered through a small celite/cotton wool plug to remove any organic-insoluble salts and diluted with CDCl<sub>3</sub> before running the NMR experiment. The final conversion was calculated by measuring the ratio of the diagnostic peaks at 6.80 ppm for *N*-benzyl-4-bromo-6-methylpyridin-2-one and 6.85 ppm for *N*-benzyl-4-cyano-6-methylpyridin-2-one.

All peak absorption data for 2238 cm<sup>-1</sup>, 2045 cm<sup>-1</sup> and any other peaks of interest were exported into Excel in three forms: i) with no reference subtraction; ii) after subtraction of a reference spectrum of DMAc at reaction temperature; iii) after subtraction of a reference spectrum of the reaction mixture before substrate addition, at reaction temperature °C. All subsequent analysis was carried out on dataset iii). All kinetic traces (conversions) were normalised using the final reaction conversion (as calculated *vide supra*) and the absorption value of an appropriate data point at 2238 cm<sup>-1</sup> (mid data scatter) after reaction completion.

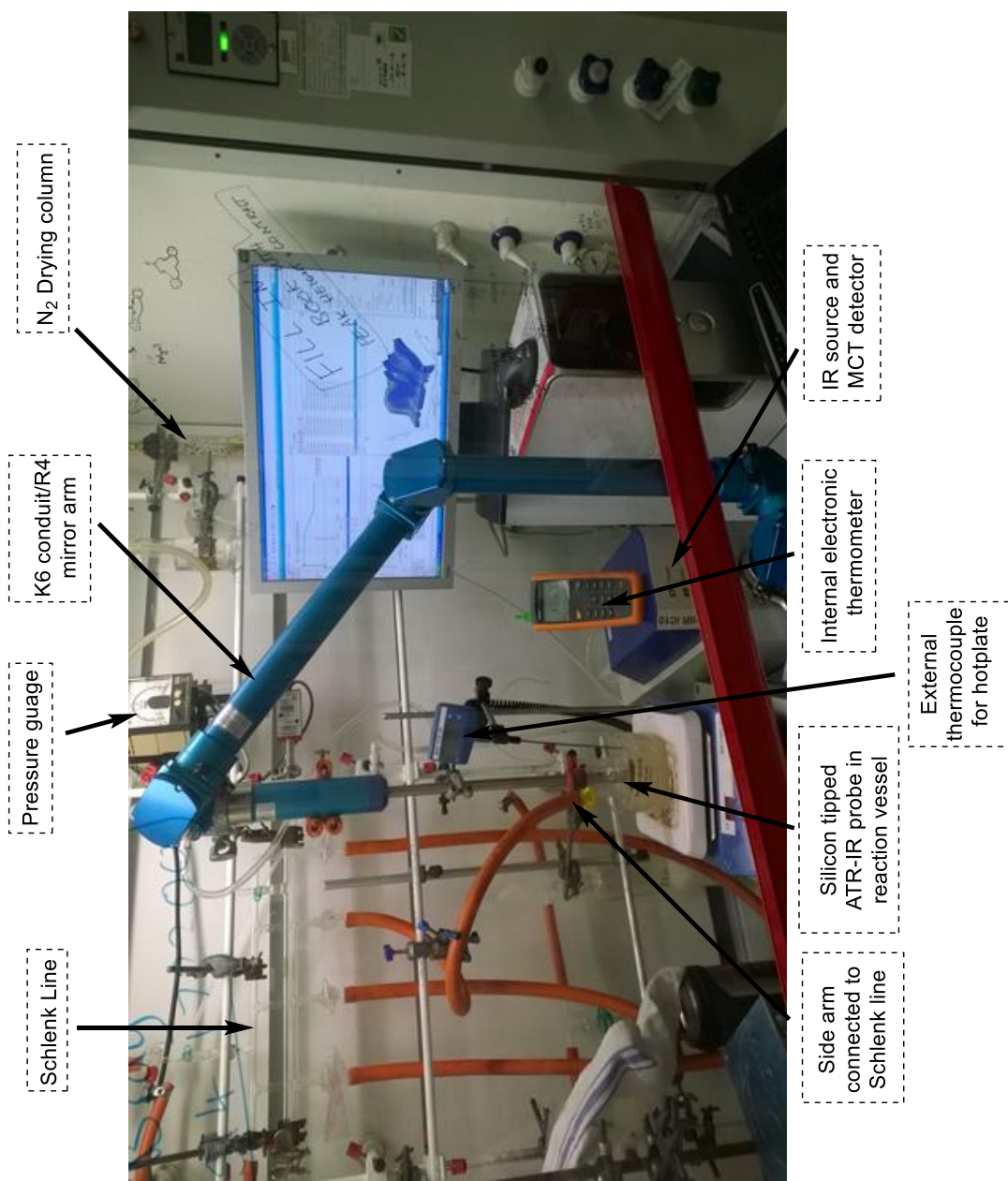


Figure 118 Picture of experimental set up for kinetic experiments using the React IR.

### 7.3.2. General procedure B: the synthesis of *trans*-Pd(OAc)<sub>2</sub>(HNR<sub>2</sub>)<sub>2</sub> complexes<sup>110</sup>

A flame dried Schlenk tube was charged with Pd<sub>3</sub>(OAc)<sub>6</sub> (100 mg, 0.148 mmol, 1 eq.) and backfilled with N<sub>2</sub> (3 x). To the Pd<sub>3</sub>(OAc)<sub>6</sub>, dry THF (5 ml) was added and the mixture was stirred until complete dissolution (*ca.* 5 minutes) to give a reddish-brown solution, if necessary then gentle heating was applied to assist dissolution. To the Pd<sub>3</sub>(OAc)<sub>6</sub> solution, freshly distilled amine (0.89 mmol, 6 eq.) was added dropwise *via* a septum. In all cases this resulted in a colour change from reddish-brown through dark red (indicating the formation of Pd<sub>2</sub>(OAc)<sub>4</sub>(HNR<sub>2</sub>)<sub>2</sub> dimer complex at the halfway point of amine addition) to dark yellow/light green after complete addition. The reaction mixture was stirred at room temperature for a further 5 minutes. The solvent was removed *in vacuo* directly to provide a solid. Trituration with dry degassed diethyl ether can be used to remove residual THF. If purification was necessary this was performed by layered recrystallisation from dry degassed CH<sub>2</sub>Cl<sub>2</sub>/hexane or CH<sub>2</sub>Cl<sub>2</sub>/pentane under Schlenk conditions at *ca.* -18 °C over night. In all cases exposure to ambient temperature while in solution resulted in fairly rapid decomposition (over the course of *ca.* 5 minutes) – formation of “Pd black”.

### 7.3.3. General procedure C: the synthesis of [Pd(OAc)<sub>2</sub>(HNR<sub>2</sub>)]<sub>2</sub> dimer complexes

A flame dried Schlenk tube was charged with Pd<sub>3</sub>(OAc)<sub>6</sub> (100 mg, 0.148 mmol, 1 eq.) and backfilled with N<sub>2</sub> (3 x). To the Pd<sub>3</sub>(OAc)<sub>6</sub>, dry THF (5 ml) was added and the mixture was stirred until complete dissolution (*ca.* 5 minutes) to give a reddish-brown solution, if necessary then gentle heating was applied to assist dissolution. To the Pd<sub>3</sub>(OAc)<sub>6</sub> solution, freshly distilled amine (0.45 mmol, 3 eq.) was added dropwise *via* a septum. In all cases this resulted in a colour change from reddish-brown to dark red. The reaction mixture was stirred at room temperature for a further 5 minutes. The solvent was removed *in vacuo* directly to provide red solids. Purification was performed by double layered recrystallisation from dry, degassed CH<sub>2</sub>Cl<sub>2</sub>/pentane under Schlenk conditions at *ca.* -18 °C. In all cases exposure to ambient temperature while in solution results in fairly rapid decomposition (over the course of *ca.* 5 minutes) – formation of “Pd black”.

### 7.3.4. General procedure D: NMR spectroscopy studies of the aminolysis of Pd<sub>3</sub>(OAc)<sub>6</sub>

In a glove box an oven dried Young's tap NMR tube was charged with Pd<sub>3</sub>(OAc)<sub>6</sub> (10 mg,  $1.49 \times 10^{-5}$  mol, 1 eq.). This was dissolved in dry, degassed CD<sub>2</sub>Cl<sub>2</sub> and a <sup>1</sup>H NMR spectrum measured. To this mixture, in a glovebox, the appropriate amount of dry, degassed piperidine (1.5 – 4.4 μl,  $1.49 - 4.47 \times 10^{-5}$  mol, 1 – 3 eq.) was added *via* a microsyringe. The tube was then sealed, shaken and a <sup>1</sup>H NMR spectrum measured as soon as possible, and repeated until the end of the experiment. In the instance where 3 equivalents of dry, degassed piperidine was added, the reaction tube was placed into a –15 °C ice/salt bath immediately after removal from the glovebox until the first NMR spectrum was measured.

*Lab book reference numbers:* 1 eq.: JTWB-6-414; 2 eq.: JTWB-6-419; 3 eq. JTWB-6-420.

### 7.3.5. General procedure E: Non-kinetic Pd-precatalyst screens in the Pd-catalysed arylcyanation of 65<sup>102b</sup>

To a flame dried Schlenk tube was added *N*-benzyl-4-bromo-6-methylpyridin-2-one (50 mg, 0.18 mmol, 1 eq.), Na<sub>2</sub>CO<sub>3</sub> (19 mg, 0.18 mmol, 1 eq., freshly ground in a pestle and mortar) and K<sub>4</sub>[Fe(CN)<sub>6</sub>]·3H<sub>2</sub>O (17 mg,  $0.39 \times 10^{-4}$  mol, 0.22 eq., freshly ground in a pestle and mortar) then the reaction vessel was backfilled with nitrogen (3 ×). The reaction mixture was stirred while dry, degassed DMAc (0.32 ml) was added through a septum, followed by the required amount of the appropriate Pd catalyst (added as a 25 mmol dm<sup>-3</sup> stock solution in dry, degassed DMAc). The reaction was heated at 120 °C for 4 hrs (or time required for methodology) and their final conversions analysed by <sup>1</sup>H NMR of the crude reaction mixtures. This was calculated by measuring the ratio of the diagnostic peaks at 6.80 ppm for *N*-Benzyl-4-Bromo-6-methylpyridin-2-one and 6.85 ppm for *N*-benzyl-4-cyano-6-methylpyridin-2-one.

*Representative lab book reference number:* JTWB-4-244

### 7.3.6. General experimental procedure F: Preparative 47-catalysed cyanation of aryl halides.

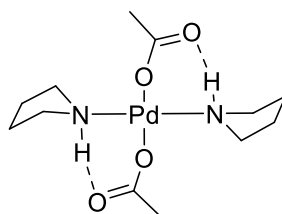
To a flame dried 30 mL Schlenk tube charged with a stirrer bar was added aryl bromide (1.4 mmol), freshly ground K<sub>4</sub>[Fe(CN)<sub>6</sub>] (130 mg, 3.08 mmol, 0.22 eq.), freshly ground Na<sub>2</sub>CO<sub>3</sub> (148 mg, 1.4 mmol, 1 eq.). The vessel was then backfilled with N<sub>2</sub> with stirring (3 ×). To a separate 10 mL flame dried Schlenk tube charged with a stirrer bar was added **47** (10 mg,

$2.53 \times 10^{-5}$  mol) and the vessel backfilled with  $N_2$  with stirring (3  $\times$ ). Dry DMAc (2 ml) was added via a septum to the reaction vessel containing the aryl bromide, then this reaction mixture was added to an oil bath preheated to 140 °C. Concomitantly, dry DMAc (1 ml) was added to the Schlenk tube containing **47** and was stirred until complete dissolution of the precatalyst was observed to give a precatalyst solution with a concentration of 25 mmol dm<sup>-3</sup>. Immediately after complete dissolution of **47**, the required amount of precatalyst solution was added using an appropriate microsyringe through a septum to the preheated reaction mixture. The resulting reaction mixture was stirred vigorously under a static  $N_2$  atmosphere at 140 °C for 16 h. After reaction completion the mixture was then allowed to cool to room temperature and purified directly by silica gel column chromatography with an appropriate solvent system.

#### 7.4. Synthetic procedures and compound data

Throughout this chapter, references to specific *via* laboratory notebook numbers are given for the experiment from which the procedure is quoted. Known compounds are indicated with a literature reference next to the compound name.

##### ***Bis-trans*-[pyrrolidinyl- $\kappa$ -NH]palladium(II) diacetate (**48**)**



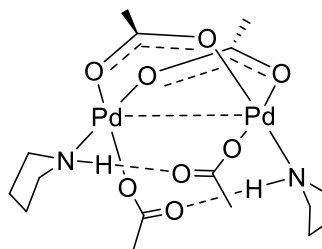
Prepared using general procedure B (Amine = pyrrolidine). Recrystallisation from  $CH_2Cl_2$ /hexane gave the *title compound* as a light yellow crystalline powder (81.3 mg, 50%). Single crystals were grown by vapour diffusion of pentane into a saturated solution of the compound in  $CH_2Cl_2$  at *ca.* -18 °C.

Yield: 81.3 mg, 50%; MP 140.2 – 142.3 (decomp.); <sup>1</sup>H NMR (400 MHz,  $CDCl_3$ )  $\delta$  5.98 (s, 2H, NH), 3.02 – 2.92 (m, 4H,  $CH_2$ ), 4.74 – 2.58 (m, 4H,  $CH_2$ ), 1.86 (s, 6H, COMe), 1.78 – 1.65 (m, 4H,  $CH_2$ ), 1.80-1.53 (m, 4H,  $CH_2$ ); <sup>13</sup>C NMR (101 MHz,  $CDCl_3$ )  $\delta$  180.6, 48.5, 24.1, 23.9; LIFDI MS, *m/z* 368 [M<sup>+</sup>];  $\nu_{max}/cm^{-1}$  (ATR) 3469, 3393, 3182, 2964, 1573, 1371, 1315, 1260, 1014, 907, 800, 694, 620.

For X-Ray crystallographic data see Appendices **3** and **4**.

Lab book reference number: JTWB-4-188

**Di- $\mu$ -acetato-bis-[*trans*-{pyrrolidinyl- $\kappa$ -NH}]palladium(II) diacetate (49)**



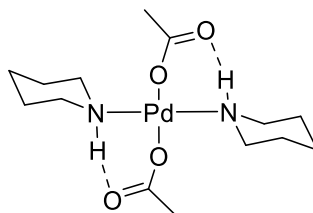
Prepared using general procedure C (Amine = pyrrolidine), affording the *title compound* as a dark red crystalline solid (27 mg, 21 %). Single crystals were grown by layered recrystallisation from dry, degassed CH<sub>2</sub>Cl<sub>2</sub>/hexane under Schlenk conditions at *ca.* -18 °C.

MP 130-137 °C (decomp.); <sup>1</sup>H NMR (400 MHz, CD<sub>2</sub>Cl<sub>2</sub>) δ 7.03 (bs, 2H, NH), 3.04 – 2.89 (m, 5H, pyr. CH's), 2.83 – 2.71 (m, 3H, pyr. CH's), 2.67 – 2.55 (m, 3H, pyr. CH's), 1.85 (s, 6H, bridging COMe), 1.81 (s, 6H, terminal COMe), 1.76 – 1.64 (m, 5H, pyr. CH's); <sup>13</sup>C NMR (101 MHz, CD<sub>2</sub>Cl<sub>2</sub>) δ 185.3, 180.0, 48.5, 24.1, 23.9, 26.6, 23.2, 22.9; Elemental analysis: (calc) C, 32.50; H, 5.11; N, 4.74; Other; 57.65 (obs) C, 32.40; H, 5.00; N, 4.49 Other: 58.11; LIFDI MS, *m/z* 592.02 [M<sup>+</sup>];  $\nu_{\max}/\text{cm}^{-1}$  (ATR) 3070, 2964, 2873, 1615, 1565, 1416, 1367, 1320, 1023, 909, 680, 616.

For X-Ray crystallographic data see Appendices 3 and 4.

Lab book reference numbers: JTWB-4-189

**Bis-*trans*-[piperidinyl- $\kappa$ -NH]palladium(II) diacetate (47)<sup>110</sup>**

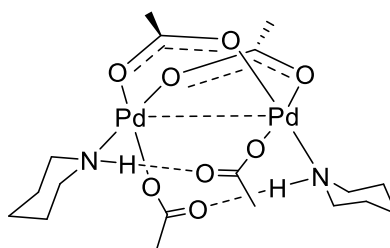


Prepared using general procedure B (Amine = piperidine). Recrystallisation from CH<sub>2</sub>Cl<sub>2</sub>/hexane at *ca.* -18 °C gave the *title compound* as a light yellow crystalline powder (175 mg, 90%).

MP 165.0 – 168.4 °C (dec.)  $^1\text{H}$  NMR (400 MHz,  $\text{CDCl}_3$ )  $\delta$  5.54 (bt,  $J = 10.9$  Hz, 2H, NH), 3.14 (d,  $J = 12.8$  Hz, 4H, C2 & C6 CH's), 2.56 (qd,  $J = 2.8, 12.8$  Hz, 4H, C2 & C6 CH's), 1.95 (s, 6H, COMe), 1.75- 1.56(m, 6H, C3-5 CH's), 1.51 – 1.30 (m, 6H, C3-5 CH's);  $^{13}\text{C}$  NMR (101 MHz,  $\text{CDCl}_3$ )  $\delta$  181.0, 49.5, 26.5, 24.0, 23.0; LIFDI MS,  $m/z$  394.12  $[\text{M}^+]$ ;  $\nu_{\text{max}}/\text{cm}^{-1}$  (ATR): 3486, 3420, 3190, 2941, 2861, 1675, 1573, 1448, 1392, 1368, 1332, 1319, 1194, 1112, 1022, 1012, 944, 880, 813, 695, 654, 627, 601, 466.

Lab book reference number: JTWB-8-586

***Di- $\mu$ -acetato-bis-[trans-{piperidiny- $\kappa$ -NH}palladium(II) diacetate] (50)***



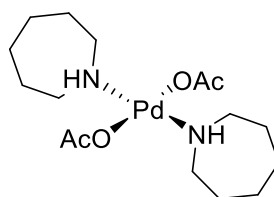
Prepared using general procedure C (Amine = piperidine), affording the *title compound* as a dark red crystalline solid (19 mg, 14 %). Single crystals were grown by layered recrystallisation from dry, degassed  $\text{CH}_2\text{Cl}_2$ /hexane under Schlenk conditions at *ca.*  $-18$  °C.

MP 138-140 °C (dec.);  $^1\text{H}$  NMR (400 MHz,  $\text{CD}_2\text{Cl}_2$ )  $\delta$  6.99 (bs, 2H, NH), 3.33 (d,  $J = 13.3$  Hz, 2H, pip. CH's), 3.14 (d,  $J = 13.3$  Hz, 2H, pip. CH's), 2.75 – 2.59 (m, 4H, pip CH's), 1.87 (s, 6H, bridging COMe), 1.82 (s, 6H, term. COMe) 1.66 – 1.53 (m, 10H, pip. CH's), 1.36 – 1.34 (m, 2H, pip CH's);  $^{13}\text{C}$  NMR (101 MHz,  $\text{CDCl}_3$ )  $\delta_c$ : 185.0, 180.5, 49.3, 26.6, 24.1, 24.0, 24.0, 23.9, 23.3; LIFDI MS,  $m/z$  618  $[\text{M}^+]$ ;  $\nu_{\text{max}}/\text{cm}^{-1}$  (ATR): 3090, 2945, 2865, 1622, 1567, 1417, 1372, 1321, 1260, 1081, 1014, 884, 856, 798, 681, 618.

For X-Ray crystallographic data see Appendices 3 and 4.

Lab book reference number: JTWB-4-201

***Bis-trans-[azepiny- $\kappa$ -NH]palladium(II) diacetate (52)***



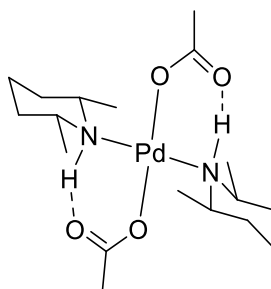
Prepared using general procedure B (Amine = azepane), recrystallisation from  $\text{CH}_2\text{Cl}_2$ /hexane at *ca.*  $-18\text{ }^\circ\text{C}$  gave the *title compound* as a light yellow microcrystalline powder (143 mg, 75%). Single crystals were grown vapour diffusion of pentane into a concentrated solution of the compound in  $\text{CH}_2\text{Cl}_2$  at *ca.*  $-18\text{ }^\circ\text{C}$ .

MP  $110.1 - 114.0$  (dec.);  $^1\text{H NMR}$  (400 MHz,  $\text{CD}_2\text{Cl}_2$ )  $\delta$  5.96 (bt,  $J = 8.6$  Hz, 2H, NH), 3.24 (ddt,  $J = 13.6, 6.7, 3.2$  Hz, 4H, aze. CH's), 2.6 (dddd,  $J = 13.6, 9.9, 8.6, 3.2$  Hz, 4H, aze. CH's), 1.93 (s, 6H, COMe), 1.73 – 1.61 (m, 4H, aze. CH's), 1.61 – 1.41 (m, 12H, aze. CH's);  $^{13}\text{C NMR}$  (101 MHz,  $\text{CDCl}_3$ )  $\delta$  180.6, 50.8, 28.1, 26.6, 24.0; LIFDI MS,  $m/z$  422.12 [M<sup>+</sup>];  $\nu_{\text{max}}/\text{cm}^{-1}$  (ATR) 3187, 2925, 1592, 1463, 1357, 1308, 1261, 1014, 846, 801, 691.

For X-Ray crystallographic data see Appendices 3 and 4.

Lab book reference number: JTWB-4-193.

***Bis-trans*-[2,6-*cis* dimethylpiperidiny]κ-NH]palladium(II) diacetate (53)**



Prepared using general procedure B (Amine = 2, 6-*cis* dimethylpiperidine). Recrystallisation from  $\text{CH}_2\text{Cl}_2$ /hexane at *ca.*  $-18\text{ }^\circ\text{C}$  gave the *title compound* as a brown/green powder (200 mg, 72%). Single crystals were grown by slow evaporation of  $\text{CDCl}_3$  at room temperature.

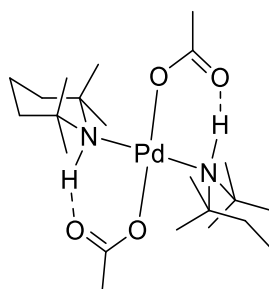
MP  $157-158\text{ }^\circ\text{C}$  (decomp.);  $^1\text{H NMR}$  (400 MHz,  $\text{CD}_6\text{D}_6$ )  $\delta$  8.06 (bs, 2H, NH), 2.75-2.60 (m, 4 H, NCH), 2.14 (d,  $J = 6.5$  Hz, 6H, CHMe), 2.09 (d,  $J = 6.4$  Hz, 6H, CHMe), 2.00 (s, 6H, COMe), 1.96 – 1.92 (m, 8H, C3& C5  $\text{CH}_2$ ), 1.93 – 1.70 (m, 4 H, C4  $\text{CH}_2$ );  $^{13}\text{C NMR}$  (101 MHz,  $\text{CDCl}_3$ )  $\delta$  181.0, 56.7, 33.8, 29.3, 24.4, 24.3, 23.2, 23.1, 22.7; LIFDI MS,  $m/z$  450

[M<sup>+</sup>];  $\nu_{\max}/\text{cm}^{-1}$  (ATR) 3059, 2963, 2927, 2863, 1585, 1449, 1370, 1320, 1260, 1171, 1104, 1015, 652, 926, 801, 687, 614, 544.

For X-Ray crystallographic data see Appendices 3 and 4.

Lab book reference number: JTWB-5-324

**Bis-*trans*-[2,2,6,6-tetramethylpiperidiny- $\kappa$ -NH]palladium(II) diacetate<sup>115</sup> (51)**

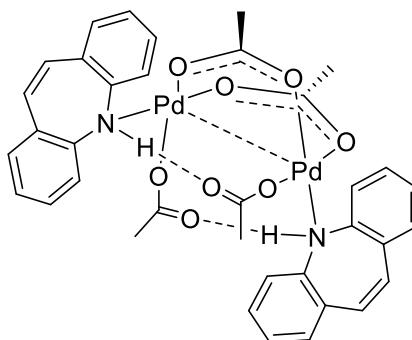


Prepared using general procedure B (Amine = 2,2,6,6-tetramethylpiperidine). Recrystallisation from CH<sub>2</sub>Cl<sub>2</sub>/hexane at *ca.* -18 °C gave the *title compound* as a brown/green powder (132 mg, 59%). Single crystals were grown by slow evaporation of CDCl<sub>3</sub> at room temperature.

MP 157-158 °C (decomp.); <sup>1</sup>H NMR (400 MHz, CDCl<sub>3</sub>)  $\delta$  8.06 (bs, 2H, NH), 1.90 (s, 12H, NCMe), 1.84 (s, 6 H, COMe), 1.46 (s, 12H, NCMe), 1.48-1.42 (m, 12H, TMP CH<sub>2</sub>'s); <sup>13</sup>C NMR (101 MHz, CDCl<sub>3</sub>)  $\delta$  180.5, 58.2, 38.3, 33.9, 26.4, 24.4, 18.0; LIFDI MS, *m/z* 450 [M<sup>+</sup>];  $\nu_{\max}/\text{cm}^{-1}$  (ATR) 3059, 2963, 2927, 2863, 1585, 1449, 1370, 1320, 1260, 1171, 1104, 1015, 652, 926, 801, 687, 614, 544.

Lab book reference number: JTWB-5-323

**Di- $\mu$ -acetato-bis-[*trans*-{dibenzazepine- $\kappa$ -NH}]palladium(II) diacetate] (58)**



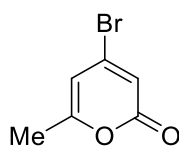
A flame dried Schlenk tube was charged with Pd<sub>3</sub>(OAc)<sub>6</sub> (537 mg, 0.798 mmol, 1 eq.) and dibenzazepine (2.39 mmol, 3 eq.) and backfilled with N<sub>2</sub> (3 ×). To the mixture, dry degassed CH<sub>2</sub>Cl<sub>2</sub> (27 ml) was added and the reaction mixture was stirred at room temperature for 30 minutes. During this time the reaction mixture changed from a dark brown/orange suspension to a dark red solution. The solvent was removed *in vacuo* directly until the reaction mixture had reached a third of the original volume. This solution was then layered with dry, degassed hexane (4 × volume of compound solution) and placed in the freezer (*ca.* -18 °C) for 7 days to provide *the title compound* as a red crystalline solid suitable for X-ray diffraction (992 mg, 99%).

MP 173-176°C (dec.) <sup>1</sup>H NMR (400 MHz, CDCl<sub>3</sub>) δ 11.59 (bs, 2H, NH), 7.84 (d, *J* = 7.8 Hz, H, ArH), 7.72 (d, *J* = 11.5 Hz, 2H, alkene CH), 7.66 (d, *J* = 11.5 Hz, 2H, alkene CH), 7.41 (d, *J* = 7.8 Hz, 2H, ArH) 7.38 (dd, *J* = 7.8, 7.4 Hz, 2H, ArH), 7.30 (d, *J* = 7.4, 4H, ArH), 7.10 (dd, *J* = 7.4, 7.5 Hz, 2H, ArH) 7.05 (d, *J* = 7.5 Hz, 2H, ArH), 6.98 (dd, *J* = 7.5, 7.5 Hz, 2H, ArH), 1.43 (s, 6H, bridging COMe), 0.99 (s, 6H, term. COMe); <sup>13</sup>C NMR (101 MHz, CDCl<sub>3</sub>) δ<sub>c</sub>: 185.2, 179.3, 143.4, 143.2, 133.4, 133.3, 131.8, 131.7, 129.4, 129.2, 129.1, 128.8, 126.3, 126.1, 122.0, 120.5, 22.1, 21.5; LIFDI MS, *m/z* 806 [M -OAc +OMe+]; ν<sub>max</sub>/cm<sup>-1</sup> (ATR): 2922, 5856, 1615, 1552, 1467, 1418, 1370, 1332, 1194, 1147, 1098, 1038, 908, 843, 793, 784, 763, 729, 688, 652, 627, 618, 606, 454.

For X-Ray crystallographic data see Appendices 3 and 4.

*Lab book reference numbers:* JTWB-8-583 and JTWB-8-587

#### 4-Bromo-6-methylpyran-2-one<sup>131</sup> (60)



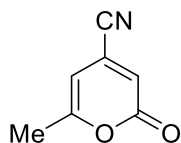
4-hydroxy-6-methylpyran-2-one (5.00 g, 3.97 mmol, 1 eq.), freshly weighed out P<sub>2</sub>O<sub>5</sub> (13.41 g, 9.45 mmol, 2.38 eq.) and Bu<sub>4</sub>NBr (14.86, 4.61 mmol, 1.16 eq.) was added to a large three necked round bottomed flask equipped with a thermometer, mechanical stirrer and condenser. Toluene was added (200 ml) and the mixture was heated to reflux (110 °C) with vigorous mechanical stirring for 2 hours. The reaction mixture was allowed to cool to room temperature and the upper toluene layer was collected. The lower layer was extracted with toluene (100 ml), then the combined organic layers were washed with

saturated NaHCO<sub>3</sub> solution (70 ml), saturated brine (50 ml), dried over anhydrous MgSO<sub>4</sub>, filtered then concentrated *in vacuo* to afford the desired compound (6.7 g, 90%). If necessary product can be purified by recrystallisation from hot hexane.

<sup>1</sup>H NMR (400 MHz, CDCl<sub>3</sub>) δ 6.46 (dq, *J* = 1.4, 0.7 Hz, 1H, C3 CH), 6.19 (dq, *J* = 1.4, 0.9 Hz, 1H, C5 CH), 2.25 (dd, *J* = 0.7, 0.9 Hz, 3H, CH<sub>3</sub>); <sup>13</sup>C (101 MHz, CDCl<sub>3</sub>) δ<sub>c</sub> 162.2, 160.8, 141.2, 114.9, 108.5, 19.9; *m/z* (ESI<sup>+</sup>) 187.9474 [(M+H)<sup>+</sup>, Br<sup>79</sup>], 210.9375 [(M+Na)<sup>+</sup>, Br<sup>79</sup>]; *v*<sub>max</sub>/cm<sup>-1</sup> (ATR); 3084, 3062, 1713, 1615, 1540, 1427, 1303, 1209, 1129, 1042, 1027, 864, 832, 804, 726, 625, 578, 513.

*Lab book reference number:* JTWB-3-156.

#### 4-Cyano-6-methylpyran-2-one (61)



This compound was prepared according to an adapted literature procedure.<sup>132</sup> To an oven dried Schlenk tube was added 4-bromo-6-methylpyran-2-one (100 mg, 0.529 mmol, 1 eq.) and CuCN (52 mg, 0.582 mmol, 1.1 eq.) then the reaction vessel was then backfilled with nitrogen (3 ×). The reaction mixture was stirred while DMF (0.5 ml) was added through a septum. The reaction was heated at 130 °C for 2 hrs, then allowed to cool to room temperature. The DMF was removed *in vacuo* and then the reaction mixture was diluted with CH<sub>2</sub>Cl<sub>2</sub> (3 ml) and an aqueous NH<sub>4</sub>OH solution (10%). The aqueous layer was extracted with CH<sub>2</sub>Cl<sub>2</sub> (3 × 3 ml) and the combined organic layers were washed with aqueous NH<sub>4</sub>OH solution (10%, 3 × 3 ml, until no blue colour remains), water (2 × 3 ml), brine (1 × 3 ml) and dried over anhydrous MgSO<sub>4</sub> and filtered. The filtrate solvent was removed *in vacuo* to afford 4-cyano-6-methylpyran-2-one. Flash chromatography (SiO<sub>2</sub>, 25% EtOAc/petrol) afforded *the title compound* as a white crystalline solid (59 mg, 82%).

MP 101 – 103.5 °C; <sup>1</sup>H NMR (400 MHz, CDCl<sub>3</sub>) δ 6.54 (s, 1H, C3 CH), 6.07 (s, 1H, C5 CH), 2.31 (s, 3H, CH<sub>3</sub>) δ <sup>13</sup>C (101 MHz, CDCl<sub>3</sub>) δ 165.3, 159.6, 127.8, 119.5, 114.7, 102.2, 20.4; *v*<sub>max</sub>/cm<sup>-1</sup> (ATR) 3093, 3063, 2238, 1746, 1727, 1629, 1541, 1441, 1379, 1316, 1227, 1140, 1031, 987, 942, 868, 851, 832, 718, 663, 614, 535, 457, 424; Elemental analysis: (calc) C, 62.22; H, 3.73; N, 10.37; Other; 23.68 (obs) C, 61.91; H, 3.83; N, 12.27 Other: 24.00; *m/z* (APCI<sup>+</sup>) 136.0402 [(M+H)<sup>+</sup>]; *R*<sub>f</sub> = 0.3 (15% EtOAc/petrol).

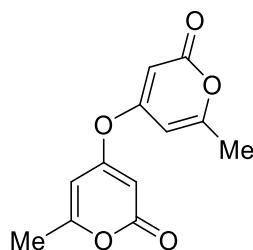
Lab book reference number: JTWB-3-154.

### DMF-stabilised palladium nanoparticles<sup>19a</sup>

To a round-bottomed flask equipped with a reflux condenser containing dry DMF (15 ml) at 140 °C under air was added a suspension of PdCl<sub>2</sub> in H<sub>2</sub>O (0.1 M, 150 μL, 0.015 mmol). The resulting solution was stirred for 6 h at 140 °C, before being cooled and stored at 5 °C. Aliquots of the 1 mM solution were used directly in the relevant reactions.

Lab book reference number: JTWB-3-138.

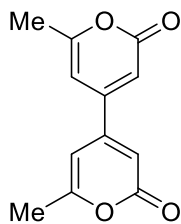
### 4,4'-Oxybis(6-methyl-2H-pyran-2-one) (62)



To a flame dried Schlenk tube charged with a magnetic stirrer bar was added 4-hydroxy-6-methylpyran-2-one (66 mg, 0.529 mmol, 1 eq.) and 5-bromo-6-methylpyran-2-one (100 mg, 0.529 mmol, 1 eq.) and Na<sub>2</sub>CO<sub>3</sub> (56 mg, 0.529 mmol, 1 eq.). The Schlenk tube was backfilled with nitrogen (3 ×) then dry, degassed DMF (1 ml) was added. The mixture was then stirred at 100 °C for 2 hours, during which a deep red colour formed. Upon reaction completion the reaction mixture was concentrated *in vacuo*, dissolved in acetone (25 ml) then filtered through a sintered glass funnel. The filtrate was concentrated *in vacuo* to provide the crude product. Flash chromatography (SiO<sub>2</sub>, 75% EtOAc/Petrol) afforded *the title compound* as a white crystalline solid (121 mg, 100%).

MP 172.2 – 173.5; <sup>1</sup>H NMR (400 MHz, Acetone-*d*<sub>6</sub>) δ 6.23 (dq, *J* = 1.9, 0.9 Hz, 2H, C3 CH), 5.75 (dq, *J* = 2.2, 0.7 Hz, 2H, C5 CH), 2.27 (bs, 6H, CH<sub>3</sub>); <sup>13</sup>C NMR (101 MHz, Acetone-*d*<sub>6</sub>) δ 167.1, 165.8, 163.3, 100.3, 97.6, 20.0; *m/z* (ESI+) 235.0592 [(M+H)<sup>+</sup>], 257.0412 [(M+Na)<sup>+</sup>]. *v*<sub>max</sub>/cm<sup>-1</sup> (ATR): 3100, 3083, 2967, 2925, 1709, 1638, 1567, 1438, 1400, 1379, 1317, 1232, 1214, 1185, 1142, 1127, 1029, 999, 949, 855, 830, 821, 729, 626, 527, 519, 504, 470; *R*<sub>f</sub> 0.48 (100% EtOAc).

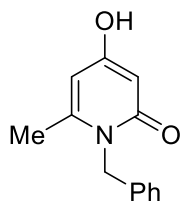
Lab book reference number: JTWB-4-226

**6,6'-Dimethyl-2H,2'H-4,4'-bipyran-2,2'-dione (63)**

To a flame dried Schlenk tube was added 4-bromo-6-methylpyran-2-one (50 mg, 0.265 mmol, 1 eq.),  $\text{Na}_2\text{CO}_3$  (28 mg, 0.265 mmol, 1 eq., freshly ground in a pestle and mortar),  $\text{K}_4[\text{Fe}(\text{CN})_6]$  (20 mg,  $5.3 \times 10^{-5}$  mol, 0.2 eq., freshly ground in a pestle and mortar) and *Bis-trans*-[piperidiny- $\kappa$ -*NH*]Palladium(II) diacetate (1.05 mg,  $2.65 \times 10^{-6}$  mol, 1 mol%). The reaction vessel was backfilled with nitrogen (3  $\times$ ) and the reaction mixture was stirred while dry DMAc (0.5 ml) was added through a septum). The reaction mixture was heated at 100  $^\circ\text{C}$  for 18 hours during which a dark black colour formed. After reaction completion the reaction mixture was directly concentrated *in vacuo*, then ethyl acetate (2 ml) and water (2 ml) were added. The crude mixture was then stirred until all the solid residues were dissolved. The aqueous layer was then extracted with ethyl acetate (3  $\times$  3 ml), the organics combined then dried over  $\text{Mg}_2\text{SO}_4$ , filtered then concentrated *in vacuo*. Flash chromatography ( $\text{SiO}_2$ , 50% EtOAc/Petrol) afforded *the title compound* as an off white powder (8.9 mg, 16%).

$^1\text{H}$  NMR (400 MHz,  $\text{CDCl}_3$ )  $\delta$  6.32 (s, 2H, C3 CH), 6.11 (s, 2H, C5 CH), 2.33 (s, 6H, CH<sub>3</sub>);  $^{13}\text{C}$  (101 MHz,  $\text{CDCl}_3$ )  $\delta$  163.7, 162.2, 150.6, 110.7, 101.5, 20.4; *m/z* (ESI+) 219.0655 [(M+H)<sup>+</sup>], 241.0471 [(M+Na)<sup>+</sup>].

*Lab book reference number:* JTWB-3-134

**N-Benzyl-4-Hydroxy-6-methylpyridin-2-one<sup>123a</sup> (66)**

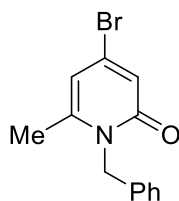
To a 1 litre round bottomed flask was added 4-hydroxy-6-methyl-2H-pyran-2-one (20 g, 0.16 mol, 1 eq.) and water (300 ml). Benzylamine (17g, 0.16 mol, 1 eq.) was added slowly with stirring and the reaction was heated to reflux over the course of 1 hour. The reaction was stirred under reflux for a further 2 hours; after 30 minutes a brown precipitate began to form.

At completion the reaction mixture was cooled to 0 °C, causing precipitation of the crude title compound as a light brown solid. The precipitate was collected by filtration and purified by trituration from hot EtOH. The solid was dried under vacuum to afford N-Benzyl-4-Hydroxy-6-methylpyridin-2-one as an off white crystalline solid (13.1347g, 77%).

MP 223.0 – 225.5 °C (Lit.<sup>123a</sup> MP: 212 – 213 °C) ; <sup>1</sup>H NMR (DMSO-*d*<sub>6</sub>, 400 MHz) δ 10.53 (brs, 1H, OH), 7.32 (m, 2H, ArH), 7.23 (tdd, *J* = 7.5, 2.0, 1.2, 1H, ArH), 7.09 (d, *J* = 7.0, 2H, ArH), 5.79 (dd, *J* = 2.5, 1.0, 1H, C3 CH), 5.59 (d, *J* = 2.5, 1H, C5 CH), 5.18 (s, 2H, CH<sub>2</sub>), 2.16 (s, 3H, CH<sub>3</sub>); <sup>13</sup>C NMR (DMSO-*d*<sub>6</sub>, 101 MHz) δ 165.9, 164.0, 147.7, 137.8, 128.6, 126.9, 126.1, 100.5, 95.9, 45.3, 20.0; Elemental analysis: (calc) C, 72.54; H, 6.09; N, 6.51; Other, 14.86 (obs) C, 72.68; H, 6.11; N, 6.50; Other, 14.72; *m/z* (ESI<sup>+</sup>): 216.1016 [(M+H)<sup>+</sup>] 238.0838 [M+Na<sup>+</sup>]; *v*<sub>max</sub>/cm<sup>-1</sup> (ATR) 1865, 1613, 1507, 1451, 1426, 1315, 1230, 1207, 1155, 988, 831, 732, 964, 640, 597, 528, 505, 475, 447, 418.

Lab book reference number: JTWB-3-157, JTWB-4-197

#### N-Benzyl-4-Bromo-6-methylpyridin-2-one (65)



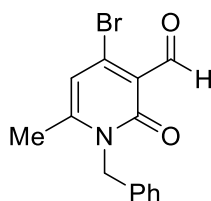
This compound was prepared according to an adapted literature procedure.<sup>131</sup> A large three necked round bottomed flask equipped with a thermometer, mechanical stirrer and condenser was purged with a flow of N<sub>2</sub> for 20 minutes before addition of 4-hydroxy-6-methyl-N-benzyl-pyridin-2(*1H*)-one (5 g, 2.52 mmol, 1 eq.) followed by freshly weighed out P<sub>2</sub>O<sub>5</sub> (7.84 g, 5.52 mmol, 2.38 eq.), then purged for a further 5 minutes. Dry toluene was added (200 ml) and the mixture was heated to 80 °C with mechanical stirring for 1 hour, forming a yellow suspension. Bu<sub>4</sub>NBr (8.67g, 2.62 mmol, 1.16 eq.) was added and the reaction subsequently heated to reflux (110 °C) with vigorous mechanical stirring for 2 hours. The reaction mixture was allowed to cool to room temperature and the upper toluene layer was collected. The lower (resinous) layer was extracted with toluene (100 ml), then the combined organic layers were washed with saturated NaHCO<sub>3</sub> (aq.) solution (70 ml), saturated brine (50 ml), dried over anhydrous MgSO<sub>4</sub>, filtered then concentrated *in vacuo* to afford the crude product. Saturated NaHCO<sub>3</sub> (aq.) (100 ml) was slowly added to the lower resinous layer (vigorous evolution of CO<sub>2</sub>) and stirred until all solid material was dissolved (*ca.* 1 hr.). The resulting

solution was then extracted with toluene (50 ml  $\times$  2) the organics combined and washed with saturated brine solution (50 ml), dried over anhydrous  $\text{MgSO}_4$ , filtered and the solvent removed *in vacuo* to provide additional crude product. Flash chromatography ( $\text{SiO}_2$ , 40% EtOAc/Petrol) afforded the title compound as a white crystalline solid (2.4535 g, 38%).

MP 98.0 – 100.5 °C.;  $^1\text{H}$  NMR (400 MHz,  $\text{CDCl}_3$ )  $\delta$  7.35 – 7.28 (m, 2H, ArH), 7.28 – 7.23 (m, 1H, ArH), 7.14 (d,  $J = 7.5$  Hz, 2H, ArH), 6.80 (d,  $J = 2.0$  Hz, 1H, C3 CH), 6.22 (d,  $J = 2.0$  Hz, 1H, C5 CH), 5.29 (s, 2H,  $\text{CH}_2$ ), 2.25 (s, 3H,  $\text{CH}_3$ );  $^{13}\text{C}$  (101 MHz,  $\text{CDCl}_3$ )  $\delta$  160.5, 147.0, 135.9, 135.6, 129.0, 127.7, 126.5, 120.1, 111.2, 47.3, 20.5; Elemental analysis: (calc) C, 56.14; H, 4.35; N, 5.04; Other; 34.48 (obs) C, 56.22; H, 4.41; N, 5.01; Other: 34.48;  $m/z$  ( $\text{ESI}^+$ ) 278.0175 [(M+H) $^+$ ,  $\text{Br}^{79}$ ], 299.9996 [(M+Na) $^+$ ,  $\text{Br}^{79}$ ];  $\nu_{\text{max}}/\text{cm}^{-1}$  (ATR) 3055, 1647, 1572, 1541, 1409, 1345, 1180, 888, 845, 804, 739, 725, 696, 594, 524, 429;  $R_f$  0.4 (40% EtOAc/Petrol).

Lab book reference number: JTWB-5-317

#### ***N*-Benzyl-3-acetyl-4-bromo-6-methylpyridin-2-one (67)**

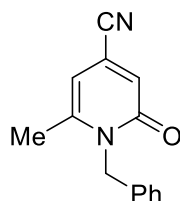


A 100 ml three necked round bottomed flask was equipped with a mechanical stirrer, condenser, thermometer and a  $\text{N}_2$  bubbler. *N*-benzyl-4-hydroxy-6-methylpyridin-2-one (3.546 g, 1.665 mmol, 1 eq.) was added and the vessel purged with  $\text{N}_2$  for 15 minutes. Dry DMF (7 ml) and dry *n*- $\text{Bu}_2\text{O}$  (3.3 ml) was added with stirring and the flask was cooled to 0 °C. To the solution was added  $\text{PBr}_3$  (4.506 g, 1.665 mmol, 1 eq.) dropwise *via* a septum, then heated to 100 °C for 2 hours. Shortly after addition of the  $\text{PBr}_3$ , the reaction mixture turned very thick and dark red. The reaction mixture was allowed to cool to room temperature, then a small amount of water (*ca.* 5 ml) was added slowly. The crude mixture was then neutralised by dropwise addition of  $\text{NaHCO}_3$  (10 % solution). EtOAc (150 ml) and water (150 ml) was then added, the organic layer collected and the aqueous layer extracted with EtOAc (3  $\times$  50 ml). The combined organics were then dried over  $\text{Na}_2\text{SO}_4$ , filtered and the filtrate solvent removed *in vacuo*. Flash chromatography ( $\text{SiO}_2$ , 50% EtOAc/Petrol) afforded the title compound as a light yellow crystalline solid (257 mg, 5%).

MP 131.1 – 134.4;  $^1\text{H}$  NMR (400 MHz,  $\text{CDCl}_3$ )  $\delta$  10.23 (s, 1H, CHO), 7.37 – 7.30 (m, 3 H, ArH), 7.17 (app d,  $J = 7$  Hz, 2H, ArH), 6.42 (s, 1H, C5 CH), 5.32 (s, 2H,  $\text{CH}_2$ ), 2.34 (s, 3H,  $\text{CH}_3$ );  $^{13}\text{C}$  NMR (101 MHz,  $\text{CDCl}_3$ )  $\delta$  193.7, 189.5, 152.6, 139.8, 134.9, 129.1, 128.0, 126.6, 120.2, 113.7, 47.5, 21.0;  $m/z$  (ESI $^+$ ) 306.0126 [(M+H) $^+$ , Br $^{79}$ ], 327.9949 [(M+Na) $^+$ , Br $^{79}$ ], 360.0210 [(M+Na+MeOH) $^+$ , Br $^{79}$ ];  $\nu_{\text{max}}/\text{cm}^{-1}$  (ATR); 2955, 2869, 1682, 1625, 1562, 1527, 1492, 1462, 1452, 1414, 1380, 1346, 1335, 1306, 1290, 1261, 1159, 949, 772, 762, 737, 701, 605, 552, 520, 436;  $R_f$  0.33 (50% EtOAc/Petrol).

Lab book reference number: JTWB-4-194

### ***N*-benzyl-4-cyano-6-methylpyridin-2-one (69)**



This compound was prepared according to an adapted literature procedure.<sup>132</sup> To a flame dried Schlenk tube was added *N*-benzyl-4-bromo-6-methylpyridin-2-one (283.7 mg, 1.02 mmol, 1 eq.) and CuCN (100 mg, 1.12 mmol, 1.1 eq.) then the reaction vessel was then backfilled with nitrogen (3  $\times$ ). The reaction mixture was stirred while dry DMF (1 ml) was added through a septum. The reaction was heated at 130  $^\circ\text{C}$  for 2 hours (or until complete by TLC), then allowed to cool to room temperature. The DMF was removed *in vacuo* and then the reaction mixture was diluted with  $\text{CHCl}_3$  (3 ml) and an aqueous  $\text{NH}_4\text{OH}$  solution (10%, 3 ml). The aqueous layer was extracted with  $\text{CHCl}_3$  (3  $\times$  3 ml) and the combined organic layers were washed with aqueous  $\text{NH}_4\text{OH}$  solution (10%, 3  $\times$  3 ml, until no blue colour remains), water (2  $\times$  3 ml), brine (1  $\times$  3 ml) and dried over anhydrous  $\text{MgSO}_4$  and filtered. The solvent was removed *in vacuo* to afford the crude product. Flash chromatography ( $\text{SiO}_2$ , 40% EtOAc/petrol) afforded *the title compound* as a white crystalline solid (118 mg, 52%).

MP 116.9 – 120  $^\circ\text{C}$ ;  $^1\text{H}$  NMR (400 MHz,  $\text{CDCl}_3$ )  $\delta$  7.34 – 7.27 (m, 3H, ArH), 7.12 (ddt,  $J = 7.1, 1.3, 0.7$  Hz, 2H, ArH), 6.85 (dq,  $J = 1.8, 0.8$  Hz, 1H, C3 CH), 6.13 (dq,  $J = 1.8, 0.8$  Hz, 1H, C5 CH), 5.31 (s, 2H,  $\text{CH}_2$ ), 2.31 (dd,  $J = 0.8, 0.8$  Hz, 3H,  $\text{CH}_3$ );  $^{13}\text{C}$  NMR (101 MHz,  $\text{CDCl}_3$ )  $\delta$  162.1, 149.4, 135.1, 129.1, 127.9, 126.6, 123.4, 123.3, 116.1, 106.1, 47.8, 20.9; Elemental analysis: (calc) C, 74.98; H, 5.39; N, 12.49; Other; 7.13 (obs) C, 75.01; H, 5.45; N, 12.36 Other: 7.18;  $m/z$  (ESI $^+$ ) 225.1023 [(M+H) $^+$ ], 247.0841 [(M+Na) $^+$ ];  $\nu_{\text{max}}/\text{cm}^{-1}$  (ATR)

3089, 3066, 3031, 2967, 2237, 1666, 1575, 1531, 1412, 1345, 1172, 1099, 1031, 966, 924, 865, 819, 723, 692, 657, 639, 600, 574, 478, 444;  $R_f$ : 0.3 (40% EtOAc/Petrol).

*Lab book reference number:* JTWB-3-162

For X-Ray crystallographic data see Appendices 3 and 4.

### **Pd(OAc)<sub>2</sub>/Piperidine solution catalyst aging studies**

To a flame dried Schlenk tube was added Pd<sub>3</sub>(OAc)<sub>6</sub> (1.1 mg, 1.63 μmol, 1 eq.) and a magnetic stirrer bar. The reaction vessel was backfilled with nitrogen (3 ×) and to this was added dry, degassed DMAc (5 ml) to make a solution of 0.37 mmol dm<sup>-3</sup>. Upon complete dissolution of the Pd<sub>3</sub>(OAc)<sub>6</sub> dry, degassed piperidine (0.97 μl, 9.8 μmol, 6 eq.) was added by microsyringe *via* a septum. An aliquot was taken immediately for arylcyanation reaction conducted at catalyst “t<sub>0</sub>”. The catalyst solution was then placed in an oil bath preheated to 80 °C and aliquots taken for addition to arylcyanation reactions at designated time intervals.

The cyanation reactions were carried out according to General procedure E, using the catalyst solution described above at the time intervals after piperidine addition 0 hours, 0.5 hours, 1 hour, 2 hours and 4 hours.

*Lab book reference numbers and respective conversions:* T<sub>0</sub>: JTWB-4-216, 77%; 0.5 h. JTWB-4-217, 32%; 1 h. JTWB-4-218, 31%; 2 h. JTWB-4-219, 17%; JTWB-4-220, trace product.

### **Non-kinetic Pd precatalyst loading screens while maintaining a constant [Pd] in 52-catalysed arylcyanation of 65.**

To a flame dried Schlenk tube was added *N*-benzyl-4-bromo-6-methylpyridin-2-one (1 eq.), Na<sub>2</sub>CO<sub>3</sub> (1 eq., freshly ground in a pestle and mortar) and K<sub>4</sub>[Fe(CN)<sub>6</sub>]·3H<sub>2</sub>O (0.22 eq., freshly ground in a pestle and mortar) then the reaction vessel was backfilled with nitrogen (3 ×). In parallel, a small oven dried Schlenk tube was charged with catalyst and backfilled with nitrogen (3 ×). The appropriate amount of dry, degassed DMAc was added to the small Schlenk containing the precatalyst to make the correct amount of stock solution of concentration 0.36 mmol dm<sup>-3</sup> required for the desired catalyst loading. After complete dissolution of the precatalyst, the entire quantity of precatalyst solution was added to the dry reagents *via* cannula transfer and the reaction vessel placed into an oil bath preheated to 120 °C. The reactions were left for the appropriate times and their final conversions analysed by

<sup>1</sup>H NMR of the crude reaction mixtures by measuring the ratio of the diagnostic peaks at 6.80 ppm for *N*-Benzyl-4-Bromo-6-methylpyridin-2-one and 6.85 ppm for *N*-benzyl-4-cyano-6-methylpyridin-2-one. Purification was carried out by direct flash chromatography (SiO<sub>2</sub>, 40% EtOAc/petrol) to give **69** as a white crystalline solid.

*Representative lab book reference number: JTWB-4-263*

### **Kinetic investigation into catalyst loading effects on the 47-catalysed cyanations under hydrous conditions**

All kinetic experiments utilising **47** as a precatalyst and K<sub>4</sub>[Fe(CN)<sub>6</sub>]·3H<sub>2</sub>O (234 mg, 0.55 mmol, 0.22 eq.), Na<sub>2</sub>CO<sub>3</sub> (267 mg, 2.52 mmol, 1 eq.) were carried out according to General procedure A at 120 °C. All reactions performed under these conditions were carried out on a 700 mg/2.517 mmol scale with respect to **65**.

*Lab book reference numbers and respective conversions: 0.05 mol%: JTWB-5-299, 99%; 0.1 mol%: JTWB-5-285, 93%; 0.5 mol%: JTWB-5-295, 99%; 0.75 mol%: JTWB-5-343, 89%; 1 mol%: JTWB-5-289, 82%; 1.75 mol%: JTWB-5-345, 84%; 2.5 mol%: JTWB-5-292, 88%.*

### **Mercury poisoning test of 47-catalysed arylcyanation under hydrous conditions**

Mercury poisoning test of **47**-catalysed cyanation under hydrous conditions was carried out according to General procedure A at 120 °C using **47** as a precatalyst (0.5 ml as a 25 mmol dm<sup>-3</sup> stock solution, 1.25 × 10<sup>-5</sup> mol, 0.5 mol%), K<sub>4</sub>[Fe(CN)<sub>6</sub>]·3H<sub>2</sub>O (234 mg, 0.55 mmol, 0.22 eq.) and Na<sub>2</sub>CO<sub>3</sub> (267 mg, 2.52 mmol, 1 eq.) on a 700 mg scale with respect to **65**. The reaction was stirred at 120 °C for 1 hour 33 minutes and 57 seconds after the addition of the precatalyst, then Hg<sup>0</sup> (0.5 g, 2.156 mmol, 200 eq. with respect to Pd) was added by a microsyringe *via* a septum. Two hours after the addition of the Hg<sup>0</sup>, the reaction was allowed to cool to room temperature.

Reaction conversion at end point: 35%

*Lab book reference number: JTWB-5-305*

### **Measurement of infrared spectrum of KCN in DMAc**

An oven dried, 100 ml three necked round bottomed flask equipped with a small stirrer bar was attached to the React-IR, then backfilled with nitrogen three times. At all points of the experiment hereafter, the reaction vessel was open to a steady flow of N<sub>2</sub>.

After backfilling the round bottomed flask with dry N<sub>2</sub>, a background spectrum was collected and dry, degassed DMAc added (5.5 ml). At this point a reference spectrum was recorded with stirring. After sequence initiation, the reaction was stirred at room temperature for 5 minutes, before being heated to reaction temperature (as monitored by the internal thermocouple) by being placed in a silicon oil bath set to 120 °C. After the solvent reached the correct temperature it was stirred for a further five minutes and a spectrum used as a reference. The hot solvent was then stirred for a further hour to give an adequate “flat line” in the absence of KCN. After this time KCN (27.5 mg, 0.422 mmol) was then added and the solution was stirred until no further increase in absorption was observed at 2045 cm<sup>-1</sup>.

After the absorbance at 2045 cm<sup>-1</sup> had reached a constant value for 1.5 hours the experiment was stopped and the reaction mixture allowed to *cool to room temperature before being quenched with a dilute aqueous bleach, 1M NaOH solution mixture.*<sup>166</sup> *Important safety note: KCN is extremely toxic. Appropriate care and precaution must be exercised during its use. Furthermore, the exposure of hot KCN solutions to water (via atmospheric air) COULD result in the formation of a significant quantity of HCN gas via hydrolysis.*<sup>93-94, 107</sup> *It is therefore imperative that these should be allowed to cool fully, and any manipulation should be carried out in a fume cupboard with appropriate PPE.*

All peak absorption data for 2045 cm<sup>-1</sup> and any other peaks of interest were exported into Excel in two forms: i) with no reference subtraction; ii) after subtraction of a reference spectrum of DMAc at reaction temperature. All subsequent analysis was carried out on dataset ii).

*Lab book reference number: JTWB-5-287*

### **Kinetic study of the arylcyanation reaction conditions in the absence of Pd.**

The experiment was carried out according to General procedure A at 120 °C, but without the addition of a Pd catalyst. The reaction was conducted using K<sub>4</sub>[Fe(CN)<sub>6</sub>]·3H<sub>2</sub>O (234 mg, 0.55 mmol, 0.22 eq.), Na<sub>2</sub>CO<sub>3</sub> (267 mg, 2.52 mmol, 1 eq.) on a 700 mg scale with respect to **65**. The experiment was stopped after 18.5 hours and the reaction mixture allowed to cool before analysis of the crude reaction mixture by <sup>1</sup>H NMR spectroscopy.

Reaction conversion at end point: 0%

*Lab book reference number:* JTWB-5-288

**Kinetic study of the arylycyanation reaction conditions in the absence of an additive (Na<sub>2</sub>CO<sub>3</sub>)**

The experiment was carried out according to General procedure A at 120 °C, but without an additive (Na<sub>2</sub>CO<sub>3</sub>). The reaction was conducted using K<sub>4</sub>[Fe(CN)<sub>6</sub>]·3H<sub>2</sub>O (234 mg, 0.55 mmol, 0.22 eq.) in the presence of **47** (50 µl as a 25 mmol dm<sup>-3</sup> stock solution, 1.25 × 10<sup>-6</sup> mol, 0.05 mol%) on a 700 mg scale with respect to **65**. It was noted that at 8 hours after the addition of the precatalyst a precipitate began to form. After 18 hours the experiment was stopped and the reaction allowed to cool. The reaction mixture supernatant (dark grey suspension) was collected by filter cannula and allowed to settle. The resulted green precipitate (106 mg) was again collected by removal of the supernatent *via* filter cannula. The filtrate was analysed by <sup>1</sup>H NMR spectroscopy and it was confirmed that no product was formed. The precipitate was analysed by ATR infrared spectroscopy in comparison with an authentic sample of K<sub>4</sub>[Fe(CN)<sub>6</sub>]·3H<sub>2</sub>O.

Green precipitate from reaction:  $v_{\max}/\text{cm}^{-1}$  (ATR) 2093, 2072, 2062, 2040, 2023, 1598, 582, 418.

K<sub>4</sub>[Fe(CN)<sub>6</sub>]·3H<sub>2</sub>O:  $v_{\max}/\text{cm}^{-1}$  (ATR) 2093, 2072, 2062, 2040, 2023, 1594, 1362, 776, 562.

Reaction conversion at end point: 0%

*Lab book reference number:* JTWB-5-354

**Varying the equivalents of K<sub>4</sub>[Fe(CN)<sub>6</sub>]·3H<sub>2</sub>O in the arylycyanation of **65**.**

The experiments were carried out according to General procedure A at 120 °C using K<sub>4</sub>[Fe(CN)<sub>6</sub>]·3H<sub>2</sub>O (0.167-0.5 eq.) Na<sub>2</sub>CO<sub>3</sub> (267 mg, 2.52 mmol, 1 eq.) and **47** (0.5 ml as a 25 mmol dm<sup>-3</sup> stock solution, 1.25 × 10<sup>-5</sup> mol, 0.5 mol%) on a 700 mg scale with respect to **65**.

*Lab book reference numbers and respective conversions:* 0.167 eq.: JTWB-5-307, 90%; 0.20 eq.: JTWB-5-308, 97%; 0.22 eq.: JTWB-5-295, 99%; 0.25 eq.: JTWB-5-310, 98%; 0.5 eq.: JTWB-5-311, 96%.

**Kinetic screening of trans-Pd(OAc)<sub>2</sub>(HNR<sub>2</sub>)<sub>2</sub> precatalysts in the anhydrous arylcyanation of **65** (72 μM, 7 ppm Pd)**

The experiments were carried out according to General procedure A at 140 °C using K<sub>4</sub>[Fe(CN)<sub>6</sub>] (408 mg, 1.11 mmol, 0.22 eq.), Na<sub>2</sub>CO<sub>3</sub> (534 mg, 5.02 mmol, 1 eq.) and precatalysts **48**, **47**, **52**, **53**, **51** (20 μl as a 25 mmol dm<sup>-3</sup> stock solutions, 5.02 × 10<sup>-7</sup> mol, 0.01 mol%) on a 1.4 g scale with respect to **65**. These reactions were conducted in a total reaction solvent volume of 7 ml.

*Lab book reference numbers and respective conversions:* **48**: JTWB-6-400, 57%; **47**: JTWB-6-387, 77%; **52**: JTWB-6-404, 86%; **53**: JTWB-6-402, 35%; **51**: JTWB-6-405, 93%.

**Kinetic investigation of the anhydrous arylcyanation of **65** using **47** at 0.005 mol%, 36 μM, 3.5 ppm Pd**

The experiment was carried out according to General procedure A at 140 °C using K<sub>4</sub>[Fe(CN)<sub>6</sub>] (312 mg, 0.95 mmol, 0.20 eq.), Na<sub>2</sub>CO<sub>3</sub> (457 mg, 4.3 mmol, 1 eq.) and **47** (8.6 μl as a 25 mmol dm<sup>-3</sup> stock solution, 0.216 μmol, 0.005 mol%) on a 1.2 g scale with respect to **65**. The total reaction solvent volume was 6 ml.

Reaction conversion at end point was 26%.

*Lab book reference number:* JTWB-6-367

**Kinetic investigation of the anhydrous arylcyanation of **65** using **47** at 0.005 mol%, 72 μM, 7.0 ppm Pd**

The experiment was carried out according to General procedure A at 140 °C using K<sub>4</sub>[Fe(CN)<sub>6</sub>] (625 mg, 1.90 mmol, 0.20 eq.), Na<sub>2</sub>CO<sub>3</sub> (914 mg, 8.61 mmol, 1 eq.) and **47** (17 μl as a 25 mmol dm<sup>-3</sup> stock solution, 0.43 μmol, 0.005 mol%) on a 2.4 g scale with respect to **65**. The total reaction solvent volume was 6 ml.

Reaction conversion at end point was 38%.

*Lab book reference number:* JTWB-6-371

**Kinetic investigation of the anhydrous arylocyanation of 65 using 47 at 0.05 mol%, 180  $\mu\text{M}$ , 17.5 ppm Pd**

The experiment was carried out according to General procedure A at 120 °C using  $\text{K}_4[\text{Fe}(\text{CN})_6]$  (204 mg, 0.55 mmol, 0.22 eq.),  $\text{Na}_2\text{CO}_3$  (267 mg, 2.52 mmol, 1 eq.) and **47** (50  $\mu\text{l}$  as a 25 mmol  $\text{dm}^{-3}$  stock solution, 1.25  $\mu\text{mol}$ , 0.05 mol%) on a 700 mg scale with respect to **65**.

*Lab book reference numbers and respective conversions: JTWB-5-350, 95% and JTWB-5-332, 99%.*

**Kinetic investigation of the anhydrous arylocyanation of 65 using 47 at 0.1 mol%, 360  $\mu\text{M}$ , 35 ppm Pd**

The experiment was carried out according to General procedure A at 120 °C using  $\text{K}_4[\text{Fe}(\text{CN})_6]$  (204 mg, 0.55 mmol, 0.22 eq.),  $\text{Na}_2\text{CO}_3$  (267 mg, 2.52 mmol, 1 eq.) and **47** (100  $\mu\text{l}$  as a 25 mmol  $\text{dm}^{-3}$  stock solution, 2.5  $\mu\text{mol}$ , 0.1 mol%) on a 700 mg scale with respect to **65**.

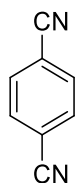
*Lab book reference numbers and respective conversion: JTWB-5-330, 99%.*

**Anhydrous arylocyanation of 65 using 47 at 0.01 mol%, 36  $\mu\text{M}$ , 3.5 ppm Pd**

The experiment was carried out according to General procedure A at 140 °C using  $\text{K}_4[\text{Fe}(\text{CN})_6]$  (204 mg, 0.55 mmol, 0.22 eq.),  $\text{Na}_2\text{CO}_3$  (267 mg, 2.51 mmol, 1 eq.) and **47** (10  $\mu\text{l}$  as a 25 mmol  $\text{dm}^{-3}$  stock solution, 0.25  $\mu\text{mol}$ , 0.01 mol%) on a 700 mg scale with respect to **65**.

Reaction conversion at end point was 53%.

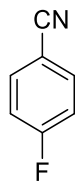
*Lab book reference number: JTWB-5-346*

**1,4-Dicyanobenzene<sup>167</sup> (72)**

The *title compound* was prepared with **47** (0.05 mol%) using  $\text{K}_4[\text{Fe}(\text{CN})_6]$  (260 mg, 0.62 mmol, 0.44 eq.) according to general experimental procedure F. Flash chromatography ( $\text{SiO}_2$ , 20% EtOAc/petrol) afforded a white crystalline solid (155 mg, 90%).

$^1\text{H}$  NMR ( $\text{CDCl}_3$ , 400 MHz):  $\delta$  7.80 (s, 4H, ArH);  $^{13}\text{C}$  NMR (101 MHz,  $\text{CDCl}_3$ ):  $\delta$  132.9, 117.2, 116.9;  $m/z$  (ESI<sup>+</sup>) 129.0450 [(M+H)<sup>+</sup>];  $R_f$  0.26 (20% EtOAc/petrol).

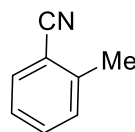
*Lab book reference number:* JTWB-8-563

**4-Fluorobenzonitrile<sup>168</sup> (73)**

The *title compound* was prepared with **47** (0.05 mol%) according to general experimental procedure F. Flash chromatography ( $\text{SiO}_2$ , 5%  $\text{Et}_2\text{O}$ /petrol) afforded a volatile, white crystalline solid (153 mg, 93%).

$^1\text{H}$  NMR ( $\text{CDCl}_3$ , 400 MHz):  $\delta$  7.70 – 7.64 (m, 2H, ArH), 7.20-7.13 (m, 2H, ArH);  $^{13}\text{C}$  NMR (101 MHz,  $\text{CDCl}_3$ ):  $\delta$  165.0 (d,  $J = 256$  Hz), 134.6 (d,  $J = 9$  Hz), 118.0, 116.8 (d,  $J = 24$  Hz), 108.5 (d,  $J = 4$  Hz);  $^{19}\text{F}$  NMR ( $\text{CDCl}_3$ , 376 MHz)  $\delta$  102.3 (m, 1F);  $m/z$  (ESI<sup>+</sup>) 122.0405 [(M+H)<sup>+</sup>];  $R_f$  0.19 (5%  $\text{Et}_2\text{O}$ /petrol).

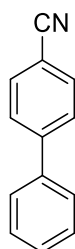
*Lab book reference number:* JTWB-7-507

**2-Methylbenzonitrile<sup>168</sup> (74)**

The *title compound* was prepared with **47** (0.1 mol%) according to general experimental procedure F. Flash chromatography (SiO<sub>2</sub>, 10-20% Et<sub>2</sub>O/petrol) afforded a white crystalline solid (133 mg, 81%).

<sup>1</sup>H NMR (CDCl<sub>3</sub>, 400 MHz): δ 7.60 (dd, *J* = 7.7, 1.4 Hz, 1H, H6), 7.48 (ddd, *J* = 7.7, 7.7, 1.4 Hz, 1H, H4), 7.32 (dd, *J* = 7.7, 7.7 Hz, 1H, H5), 7.28 (d, *J* = 7.7 Hz, 1H, H3), 2.55 (s, 3H, CH<sub>3</sub>); <sup>13</sup>C NMR (101 MHz, CDCl<sub>3</sub>): δ 142.0, 132.8, 132.7, 130.4, 126.4, 118.3, 112.9, 20.6; *m/z* (APCI<sup>+</sup>) 118.0650 [(M+H)<sup>+</sup>]; R<sub>f</sub> 0.15 (10% Et<sub>2</sub>O/petrol).

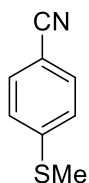
*Lab book reference number:* JTWB-6-430

**4-Phenylbenzonitrile<sup>167</sup> (75)**

The *title compound* was prepared with **47** (0.025 mol%) according to general experimental procedure F. Flash chromatography (SiO<sub>2</sub>, 100% petrol) afforded a white crystalline solid (207 mg, 84%).

<sup>1</sup>H NMR (CDCl<sub>3</sub>, 400 MHz): δ 7.73 (d, *J* = 8.4 Hz, 2H), 7.69 (d, *J* = 8.4 Hz, 2H), 7.6 (d, *J* = 7.1, 2H), 7.49 (ddd, *J* = 7.1, 7.1 Hz, 2H), 7.43 (dd, *J* = 7.1, 7.1 Hz, 1H); <sup>13</sup>C NMR (101 MHz, CDCl<sub>3</sub>): δ 145.8, 139.3, 132.7, 129.2, 128.8, 127.9, 127.4, 119.1, 111.0; *m/z* (ESI<sup>+</sup>) 180.0810 [(M+H)<sup>+</sup>]; R<sub>f</sub> 0.20 (100% Petrol).

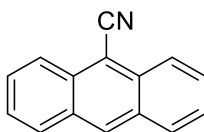
*Lab book reference number:* JTWB-7-511

**4-(Methylthio)benzonitrile<sup>169</sup> (76)**

The *title compound* was prepared with **47** (0.1 mol%) according to general experimental procedure F. Flash chromatography (SiO<sub>2</sub>, 10-30% Et<sub>2</sub>O/petrol) afforded a white crystalline solid (125 mg, 60%).

<sup>1</sup>H NMR (CDCl<sub>3</sub>, 400 MHz): δ 7.52 (d, *J* = 8.7 Hz, 2H, ArH), 7.25 (d, *J* = 8.7 Hz, 2H, ArH), 2.50 (s, 3H, CH<sub>3</sub>); <sup>13</sup>C NMR (101 MHz, CDCl<sub>3</sub>): δ 146.2, 132.2, 125.5, 119.1, 107.7, 14.8; *m/z* (ESI<sup>+</sup>) 130.0365 [(M+H)<sup>+</sup>]; R<sub>f</sub> 0.23 (10% Et<sub>2</sub>O/Petrol).

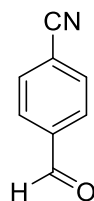
*Lab book reference number:* JTWB-8-569

**9-Cyanoanthracene<sup>168</sup> (77)**

The *title compound* was prepared with **47** (0.05 mol%) according to general experimental procedure F. Flash chromatography (SiO<sub>2</sub>, 1% Et<sub>2</sub>O/petrol) afforded a bright yellow, crystalline solid (174 mg, 61%).

<sup>1</sup>H NMR (CDCl<sub>3</sub>, 400 MHz): δ 8.66 (s, 1H, H10), 8.41 (ddd, *J* = 8.7, 1.8, 1.0 Hz, 2H, H1 & H8), 8.07 (dd, *J* = 8.5, 1.0 Hz, 2H, H4 & H5), 7.71 (ddd, *J* = 8.7, 6.7, 1.2 Hz, 2H, H2 & H7), 7.58 (ddd, *J* = 8.5, 6.7, 1.2 Hz, 2H, H3 & H6); <sup>13</sup>C NMR (101 MHz, CDCl<sub>3</sub>): δ 133.4, 132.9, 130.7, 130.8, 129.1, 126.5, 125.4, 117.4, 105.6; *m/z* (ESI<sup>+</sup>) 204.0826 [(M+H)<sup>+</sup>]; R<sub>f</sub> 0.25 (1% Et<sub>2</sub>O/Petrol).

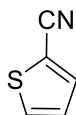
*Lab book reference number:* JTWB-8-549

**4-Formylbenzonitrile<sup>43</sup> (78)**

The *title compound* was prepared with **47** (0.05 mol%) according to general experimental procedure F. Flash chromatography (SiO<sub>2</sub>, 20% EtOAc/petrol) afforded a white, crystalline solid (125 mg, 68%).

<sup>1</sup>H NMR (CDCl<sub>3</sub>, 400 MHz): δ 10.10 (s, 1H, CHO), 8.00 (d, *J* = 8.4 Hz, 2H, ArH), 7.85 (d, *J* = 8.4 Hz, 2H, ArH); <sup>13</sup>C NMR (101 MHz, CDCl<sub>3</sub>): δ 190.8, 138.8, 133.0, 130.0, 117.8, 117.7; *m/z* (ESI<sup>+</sup>) 164.0684 [(M+MeOH)<sup>+</sup>]; R<sub>f</sub> 0.12 (20% EtOAc/Petrol).

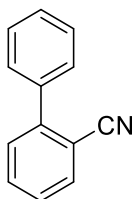
*Lab book reference number:* JTWB-8-559

**2-Thiophenecarbonitrile<sup>170</sup> (79)**

The *title compound* was prepared with **47** (0.1 mol%) according to general experimental procedure F. Flash chromatography (SiO<sub>2</sub>, 1-5% Et<sub>2</sub>O/petrol) afforded a colourless oil (125 mg, 84%).

<sup>1</sup>H NMR (CDCl<sub>3</sub>, 400 MHz): δ 7.64 (dd, *J* = 1.1, 3.6 Hz, 1H, H3), 7.61 (dd, *J* = 1.1, 5.1 Hz, 1H, H5), 7.14 (dd, 5.1, 3.6 Hz, 1H, H4); <sup>13</sup>C NMR (101 MHz, CDCl<sub>3</sub>): δ 137.6, 132.7, 127.8, 114.4, 110.1; *m/z* (APCI<sup>+</sup>) 110.065 [(M+MeOH)<sup>+</sup>]; R<sub>f</sub> 0.32 (1% Et<sub>2</sub>O/Petrol).

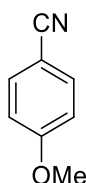
*Lab book reference number:* JTWB-8-566

**2-Phenylbenzonitrile<sup>171</sup> (80)**

The *title compound* was prepared with **47** (0.1 mol%) according to general experimental procedure F. Flash chromatography (SiO<sub>2</sub>, 5% Et<sub>2</sub>O/petrol) afforded a colourless oil (41.3 mg, 16%).

<sup>1</sup>H NMR (CDCl<sub>3</sub>, 400 MHz): δ 7.77 (d, *J* = 7.8, ArH), 7.65 (ddd, *J* = 7.8, 7.8, 1.4 Hz, 1H, ArH), 7.60 – 7.41 (m, 7 H, ArH); <sup>13</sup>C NMR (101 MHz, CDCl<sub>3</sub>): 145.6, 138.2, 133.8, 132.9, 130.2, 128.8, 128.7, 128.7, 127.6, 118.8, 111.4; *m/z* (ESI<sup>+</sup>) 180.0815 [(M+H)<sup>+</sup>], 202.0624 [(M+Na)<sup>+</sup>]; R<sub>f</sub> 0.13 (5 % Et<sub>2</sub>O/Petrol).

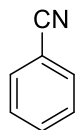
*Lab book reference number:* JTWB-8-513

**4-Methoxybenzonitrile<sup>167</sup> (81)**

The *title compound* was prepared with **47** (0.05 mol%) according to general experimental procedure F. Flash chromatography (SiO<sub>2</sub>, 20% Et<sub>2</sub>O/petrol) afforded a crystalline solid (57 mg, 31%).

<sup>1</sup>H NMR (CDCl<sub>3</sub>, 400 MHz): δ 7.59 (d, *J* = 8.9 Hz, 2H, H<sub>2</sub> & H<sub>6</sub>), 6.95 (d, *J* = 8.9 Hz, 2H, H<sub>3</sub> & H<sub>5</sub>), 3.86 (s, 3H, CH<sub>3</sub>); <sup>13</sup>C NMR (101 MHz, CDCl<sub>3</sub>): δ 162.9, 134.1, 119.3, 114.8, 104.1, 55.6; *m/z* (ESI<sup>+</sup>) 134.0621 [(M+H)<sup>+</sup>]; R<sub>f</sub> 0.21 (20 % Et<sub>2</sub>O/Petrol).

*Lab book reference number:* JTWB-6-422

**Benzonitrile<sup>43</sup> (82)**

The *title compound* was prepared with **47** (0.05 mol%) according to general experimental procedure F. A short silica plug (SiO<sub>2</sub>, 30% EtOAc/petrol) afforded a colourless oil (141 mg, 98%).

<sup>1</sup>H NMR (CDCl<sub>3</sub>, 400 MHz): δ 7.68-7.65 (m, 2H, H2 & H6), 7.61 (dd, *J* = 7.6, 7.1 Hz, 1H, H4), 7.48 (dd, *J* = 7.1, 7.1 Hz, 2H, H3 & H5); <sup>13</sup>C NMR (101 MHz, CDCl<sub>3</sub>): δ 132.9, 132.3, 129.2, 119.0, 112.5; *m/z* (ESI<sup>+</sup>) 104.0500 [(M+H)<sup>+</sup>]; *R<sub>f</sub>* 0.70 (30 % EtOAc/Petrol).

*Lab book reference number:* JTWB-6-421

**Screening of precatalyst 58 in the anhydrous arylocyanation of 65 (72 μM, 7 ppm Pd).**

The experiments were carried out according to General procedure A at 140 °C using K<sub>4</sub>[Fe(CN)<sub>6</sub>] (350 mg, 0.95 mmol, 0.22 eq.), Na<sub>2</sub>CO<sub>3</sub> (457 mg, 5.31 mmol, 1 eq.) and **58** (18 μl as a 12.5 mmol dm<sup>-3</sup> stock solution, 2.15 × 10<sup>-7</sup> mol, 0.005 mol% with respect to catalyst, 0.01 mol% with respect to Pd) on a 1.2 g scale with respect to **65**. This reaction was conducted in a total reaction solvent volume of 6 ml.

Reaction conversion: 51%.

*Lab book reference numbers:* JTWB-8-585.

**Kinetic study of the arylocyanation of 65 with 0.25 eq. of Na<sub>2</sub>CO<sub>3</sub>.**

The experiments were carried out according to General procedure A at 120 °C using K<sub>4</sub>[Fe(CN)<sub>6</sub>] (204 mg, 0.55 mmol, 0.22 eq.), Na<sub>2</sub>CO<sub>3</sub> (67 mg, 0.63 mmol, 0.25 eq.) and **47** (50 μl as a 25 mmol dm<sup>-3</sup> stock solution, 1.25 × 10<sup>-6</sup> mol, 0.05 mol%) on a 700 mg scale with respect to **65**.

Reaction conversion at end point: 73%

*Lab book reference number:* JTWB-5-338.

**Kinetic study of the arylycyanation of 65 with K<sub>2</sub>CO<sub>3</sub>**

The experiment was carried out according to General procedure A at 140 °C using K<sub>4</sub>[Fe(CN)<sub>6</sub>] (313 mg, 0.95 mmol, 0.20 eq.), K<sub>2</sub>CO<sub>3</sub> (595 mg, 4.31 mmol, 1.0 eq.) and **47** (17 μl as a 25 mmol dm<sup>-3</sup> stock solution, 4.31×10<sup>-7</sup> mol, 0.01 mol%) on a 1.2 g scale with respect to **65**. This reaction was conducted in a total reaction solvent volume of 6 ml.

Reaction conversion at end point: 0%

*Lab book reference number: JTWB-6-372.*

**Kinetic study of the arylycyanation of 65 with Cs<sub>2</sub>CO<sub>3</sub>**

The experiments were carried out according to General procedure A at 140 °C using K<sub>4</sub>[Fe(CN)<sub>6</sub>] (313 mg, 0.95 mmol, 0.20 eq.), Cs<sub>2</sub>CO<sub>3</sub> (1.521 g, 4.31 mmol, 1.0 eq.) and **47** (17 μl as a 25 mmol dm<sup>-3</sup> stock solution, 4.31×10<sup>-7</sup> mol, 0.01 mol%) on a 1.2 mg scale with respect to **65**. This reaction was conducted in a total reaction solvent volume of 6 ml.

Reaction conversion at end point: 0%

*Lab book reference number: JTWB-6-373.*

**Using NaX salts as additives in the arylycyanation of 65.**

To a flame dried Schlenk tube was added *N*-Benzyl-4-Bromo-6-methylpyridin-2-one (50 mg, 0.18 mmol, 1 eq.), NaX additive (0.18 mmol, 1 eq., freshly ground in a pestle and mortar) and K<sub>4</sub>[Fe(CN)<sub>6</sub>] (17 mg, 0.46 × 10<sup>-4</sup> mol, 0.25 eq., freshly ground in a pestle and mortar) then the reaction vessel was backfilled with nitrogen (3 ×). To a separate 10 ml flame dried Schlenk tube charged with a stirrer bar was added **47** (10 mg, 2.53 × 10<sup>-5</sup> mol) and the vessel backfilled with N<sub>2</sub> with stirring (3 ×). The reaction mixture was stirred while dry, degassed DMAc (0.5 ml) was added through a septum, then it was placed into an oil bath preheated to 120 °C. Concomitantly, dry DMAc (1 ml) was added to the Schlenk tube containing **47** and was stirred until complete dissolution was observed to give a precatalyst solution with a concentration of 25 mmol dm<sup>-3</sup>. Immediately after complete dissolution of **47**, the precatalyst (3.6 μl, 0.1 μmol, 0.05 mol%) was added using a microsyringe through a septum to the preheated reaction mixture. The reaction was heated at 120 °C for 17 hrs then allowed to cool. A small aliquot was filtered through a small Celite plug prior to calculating their final conversions analysed by <sup>1</sup>H NMR of the crude reaction mixtures.

Reaction conversion at end points: NaCl: 7%; NaBr: 12%; NaI: 16%.

*Lab book reference numbers:* JTWB-6-397, JTWB-6-398, JTWB-6-399.

**Using alternative hexacyanoferrate salts as cyanide sources in the arylation of 65.**

To a flame dried Schlenk tube was added *N*-Benzyl-4-Bromo-6-methylpyridin-2-one (50 mg, 0.18 mmol, 1 eq.), NaCO<sub>3</sub> additive (19 mg, 0.18 mmol, 1 eq., freshly ground in a pestle and mortar) and hexacyanoferrate additive ( $0.40 \times 10^{-4}$  mol, 0.22 eq., freshly ground in a pestle and mortar) then the reaction vessel was backfilled with nitrogen (3 ×). To a separate 10 ml flame dried Schlenk tube charged with a stirrer bar was added **47** (10 mg,  $2.53 \times 10^{-5}$  mol) and the vessel backfilled with N<sub>2</sub> with stirring (3 ×). The reaction mixture was stirred while dry, degassed DMAc (0.5 ml) was added through a septum, then it was placed into an oil bath preheated to 120 °C. Concomitantly, dry DMAc (1 ml) was added to the Schlenk tube containing **47** and was stirred until complete dissolution was observed to give a precatalyst solution with a concentration of 25 mmol dm<sup>-3</sup>. Immediately after complete dissolution of **47**, the appropriate amount of precatalyst (0.01 - 0.5 mol%) was added using a microsyringe through a septum to the preheated reaction mixture. The reaction was heated at 120 °C for 5 hrs then allowed to cool. A small aliquot was filtered through a small Celite plug prior to calculating their final conversions analysed by <sup>1</sup>H NMR of the crude reaction mixtures.

*Lab book reference numbers and respective conversions:* KFe<sup>III</sup>[Fe<sup>II</sup>(CN)<sub>6</sub>], **47** (0.5 mol%): JTWB-5-349, 0%; K<sub>3</sub>[Fe<sup>III</sup>(CN)<sub>6</sub>], **47** (0.5 mol%): JTWB-5-348, 53%; Na<sub>4</sub>[Fe<sup>II</sup>(CN)<sub>6</sub>], **47** (0.01 mol%): JTWB-6-392, 16%; Na<sub>4</sub>[Fe<sup>II</sup>(CN)<sub>6</sub>]·10H<sub>2</sub>O, **47** (0.05 mol%): JTWB-6-393, 0%.

**Using Na<sub>4</sub>[Fe(CN)<sub>6</sub>] as cyanide source in the absence of Na<sub>2</sub>CO<sub>3</sub> for the arylation of 65.**

To a flame dried Schlenk tube was added *N*-Benzyl-4-Bromo-6-methylpyridin-2-one (50 mg, 0.18 mmol, 1 eq.), NaCO<sub>3</sub> additive (19 mg, 0.18 mmol, 1 eq., freshly ground in a pestle and mortar) and Na<sub>4</sub>[Fe(CN)<sub>6</sub>] (12 mg,  $0.40 \times 10^{-4}$  mol, 0.22 eq., freshly ground in a pestle and mortar) then the reaction vessel was backfilled with nitrogen (3 ×). To a separate 10 ml flame dried Schlenk tube charged with a stirrer bar was added **47** (10 mg,  $2.53 \times 10^{-5}$  mol) and the vessel backfilled with N<sub>2</sub> with stirring (3 ×). The reaction mixture was stirred while dry, degassed DMAc (0.5 ml) was added through a septum, then it was placed into an oil bath preheated to 120 °C. Concomitantly, dry DMAc (1 ml) was added to the Schlenk tube containing **47** and was stirred until complete dissolution was observed to give a precatalyst

solution with a concentration of  $25 \text{ mmol dm}^{-3}$ . Immediately after its complete dissolution, **47** (0.05 or 0.1 mol%) was added using a microsyringe through a septum to the preheated reaction mixture. The reaction was heated at  $120 \text{ }^\circ\text{C}$  for 5 hrs then allowed to cool. A small aliquot was filtered through a small Celite plug prior to calculating their final conversions by  $^1\text{H}$  NMR analysis by of the crude reaction mixtures.

*Lab book reference numbers and respective conversions:* 0.05 mol% Pd: JTWB-6-396, 0%; 0.1 mol% Pd: JTWB-7-529, 0%.

**Kinetic study of the arylycyanation of 65 with 47 (0.01 mol%, 72  $\mu\text{M}$ , 7 ppm) and  $\text{Na}_4[\text{Fe}(\text{CN})_6]$**

The experiment was carried out according to General procedure A at  $140 \text{ }^\circ\text{C}$  using  $\text{Na}_4[\text{Fe}(\text{CN})_6]$  (335 mg, 1.1 mmol, 0.22 eq.),  $\text{Na}_2\text{CO}_3$  (534 mg, 5.0 mmol, 1.0 eq.) and **47** (20  $\mu\text{l}$  as a  $25 \text{ mmol dm}^{-3}$  stock solution,  $5.02 \times 10^{-7}$  mol, 0.01 mol%) on a 1.4 g scale with respect to **65**. This reaction was conducted in a total reaction solvent volume of 7 ml.

Reaction conversion at end point: 16%

*Lab book reference number:* JTWB-6-395.

**Kinetic study of the arylycyanation of 65 with 47 (0.5 mol%, 1.8 mM, 175 ppm) and  $\text{K}_3[\text{Fe}(\text{CN})_6]$**

The experiment was carried out according to General procedure A at  $120 \text{ }^\circ\text{C}$  using  $\text{K}_3[\text{Fe}(\text{CN})_6]$  (182 mg, 0.55 mmol, 0.22 eq.),  $\text{Na}_2\text{CO}_3$  (267 mg, 2.51 mmol, 1.0 eq.) and **47** (0.5 ml as a  $25 \text{ mmol dm}^{-3}$  stock solution,  $1.26 \times 10^{-5}$  mol, 0.5 mol%) on a 700 mg scale with respect to **65**. This reaction was conducted in a total reaction solvent volume of 7 ml.

Reaction conversion at end point: 85%

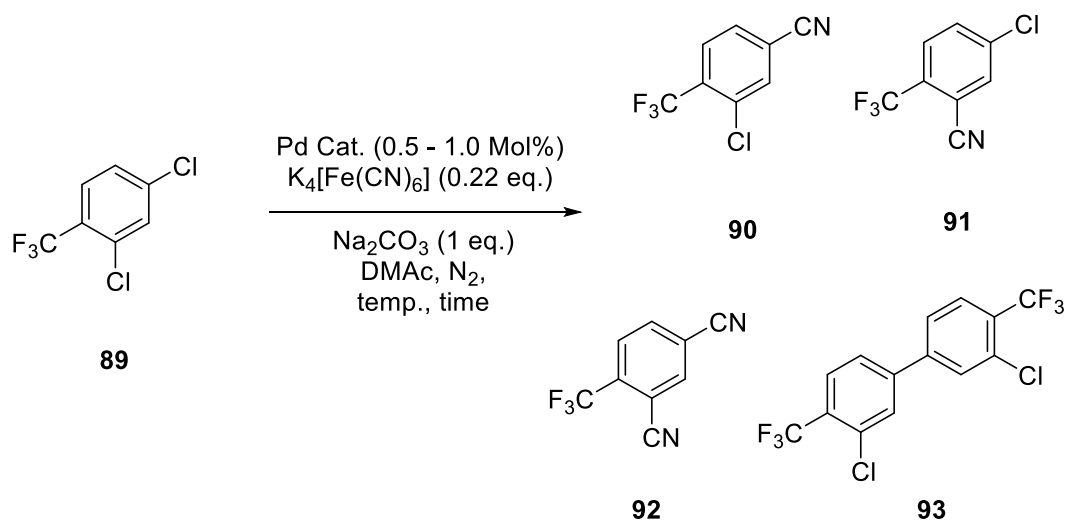
## Appendix 1: Published papers

The following papers have been published with contributions of the author of this thesis following involvement in other, unrelated projects through the supervision of summer project, MChem and Erasmus exchange students. The work submitted in this thesis is currently being prepared for patent filing and subsequent publication.

1. Thomas J. Williams, Joshua T. W. Bray Benjamin R. M. Lake, Charlotte E. Willans, Nasir A. Rajabi, Alireza Ariaferd, Chiara Manzini, Fabio Bellina, Adrian C. Whitwood and Ian J. S. Fairlamb; Mechanistic Elucidation of the Arylation of Non-Spectator *N*-Heterocyclic Carbenes at Copper Using a Combined Experimental and Computational Approach, *Organometallics*, **2015**, *34*, 3497 – 3507.
2. Nasiru P. Yahaya, Kate M. Appleby, Magdalene Teh, Conrad Wagner, Erik Troschke, Joshua T. W. Bray, Simon B. Duckett, L. Anders Hammarback, Jonathan S. Ward, Jessica Milani, Natalie E. Pridmore, Adrian C. Whitwood, Jason M. Lynam, and Ian J. S. Fairlamb; Manganese(I)-Catalyzed C–H Activation: The Key Role of a 7-Membered Manganacycle in H-Transfer and Reductive Elimination, *Angew. Chem. Int. Ed.* **2016**, *55*, 12455 –12459.
3. Jason M Lynam; Jonathan S Ward; Joshua T W Bray; Benjamin J Aucott; Conrad Wagner; Natalie E Pridmore; Adrian C Whitwood; James W B Moir; Ian J S Fairlamb; Photoactivated functionizable tetracarbonyl phenylpyridine manganese(I) complexes as CO-releasing molecules: a direct Suzuki-Miyaura cross-coupling on a thermally-stable CO-RM, *Eur. J. Inorg. Chem.* Accepted Author Manuscript. doi:10.1002/ejic.201600775.
4. Margot N. Wenzel, Philippa K. Owens, Joshua T. W. Bray, Jason M. Lynam, Pedro M. Aguiar, Christopher Reed, James D. Lee, Jacqui F. Hamilton, Adrian C. Whitwood and Ian J. S. Fairlamb; The redox couple involving NO<sub>x</sub> in aerobic Pd-catalyzed oxidation of sp<sup>3</sup>-C–H bonds: direct evidence for Pd-NO<sub>3</sub>–/NO<sub>2</sub>– interactions involved in oxidation and reductive elimination, *J. Am. Chem. Soc.* DOI: 10.1021/jacs.6b10853.

## Appendix 2: Tables of extended substrate screen

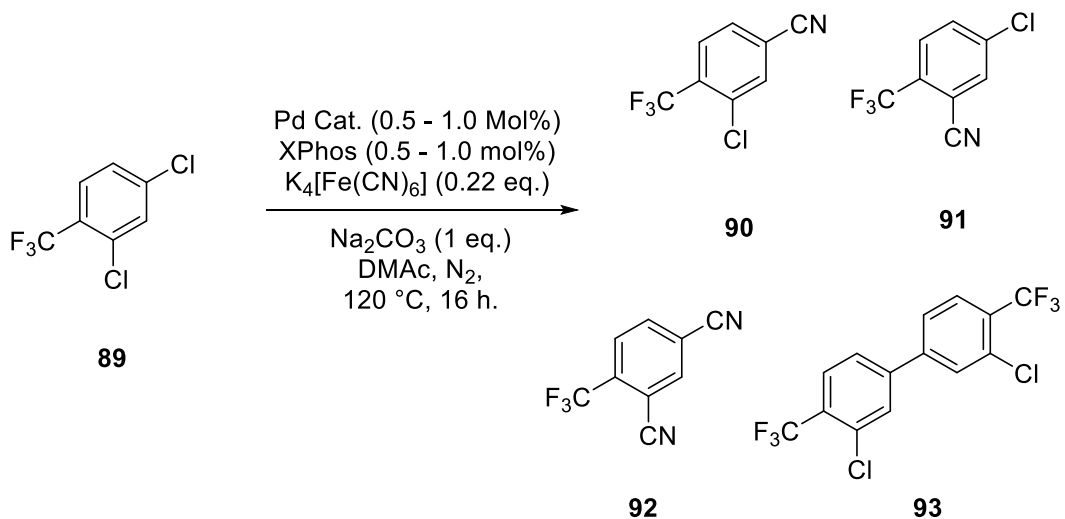
Table 11 Attempted optimisation for arylycyanation of 89



Entry	Catalyst	Cat. loading / mol%	Temp. / °C	Time / h.	Conversion <sup>a</sup> / %			
					90/91	92	93	Other
1	<b>52</b>	0.5	140	4	0.6	-	-	-
2	<b>52</b>	1	140	4	2.9	-	-	-
3	<b>52</b>	0.5	120	16	1.1	0.3	0.4	0.2
4	<b>52</b>	1	120	16	1.8	0.7	0.4	0.3
5	<b>52</b>	0.5	140	16	2.7	1.0	0.6	0.4
6	<b>52</b>	0.5	150	16	1.4	2.3	-	-
7	<b>47</b>	0.5	150	16	3.8	0.4	0.2	2.0

<sup>a</sup> Conversions calculated by gas chromatography.

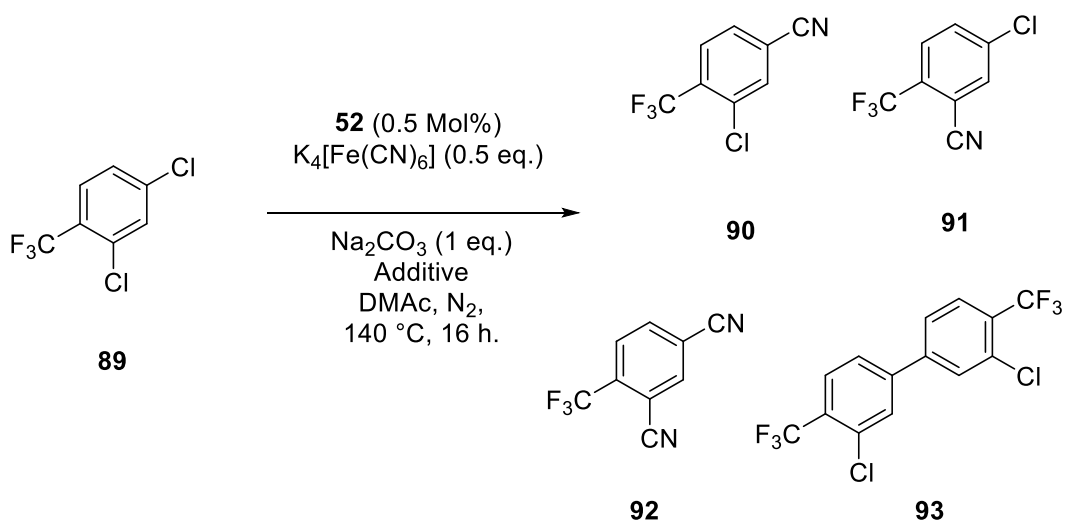
Table 12 Attempted optimisation for the arylycyanation of **89** in the presence of XPhos



Entry	Catalyst	Cat. loading / mol%	XPhos loading / mol%	Conversion <sup>a</sup> / %			
				90/91	92	93	Other
1	47	0.5	0.5	8.4	2.6	0.7	10.7
2	47	1	1	6.4	1.4	3.6	9.9
3	47	0.5	0.5	7.7	2.0	0.9	3.0
4	52	0.5	0.5	8.3	1.2	0.2	-

<sup>a</sup> Conversions calculated by gas chromatography.

Table 13 Attempted optimisation for the arylocyanation of 89 in the presence of additives.



Entry	Additives	Conversion <sup>a</sup> / %			
		90/91	92	93	Other
1	-	4.1	-	2.9	-
2	$AlCl_3$ (1 eq.)	-	-	-	-
3	$AlCl_3$ (0.1 eq.)	4.4	-	3.2	-
4	$B(Ph-F_5)_3$ (1 eq.)	-	-	-	8.1
5	$B(Ph-F_5)_3$ (0.1 eq.)	-	-	0.7	7.9
6	Zn dust (3 mol%)	-	-	1.6	-
7	Zn dust (3 mol%), $Zn(OAc)_2$ (3 mol%)	-	-	-	-
8	PMHS (10 wt.%)	-	-	-	-

<sup>a</sup> Conversions calculated by gas chromatography.

## Appendix 3: X-Ray Diffraction Data

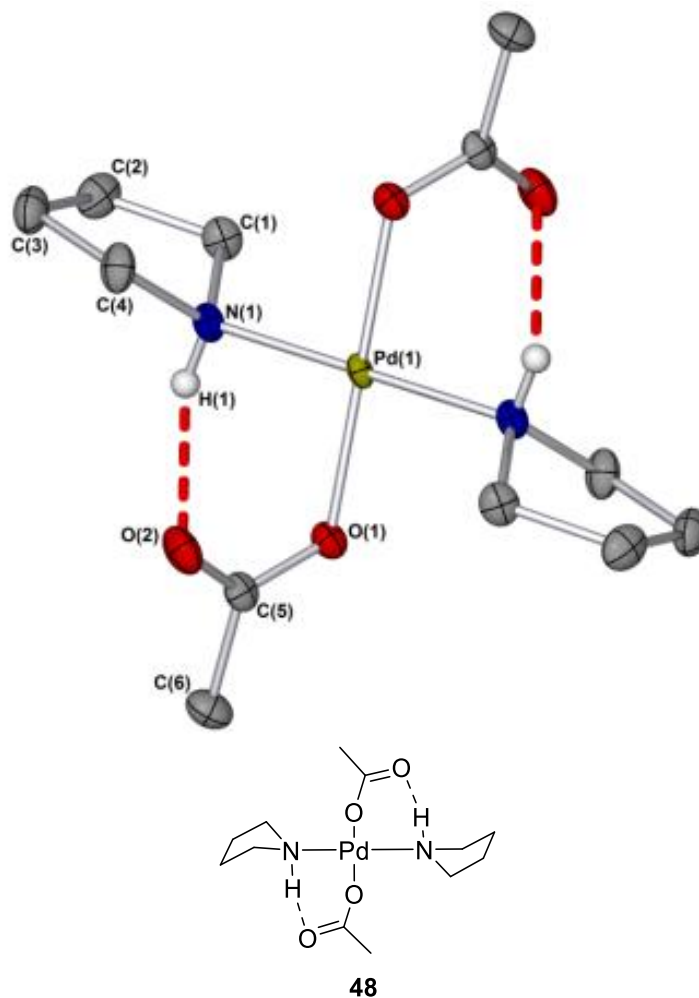
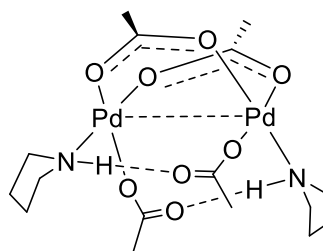
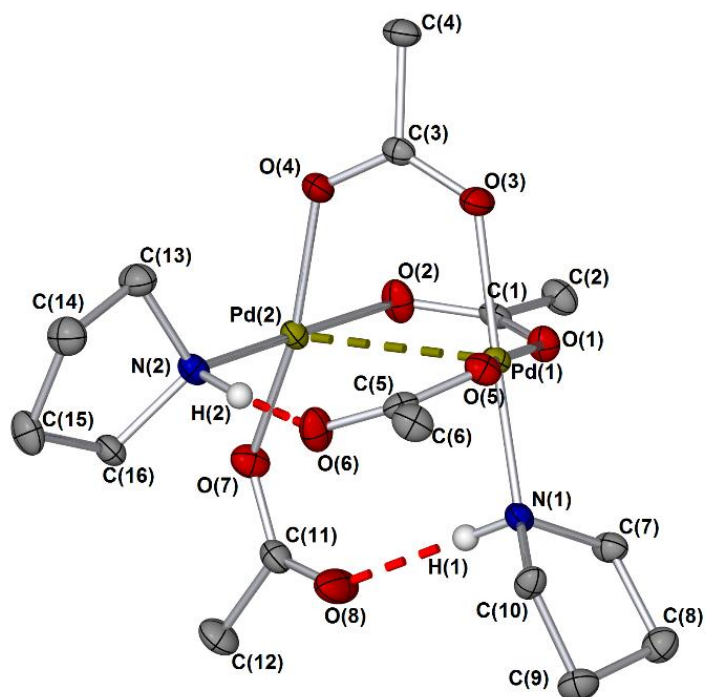
*Crystallographic data for compound 48*

Figure 119 Structure of 48, determined by X-ray diffraction; arbitrary numbering used. Selected hydrogen atoms removed for clarity. Thermal ellipsoids shown with a probability of 50%; numbers in parentheses are standard deviations from the measured value, denoting the error in the measurements. A molecule of water has been removed from the unit shell for clarity. Selected bond lengths (Å): N(1)-Pd(1): 2.043(3), O(1)-Pd(1): 2.015(2), C(1)-N(1): 1.484(4), C(5)-O(1): 1.282(4), C(5)-O(2): 1.243(4).

**Table 14 Crystal data and structure refinement for ijsf1464 (Compound 48)**

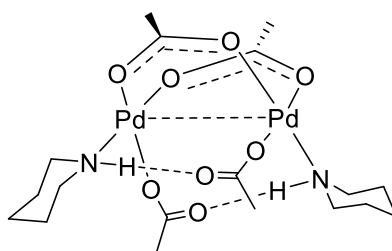
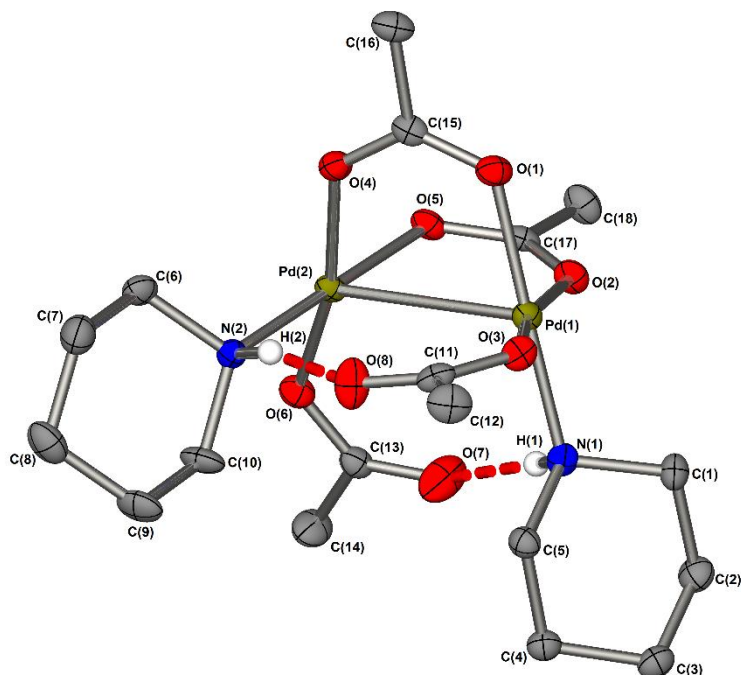
Identification code	ijsf1464
Empirical formula	C <sub>12</sub> H <sub>28</sub> N <sub>2</sub> O <sub>8</sub> Pd <sub>1</sub>
Formula weight	402.76
Temperature/K	110.05(10)
Crystal system	monoclinic
Space group	C <sub>12</sub> /C1
a/Å	17.1405(6)
b/Å	6.10222(17)
c/Å	16.0694(5)
α/°	90.00
β/°	90.140(3)
γ/°	90.00
Volume/Å <sup>3</sup>	1680.78(9)
Z	4
ρ <sub>calc</sub> /cm <sup>3</sup>	1.449
μ/mm <sup>-1</sup>	1.592
F(000)	832.0
Crystal size/mm <sup>3</sup>	0.1343 × 0.0963 × 0.0364
Radiation	CuKα (λ = 1.54184)
2θ range for data collection/°	5.15 to 69.30
Index ranges	-20 ≤ h ≤ 20, -7 ≤ k ≤ 7, -19 ≤ l ≤ 14
Reflections collected	4628
Independent reflections	1496 [R <sub>int</sub> = 0.0295, R <sub>sigma</sub> = 0.0286]
Data/restraints/parameters	1496/0/110
Goodness-of-fit on F <sup>2</sup>	1.086
Final R indexes [I ≥ 2σ (I)]	R <sub>1</sub> = 0.0290, wR <sub>2</sub> = 0.0728
Final R indexes [all data]	R <sub>1</sub> = 0.0335, wR <sub>2</sub> = 0.0759
Largest diff. peak/hole / e Å <sup>-3</sup>	1.645/-0.760

**Crystallographic data for compound 49****49**

**Figure 120** Structure of 49, determined by X-ray diffraction; arbitrary numbering used. Selected hydrogen atoms removed for clarity. Thermal ellipsoids shown with a probability of 50%; numbers in parentheses are standard deviations from the measured value, denoting the error in the measurements. Selected bond lengths (Å): N(1)-Pd(1):2.021(2), O(1)-Pd(1): 2.0394(17), O(3)-Pd(1): 2.0300(17), O(5)-Pd(1):1.9969(17), Pd(1)-Pd(2): 3.0377(3), H(1)-O(8):1.98(1).

Table 15 Crystal data and structure refinement for ijsf1331 (Compound 49)

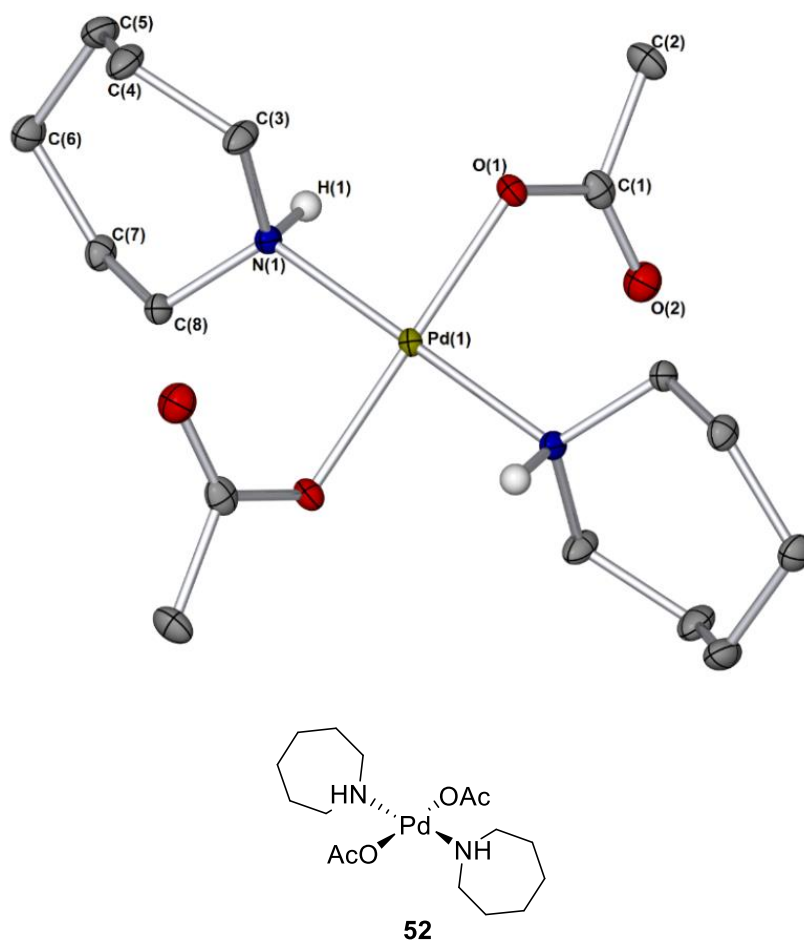
Identification code	ijsf1331
Empirical formula	C <sub>16</sub> H <sub>30</sub> N <sub>2</sub> O <sub>8</sub> Pd <sub>2</sub>
Formula weight	591.22
Temperature/K	110.05(10)
Crystal system	triclinic
Space group	P-1
a/Å	8.8183(4)
b/Å	9.5992(5)
c/Å	12.9408(6)
α/°	100.697(4)
β/°	97.441(4)
γ/°	102.503(4)
Volume/Å <sup>3</sup>	1034.29(8)
Z	2
ρ <sub>calc</sub> /mg/mm <sup>3</sup>	1.898
m/mm <sup>-1</sup>	1.783
F(000)	592.0
Crystal size/mm <sup>3</sup>	0.1401 × 0.0535 × 0.0427
Radiation	Mo Kα (λ = 0.7107)
2θ range for data collection	5.68 to 64.38°
Index ranges	-13 ≤ h ≤ 9, -13 ≤ k ≤ 13, -19 ≤ l ≤ 18
Reflections collected	10063
Independent reflections	6472 [R <sub>int</sub> = 0.0239, R <sub>sigma</sub> = 0.0416]
Data/restraints/parameters	6472/0/265
Goodness-of-fit on F <sup>2</sup>	1.058
Final R indexes [I >= 2σ (I)]	R <sub>1</sub> = 0.0301, wR <sub>2</sub> = 0.0666
Final R indexes [all data]	R <sub>1</sub> = 0.0383, wR <sub>2</sub> = 0.0717
Largest diff. peak/hole / e Å <sup>-3</sup>	1.26/-1.03

**Crystallographic data for compound 50****50**

**Figure 121 Structure of 50, determined by X-ray diffraction; arbitrary numbering used. Selected hydrogen atoms removed for clarity. Thermal ellipsoids shown with a probability of 50%; numbers in parentheses are standard deviations from the measured value, denoting the error in the measurements. Selected bond lengths (Å): N(1)-Pd(1): 2.018(4), O(1)-Pd(1): 2.034(4), O(3)-Pd(1): 1.999(4), O(2)-Pd(1): 2.033(4), Pd(1)-Pd(2): 3.0389(5), H(1)-O(7):2.00(0).**

**Table 16 Crystal data and structure refinement for ijsf1515 (Compound 50)**

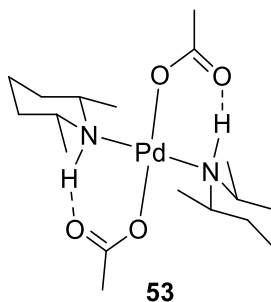
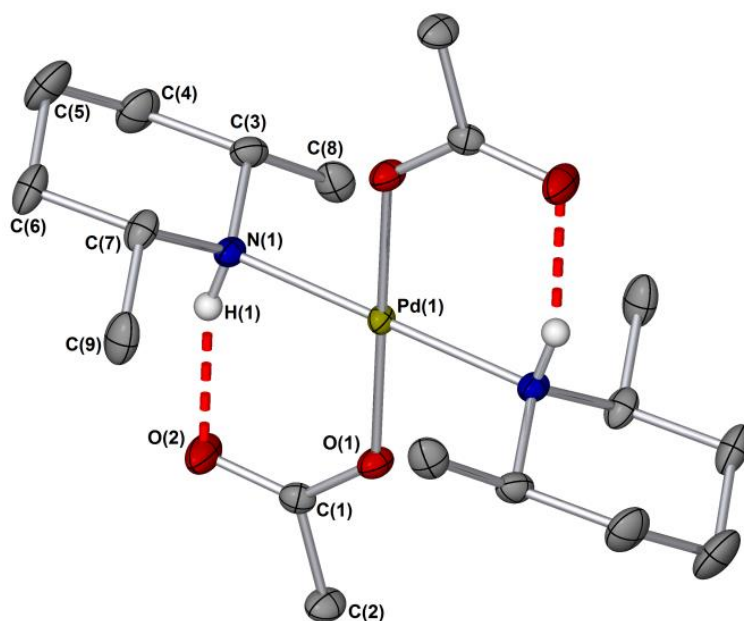
Identification code	ijsf1515
Empirical formula	C <sub>18</sub> H <sub>34</sub> N <sub>2</sub> O <sub>8</sub> Pd <sub>2</sub>
Formula weight	619.27
Temperature/K	110.05(10)
Crystal system	monoclinic
Space group	Pn
a/Å	8.8325(3)
b/Å	9.3859(3)
c/Å	14.1822(4)
α/°	90.00
β/°	94.766(3)
γ/°	90.00
Volume/Å <sup>3</sup>	1171.65(7)
Z	2
ρ <sub>calc</sub> /cm <sup>3</sup>	1.755
μ/mm <sup>-1</sup>	1.579
F(000)	624.0
Crystal size/mm <sup>3</sup>	0.1947 × 0.1642 × 0.109
Radiation	MoKα (λ = 0.71073)
2θ range for data collection/°	6.8 to 60.04
Index ranges	-11 ≤ h ≤ 12, -13 ≤ k ≤ 11, -15 ≤ l ≤ 19
Reflections collected	6465
Independent reflections	4425 [R <sub>int</sub> = 0.0272, R <sub>sigma</sub> = 0.0462]
Data/restraints/parameters	4425/2/283
Goodness-of-fit on F <sup>2</sup>	1.097
Final R indexes [I ≥ 2σ (I)]	R <sub>1</sub> = 0.0337, wR <sub>2</sub> = 0.0785
Final R indexes [all data]	R <sub>1</sub> = 0.0371, wR <sub>2</sub> = 0.0811
Largest diff. peak/hole / e Å <sup>-3</sup>	1.09/-1.93
Flack parameter	-0.03(3)

**Crystallographic data for compound 52**

**Figure 122** Structure of 52, determined by X-ray diffraction; arbitrary numbering used. Selected hydrogen atoms removed for clarity. Thermal ellipsoids shown with a probability of 50%. Selected bond lengths (Å): N(1)-Pd(1): 2.0638(14), O(1)-Pd(1): 2.0050(12), C(1)-O(1): 1.286(2), C(1)-O(2): 1.236(2).

**Table 17 Crystal data and structure refinement for ijsf1402 (Compound 52)**

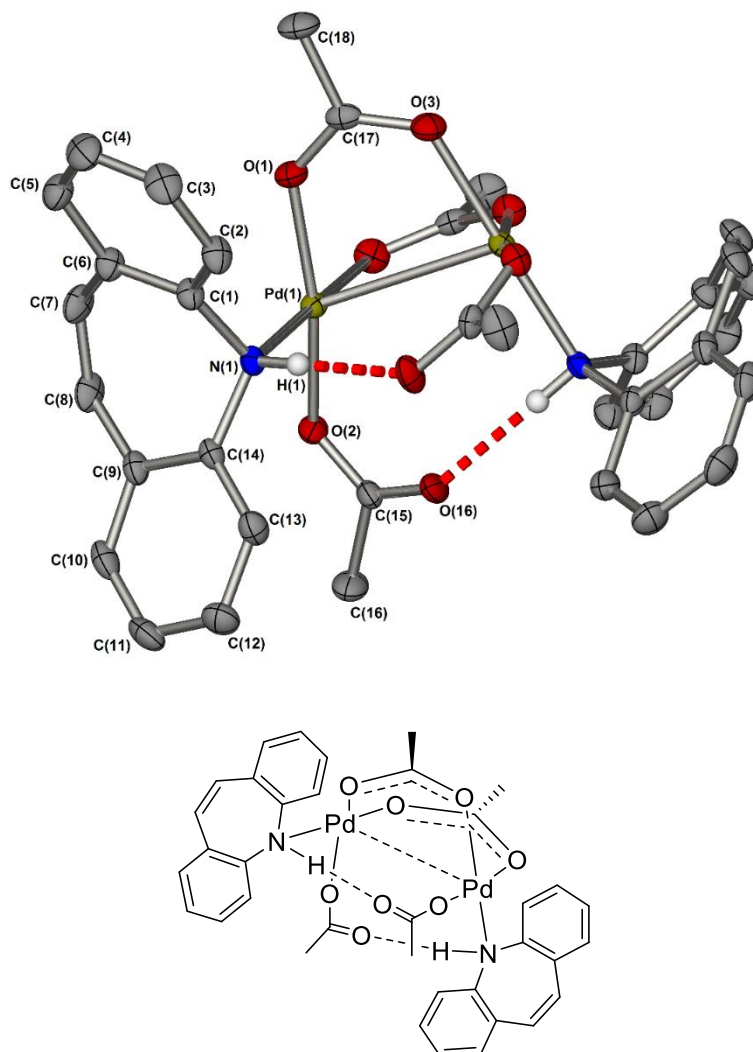
Identification code	ijsf1402
Empirical formula	C <sub>16</sub> H <sub>32</sub> N <sub>2</sub> O <sub>4</sub> Pd
Formula weight	422.83
Temperature/K	110.10(14)
Crystal system	triclinic
Space group	P-1
a/Å	6.0767(4)
b/Å	7.1046(4)
c/Å	10.4577(5)
α/°	89.399(4)
β/°	84.578(5)
γ/°	86.939(5)
Volume/Å <sup>3</sup>	448.82(4)
Z	1
ρ <sub>calc</sub> /mg/mm <sup>3</sup>	1.564
m/mm <sup>-1</sup>	1.055
F(000)	220.0
Crystal size/mm <sup>3</sup>	0.2829 × 0.1162 × 0.0986
Radiation	MoKα (λ = 0.7107)
2θ range for data collection	5.736 to 64.162°
Index ranges	-9 ≤ h ≤ 8, -10 ≤ k ≤ 10, -15 ≤ l ≤ 15
Reflections collected	8212
Independent reflections	2927 [R <sub>int</sub> = 0.0323, R <sub>sigma</sub> = 0.0372]
Data/restraints/parameters	2927/0/111
Goodness-of-fit on F <sup>2</sup>	1.081
Final R indexes [I >= 2σ (I)]	R <sub>1</sub> = 0.0251, wR <sub>2</sub> = 0.0640
Final R indexes [all data]	R <sub>1</sub> = 0.0255, wR <sub>2</sub> = 0.0645
Largest diff. peak/hole / e Å <sup>-3</sup>	1.61/-0.84

**Crystallographic data for compound 53**

**Figure 123** Structure of 53, determined by X-ray diffraction; arbitrary numbering used. Selected hydrogen atoms removed for clarity. Thermal ellipsoids shown with a probability of 50%. Selected bond lengths (Å): N(1)-Pd(1): 2.0696(18), O(1)-Pd(1): 2.0191(16), C(1)-O(1): 1.266(3), C(1)-O(2): 1.229(3), C(3)-N(1): 1.481(3).

**Table 18 Crystal data and structure refinement for ijsf1470 (Compound 53)**

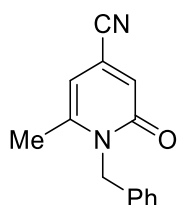
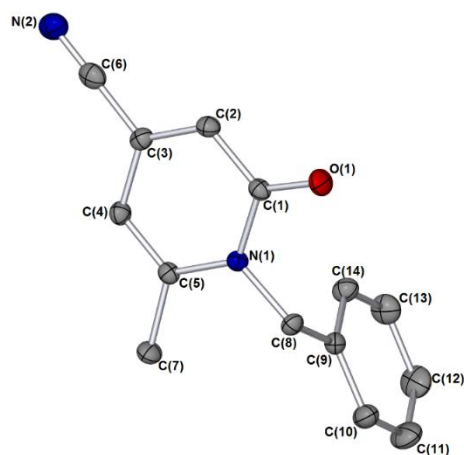
Identification code	ijsf1470
Empirical formula	C <sub>18</sub> H <sub>36</sub> N <sub>2</sub> O <sub>4</sub> Pd
Formula weight	450.89
Temperature/K	110.05(10)
Crystal system	monoclinic
Space group	P2 <sub>1</sub> /C
a/Å	7.49848(14)
b/Å	9.61025(19)
c/Å	14.3500(3)
α/°	90.00
β/°	92.4862(18)
γ/°	90.00
Volume/Å <sup>3</sup>	1033.12(3)
Z	2
ρ <sub>calc</sub> /cm <sup>3</sup>	1.449
μ/mm <sup>-1</sup>	0.921
F(000)	472.0
Crystal size/mm <sup>3</sup>	0.3156 × 0.2728 × 0.1575
Radiation	MoKα (λ = 0.71073)
2θ range for data collection/°	3.90 to 32.06
Index ranges	-11 ≤ h ≤ 11, -10 ≤ k ≤ 14, -20 ≤ l ≤ 9
Reflections collected	6182
Independent reflections	3286 [R <sub>int</sub> = 0.0237, R <sub>sigma</sub> = 0.0414]
Data/restraints/parameters	3286/0/122
Goodness-of-fit on F <sup>2</sup>	1.224
Final R indexes [I ≥ 2σ (I)]	R <sub>1</sub> = 0.0342, wR <sub>2</sub> = 0.0672
Final R indexes [all data]	R <sub>1</sub> = 0.0460, wR <sub>2</sub> = 0.0722
Largest diff. peak/hole / e Å <sup>-3</sup>	1.055/-0.574

**Crystallographic data for compound 58**

**Figure 124 Structure of 58, determined by X-ray diffraction; arbitrary numbering used. Selected hydrogen atoms and a molecule of pentane (antisolvent) have been removed for clarity. Thermal ellipsoids shown with a probability of 50%; numbers in parentheses are standard deviations from the measured value, denoting the error in the measurements. Selected bond lengths (Å): N(1)-Pd(1) 2.0757(15), Pd(1)-Pd(1) 3.0466(3), O(1)-Pd(1) 2.0147(12), O(2)-Pd(1) 1.9775(12), O(3) Pd(1) 2.0204(13), C(7)-C(8) 1.339(3), C(1)-N(1) 1.454(2).**

**Table 19 Crystal data and structure refinement for ijsf1514 (Compound 58)**

Identification code	ijsf1514
Empirical formula	C <sub>20.5</sub> H <sub>23</sub> NO <sub>4</sub> Pd
Formula weight	453.80
Temperature/K	110.05(10)
Crystal system	monoclinic
Space group	C2/c
a/Å	20.6885(4)
b/Å	8.58831(16)
c/Å	22.2594(5)
α/°	90.00
β/°	101.816(2)
γ/°	90.00
Volume/Å <sup>3</sup>	3871.21(14)
Z	8
ρ <sub>calc</sub> /cm <sup>3</sup>	1.557
μ/mm <sup>-1</sup>	0.984
F(000)	1848.0
Crystal size/mm <sup>3</sup>	0.3776 × 0.2441 × 0.1017
Radiation	MoKα (λ = 0.71073)
2θ range for data collection/°	6.6 to 60.06
Index ranges	-29 ≤ h ≤ 29, -11 ≤ k ≤ 12, -31 ≤ l ≤ 31
Reflections collected	28673
Independent reflections	5658 [R <sub>int</sub> = 0.0329, R <sub>sigma</sub> = 0.0241]
Data/restraints/parameters	5658/3/264
Goodness-of-fit on F <sup>2</sup>	1.104
Final R indexes [I ≥ 2σ (I)]	R <sub>1</sub> = 0.0246, wR <sub>2</sub> = 0.0546
Final R indexes [all data]	R <sub>1</sub> = 0.0301, wR <sub>2</sub> = 0.0583
Largest diff. peak/hole / e Å <sup>-3</sup>	0.74/-0.54

**Crystallographic data for compound 69**

**Figure 125** The structure of N-benzyl-4-cyano-6-methylpyridin-2-one (**69**) as determined by X-ray diffraction; arbitrary numbering used. Hydrogen atoms removed for clarity. Thermal ellipsoids shown with a probability of 50%; numbers in parentheses are standard deviations from the measured value, denoting the error in the measurements. Selected bond lengths (Å): C(3)-C(6):1.431(3), C(6)-N(2): 1.150(3), C(1)-O(1): 1.2379(16), C(1)-N(1):1.4052(16), C(5)-N(1): 1.3811(16), C(8)-N(1):1.4717(17).

**Table 20 Crystal data and structure refinement for ijsf1330 (Compound 69)**

Identification code	ijsf1330
Empirical formula	C <sub>13.97</sub> H <sub>12</sub> Br <sub>0.03</sub> N <sub>1.97</sub> O
Formula weight	225.87
Temperature/K	110.05(10)
Crystal system	monoclinic
Space group	P2 <sub>1</sub> /c
a/Å	11.0909(2)
b/Å	13.3680(4)
c/Å	7.95097(18)
α/°	90.00
β/°	92.498(2)
γ/°	90.00
Volume/Å <sup>3</sup>	1177.72(5)
Z	4
ρ <sub>calc</sub> /mg/mm <sup>3</sup>	1.274
m/mm <sup>-1</sup>	0.183
F(000)	475.0
Crystal size/mm <sup>3</sup>	0.1799 × 0.1320 × 0.0503
Radiation	Mo Kα (λ = 0.7107)
2θ range for data collection	5.96 to 64.1°
Index ranges	-16 ≤ h ≤ 15, -16 ≤ k ≤ 19, -11 ≤ l ≤ 10
Reflections collected	8699
Independent reflections	3781[R(int) = 0.0465]
Data/restraints/parameters	3781/6/164
Goodness-of-fit on F <sup>2</sup>	1.083
Final R indexes [I ≥ 2σ (I)]	R <sub>1</sub> = 0.0548, wR <sub>2</sub> = 0.1181
Final R indexes [all data]	R <sub>1</sub> = 0.0771, wR <sub>2</sub> = 0.1318

## Abbreviations

[M]	metal
Ac	acetyl
APCI	atmospheric pressure chemical ionisation
aq.	aqueous
ATR	attenuated total reflectance
Bn	benzyl
Bu	butyl
cat.	catalyst, catalytic
COD	1,5-cyclooctadiene
conv.	conversion
Cp	cyclopentadienyl
Cp*	pentamethylcyclopentadienyl
Cy	cyclohexyl
dba	dibenzylideneacetone
dec.	decomposition
DMAc	Dimethylacetamide
DMF	Dimethylformamide
DMP	2, 6-dimethylpiperidine
EI	electron ionisation
eq.	equivalents
ESI	electrospray ionisation
Et	Ethyl
EXAFS	extended X-ray absorption fine structure spectroscopy
IR	infrared
L	ligand
LIFDI	liquid introduced field desorption ionisation
lit.	literature
m-	meta-
M.P.	melting point
Me	methyl
Mes	mesityl
MS	Mass spectrometry
n-	normal
NMP	<i>N</i> -methylpyrrolidinone
NMR	nuclear magnetic resonance
NP	nanoparticle
Nu	nucleophile
o-	ortho-
OAc	Acetate
p-	para-
PdNPs	palladium nanoparticles
Ph	phenyl
ppm	parts per million
PVP	(poly)vinylpyrrolidinone
R <sub>f</sub>	retention factor
RT	at ambient temperature
SM	starting material
t-	tertiary
TBAB	Tetra butyl ammonium bromide
TMP	2, 2, 6, 6-tetramethylpiperidine
TEM	transmission electron microscopy

Temp.	temperature
Tf	triflic, trifluoromethanesulfonic
THF	tetrahydrofuran
TLC	thin layer chromatography
TMEDA	N,N,N',N'-tetramethylethylenediamine
UV	ultraviolet
w.r.t.	with respect to
XANES	X-ray absorption near edge spectroscopy
X-Phos	2-(dicyclohexylphosphino)-2',4',6'-triisopropylbiphenyl

## References

1. Torborg, C.; Beller, M., *Adv. Synth. Catal.* **2009**, *351*, 3027-3043.
2. (a) Ronson, T. O.; Taylor, R. J. K.; Fairlamb, I. J. S., *Tetrahedron* **2015**, *71*, 989-1009; (b) Nicolaou, K. C.; Bulger, P. G.; Sarlah, D., *Angew. Chem. Int. Ed.* **2005**, *44*, 4442-4489.
3. (a) Ronson, T. O.; Burns, M. J.; Voelkel, M. H. H.; Evans, K. J.; Lynam, J. M.; Taylor, R. J. K.; Fairlamb, I. J. S., *Chem. Eur. J.* **2015**, *21*, 18905-18909; (b) Ronson, T. O.; Voelkel, M. H. H.; Taylor, R. J. K.; Fairlamb, I. J. S., *Chem. Commun.* **2015**, *51*, 8034-8036.
4. Ronson, T. O.; Carney, J. R.; Whitwood, A. C.; Taylor, R. J. K.; Fairlamb, I. J. S., *Chem. Commun.* **2015**, *51*, 3466-3469.
5. Ronson, T. O. Ph. D. Thesis. University of York (U.K.), **2015**.
6. Bedford, R. B.; Cazin, C. S. J.; Hazelwood, S. L., *Angew. Chem. Int. Ed.* **2002**, *41*, 4120-4122.
7. de Vries, A. H. M.; Mulders, J. M. C. A.; Mommers, J. H. M.; Henderickx, H. J. W.; de Vries, J. G., *Org. Lett.* **2003**, *5*, 3285-3288.
8. de Vries, J. G., *Dalton Trans.* **2006**, 421-429.
9. Davis, J. J.; Coleman, K. S.; Busuttill, K. L.; Bagshaw, C. B., *J. Am. Chem. Soc.* **2005**, *127*, 13082-13083.
10. Ellis, P. J.; Fairlamb, I. J.; Hackett, S. F.; Wilson, K.; Lee, A. F., *Angew. Chem. Int. Ed.* **2010**, *49*, 1820-4.
11. Le Bars, J.; Specht, U.; Bradley, J. S.; Blackmond, D. G., *Langmuir* **1999**, *15*, 7621-7625.
12. (a) Tang, D.-T. D.; Collins, K. D.; Glorius, F., *J. Am. Chem. Soc.* **2013**, *135*, 7450-7453; (b) Cusati, G.; Djakovitch, L., *Tetrahedron Lett.* **2008**, *49*, 2499-2502.
13. Bellina, F.; Cauteruccio, S.; Rossi, R., *Eur. J. Org. Chem.* **2006**, *2006*, 1379-1382.
14. Lane, B. S.; Brown, M. A.; Sames, D., *J. Am. Chem. Soc.* **2005**, *127*, 8050-8057.
15. Amatore, C.; Carre, E.; Jutand, A.; M'Barki, M. A.; Meyer, G., *Organometallics* **1995**, *14*, 5605-5614.
16. (a) Jeffery, T., *Tetrahedron Lett.* **1985**, *26*, 2667-2670; (b) Beletskaya, I. P.; Cheprakov, A. V., *Chem. Rev.* **2000**, *100*, 3009-3066.
17. T. Reetz, M.; Winter, M.; Tesche, B., *Chem. Commun.* **1997**, 147-148.
18. Verbeek, S.; Meyers, C.; Franck, P.; Jutand, A.; Maes, B. U. W., *Chem. Eur. J.* **2010**, *16*, 12831-12837.
19. (a) Hyotanishi, M.; Isomura, Y.; Yamamoto, H.; Kawasaki, H.; Obora, Y., *Chem. Commun.* **2011**, *47*, 5750-5752; (b) Yano, H.; Nakajima, Y.; Obora, Y., *J. Organomet. Chem.* **2013**, *745-746*, 258-261.
20. Baumann, C. G.; De Ornellas, S.; Reeds, J. P.; Storr, T. E.; Williams, T. J.; Fairlamb, I. J. S., *Tetrahedron* **2014**, *70*, 6174-6187.
21. Fairlamb, I. J. S.; Kapdi, A. R.; Lee, A. F.; Sanchez, G.; Lopez, G.; Serrano, J. L.; Garcia, L.; Perez, J.; Perez, E., *Dalton Trans.* **2004**, 3970-3981.
22. (a) Sugimoto, K.; Kuroda-Sowa, T.; Yan, S.-G.; Maekawa, M.; Munakata, M., *Acta Crystallogr., Sect. C: Cryst. Struct. Commun.* **2000**, *56*, 414-415; (b) Robeyns, K.; Willocq,

- C.; Tinant, B.; Devillers, M.; Hermans, S., *Acta Crystallogr., Sect. E: Struct. Rep. Online* **2016**, *72*, 120-123.
23. Kannan, S.; James, A. J.; Sharp, P. R., *J. Am. Chem. Soc.* **1998**, *120*, 215-216.
24. (a) Son, S. U.; Jang, Y.; Yoon, K. Y.; Kang, E.; Hyeon, T., *Nano Lett.* **2004**, *4*, 1147-1151; (b) Kim, S.-W.; Park, J.; Jang, Y.; Chung, Y.; Hwang, S.; Hyeon, T.; Kim, Y. W., *Nano Lett.* **2003**, *3*, 1289-1291.
25. Wang, Z., Lindlar Hydrogenation. In *Comprehensive Organic Name Reactions and Reagents*, John Wiley & Sons, Inc.: 2010.
26. Philippot, K.; Serp, P., Concepts in Nanocatalysis. In *Nanomaterials in Catalysis*, Wiley-VCH Verlag GmbH & Co. KGaA: 2013; pp 1-54.
27. Thomas, S. J. M., *ChemCatChem* **2010**, *2*, 127-132.
28. Laskar, M.; Skrabalak, S. E., *ACS Catal.* **2014**, *4*, 1120-1128.
29. Medlin, J. W.; Allendorf, M. D., *J. Phys. Chem. B* **2002**, *107*, 217-223.
30. Whitesides, G. M.; Hackett, M.; Brainard, R. L.; Lavalleye, J. P. P. M.; Sowinski, A. F.; Izumi, A. N.; Moore, S. S.; Brown, D. W.; Staudt, E. M., *Organometallics* **1985**, *4*, 1819-1830.
31. Widegren, J. A.; Finke, R. G., *J. Mol. Catal. A: Chem.* **2003**, *198*, 317-341.
32. Crabtree, R. H., *Chem. Rev.* **2012**, *112*, 1536-1554.
33. Watzky, M. A.; Finke, R. G., *J. Am. Chem. Soc.* **1997**, *119*, 10382-10400.
34. (a) Gaikwad, A. V.; Rothenberg, G., *Phys. Chem. Chem. Phys.* **2006**, *8*, 3669-3675; (b) Özkar, S.; Finke, R. G., *Langmuir* **2016**, *32*, 3699-3716; (c) Weddle, K. S.; Aiken, J. D.; Finke, R. G., *J. Am. Chem. Soc.* **1998**, *120*, 5653-5666; (d) Widegren, J. A.; Bennett, M. A.; Finke, R. G., *J. Am. Chem. Soc.* **2003**, *125*, 10301-10310; (e) Widegren, J. A.; Aiken, J. D.; Özkar, S.; Finke, R. G., *Chem. Mater.* **2001**, *13*, 312-324.
35. Mower, M. P.; Blackmond, D. G., *J. Am. Chem. Soc.* **2015**, *137*, 2386-2391.
36. Rosner, T.; Pfaltz, A.; Blackmond, D. G., *J. Am. Chem. Soc.* **2001**, *123*, 4621-4622.
37. Koelsch, C. F.; Whitney, A. G., *J. Org. Chem.* **1941**, *06*, 795-803.
38. (a) Rosner, T.; Le Bars, J.; Pfaltz, A.; Blackmond, D. G., *J. Am. Chem. Soc.* **2001**, *123*, 1848-1855; (b) Tan, Y.; Barrios-Landeros, F.; Hartwig, J. F., *J. Am. Chem. Soc.* **2012**, *134*, 3683-3686.
39. (a) Anton, D. R.; Crabtree, R. H., *Organometallics* **1983**, *2*, 855-859; (b) Lewis, L. N.; Lewis, N., *J. Am. Chem. Soc.* **1986**, *108*, 7228-7231; (c) Crabtree, R. H.; Mellea, M. F.; Mihelcic, J. M.; Quirk, J. M., *J. Am. Chem. Soc.* **1982**, *104*, 107-113.
40. Fang, P.-P.; Jutand, A.; Tian, Z.-Q.; Amatore, C., *Angew. Chem. Int. Ed.* **2011**, *50*, 12184-12188.
41. Lin, Y.; Finke, R. G., *Inorg. Chem.* **1994**, *33*, 4891-4910.
42. Vargaftik, M. N.; Zagorodnikov, V. P.; Stolarov, I. P.; Moiseev, I. I.; Kochubey, D. I.; Likholobov, V. A.; Chuvilin, A. L.; Zamaraev, K. I., *J. Mol. Catal.* **1989**, *53*, 315-348.
43. Gerber, R.; Oberholzer, M.; Frech, C. M., *Chem. Eur. J.* **2012**, *18*, 2978-2986.
44. (a) Jones, R. A.; Real, F. M.; Wilkinson, G.; Galas, A. M. R.; Hursthouse, M. B., *Journal of the Chemical Society, Dalton Transactions* **1981**, 126-131; (b) Stein, J.; Lewis, L. N.; Gao, Y.; Scott, R. A., *J. Am. Chem. Soc.* **1999**, *121*, 3693-3703.
45. Strohmeier, W.; Müller, F.-J., *Chem. Ber.* **1967**, *100*, 2812-2821.

46. Tolman, C. A., *Chem. Rev.* **1977**, *77*, 313-348.
47. Marcone, J. E.; Moloy, K. G., *J. Am. Chem. Soc.* **1998**, *120*, 8527-8528.
48. Jakupec, M. A.; Reisner, E.; Eichinger, A.; Pongratz, M.; Arion, V. B.; Galanski, M.; Hartinger, C. G.; Keppler, B. K., *J. Med. Chem.* **2005**, *48*, 2831-2837.
49. Amatore, C.; Jutand, A.; Khalil, F.; M'Barki, M. A.; Mottier, L., *Organometallics* **1993**, *12*, 3168-3178.
50. Sehnaal, P.; Taghzouti, H.; Fairlamb, I. J. S.; Jutand, A.; Lee, A. F.; Whitwood, A. C., *Organometallics* **2009**, *28*, 824-829.
51. Fairlamb, I. J. S.; Kapdi, A. R.; Lee, A. F., *Org. Lett.* **2004**, *6*, 4435-4438.
52. Fairlamb, I. J. S.; Lee, A. F., *Organometallics* **2007**, *26*, 4087-4089.
53. Fairlamb, I. J. S.; Kapdi, A. R.; Lee, A. F.; McGlacken, G. P.; Weissburger, F.; de Vries, A. H. M.; Schmieder-van de Vondervoort, L., *Chem. Eur. J.* **2006**, *12*, 8750-8761.
54. Firmansjah, L.; Fu, G. C., *J. Am. Chem. Soc.* **2007**, *129*, 11340-11341.
55. Nasielski, J.; Hadei, N.; Achonduh, G.; Kantchev, E. A. B.; O'Brien, C. J.; Lough, A.; Organ, M. G., *Chem. Eur. J.* **2010**, *16*, 10844-10853.
56. Walker, S. D.; Barder, T. E.; Martinelli, J. R.; Buchwald, S. L., *Angew. Chem. Int. Ed.* **2004**, *43*, 1871-1876.
57. (a) Biscoe, M. R.; Barder, T. E.; Buchwald, S. L., *Angew. Chem. Int. Ed.* **2007**, *46*, 7232-7235; (b) Biscoe, M. R.; Fors, B. P.; Buchwald, S. L., *J. Am. Chem. Soc.* **2008**, *130*, 6686-6687.
58. (a) Albert, J.; D'Andrea, L.; Granell, J.; Zafrilla, J.; Font-Bardia, M.; Solans, X., *J. Organomet. Chem.* **2007**, *692*, 4895-4902; (b) Albert, J.; Granell, J.; Zafrilla, J.; Font-Bardia, M.; Solans, X., *J. Organomet. Chem.* **2005**, *690*, 422-429.
59. Tselikhovsky, D.; Buchwald, S. L., *J. Am. Chem. Soc.* **2010**, *132*, 14048-14051.
60. Kinzel, T.; Zhang, Y.; Buchwald, S. L., *J. Am. Chem. Soc.* **2010**, *132*, 14073-14075.
61. Bruno, N. C.; Tudge, M. T.; Buchwald, S. L., *Chem. Sci.* **2013**, *4*, 916-920.
62. Amatore, C.; Jutand, A.; M'Barki, M. A., *Organometallics* **1992**, *11*, 3009-3013.
63. Carole, W. A.; Colacot, T. J., *Chem. Eur. J.* **2016**, *22*, 7686-7695.
64. Bajwa, S. E.; Storr, T. E.; Hatcher, L. E.; Williams, T. J.; Baumann, C. G.; Whitwood, A. C.; Allan, D. R.; Teat, S. J.; Raithby, P. R.; Fairlamb, I. J. S., *Chem. Sci.* **2012**, *3*, 1656-1661.
65. Fairlamb, I. J. S., *Angew. Chem. Int. Ed.* **2015**, *54*, 10415-10427.
66. Anderson, C. E.; Kirsch, S. F.; Overman, L. E.; Richards, C. J.; Watson, M. P., *Org. Synth.* **2007**, *84*, 148.
67. Carole, W. A.; Bradley, J.; Sarwar, M.; Colacot, T. J., *Org. Lett.* **2015**, *17*, 5472-5475.
68. Bedford, R. B.; Bowen, J. G.; Davidson, R. B.; Haddow, M. F.; Seymour-Julen, A. E.; Sparkes, H. A.; Webster, R. L., *Angew. Chem. Int. Ed.* **2015**, *54*, 6591-6594.
69. Tao, B.; Boykin, D. W., *J. Org. Chem.* **2004**, *69*, 4330-4335.
70. (a) Adrio, L. A.; Nguyen, B. N.; Guilera, G.; Livingston, A. G.; Hii, K. K., *Catal. Sci. Tech.* **2012**, *2*, 316-323; (b) Liu, L.; Dong, Y.; Pang, B.; Ma, J., *J. Org. Chem.* **2014**, *79*, 7193-7198.

71. Chen, J.-S.; Vasiliev, A. N.; Panarello, A. P.; Khinast, J. G., *Appl. Catal., A* **2007**, *325*, 76-86.
72. Böck, K.; Feil, J. E.; Karaghiosoff, K.; Koszinowski, K., *Chem. Eur. J.* **2015**, *21*, 5548-5560.
73. Ford, M. RSC BMCS – H&SG Symposium: Synthesis in the Agrisciences, London, UK, 14 April 2016.
74. Kapdi, A. R.; Dhangar, G.; Serrano, J. L.; Perez, J.; Garcia, L.; Fairlamb, I. J. S., *Chem. Commun.* **2014**, *50*, 9859-9861.
75. Wei, C. S.; Davies, G. H. M.; Soltani, O.; Albrecht, J.; Gao, Q.; Pathirana, C.; Hsiao, Y.; Tummala, S.; Eastgate, M. D., *Angew. Chem. Int. Ed.* **2013**, *52*, 5822-5826.
76. Haines, B. E.; Berry, J. F.; Yu, J.-Q.; Musaev, D. G., *ACS Catal.* **2016**, *6*, 829-839.
77. Finney, E. E.; Finke, R. G., *J. Colloid Interface Sci.* **2008**, *317*, 351-374.
78. Wang, F.; Li, C.; Sun, L.-D.; Wu, H.; Ming, T.; Wang, J.; Yu, J. C.; Yan, C.-H., *J. Am. Chem. Soc.* **2011**, *133*, 1106-1111.
79. Bolliger, J. L.; Frech, C. M., *Chem. Eur. J.* **2010**, *16*, 4075-4081.
80. Besson, C.; Finney, E. E.; Finke, R. G., *J. Am. Chem. Soc.* **2005**, *127*, 8179-8184.
81. Agrawal, D.; Schröder, D.; Frech, C. M., *Organometallics* **2011**, *30*, 3579-3587.
82. (a) Bolliger, J. L.; Frech, C. M., *Chem. Eur. J.* **2010**, *16*, 11072-11081; (b) Oberholzer, M.; Gerber, R.; Frech, C. M., *Adv. Synth. Catal.* **2012**, *354*, 627-641.
83. Cao, M.; Lin, J.; Yang, H.; Cao, R., *Chem. Commun.* **2010**, *46*, 5088-5090.
84. Cao, M.; Wei, Y.; Gao, S.; Cao, R., *Catal. Sci. Tech.* **2012**, *2*, 156-163.
85. (a) Narayanan, R.; El-Sayed, M. A., *J. Am. Chem. Soc.* **2003**, *125*, 8340-8347; (b) Chen, Z.; Cui, Z.-M.; Niu, F.; Jiang, L.; Song, W.-G., *Chem. Commun.* **2010**, *46*, 6524-6526; (c) Cano, M.; Benito, A. M.; Maser, W. K.; Urriolabeitia, E. P., *New J. Chem.* **2013**, *37*, 1968-1972; (d) Siamaki, A. R.; Khder, A. E. R. S.; Abdelsayed, V.; El-Shall, M. S.; Gupton, B. F., *J. Catal.* **2011**, *279*, 1-11.
86. (a) Rosenmund, K. W.; Struck, E., *Berichte der deutschen chemischen Gesellschaft (A and B Series)* **1919**, *52*, 1749-1756; (b) Sandmeyer, T., *Berichte der deutschen chemischen Gesellschaft* **1885**, *18*, 1492-1496; (c) Sandmeyer, T., *Berichte der deutschen chemischen Gesellschaft* **1885**, *18*, 1496-1500.
87. Yeung, K.-S.; Farkas, M. E.; Kadow, J. F.; Meanwell, N. A., *Tetrahedron Lett.* **2005**, *46*, 3429-3432.
88. (a) Alterman, M.; Hallberg, A., *J. Org. Chem.* **2000**, *65*, 7984-7989; (b) Srihari, P.; Dutta, P.; Rao, R. S.; Yadav, J. S.; Chandrasekhar, S.; Thombare, P.; Mohapatra, J.; Chatterjee, A.; Jain, M. R., *Bioorg. Med. Chem. Lett.* **2009**, *19*, 5569-5572; (c) Moreau, J. J. E.; Pichon, B. P.; Bied, C.; Man, M. W. C., *J. Mater. Chem.* **2005**, *15*, 3929-3936.
89. Young, A. M.; Audus, K. L.; Proudfoot, J.; Yazdanian, M., *J. Pharm. Sci.* **2006**, *95*, 717-725.
90. Semenov, B. B.; Smushkevich, Y. I., *Russ. Chem. Bull.* **2002**, *51*, 357-358.
91. Takagi, K.; Okamoto, T.; Sakakibara, Y.; Oka, S., *Chem. Lett.* **1973**, *2*, 471-474.
92. (a) Jaegli, S.; Vors, J.-P.; Neuville, L.; Zhu, J., *Synlett* **2009**, *2009*, 2997-2999; (b) Pinto, A.; Jia, Y.; Neuville, L.; Zhu, J., *Chem. Eur. J.* **2007**, *13*, 961-967.
93. Dobbs, K. D.; Marshall, W. J.; Grushin, V. V., *J. Am. Chem. Soc.* **2007**, *129*, 30-31.

94. (a) Erhardt, S.; Grushin, V. V.; Kilpatrick, A. H.; Macgregor, S. A.; Marshall, W. J.; Roe, D. C., *J. Am. Chem. Soc.* **2008**, *130*, 4828-4845; (b) Anbarasan, P.; Schareina, T.; Beller, M., *Chem. Soc. Rev.* **2011**, *40*, 5049-5067.
95. Erker, T.; Nemeč, S., *Synthesis* **2004**, *2004*, 23-25.
96. Sundermeier, M.; Zapf, A.; Mutyala, S.; Baumann, W.; Sans, J.; Weiss, S.; Beller, M., *Chem. Eur. J.* **2003**, *9*, 1828-1836.
97. Yang, C.; Williams, J. M., *Org. Lett.* **2004**, *6*, 2837-2840.
98. Nair, V.; Purdy, D. F.; Sells, T. B., *J. Chem. Soc., Chem. Commun.* **1989**, 878-879.
99. Gunderson, L.-L., *Acta. Chem. Scand.* **1996**, 58.
100. Chidambaram, R., *Tetrahedron Lett.* **2004**, *45*, 1441-1444.
101. Shevlin, M., *Tetrahedron Lett.* **2010**, *51*, 4833-4836.
102. (a) Schareina, T.; Zapf, A.; Beller, M., *J. Organomet. Chem.* **2004**, *689*, 4576-4583; (b) Weissman, S. A.; Zewge, D.; Chen, C., *J. Org. Chem.* **2005**, *70*, 1508-1510.
103. Zhu, Y.-Z.; Cai, C., *Eur. J. Org. Chem.* **2007**, *2007*, 2401-2404.
104. (a) Chen, G.; Weng, J.; Zheng, Z.; Zhu, X.; Cai, Y.; Cai, J.; Wan, Y., *Eur. J. Org. Chem.* **2008**, *2008*, 3524-3528; (b) Zhu, Y. Z.; Cai, C., *Synth. Commun.* **2007**, *37*, 3359-3366.
105. Chattopadhyay, K.; Dey, R.; Ranu, B. C., *Tetrahedron Lett.* **2009**, *50*, 3164-3167.
106. Mondal, B.; Acharyya, K.; Howlader, P.; Mukherjee, P. S., *J. Am. Chem. Soc.* **2016**, *138*, 1709-1716.
107. Senecal, T. D.; Shu, W.; Buchwald, S. L., *Angew. Chem. Int. Ed.* **2013**, *52*, 10035-10039.
108. Lee, H. G.; Milner, P. J.; Placzek, M. S.; Buchwald, S. L.; Hooker, J. M., *J. Am. Chem. Soc.* **2015**, *137*, 648-651.
109. Klinkenberg, J. L.; Hartwig, J. F., *J. Am. Chem. Soc.* **2012**, *134*, 5758-5761.
110. Storr, T. E.; Baumann, C. G.; Thatcher, R. J.; De Ornellas, S.; Whitwood, A. C.; Fairlamb, I. J. S., *J. Org. Chem.* **2009**, *74*, 5810-5821.
111. Milani, J.; Pridmore, N. E.; Whitwood, A. C.; Fairlamb, I. J. S.; Perutz, R. N., *Organometallics* **2015**, *34*, 4376-4386.
112. A. Shvekhgeimer, M.-G., *Russ. Chem. Rev.* **1998**, *67*, 1031-1060.
113. Fulmer, G. R.; Miller, A. J. M.; Sherden, N. H.; Gottlieb, H. E.; Nudelman, A.; Stoltz, B. M.; Bercaw, J. E.; Goldberg, K. I., *Organometallics* **2010**, *29*, 2176-2179.
114. Haynes, W. M.; Lide, D. R., *CRC handbook of chemistry and physics : a ready-reference book of chemical and physical data*. CRC Press: Boca Raton, Fla., 2011.
115. McNally, A.; Haffemayer, B.; Collins, B. S. L.; Gaunt, M. J., *Nature* **2014**, *510*, 129-133.
116. Bercaw, J. E.; Durrell, A. C.; Gray, H. B.; Green, J. C.; Hazari, N.; Labinger, J. A.; Winkler, J. R., *Inorg. Chem.* **2010**, *49*, 1801-1810.
117. McGlacken, G. P.; Fairlamb, I. J. S., *Nat. Prod. Rep.* **2005**, *22*, 369-385.
118. (a) Au, T. Y.; Cheung, H. T.; Sternhell, S., *Journal of the Chemical Society, Perkin Transactions 1* **1973**, 13-16; (b) Hotellier, F.; Delaveau, P.; Pousset, J.-L., *Phytochemistry* **1975**, *14*, 1407-1409; (c) Gross, H.; Goeger, D. E.; Hills, P.; Mooberry, S. L.; Ballantine, D. L.; Murray, T. F.; Valeriote, F. A.; Gerwick, W. H., *J. Nat. Prod.* **2006**, *69*, 640-644; (d) Gray, D.; Gallagher, T., *Angew. Chem. Int. Ed.* **2006**, *45*, 2419-2423; (e) de Silva, E. D.;

- Geiermann, A.-S.; Mitova, M. I.; Kuegler, P.; Blunt, J. W.; Cole, A. L. J.; Munro, M. H. G., *J. Nat. Prod.* **2009**, *72*, 477-479.
119. Salem, M. S.; Sakr, S. I.; El-Senousy, W. M.; Madkour, H. M. F., *Arch. Pharm. (Weinheim, Ger.)* **2013**, *346*, 766-773.
120. Manna, F.; Chimenti, F.; Bolasco, A.; Filippelli, A.; Palla, A.; Filippelli, W.; Lampa, E.; Mercantini, R., *Eur. J. Med. Chem.* **1992**, *27*, 627-632.
121. Fleming, F. F.; Yao, L.; Ravikumar, P. C.; Funk, L.; Shook, B. C., *J. Med. Chem.* **2010**, *53*, 7902-7917.
122. (a) Moulton, B. E.; Dong, H.; O'Brien, C. T.; Duckett, S. B.; Lin, Z.; Fairlamb, I. J. S., *Org. Biomol. Chem.* **2008**, *6*, 4523-4532; (b) Fairlamb, I. J. S.; Lee, A. F.; Loe-Mie, F. E. M.; Niemelä, E. H.; O'Brien, C. T.; Whitwood, A. C., *Tetrahedron* **2005**, *61*, 9827-9838.
123. (a) Nolan, M.-T.; Bray, J. T. W.; Eccles, K.; Cheung, M. S.; Lin, Z.; Lawrence, S. E.; Whitwood, A. C.; Fairlamb, I. J. S.; McGlacken, G. P., *Tetrahedron* **2014**, *70*, 7120-7127; (b) Burns, M. J.; Thatcher, R. J.; Taylor, R. J. K.; Fairlamb, I. J. S., *Dalton Trans.* **2010**, *39*, 10391-10400.
124. (a) Edstrom, E. D.; Yu, T., *Tetrahedron Lett.* **1994**, *35*, 6985-6988; (b) Coffman, K.; Brodney, M.; Cook, J.; Lanyon, L.; Pandit, J.; Sakya, S.; Schachter, J.; Tseng-Lovering, E.; Wessel, M., *Bioorg. Med. Chem. Lett.* **2011**, *21*, 1429-1433.
125. Engel, N.; Bokarev, S. I.; Suljoti, E.; Garcia-Diez, R.; Lange, K. M.; Atak, K.; Golnak, R.; Kothe, A.; Dantz, M.; Kühn, O.; Aziz, E. F., *J. Phys. Chem. B* **2014**, *118*, 1555-1563.
126. (a) Li, Z.; Liu, C.; Zhang, Y.; Li, R.; Ma, B.; Yang, J., *Synlett* **2012**, *23*, 2567-2571; (b) Li, Z.; Li, R.; Zheng, H.; Wen, F.; Li, H.; Yin, J.; Yang, J., *J. Braz. Chem. Soc.* **2013**, *24*, 1739-1743.
127. Lyukmanov, N. F.; Kovshev, E. I., *Chem. Heterocycl. Compd.* **1982**, 804.
128. Hultgren, S. J.; Pinkner, J. S.; Almqvist, F.; Pemberton, N.; Aberg, V.; Larsson, A., Amino methylated 2-pyridinones. Google Patents: 2008.
129. Crawforth, C. M.; Fairlamb, I. J. S.; Kapdi, A. R.; Serrano, J. L.; Taylor, R. J. K.; Sanchez, G., *Adv. Synth. Catal.* **2006**, *348*, 405-412.
130. Ongoing work within the Fairlamb group has found that under certain conditions of Stille reactions, trans-CatCat has been found to form uniform Pd NPs in DMF.
131. Kato, Y.; Okada, S.; Tomimoto, K.; Mase, T., *Tetrahedron Lett.* **2001**, *42*, 4849-4851.
132. Jung, M. E.; Allen, D. A., *Org. Lett.* **2009**, *11*, 757-760.
133. Marrison, L. R. PhD Thesis. Manchester Metropolitan University, UK, **1998**.
134. Peter Herold; S. Stutz; R. Mah; V. Tschinke; Stojanovic, A.; N. Jotterand; Quirnbach, M.; Behnke, D.; Marti, C. 5-Amino-4-hydroxy-7-(1H-indol)-8-methylnonamide derivatives as renin inhibitors for the treatment of hypertension. 2005.
135. Sun, J.; Li, H.; Wang, C.; Yuan, D.; Stubbs, L. P.; He, C., *Macromol. Chem. Phys.* **2016**, *217*, 1065-1073.
136. Teo, B. K.; Sloane, N. J. A., *Inorg. Chem.* **1985**, *24*, 4545-4558.
137. Woodward, R. B.; Cava, M. P.; Ollis, W. D.; Hunger, A.; Daeniker, H. U.; Schenker, K., *J. Am. Chem. Soc.* **1954**, *76*, 4749-4751.
138. (a) Åberg, J. B.; Warner, M. C.; Bäckvall, J.-E., *J. Am. Chem. Soc.* **2009**, *131*, 13622-13624; (b) Capriati, V.; Florio, S.; Luisi, R.; Perna, F. M.; Spina, A., *J. Org. Chem.* **2008**, *73*,

- 9552-9564; (c) Shi, W.; Luo, Y.; Luo, X.; Chao, L.; Zhang, H.; Wang, J.; Lei, A., *J. Am. Chem. Soc.* **2008**, *130*, 14713-14720; (d) Hansen, J. r.; Li, B.; Dikarev, E.; Autschbach, J.; Davies, H. M. L., *J. Org. Chem.* **2009**, *74*, 6564-6571.
139. Atkins, P.; De Paula, J.; Walters, V., *Physical Chemistry*. Macmillan Higher Education: 2006.
140. Bayram, E.; Linehan, J. C.; Fulton, J. L.; Szymczak, N. K.; Finke, R. G., *ACS Catal.* **2015**, *5*, 3876-3886.
141. Kemmer, G.; Keller, S., *Nat. Protocols* **2010**, *5*, 267-281.
142. Köhler, K.; Heidenreich, R. G.; Krauter, J. G. E.; Pietsch, J., *Chem. Eur. J.* **2002**, *8*, 622-631.
143. Reutov, O. A.; Nesmeyanov, A. N., *Bulletin of the Academy of Sciences of the USSR, Division of chemical science* **1953**, *2*, 589-596.
144. Bumagin, N. A.; More, P. G.; Beletskaya, I. P., *J. Organomet. Chem.* **1989**, *364*, 231-234.
145. (a) Alexander, J. J.; Gray, H. B., *J. Am. Chem. Soc.* **1968**, *90*, 4260-4271; (b) Vinogradov, A. S.; Preobrajenski, A. B.; Krasnikov, S. A.; Chassé, T.; Szargan, R.; Knop-Gericke, A.; Schlögl, R.; Bressler, P., *Surf. Rev. Lett.* **2002**, *09*, 359-364; (c) Griffith, W. P., *Q. Rev. Chem. Soc.* **1962**, *16*, 188-207.
146. Meek, S. J.; Pitman, C. L.; Miller, A. J. M., *J. Chem. Educ.* **2016**, *93*, 275-286.
147. Kozuch, S.; Martin, J. M. L., *ACS Catal.* **2012**, *2*, 2787-2794.
148. (a) Cohen, S. R.; Plane, R. A., *J. Phys. Chem.* **1957**, *61*, 1096-1100; (b) Getman, F. H., *J. Phys. Chem.* **1920**, *25*, 147-159.
149. Buser, H. J.; Schwarzenbach, D.; Petter, W.; Ludi, A., *Inorg. Chem.* **1977**, *16*, 2704-2710.
150. (a) Wang, Y.; Chen, Y.; He, Q.; Xie, Y.; Yang, C., *Helv. Chim. Acta* **2013**, *96*, 296-308; (b) Fuenfschilling, P. C.; Zaugg, W.; Beutler, U.; Kaufmann, D.; Lohse, O.; Mutz, J.-P.; Onken, U.; Reber, J.-L.; Shenton, D., *Org. Process Res. Dev.* **2005**, *9*, 272-277.
151. (a) Vásquez-Céspedes, S.; Ferry, A.; Candish, L.; Glorius, F., *Angew. Chem. Int. Ed.* **2015**, *54*, 5772-5776; (b) Tang, D.-T. D.; Collins, K. D.; Ernst, J. B.; Glorius, F., *Angew. Chem. Int. Ed.* **2014**, *53*, 1809-1813.
152. Collins, K. D.; Honeker, R.; Vasquez-Céspedes, S.; Tang, D.-T. D.; Glorius, F., *Chem. Sci.* **2015**, *6*, 1816-1824.
153. Reay, A. J.; Neumann, L. K.; Fairlamb, I. J. S., *Synlett* **2016**, *27*, 1211-1216.
154. Ackermann, L.; Vicente, R.; Kapdi, A. R., *Angew. Chem. Int. Ed.* **2009**, *48*, 9792-9826.
155. (a) Beck, E. M.; Grimster, N. P.; Hatley, R.; Gaunt, M. J., *J. Am. Chem. Soc.* **2006**, *128*, 2528-2529; (b) Grimster, N. P.; Gauntlett, C.; Godfrey, C. R. A.; Gaunt, M. J., *Angew. Chem. Int. Ed.* **2005**, *44*, 3125-3129.
156. Stuart, D. R.; Villemure, E.; Fagnou, K., *J. Am. Chem. Soc.* **2007**, *129*, 12072-12073.
157. (a) Kozitsyna, N. Y.; Nefedov, S. E.; Dolgushin, F. M.; Cherkashina, N. V.; Vargaftik, M. N.; Moiseev, I. I., *Inorg. Chim. Acta* **2006**, *359*, 2072-2086; (b) Kozitsyna, N. Y.; Nefedov, S. E.; Vargaftik, M. N.; Moiseev, I. I., *Mendeleev Commun.* **2005**, *15*, 223-224; (c) Kozitsyna, N. Y.; Nefedov, S. E.; Klyagina, A. P.; Markov, A. A.; Dobrokhotova, Z. V.; Velikodny, Y. A.; Kochubey, D. I.; Zyubina, T. S.; Gekhman, A. E.; Vargaftik, M. N.; Moiseev, I. I., *Inorg. Chim. Acta* **2011**, *370*, 382-387; (d) Kozitsyna, N. Y.; Nefedov, S. E.; Yakushev, I. A.; Dobrokhotova, Z. V.; Vargaftik, M. N.; Moiseev, I. I., *Mendeleev Commun.*

- 2007**, *17*, 261-263; (e) Nefedov, S. E.; Kozitsyna, N. Y.; Akhmadullina, N. S.; Cherkashina, N. V.; Vargaftik, M. N.; Moiseev, I. I., *Inorg. Chem. Commun.* **2011**, *14*, 554-557; (f) Tkachenko, O.; Stakheev, A.; Kustov, L.; Mashkovsky, I.; van den Berg, M.; Grünert, W.; Kozitsyna, N.; Dobrokhotova, Z.; Zhilov, V.; Nefedov, S.; Vargaftik, M.; Moiseev, I., *Catal. Lett.* **2006**, *112*, 155-161.
158. Akhmadullina, N. S.; Cherkashina, N. V.; Kozitsyna, N. Y.; Stolarov, I. P.; Perova, E. V.; Gekhman, A. E.; Nefedov, S. E.; Vargaftik, M. N.; Moiseev, I. I., *Inorg. Chim. Acta* **2009**, *362*, 1943-1951.
159. Nefedov, S. E.; Kozitsyna, N. Y.; Vargaftik, M. N.; Moiseev, I. I., *Polyhedron* **2009**, *28*, 172-180.
160. Williams, T. J.; Reay, A. J.; Whitwood, A. C.; Fairlamb, I. J. S., *Chem. Commun.* **2014**, *50*, 3052-3054.
161. Sloan, O. D.; Thornton, P., *Inorg. Chim. Acta* **1986**, *120*, 173-175.
162. Amatore, C.; El Kaïm, L.; Grimaud, L.; Jutand, A.; Meignié, A.; Romanov, G., *Eur. J. Org. Chem.* **2014**, *2014*, 4709-4713.
163. Shan, S.; Luo, J.; Yang, L.; Zhong, C.-J., *Catal. Sci. Tech.* **2014**, *4*, 3570-3588.
164. (a) Palatinus, L.; Prathapa, S. J.; van Smaalen, S., *J. Appl. Crystallogr.* **2012**, *45*, 575-580; (b) Palatinus, L.; Chapuis, G., *J. Appl. Crystallogr.* **2007**, *40*, 786-790; (c) Palatinus, L.; van der Lee, A., *J. Appl. Crystallogr.* **2008**, *41*, 975-984.
165. Sheldrick, G., *Acta Crystallographica Section A* **2008**, *64*, 112-122.
166. Lunn, G.; Sansone, E. B., *Anal. Biochem.* **1985**, *147*, 245-250.
167. Kim, J.; Choi, J.; Shin, K.; Chang, S., *J. Am. Chem. Soc.* **2012**, *134*, 2528-2531.
168. Shu, Z.; Ye, Y.; Deng, Y.; Zhang, Y.; Wang, J., *Angew. Chem. Int. Ed.* **2013**, *52*, 10573-10576.
169. Laube, M.; Gassner, C.; Sharma, S. K.; Günther, R.; Pigorsch, A.; König, J.; Köckerling, M.; Wuest, F.; Pietzsch, J.; Kniess, T., *J. Org. Chem.* **2015**, *80*, 5611-5624.
170. Reeves, J. T.; Malapit, C. A.; Buono, F. G.; Sidhu, K. P.; Marsini, M. A.; Sader, C. A.; Fandrick, K. R.; Busacca, C. A.; Senanayake, C. H., *J. Am. Chem. Soc.* **2015**, *137*, 9481-9488.
171. Zhou, C.; Liu, Q.; Li, Y.; Zhang, R.; Fu, X.; Duan, C., *J. Org. Chem.* **2012**, *77*, 10468-10472.